Dissertation

submitted to the

Combined Faculty of Natural Sciences and Mathematics

of the Ruperto Carola University Heidelberg, Germany

for the degree of

Doctor of Natural Sciences

Presented by

M.Sc. Isabell Schneider

born in Lörrach, Germany

Oral examination: 17.03.2021

Investigating spindle assembly in mammalian zygotes using light sheet microscopy

---

Referees: Dr. Takashi Hiiragi

Dr. Sylvia Erhardt

PUBLICATION LIST

Schneider, I.*, M. de Ruijter-Villani*, M.J. Hossain, T.A.E. Stout, and J. Ellenberg. 2020. Non-rodent mammalian zygotes assemble dual spindles despite the presence of paternal centrosomes. *bioRxiv*. 2020.10.16.342154. doi:10.1101/2020.10.16.342154.

Schneider, I., and J. Ellenberg. 2019. Mysteries in embryonic development: How can errors arise so frequently at the beginning of mammalian life? *PLoS Biol.* 17. doi:10.1371/journal.pbio.3000173.

Reichmann, J.*, M. Eguren*, Y. Lin*, I. Schneider*, and J. Ellenberg. 2018. Live imaging of cell division in preimplantation mouse embryos using inverted light-sheet microscopy. Methods Cell Biol. 145:279–292. doi:10.1016/BS.MCB.2018.03.030.

Reichmann, J., B. Nijmeijer, M.J. Hossain, M. Eguren, I. Schneider, A.Z. Politi, M.J. Roberti, L. Hufnagel, T. Hiiragi, and J. Ellenberg. 2018. Dual-spindle formation in zygotes keeps parental genomes apart in early mammalian embryos. Science. 361:189–193. doi:10.1126/science.aar7462.

Schneider, I., and P. Lénárt. 2017. Chromosome Segregation: Is the Spindle All About Microtubules? *Curr. Biol.* 27. doi:10.1016/j.cub.2017.09.022.

* These authors contributed equally.
Parts of this thesis have been published in the above-mentioned articles.

ABSTRACT

Mammalian life starts with the formation of a zygote through fertilization of an oocyte by the sperm; subsequently the first mitotic divisions take place. Errors in these earliest divisions can easily propagate throughout preimplantation development and can lead to pregnancy loss prior to its clinical recognition. Albeit one would expect that these divisions should be particularly safeguarded due to their fundamental importance for reproduction, the first embryonic mitoses are much more error-prone than mitosis in somatic cells. Interestingly, this is a paradox observed in all mammalian species analyzed so far, including human.

The essential structure mediating chromosome segregation is the microtubule-based mitotic spindle, which has been extensively studied in cell-free systems, somatic cells and embryonic model systems, such as *Drosophila melanogaster* and *Caenorhabditis elegans*. By contrast, in mammals, we understand surprisingly little about the mechanisms and regulation of spindle assembly during preimplantation development.

In this thesis I therefore studied the assembly of the first mitotic spindle in two mammalian model systems, mouse and cow, to obtain insights into the mechanisms that may underlie early embryonic division errors. In both systems, I found that the first mitotic division is mediated by a pair of spindles that handle the parental genomes separately. The data indicate that this dual spindle assembly is predominantly driven by chromosomal microtubule nucleation and subsequent self-organization of the microtubules around the two spatially separated genomes.

First, I used the mouse embryo—a powerful and well-established research model—in which the dual spindle assembles in the presence of many acentriolar cytoplasmic microtubule organizing centers (MTOCs) that were assumed to functionally replace centrosomes. I developed several imaging-based assays to investigate spindle assembly mechanisms in live and fixed mouse embryos and could show that, surprisingly, initial spindle microtubules in the zygote are formed by chromosomal and kinetochore-based microtubule nucleation. By contrast, only some of the many cytoplasmic MTOCs participate in spindle assembly and seem to be more important for stabilization of the spindle than for its initial assembly.

Second, I studied zygotic spindle assembly in the bovine embryo, which is in general physiologically more similar to humans, and in particular, the cow zygote also inherits a centrosome from the sperm. However, it is much less established for cell biological research.

Using custom-developed light sheet microscopy, I could image live bovine embryos with high spatial and unprecedented temporal resolution and thereby established this system as a valuable model to study cellular mechanisms of mammalian preimplantation development. I could show that dual spindle assembly is conserved in bovine zygotes, despite the presence of two centrosomes. Interestingly, I discovered that the centrosomes are not very active in spindle assembly, and it is thus very likely that the spindle assembly mechanism of chromosomal nucleation and microtubule self-organization, which I observed in the mouse model, is conserved.

Overall, my work shows that dual spindle assembly can be found in both acentrosomal and centrosomal zygotes. It is thus likely that this mechanism is conserved across mammalian species, where the parental genomes are present in separate pronuclei in early mitosis. This is also the case in human embryos, and thus my work has significant biomedical implications. In addition, the data presented in this thesis further strengthen the hypothesis that likely also in human zygotes the parental genomes do not mix during the first mitosis, which would have substantial legal and ethical implications for the definition of the beginning of human life.

ZUSAMMENFASSUNG

Das Leben eines Säugetiers beginnt mit der Befruchtung einer Eizelle durch ein Spermium, wodurch sich eine Zygote bildet; im Anschluss finden die ersten mitotischen Zellteilungen statt. Fehler, die in den ersten Teilungen passieren, können in den folgenden Zellteilungen des frühen Embryos leicht weitergegeben werden und sich damit während der Präimplantationsentwicklung vermehren, was häufig zu einem natürlichen Abbruch der Schwangerschaft führt, bevor diese überhaupt klinisch erkannt wird. Obwohl man annehmen würde, dass diese ersten Zellteilungen aufgrund ihrer fundamentalen Bedeutung für die Fortpflanzung besonders zuverlässig und kontrolliert ablaufen, sind sie viel fehleranfälliger als mitotische Teilungen in somatischen Zellen. Interessanterweise lässt sich dieses Paradoxon in allen bislang untersuchten Säugetierarten, inklusive dem Menschen, beobachten.

Entscheidend für die Verteilung der Chromosomen ist die Mikrotubuli-basierte mitotische Spindel, die in zellfreien Systemen, somatischen Zellen, sowie in Embryomodellen, wie zum Beispiel *Drosophila melanogaster* und *Caenorhabditis elegans*, ausgiebig untersucht wurde. Im Gegensatz dazu verstehen wir erstaunlich wenig darüber, wie sich die Spindel während der Präimplantationsentwicklung von Säugetieren formt, und wie diese Mechanismen kontrolliert werden.

Um besser verstehen zu können, welche Mechanismen den Teilungsfehlern im frühen Embryo zu Grunde liegen, habe ich in dieser Thesis daher untersucht, wie sich die erste mitotische Spindel in der Zygote zweier unterschiedlicher Tiermodelle formt, in der Maus und in der Kuh. In beiden Modellen konnte ich beobachten, dass die erste Teilung durch ein Spindelpaar erfolgt, wobei eine der beiden Spindeln das mütterliche, und die andere das väterliche Erbgut organisiert. Die Daten weisen darauf hin, dass sich Zwillingsspindeln dadurch bilden, dass Spindelmikrotubuli hauptsächlich um Chromosomen nukleiert werden und sich anschließend selbständig um die beiden räumlich getrennten Genome organisieren. Zuerst habe ich die Teilung in der Zygote des für die Forschung sehr bedeutenden und etablierten Mausmodell untersucht. Darin bilden sich die Zwillingsspindeln in Anwesenheit vieler nicht-centriolärer Mikrotubuli-Organisationszentren (MTOCs), bei denen man davon ausging, dass sie die Centrosomen im frühen Mausembryo funktionell ersetzen. Ich habe mehrere Mikroskopie-basierte Experimente mit lebenden und fixierten Mausembryonen entworfen und durchgeführt, um zu untersuchen, wie sich die Spindeln bilden.

Überraschenderweise formen sich die ersten Spindelmikrotubuli in der Zygote durch Chromosomen- und Kinetochor-basierte Nukleation. Wider Erwarten sind nur wenige der cytoplasmatischen MTOCs tatsächlich an der Spindelformierung beteiligt und sie scheinen wichtiger für die Stabilisierung der Spindel zu sein als für ihren anfängliche Aufbau.

Im Anschluss habe ich die zygotische Spindelformierung im Kuhembryo untersucht, welcher dem humanen Embryo physiologisch generell ähnlicher ist; insbesondere erhält die Kuhzygote auch ein Centrosom vom Spermium. Dieses Modell ist aber weitaus weniger in der zellbiologischen Forschung etabliert.

Ich habe ein speziell entwickeltes Lichtblattmikroskop verwendet, um lebende Kuhembryonen mit hoher räumlicher und bisher noch nicht erreichter zeitlicher Auflösung aufzunehmen. Damit habe ich den Kuhembryo als wertvolles Modell etabliert, um zelluläre Mechanismen während der Präimplantationsentwicklung zu untersuchen. Ich konnte zeigen, dass die Formierung von Zwillingsspindeln in der Kuhzygote konserviert ist, obwohl zwei Centrosomen vorhanden sind. Interessanterweise sind die Centrosomen nicht sehr aktiv in der Spindelformierung und es ist sehr wahrscheinlich, dass die Mechanismen der Mikrotubuli-Nukleation um Chromosomen und anschließender Eigenorganisation, wie ich sie im Mausmodell beobachtet und beschrieben habe, konserviert sind.

Insgesamt zeigt meine Arbeit, dass die Bildung von Zwillingsspindeln in Zygoten mit und ohne Centrosomen beobachtet werden kann. Es ist daher wahrscheinlich, dass dieser Mechanismus in Säugetieren konserviert ist, in denen sich die elterlichen Genome in der Zygote zu Beginn der ersten Mitose in unterschiedlichen Vorkernen befinden. Das gilt auch für die menschliche Zygote und meine Arbeit hat daher eine signifikante biomedizinische Bedeutung. Da die Daten dieser Arbeit die Hypothese weiter stärken, dass sich auch in der menschlichen Zygote die elterlichen Genome während der ersten Zellteilung nicht mischen, hat diese Arbeit vermutlich auch weitreichende rechtliche und ethische Implikationen für die Definition vom Beginn des menschlichen Lebens.

TABLE OF CONTENT

LIST OF ABBREVIATIONS

AF	Alexa Fluor
APC/C	Anaphase promoting complex/cyclosome
ATP	Adenosine triphosphate
AUC	Area under the curve
BSA	Bovine serum albumin
C. elegans	*Caenorhabditis elegans*
CAKs	Cdk-activating kinases
CAMSAP	Calmodulin regulated spectrin-associated protein
CCAN	Constitutive centromere associated network
Cdc	Cell division cycle
Cdk	Cyclin dependent kinases
CDK5RAP2	Cdk5 regulatory subunit-associated protein 2
Cep192	Centrosomal protein 192
Cep192	Centrosomal protein 152
CKIs	Cdk inhibitors
COCs	Cumulus-oocyte complexes
CPAP	Centromere protein J
CPC	Chromosomal passenger complex
Cyclins	Cycling proteins
Dgt	Dim gamma-tubulin
DMSO	Dimethyl sulfoxide
DNA	Deoxyribonucleic acid
EB1	Microtubule end binding protein 1
EBs	Microtubule end binding proteins
ELYS	Embryonic large molecule derived from yolk sac
FEP	Fluorinated ethylene propylene
FWHM	Full width half maximum
G_1-phase	Gap phase 1
G2-phase	Gap phase 2

GCP	Gamma-tubulin complex component
GDP	Guanosine diphosphate
GTP	Guanosine triphosphate
H2B	Histone 2B
HAUS	Human Augmin complex
hCG	Human chorionic gonadotropin
HEPES	4-(2-hydroxyethyl)-1-piperazineethanesulfonic acid
HSET	Kinesin-like protein KIFC1
ICM	Inner cell mass
IF	Immunofluorescence
INCENP	Inner centromere protein
iSPIM	Inverted single plane illumination microscope
IVF	*In vitro* fertilization
K-fibers	Kinetochore fibers
KANSL	KAT8 regulatory NSL complex subunit
Kif15	Kinesin like protein KIF15
KMN network	KNL1, Mis12, Ndc80 network
LINC	Linker of nucleoskeleton and cytoskeleton
M-phase	Mitosis and cytokinesis
MAP4	Microtubule associated protein 4
MAPs	Microtubule-associated proteins
MCAK	Mitotic centromere-associated kinesin
MCRS1	Microspherule protein 1
MOPS	3-Morpholinopropane-1-sulfonic acid
mRNA	Messenger RNA
MTOCs	Microtubule organizing centers
NEBD	Nuclear envelope breakdown
NEDD1	Neural precursor cell expressed, developmentally down-regulated 1
NPC	Nuclear pore complex
NTF2	Nuclear transport factor 2
NuMA	Nuclear mitotic apparatus protein 1

PBS	Phosphate buffered saline
PBS-T	3 % BSA in PBS with 0.1 % Triton X-100
PCM	Pericentriolar material
PFA	Paraformaldehyde
PIPES	1,4-Piperazinediethanesulfonic acid
Plk	Polo-like kinase
PMSG	Pregnant mare's serum gonadotropin
PN	Pronucleus
PP2A	Protein phosphatase 2A
PRC1	Protein regulator of cytokinesis 1
R26	Rosa26
Ran	Ras related nuclear protein
RanGAP1	Ran GTPase activating protein 1
RCC1	Regulator of chromatin condensation 1
RNA	Ribonucleic acid
ROS	Reactive oxygen species
S-phase	Synthesis phase
SAC	Spindle assembly checkpoint
SAFs	Spindle assembly factors
SAS-6	Spindle assembly abnormal protein 6 homolog
SOF	Synthetic oviductal fluid
SPIM	Single plane illumination microscopy
TMR	Tetramethylrhodamine
TPX2	Targeting protein for Xenopus kinesin like protein 2
WT	Wild type
X. laevis	*Xenopus laevis*
γTURC	Gamma-tubulin ring complex
γTUSC	Gamma-tubulin small complex

1 INTRODUCTION

1.1 Cell division errors at the beginning of mammalian life

During cell division, the two copies of genetic material are equally distributed among the newly forming daughter cells. Of each chromosome, which consists of two sister chromatids, one intact chromatid is sorted into the nucleus of each daughter cell. If the chromatids are not properly segregated during mitosis, numerical errors can arise, so-called aneuploidies. But usually, chromosome segregation is extremely faithful in mammalian somatic cells: Using single cell sequencing of human skin and brain cells, it has been shown that aneuploidy occurs on average in less than 1 % of these cells and even in liver cells of donors with an alcohol or alternative drug history, aneuploidy frequency did not exceed 4 % (*1*). Female meiosis in humans and other mammals often goes along with whole chromosome loss or gain and increasing maternal age seems to increase the frequency of these errors (*2*). However, the higher error rate was assumed to result from the different nature of the meiotic divisions and the long oocyte arrest, which can last several decades [discussed in (*3*)]. It is acknowledged in the field that the age effect mostly results from premature separation and distribution of the two sister chromatids in meiosis I, when in principle only the intact homologous chromosomes should be segregated.

Surprisingly, it has also been shown that more than 50 % of preimplantation embryos in fertility clinics contain aneuploid cells, which do not only result from meiotic errors, but also from errors in post-zygotic mitosis that occur independent of maternal age (*4*–*9*). Dependent on the stage at which the segregation error occurs, only a subset of cells in the embryo is affected and cells with different chromosomal content constitute the embryo. The reported incidences of this complex mosaic aneuploidy vary, but it has been reported in up to 90 % of human preimplantation embryos in fertility clinics (*6*, *8*, *10*–*14*). Segmental aneuploidies and polyploidy have also been observed in these early embryos, but less frequent (*11*). Although this data comes primarily from analyzing preimplantation embryo biopsies from parents with reduced fertility, and thus, after *in vitro* fertilization of the eggs, it is likely that similarly high frequencies of early aneuploidy occur in embryos conceived naturally. Studies have indicated that only ~30 % of natural conceptions result in a live birth and most pregnancy losses occur during the preimplantation stage (*15*). Aneuploidies are an important cause for these early pregnancy losses; however, it is worth noting that the timing and the kind of aneuploidies

seem to determine the fate of the embryo as a whole. Embryos with certain single chromosome abnormalities formed during Meiosis (like a trisomy of chromosome 21) frequently survive and develop to term, here all cells of the embryo are affected (*4*). For postzygotic aneuploidies the situation is different. The earlier an error occurs the more cells are affected, and complex mosaic aneuploidies emerge when distinct errors occur at multiple cleavages. The complex aneuploidies seem to account for most early pregnancy losses, as such embryos rarely survive until the blastocyst stage (*4*). However, some mosaic embryos can survive and develop to term (*16*, *17*). In these instances, different mechanisms have been proposed to account for a healthy development. One possibility is that the euploid blastomeres effectively outcompete the aneuploid cells and thus functionally compensate these early mitotic errors (*18*). Alternatively it has been suggested that aneuploid blastomeres can be directly removed by selective apoptosis (*19*). Nevertheless, in fertility clinics, aneuploidy and embryonic mosaicism are reportedly linked to developmental failure and pregnancy loss and they are an obstacle when assessing embryo quality for transfer (*6*, *8*, *13*, *20*, *21*). Thus still, many open questions remain to understand to what degree aneuploidies are compatible with healthy embryonic development.

Interestingly, many mammalian species have similar frequencies of embryonic aneuploidy and mosaicism, as shown in porcine, non-human primate, murine, bovine and equine embryos in the last two decades (*17*, *22–26*). But despite the high frequency with which embryonic blastomeres divide incorrectly, we understand very little about the underlying mitotic mechanisms. While we have gained detailed insights into the complex mechanisms of mitosis in many model systems and somatic cells, we are only just starting to get an idea how the mitotic apparatus and the cell cycle control mechanisms actually function or malfunction, and how they might be regulated during mammalian preimplantation development.

1.2 The regular cell cycle

Cell duplication is the basis for the continuity of life. Before producing a new cell an existing one has to duplicate its genomic information to then distribute it equally among the forming two daughter cells. Usually, duplication of the genome also goes along with duplication of the organelles and cellular macromolecules so that the cells do not shrink with each division. This sequence of events is called the cell cycle (Schematic shown in Figure 1). The cell cycle consists

of the M-phase and interphase. M-phase comprises mitosis—the division of the chromosome copies, called the sister chromatids—and cytokinesis—the division of the cytoplasm. Interphase is subdivided into G_1, S- and G_2-Phase. In S-phase the chromosomes are duplicated in preparation for the next M-phase. M-phase and S phase are interspersed by transitional gap (G) phases: G_1 and G_2, respectively. These gap phases allow for cell growth and duplication of the cytoplasmic components and checkpoints in these phases are also essential to tightly control cell cycle progression. At each phase transition these control mechanisms assess whether the environmental and cellular criteria are fulfilled to enter the next cell cycle phase. Such restriction points are at the end of G_1 and the G_2-M transition. After passing these points, cells are committed irreversibly to progress through the next phase. During the usually long G_1-phase, nutrients and growth factors also determine whether the cell enters the next cycle at all. Here, cells may also temporarily or permanently exit the cell cycle by entering the non-proliferative G_0-phase, a resting stage (*27*).

The cell cycle is largely driven by cycling proteins (Cyclins), whose synthesis and proteasomal degradation oscillate [reviewed in (*28*)]. These Cyclins bind to so-called Cyclin dependent kinases (Cdks) and regulate their enzymatic activity, thus modulating the phosphorylation of proteins involved in the different cell cycle phases. The activity of Cdks is further regulated by complementary mechanisms. Cdk-activating kinases (CAKs) boost the kinase activity even further by changing the confirmation of the active site of Cyclin-bound Cdks through site-specific phosphorylation (*29*). Conversely, inhibitory phosphorylations by other kinases or binding of inhibitory proteins (CKIs) to the Cdk-Cyclin complex can inactivate the Cdks through structural rearrangements.

Thus, in addition to regulated expression of Cyclin encoding genes, also the regulated transcription of CKIs and other Cdk regulators determine Cdk activity and cell cycle progression. The cell cycle phases are linked as Cdk activity of one phase is often required to initialize Cyclin synthesis required for Cdk activity of the next phase.

1.2.1 Mitosis

Mitosis itself is characterized by specific phases (*27*), Figure 1 shows a schematic overview. The earliest stage of mitosis is prophase. At the end of the G_2-phase, the genetic material is loosely packed within the nucleus and the sister chromatids are intertwined and held together by Cohesin protein complexes. In prophase, the chromosomes start to compact and

condense though architectural changes in chromatin organization, but the sister chromatids remain linked through Cohesin protein complexes. When the nuclear envelope breaks apart, the microtubule spindle forms around the condensing chromosomes starting to congress them together during prometaphase. In metaphase, this spindle is organized as bipolar microtubule array. The chromosomes are allocated centrally, and the two sister chromatids of each chromosome are linked to opposite poles by microtubules. Forces between spindle poles further congress the rod-shaped chromosomes to the very center of the spindle, where they form the metaphase plate. In anaphase A, chromatid cohesion is removed, and the sister chromatids are segregated by shortening kinetochore microtubules pulling them towards the opposite spindle poles (*30*). The poles are further pushed apart in anaphase B (*31*), and the two batches of segregated chromatids are finally enclosed into two new nuclei during telophase. Cytokinesis immediately follows mitosis and completes cell division by partitioning the cytoplasmic components among the genetically identical daughter cells.

The early phases of mitosis from prophase until metaphase, are usually triggered by high Cdk1 activity regulated by the mitotic Cyclins: Cyclin B dependent Cdk1 seems to initiate chromosome condensation, nuclear envelope breakdown (NEBD), cytoskeletal and Golgi rearrangements as well as spindle assembly and sister chromatid attachment to microtubule bundles through Cdk1 mediated phosphorylation of proteins involved in these processes. Cdk1 is supported, but also in part regulated, by two other mitotic kinase families: The Aurora kinases (especially Aurora kinase A and B) and Polo-like kinases (Plk, especially Plk1) [reviewed in (*32*)].

In most cell types, Cyclin B levels increase at the G_2-M transition, thus the concentration of Cyclin B-Cdk1 complexes increases. However, even though the active site of the complex is phosphorylated by a CAK, it remains inactive as inhibitory kinases of the Wee1 family add two further inhibitory phosphates (*33*, *34*). The final activation and regulation of the Cdk1 complex at mitotic entry is thus achieved by the phosphatase Cdc25, which removes these inhibitory phosphorylations (*35*, *36*). At the same time Wee1 kinases become suppressed and degraded (*37*). How Cdc25 itself is activated in mammalian somatic cells to initialize Cdk1 activity at mitotic entry is still not entirely clear. The Cyclin A-Cdk1 complex might play an important role. Cyclin A-Cdk1 seems to be differently affected by the inhibitory Wee1 kinases compared to Cyclin B-Cdk1. There is some evidence that low Cyclin A-Cdk1 activity might initially help to phosphorylate and activate Aurora A in the nucleus, potentially with the adaptor protein

WAC. This complex might in turn activate Plk1 (*38*). In the cytoplasm, Plk1 is activated by phosphorylation of the scaffold protein Bora through Aurora A (*39*, *40*) and can subsequently accumulate in the nucleus (*41*). Plk1 is the kinase finally phosphorylating and activating the Cdc25C phosphatase (*38*, *42*). Active Cdc25 triggers fast mitotic entry as Cyclin B-dependent Cdk1 activity will quickly rise and phosphorylate many downstream targets to initiate mitosis. This activity is further stimulated by positive feedback mechanisms, once Cyclin B-Cdk1 is active. Additionally, the Cyclin-Cdk1 activity at mitotic entry is modulated by inhibiting and balancing inhibitory phosphatases [reviewed in (*43*)].

While early mitotic events are dependent on protein phosphorylation driven by increasing Cyclin B expression and thus high Cdk1 activity, the metaphase-to-anaphase transition, when sister chromatids are segregated, is initialized by protein degradation. This is regulated through the Anaphase promoting complex/Cyclosome (APC/C) [reviewed in (*44*)]. This E3-ligase polyubiquitiylates proteins — which keep the cell in metaphase — and targets them for proteasomal degradation, allowing the cell to progress into anaphase. Among others, the APC/C targets the mitotic Cyclins for degradation (Cyclin A and B). Thus, the respective Cdks are inactivated and their targets become progressively dephosphorylated by phosphatases, leading to exit from M-phase. The APC/C comes in two flavors, one is active from mid mitosis until anaphase onset, the other one from late mitosis until late G_1-phase. The two different activities of the APC/C are a consequence of differential activator binding (*45*). One activator protein is Cdc20, which binds APC/C at the metaphase to anaphase transition, the second is Cdh1, binding from anaphase onwards. The two activator proteins determine the substrate recognition of the APC/C and thus mediate ubiquitylation of different targets at different times (*46*, *47*). Early in mitosis both APC/C and Cdh1 are phosphorylated due to Cdk1 activity, allowing Cdc20 to bind to the APC/C (*48*, *49*). APC/C^{Cdc20} then triggers Cyclin degradation and thereby leads to a reduction in Cdk1 activity, consequently dephosphorylating Cdh1 and APC/C (*48*). This allows Cdh1 to bind to the APC/C and APC/C^{Cdh1} as well as APC/C^{Cdc20} ubiquitylate Cdc20 leading to its degradation (*50*).

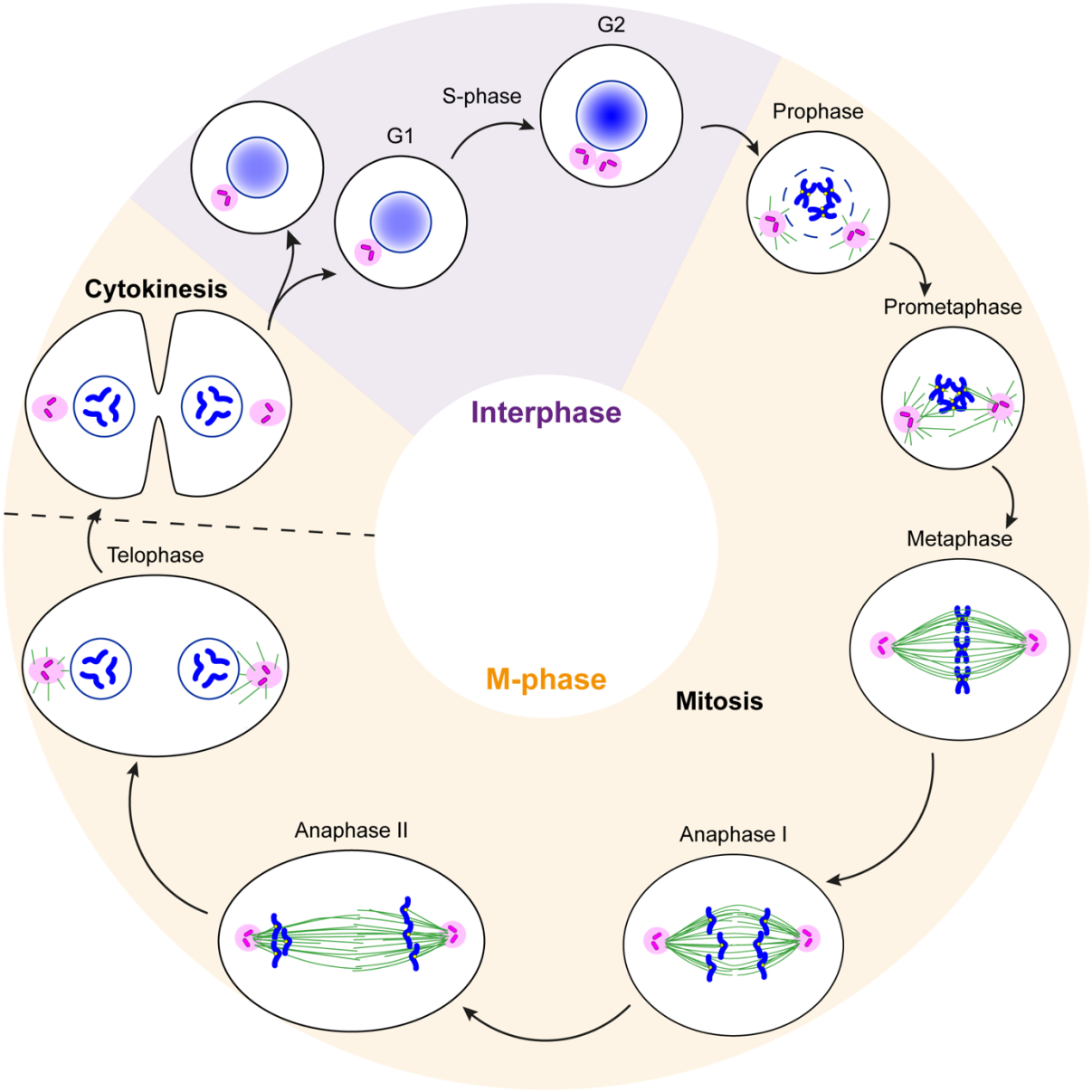

Figure 1: The somatic cell cycle is the basis of maintaining eukaryotic life. Interphase consists of two gap phases (G_1, G_2) and S-phase, in which the genomic information as well as the centrosomes are duplicated. M-phase consists of mitosis (the division of the genome) and cytokinesis (the division of cytoplasm). The illustration further highlights the sequence of events in mitosis, from prophase until telophase.

1.3 The components of the spindle and their contribution to assembly

To segregate and move sister chromatids into opposing directions in anaphase, the chromosomes need to be reorganized to allow faithful separation without any damage, and a bipolar spindle has to be assembled which can exert the required bidirectional pulling forces. The study of the mitotic spindle has started in 1882, when Flemming described the structure in animal cells (*51*), and we still do not understand the structure and the assembly in full complexity. Several exceptional features make it difficult to study: It is a transient, but

large structure within the cell, mainly composed of microtubules. But microtubules alone cannot segregate the chromatids. Instead, many copies of more than 800 additional different proteins collectively interact with the microtubules, the centrosomes and kinetochores leading to a complex multimolecular machinery that assures faithful sister chromatid segregation (*52*). Additionally, the spindle is one of the most dynamic cytoskeletal structures; it assembles a bipolar array from a very different interphase cytoskeletal organization, then dynamically segregates chromatids, and finally disassembles within about one hour in somatic cells. The basis of these complex rearrangements are dynamic microtubules with a short half-life of ~1 min (*53*). After introducing how chromosomes are restructured and prepared for sister chromatid segregation and which mechanisms drive microtubule dynamics and organization, I am later going to describe how the different spindle components regulate the intrinsic microtubule dynamics to guide spindle assembly.

1.3.1 Mitotic Chromosomes

The main purpose of mitosis is to ensure faithful distribution of the duplicated chromosomes to emerging daughter cells. Thus, the higher order structure of chromosomes has to change substantially. Chromosomes that are soft and amorphous during interphase have to be compacted to stiffer rod-shaped structures and the sister chromatids have to be disentangled. Achieving this structural change in early mitosis is essential for faithful chromatid segregation as errors in this rearrangement can lead to rupture of chromatids or mis-segregation of entire chromatids [reviewed in (*54*)].

1.3.1.1 Chromosome compaction

Restructuring is reported to be sequence independent and to rather occur along the entire length of the chromatin molecules (*55*). In mammals, different factors contribute to this chromosome compaction [reviewed in (*56*)]: To an unknown degree mitotic histone modifications and thereby changed protein interactions might favor a more compact structure, but the field currently assumes that especially the two isoforms of the Condensin protein complexes, as well as Topoisomerase IIα, drive the higher order compaction. It is also assumed that the chromokinesin KIF4A supports the restructuring. How these restructuring factors are activated at mitotic onset is not entirely clear, but it has been reported that two of the Condensin II subunits are phosphorylated by Plk1 and Cdk1, respectively (*57*, *58*).

Condensin II then seems to form large DNA loops along the chromosomal axis in early prophase driving the first axial compaction (*59*, *60*), while Condensin I only localizes to chromosomes in prometaphase after NEBD (*59*). From here until metaphase, and even until shortly after anaphase onset, chromosomes condense even further [reviewed in (*56*)]. It has been long proposed that Condensins organize the sister chromatid axes in mitosis (*61*), and these recent experiments support the hypothesis. In the current model, Condensin I would subdivide the large initial loops formed by condensin II with nested smaller loops after NEBD and again after anaphase onset (*59*, *60*).

1.3.1.2 Resolving sister chromatids

During replication in S-phase, the sister chromatids become catenated. They intertwine, but they are also tethered together topologically through the ring-like cohesin protein complexes. Cohesin usually interacts with chromatin dynamically, but stable binding and cohesion is established during replication (*62*). This is achieved by acetylation of Cohesin during replication and the exchange of Cohesin binding partners (*63*, *64*). Usually, Cohesin binds to Wapl, which renders its interaction with chromatin unstable. In contrast, the protein Sororin antagonizes Wapl binding to Cohesin, and stabilizes Cohesin mediated tethering of sister chromatids (*64*, *65*). To resolve the sister chromatids in mitosis, this stable interaction is released in two steps: firstly in prophase (prophase pathway) and finally in anaphase (*66*). In prophase, stable cohesin interaction is released along the chromosome arms, but maintained at the centromere regions. This ensures that the sister chromatids do not segregate prematurely before the chromosomes are properly bi-oriented within the spindle. The centromeric cohesion is only removed at anaphase onset. During the prophase pathway, the dynamics of cohesin are reestablished when Wapl replaces Sororin binding to cohesin again. This is achieved through phosphorylation of the cohesin SA subunit and of Sororin. Since Cdk1 and Aurora B phosphorylate Sororin (*67*), and Plk1 phosphorylates the SA subunit [reviewed in (*68*)], cohesins dissociate from the sister chromatid arms in a timely fashion in early mitosis. Not only the protein tethers are removed in prophase, most parts of the sister chromatids become decatenated by Topoisomerase IIα, which seems to act in dependency of condensin II (*69*, *70*). Later, the remaining catenation in centromeric regions can in principle be removed by pulling forces that microtubules and associated motors exert (*71*).

But while cohesion is resolved at the sister chromatid arms in prophase, it is protected at the centromeric regions by Shugoshin 1 and the phosphatase PP2A until anaphase. The Shugoshin 1 protein, which localizes to the centromeric region, becomes phosphorylated and activated by Cdk1 to directly interact with centromeric Cohesins. Together with its binding partner phosphatase PP2A, Shugoshin 1 locally keeps Sororin and the cohesin SA subunit dephosphorylated (*72*, *73*), and thus maintains the stable sister chromatid tethering at this specific chromosome site. In the past few years, it has also been shown that other pathways and factors can protect the centromeric cohesion, e.g. the Haspin kinase can bind to cohesin and antagonize Wapl mediated release of cohesin tethers at sister chromatid centromeres (*74*). It has also been reported that the chromosomal passenger complex (CPC) at the inner centromeric region supports the stable centromeric cohesion of the sister chromatids until all chromosomes are properly bi-oriented, but the underlying mechanism is unclear (*75*).
In anaphase, Separase enzymatically cleaves the centromeric cohesin complexes (*66*, *76*). The earlier mentioned ubiquitin ligase APC/C achieves the timely activation of Separase. Usually, multiple mechanisms secure the inactivation of Separase until all chromosomes are faithfully attached and mitosis can proceed into anaphase. Securin binding to Separase or Separase phosphorylation by Cyclin-Cdk1 maintain Separase inactive (*66*, *76*, *77*). And very recently, it has been shown that Shugoshin-Mad2 binding to Separase also redundantly inhibits Separase in mitotic cells (*78*). Securin and the Shugosin-Mad2 complex are among the APC/C's substrates, which become ubiquitylated and subsequently release Separase leading to its activation. Thus, APC/C activity at mid mitosis allows Separase to cleave the remaining centromeric cohesin protein complexes and stimulates the final sister chromatid separation. The inhibitory phosphorylation is also removed by phosphatases, when Cyclin B is degraded in response to its ubiquitylation by the APC/C.

1.3.1.3 Individualizing chromosomes during mitosis

To keep single chromosomes and the sister chromatid arms individualized after NEBD until telophase, Ki-67, a protein from the chromosome periphery, has been reported to densely cover the rod shaped chromosomes and to act as surfactant, which either sterically and/or electrostatically hinders individualized chromosomes to collapse on top of each other until the chromosomes are properly segregated (*79*). Intriguingly, upon mitotic exit Ki-67 reverses its behavior and mediates the clustering of chromosomes and excludes bulk cytoplasm from

the newly forming nucleus, which for example helps to exclude mature ribosomes that are too big to be exported through the nuclear pore complex later on (*80*).

1.3.2 Kinetochores

Kinetochores belong to the largest, non-polymeric protein assemblies found in cells. They crucially connect the chromosomes to the microtubules of mitotic and meiotic spindles (*81*), but also function as mechanosensors to assess proper chromosome bi-orientation.

They form on the centromeres, often specific locations on chromosomes that are marked epigenetically, mostly by CENP-A, a variant of histone H3 (*82*, *83*).

Structurally, kinetochores can be broadly subdivided into an inner and outer kinetochore. The inner kinetochore contains the constitutive centromere associated network (CCAN), which itself consists of multiple subcomplexes (*81*, *84*). Its major task is to form a very specific interaction with the centromeric CENP-A and subsequently enable the formation of the outer kinetochore (*84*). The outer kinetochore is the microtubule interaction surface and contains the KMN network, a protein complex consisting of KNL1, Mis12 and Ndc80 (*85*). While the CCAN is attached to the centromere throughout the cell cycle, the KMN network only gets recruited during mitosis to facilitate microtubule attachment (*86*).

The KMN network is further heavily regulated to ensure that it only allows stable end-on attachments later in mitosis, when it is most likely that kinetochores are attached to microtubules in an amphitelic fashion, meaning that one sister kinetochore is attached to microtubule bundles from only one of the opposing poles, respectively (*87*–*89*).

In addition to its role in mediating the interaction of spindle microtubules with the chromosomes, the kinetochore is also the central signaling hub for the spindle assembly checkpoint (SAC), an essential mitotic checkpoint ensuring proper chromosome bi-orientation. As already discussed earlier, the APC/C^{Cdc20} complex is required to enable the final release of sister chromatid cohesion. The SAC ensures that this does not happen prematurely (*90*). The SAC primarily acts through the mitotic checkpoint complex consisting of the proteins Mad2, Bub3, BubR1 and Cdc20 (*91*–*94*). As long as kinetochores are not occupied with stable microtubule ends, this complex is produced and binds the APC/C complex, effectively inhibiting it until proper amphitelic kinetochore-microtubule interactions are established.

1.3.3 Microtubules

Microtubules are cytoskeletal structures with α- and β-tubulin as their smallest building blocks. These two tubulins build heterodimers that bind non-covalently head to tail (*95*) and longitudinally in a continuous way to form protofilaments. 13-15 protofilaments bind laterally and form the hollow microtubule cylinder with a ~25 nm diameter. Such tubes can spontaneously assemble from soluble heterodimers above a critical concentration [reviewed in (*96*)]. Due to the head to tail interaction of the heterodimers and the parallel interaction of the protofilaments, the individual protofilaments and the assembled microtubule are polarized (*97*). The end of the microtubule with the β-subunits exposed is called the plus end, the end with the α-subunits at the periphery is called the minus end (*98*). The head to tail interactions of the monomers and dimers, and the lateral interactions between protofilaments also hold the tubulin subunits at the microtubule core in place [reviewed in (*99*)]. Loss and addition of subunits occurs mostly at the microtubule ends, although incorporation of tubulin dimers into the mechanically damaged or defective lattice has also been reported more recently (*100*, *101*).

1.3.3.1 Intrinsic microtubule dynamics

Microtubule ends are dynamic, they grow and shrink—polymerize and depolymerize. The polymerization rate can quickly change, fast growth can be interrupted by rapid shrinkage (catastrophe), but this shrinkage can also be 'rescued', and the tip can grow again. This rapid and stochastic change between growth, catastrophe and rescue of microtubules, is called dynamic instability (*102*). The conformation of the tubulin heterodimers, that form the protofilament are crucial to determine this balance.

α- and β-tubulin each have a binding site for guanine nucleotides. The so-called N-site within α-tubulin binds guanosine triphosphate (GTP) non-exchangeably, trapping it at the heterodimer interphase (*95*). The E-site within β-tubulin binds GTP exchangeably in the soluble tubulin dimer as well as in the polymer (*103*). Once a new heterodimer is added onto the tip of an existing protofilament, the GTP bound β-tubulin is hydrolyzed through the intrinsic GTPase activity (*103*, *104*), but the resulting GDP remains stably bound (*103*).

Upon hydrolysis of the β-tubulin bound GTP, the conformation of the tubulin dimer changes, building up strain in the lattice (*105*, *106*), and the whole tubulin polymer with bound GDP

becomes more susceptible to depolymerization. *In vitro*, protofilaments with GTP caps are straight and make regular lateral contacts within the microtubules, but tips with GDP bound tubulin dimers become curved and due to the energy release at hydrolysis the protofilaments rapidly peel off (*107*). The microtubule tip structure itself is very diverse [reviewed in (*99*)] and in addition to protofilament curvature, sheet like structures can form and the tips of the length of laterally bound protofilaments can vary resulting in a tapered structure of the entire tip (*107*, *108*), influencing the overall dynamics.

Hydrolysis and polymerization happen at different rates and the polymerization rate depends on the concentration of free tubulin dimers (*103*). Thus, if a new heterodimer subunit can be added to a protofilament before the tip located β-tubulin hydrolyzes the GTP, the polymer can start to form a stable GTP cap. At low growth rates, the microtubule tip region contains mostly tubulin dimers bound to GDP and is thus less stable: The microtubule depolymerization rate is two to three orders of magnitude higher in the GDP bound state than if it is GTP-bound (*102*, *109*, *110*). In principle, microtubules can shrink and grow at both ends, however polymerization and depolymerization rates strongly vary between them (*111*) and they grow faster at the plus ends than at the minus ends (*102*, *111*).

Modelling studies and experimental *in vitro* studies using TIRF microscopy and laser tweezers to investigate single microtubule dynamics have also shown that there is likely one more order of complexity to the intrinsic dynamics of the tips as depolymerization also seems to vary and depend on the free tubulin dimer concentration (*112*). Since tip structure changes upon growth at increasing tubulin concentrations towards presenting more protofilament tips without lateral neighbors, the dissociation of the subunits in these unstable tips is also increased.

And in addition to being dynamic at the ends, it has more recently been evaluated, whether tubulin dimers are also exchanged along the microtubule shaft. In response to mechanical damage, tubulin dimers are added into the damaged lattice *in vitro* and inside cells (*100*, *113*, *114*). And it has even been suggested that dimer exchange within the lattice could be a general mechanism to maintain long lived microtubules that could become defective over time (*101*).

Beyond these microtubule intrinsic dynamics in the cell even more layers of complexity are encountered. Tubulin dimers can assume various conformations in the microtubule lattice, and this determines the stored energy. Additionally, multiple factors can influence these

conformations, and thus the intrinsic dynamic behavior of microtubules: nucleation sites, posttranslational modifications of tubulin, and the interaction with multiple microtubule-associated proteins (MAPs).

In summary the last three decades of research revealed that microtubules are an inherently extremely dynamic and highly regulatable polymer. However, exactly these dynamics are important to allow for the rapid structural rearrangements that occur at the transition from interphase to M-phase and crucial for the formation and function of the mitotic spindle.

1.3.4 Microtubule associating proteins (MAPs)

High throughput screens have identified >200 MAPs, many of which are important for spindle assembly (*115–117*). They can be categorized according to their function and their interactions with microtubules and include microtubule motor proteins, microtubule tip binding proteins, microtubule polymerases and depolymerases, microtubule severing proteins, microtubule cross-linkers, as well as microtubule nucleation factors.

1.3.4.1 Microtubule motor and crosslinking proteins

The microtubule motor proteins use the polar microtubules as tracks to move cargo monodirectionally through the cell along these cytoskeletal structures. Cells contain two major classes of microtubule motor proteins: dynein and kinesins. Other MAPs bundle microtubules together, so called microtubule crosslinking proteins. Both of these MAP types control how microtubules arrange within the cell and respective to each other.

Cells contain one cytoplasmic dynein, which is a 1.4 MDa multiprotein complex and acts as the major minus end directed motor in eukaryotic cells (*118*). It however, only efficiently translocates along microtubules, if it is bound to a cargo-specific adaptor protein and to its universal activator dynactin (*119*).

In contrast, more than 40 different kinesins have been identified, and they can differ in their motor and cargo binding domains and are differentially regulated in space and at different times of the cell cycle [reviewed in (*120*)]. Intriguingly, the location of the microtubule motor domain is essential to define the directionality of the kinesin. While kinesins with the motor domain at their N-terminus move to the plus end, kinesins with the motor domain at the C-terminus move to the minus end and those with the motor domain in the middle depolymerize microtubules (*121*).

Some motors interact with chromosomes and kinetochores and are thus also called chromokinesins. They help to position the chromosomes differently at different phases of spindle assembly during mitosis [reviewed in (*122*)].

Motors can also bind microtubules as cargo and thus transport microtubules alongside each other. With two opposing motor domains, they can even translocate along two microtubules simultaneously and slide them alongside each other in an antiparallel fashion. This is the case for the minus-end directed dynein, and the plus end directed tetrameric vertebrate kinesin-5 (Eg5) and kinesin-12 (Kif15) (*123*–*125*). In addition to being motors, Eg5 and Kif15 can also cross-link microtubule plus ends (*124*, *125*). But there are also purely static microtubule cross-linking MAPs, which bundle microtubule together along their lattice, as e.g. PRC1, which crosslinks antiparallel arrays and helps to control the length of their overlap (*126*).

The motor protein based crosslinks together with specific non-motor crosslinking MAPs, like NuMA—that bundle microtubules together—are also important for the arrangement of astral microtubule arrays contrasting from parallel or antiparallel bundles [reviewed in (*127*)].

1.3.4.2 Microtubule tip binding proteins

Additional regulators of microtubule dynamics are microtubule plus end tracking proteins (+TIPs), which seem to bind to the limited sites of microtubule plus ends in a hierarchical manner (*128*). They can influence the intrinsic microtubule dynamics or recruit microtubule polymerases and depolymerases to the growing end. A well-studied family of these +TIPs are the microtubule end binding proteins (EBs). EB1 as an example binds to the microtubule cap region of growing microtubules and promotes transitions from GTP to GDP bound tubulin [reviewed in (*99*)]. However, EBs can in principle also bind to growing minus ends.

Other minus end binding MAPs (-TIPs) and their functions have only been described in the last decade [reviewed in (*129*)]. In mammals, the CAMSAP proteins associate with stable and dynamic minus ends of microtubules. It has been reported that CAMSAP1 is recruited to growing minus ends, while CAMSAP2 and 3 start decorating the growing lattice from minus ends to stabilize microtubules from depolymerization (*130*, *131*). CAMSAPs organize microtubule minus ends independently of centrosomes and seem to mainly act in interphase (*132*). More recent studies also reported microtubule minus end binding proteins active in mitosis: For example, a protein complex, consistent of KANSL3, KANSL1 and MCRS1, was

suggested to stabilize chromosome microtubules and K-fibers and to regulate their dynamics (*133*, *134*).

Other MAPs induce or stabilize certain dimer conformations within the microtubule lattice that either stabilize or destabilize it, and thus either promote growth or shrinkage [reviewed in (*135*)].

1.3.4.3 Microtubule depolymerases and polymerases

Microtubule depolymerases stabilize the curved dimer conformation of subunits in the lattice end leading to curved protofilaments. This curved conformation is also the conformation of soluble tubulin dimers. Examples for such depolymerases are stathmin and kinesin-13 proteins. Kinesin-13 proteins have evolved their ATP-dependent motor activity to depolymerize microtubule ends (*136*) and it has been suggested that they induce or stabilize the outward curvature of tubulin dimers at microtubule ends and finally release subunits from the filaments. In contrast, microtubule polymerases promote microtubule growth or rescue from catastrophic shrinkage. TOG domain containing XMAP215 proteins (in humans chTOG) seem to progressively interact with tubulin heterodimers at microtubule plus ends. It has been suggested that XMAP215 accumulates and tethers curved soluble tubulin dimers to still curved, bound tubulin at the microtubule plus ends (*137*).

In addition to MAPS, which mediate depolymerization and polymerization at microtubule ends, some MAPs, called severing proteins (including katanin, spastin and fidgetin), can generate internal breaks in the microtubule lattice and thereby promote microtubule disassembly (*138–140*). These enzymes can remove tubulin dimers from the wall of microtubules and thereby promote bending and kinking of the entire microtubule, which often precedes the full severing (*140*).

1.3.4.4 Microtubule nucleation factors

Another important type of MAPs are the microtubule nucleation factors, which allow assembly of filamentous microtubules, even at concentrations of the soluble tubulin dimers below the critical concentration for spontaneous polymerization. γ-tubulin is a critical nucleation factor, which is part of a complex, the γ-tubulin ring complex (γ-TURC). This complex becomes activated for nucleation within confined sites, the microtubule organizing

centers (MTOCs). In most cycling mammalian cells such MTOCs are the centrosomes or the mitotic spindle (*141–143*).

In addition to γ-tubulin, the core of the γ-TURC further consists of GCP2-6. Other proteins as NEDD1 and Mozart 1 and 2 have also been shown to associate with the γ-TURC [reviewed in (*144*)]. Several copies of the small complex γ-TUSC, consistent of GCP2 and 3 and a pair of γ-tubulin, seem to build the core of the mammalian γ-TURC. The assembly of a γ-TUSC ring was shown to consist of seven laterally binding γ-TUSC units. One of the γ-tubulins within the first γ-TUSC overlaps with the second γ-tubulin of the last γ-TUSC unit in the circle, leading to a 13-fold circular arrangement of γ-tubulin units, which was originally suggested to serve as a template to nucleate microtubules consisting of 13 protofilaments, however the radial symmetry of the γ-tubulin pairs does not perfectly match the microtubule protofilament symmetry (*145*). For the actual γ-TURC, the constitution and arrangement of GCPs and γ-tubulin were only recently described (*146*): two of the γ-TUSC subunits are replaced by γ-TURC specific subunits of GCP4-5, and GCP4-6, associating with a pair of γ-tubulin, each (*146*). Together with five γ-TUSC entities, and surprisingly an actin molecule, they formed a spiral arrangement with 14 γ-tubulin 'spokes', not matching the 13-fold symmetry of microtubules. As the radial symmetry of γ-tubulins in either the γ-TUSC or γ-TURC ring does not perfectly match the protofilament symmetry in a normal microtubule, it was suggested that conformational changes, induced e.g. by anchoring proteins, could render the complexes into active nucleation sites, e.g. CDK5RAP2 (*144*, *146*). But this still has to be structurally determined. γ-TURC is a universal nucleator in cells and is not only active at the major MTOCs (the centrosomes), but it can also be recruited to other sites. For example, the Augmin complex is an important γ-TURC recruiting machinery promoting nucleation at existing spindle microtubules and will be discussed in more detail in section 1.3.6.3.

In summary, MAPs are key regulators of microtubule structure and dynamics through multiple different functionalities—some MAPs have even more than one of the above-described functions or evolved one function into another.

Later on, I am going to discuss how microtubule dynamics are modulated during spindle assembly and how they even provide the forces to pull the sister chromatids far enough apart that they are included in separate newly forming nuclei.

1.3.5 Microtubule organizing centers and centrosomes

MTOCs in principle have two major functions. First, they are sites where microtubules are preferentially nucleated (*147*) and second, they stabilize and anchor microtubule minus ends [reviewed in (*148*)]. In most cycling animal cells, the centrosomes are the main MTOCs (*141*, *142*), where microtubules with primarily 13-protofilaments emanate (*149*).

1.3.5.1 Centrosomes

Centrosomes are membrane-less organelles organized around two microtubule-based structures—the centrioles, which can be subdivided into a mother and daughter centriole. Both centrioles have a dominant cartwheel structure, around which microtubules are ordered with ninefold radial symmetry. Mature centrioles have a defined length of about 500 nm, while having a diameter of approximately 250 nm (*150*).

Around the centrioles is the pericentriolar material (PCM), which has been shown to drive microtubule nucleation at centrosomes (*151*). The pericentriolar matrix generally regulates the microtubule dynamics and organization, but also seems to adopt a favorable structure and to concentrate the factors for centriole duplication (*152*, *153*). The best described components of the PCM are Pericentrin, Centrosomal protein 192 (Cep192), CDK5RAP2, Cep152, CPAP and γ-tubulin, which seem to be the necessary pericentriolar scaffold to recruit other regulators of centrosome function and duplication [summarized in (*154*)].

Centrioles duplicate once per cell cycle during S-phase, which is important, as overduplication causes formation of multipolar spindles during mitosis, which in turn promote chromosomal instability as frequently seen in cancer cells (*155*, *156*). Thus, most vertebrate cells contain two centrioles (one centrosome) in G_1-phase or two pairs of centrioles (two centrosomes) in G_2-phase (*157*). In resting cells, centrioles are usually restructured into basal bodies of primary cilia, which play fundamental roles in flow sensation and generation for signaling purposes, but also for cellular motion [reviewed in (*158*)]. However, as main microtubule organizing centers, the centrosomes are also important in regulating cell shape, polarity and motility, as well as spindle formation, chromosome segregation and cytokinesis. Especially for their role during cell division, the duplication in S-phase is important [reviewed in (*159*)]. Usually, both the original mother and daughter centrioles serve as parent template structures. The new procentrioles assemble at a near orthogonal angle and tightly connected to the respective parent centriole.

The structural basis of the microtubule organization into triplets of ninefold radial symmetry was shown to be the cartwheel arrangement of the SAS-6 oligomer rings (*160–163*). A stack of multiple SAS-6 rings with nine spokes, each, promotes procentriole formation with ninefold symmetry orthogonal to the parent centriole [reviewed in (*159*)]. A multitude of other proteins drives procentriole formation, e.g. CPAP seems to regulate centriole microtubule growth and CP110 was suggested to cap their tips and thus determine centriole length (*164*). Interestingly, in cells that usually contain centrosomes, these can also form *de novo* in the complete absence of template structures when the latter are destroyed beforehand (*165*, *166*). After initial duplication in S-phase, the newly generated centrioles continue to elongate throughout the remaining S- and G_2-phases.

However, they can only serve as templates in the next S-phase and only in the subsequent G_2- or M-phase do they acquire their fully mature structure with distal and subdistal appendices, which are important for ciliogenesis and microtubule anchoring [reviewed in (*159*)]. While the newly formed daughter centrioles need to mature throughout one cell cycle, the parent centrioles have reached their maturity at the G_2-/M-phase transition.

At the same time, the PCM, which surrounds these parent centrioles expands quickly. During the last decade, we have started to understand how the PCM is structured and how it reorganizes, with the development of fluorescence imaging techniques below the diffraction limit [reviewed in (*167*)]. The PCM was shown to be structured in different layers dependent on cell cycle progression. The different PCM proteins distribute in rings around the inner centrioles The PCM is structured in different layers dependent on cell cycle progression and the different PCM proteins distribute in rings around the inner centrioles (*168–171*). Pericentrin and Cep152 seem to be elongated proteins that expand away from the centrioles and seem to span the protein layers of the PCM close to centrioles (*168*, *169*). Other proteins like Cep192 and CDK5RAP2 were suggested to create a matrix at the surface of this inner PCM layers to anchor the γ-TURC and promote microtubule nucleation as described in section 1.3.4.4. At mitotic entry, expansion of the PCM happens in a less ordered fashion generating the gel-like properties of the outer PCM [reviewed in (*167*)].

An *in vitro* study with *C. elegans* PCM components has also indicated that this gel-like state and locally increased concentrations of tubulin dimers within PCM condensates might also allow microtubule nucleation independently of the γ-TURC (*172*). PCM expansion at the G2/M transition was suggested to be a consequence of Plk1 mediated phosphorylation of PCM

proteins, e.g. pericentrin and Cep192, which subsequently recruit more PCM material like other scaffolding proteins, and microtubule nucleating complexes (*173–175*). Since the PCM also contains the microtubule nucleation sites, the centrosomal maturation goes along with increased microtubule nucleation and dynamics.

Until the parent centrioles have reached their maturity, the centrosomes remain tethered together through a linker of different proteins. More recently, it had also been suggested that antiparallel microtubules support this intercentriolar link through the motor activity of a minus end directed motor proteins of the kinesin 14 family (*176*, *177*).

The duplicated centrosomes only start to separate and move apart at the beginning of mitosis by a coordinated action of dynein and Eg5 (*178*). Before NEBD, dynein is localized at the nuclear envelope through direct interaction with the linker of nucleoskeleton and cytoskeleton (LINC) complex proteins or indirect interaction with the nucleoporins of the nuclear pore complex (NPC) [reviewed in (*179*)]. Dynein can then pull on microtubules emanating from the two centrosomes and can pull them in opposite directions along the envelope (*178*). Eg5 on the other hand exerts pushing forces along antiparallel microtubules emanating from the opposing asters after NEBD, moving them apart.

1.3.5.2 Non-centrosomal MTOCs

Centrosomes are not always the main MTOCs, and non-centrosomal MTOCs exist for example in some differentiated cells, where microtubules do not have to be organized radially [reviewed in (*148*)]. Such MTOCs are found at apical sites of polar cells like epithelial cells, or at the cortex of epidermal cells. They have also been found to localize at the nuclear membrane in muscles, at preexisting microtubules in neurons, or at the Golgi apparatus or the mitochondria in multiple cell types. Also, oocytes of many species lack centrioles, including those of mammals like mouse and human (*180*, *181*).

In these oocytes, centrosomes are typically eliminated during oogenesis. In some species like *Drosophila melanogaster* and *C. elegans* it has for example been shown that the PCM is first disassembled followed by centrosome elimination (*182*, *183*). In mouse oocytes, the elimination seems to start upon follicular recruitment of incompetent germinal vesicle stage oocytes and continue throughout the entire oocyte maturation, including meiosis, but it is less clear how the PCM is involved in that process (*184*). Interestingly, however, mouse oocytes use non-centrosomal MTOCs to organize microtubules during meiotic spindle

assembly and these non-centrosomal MTOCs seem to functionally resemble centrosomes in most of their mitotic properties (*185*).

Non-centrosomal MTOCs have not yet been as extensively studied as centrosomes, and the exact composition of various non-centrosomal MTOCs at different cellular sites remains to be determined. Especially oocyte MTOCs seem to contain and functionally rely on several PCM proteins like pericentrin and Cep192 (*186–188*), but there are other MTOCs of very different composition.

If these MTOCs nucleate microtubules, they have to contain appropriate proteins, alternatively, if they only anchor and organize microtubules, they just need to contain proteins that interact with and anchor microtubule minus ends. One nucleator commonly found at centrosomes, but also acentrosomal MTOCs is the above mentioned γ-TURC. However, it does not only nucleate, but also cap microtubule minus ends, preventing these ends from growing and shrinking (*189*). The γ-TURC is anchored to the centrosome, but also to some non-centrosomal MTOCs by different PCM proteins, like Ninein (*190*), Pericentrin, Cep192 (*174*, *191*, *192*) and others. But there are non-centrosomal MTOCs, where the γ-TURC seems to be recruited differently, for example at microtubule anchored MTOCs, TPX2 and the Augmin complex have been suggested to mediate the recruitment (*193–195*). Interestingly, γ-TURC anchorage at MTOCs, does not necessarily result in microtubule nucleation. As shown in mouse keratinocytes, centrosomal localization of the γ-TURC by CDK5RAP2 did promote nucleation, while NEDD1 anchored the γ-TURC at centrosomes without inducing nucleation (*196*). Especially at MTOCs that do not nucleate microtubules, the previously described CAMSAP (Patronin) proteins, which bind to microtubule minus ends seem to be important to stabilize microtubules at these sites (*197*).

It has more recently been suggested that nucleation at MTOCs might depend on other factors than the γ-TURC. Nucleation might also be driven by locally concentrating tubulin dimers within condensates of few centrosomal proteins and by stabilizing nucleates. *In vitro*, the *C. elegans* homologue of CDK5RAP2 was shown to induce spherical condensates and together with XMAP215 and TPX2, it accumulated tubulin and induced microtubule aster formation (*172*).

1.3.6 The spindle and how it is assembled from and around the core components

The mitotic spindle is the machinery that pulls the sister chromatids apart to opposite ends within the cellular volume in anaphase. This can be achieved after the spindle has assembled into a bipolar array of microtubules and the two sister chromatids of each chromosome face the opposite spindle poles and are stably attached to microtubule bundles from only one pole, each (biorientation). Microtubule minus ends are usually focused at these poles and the plus ends radiate outwards and towards the respective opposite spindle pole.

1.3.6.1 Microtubule types in the spindle

Three types of microtubules have been categorized, which make up the spindle and are differently involved in the force generations [reviewed in (*198*)]: kinetochore microtubules, astral microtubules and non-kinetochore microtubules (see Figure 2 for a schematic overview).

Kinetochore microtubules attach to the sister chromatid kinetochores and link the chromatids to opposite poles. Tens of kinetochore microtubules attach to the kinetochore of each sister chromatid to form the kinetochore fibers (K-fibers), where the individual microtubules seem to form a common system and to be stabilized, since detachment of these fibers from the kinetochores leads to rapid depolymerization of the entire bundle (*199*). K-fibers exert the pulling forces on chromosomes at their kinetochores and they silence the spindle assembly checkpoint (SAC), which is previously generated at unattached kinetochores. The kinetochore fibers are under constant flux: While being attached to the kinetochores, the plus ends can still grow through polymerization and the minus ends are still slided to the spindle poles, where they depolymerize leading to treadmilling of the microtubules in each spindle half (*200*). In anaphase, the depolymerization at the pole is combined with depolymerization at the plus end while maintaining attachment, resulting in pulling forces on the kinetochores. Here, forces in the order of tens of pN are generated through hydrolysis of the GTP cap and outward curling of filaments within a K-fiber bundle [reviewed in (*198*)]. In addition, dynein can help to slide kinetochore bundles poleward (*201*).

Astral microtubules radiate outwards from the poles towards the cellular cortex and thus help to position the spindle, usually at the center of the cell (*202–205*). Plus ends of the astral microtubules can exert pushing forces by polymerization, but they especially interact with microtubule motors and crosslinkers at the cortex, which can then pull on the asters.

Non-kinetochore microtubules that originate from the different poles, typically overlap with their antiparallel plus ends at the spindle midzone. These provide the platform for opposing microtubule motor activities, e.g. of minus end directed dynein and plus end directed kinesin 5, which can slide antiparallel microtubules alongside each other, but in opposite directions (*123*, *124*, *206*). Such opposing sliding activities are important to establish spindle bipolarity in prometaphase. In anaphase, these interpolar microtubules are again bound by crosslinkers and motor proteins to push the poles apart and to establish a stable midzone for subsequent cytokinesis. The antiparallel microtubule crosslinker PRC1 and the microtubule depolymerase kinesin 4 have been suggested to establish this midzone (*126*, *207*, *208*). The antiparallel microtubules first grow and slide along each other by means of microtubule motors like Eg5, which push the spindle poles further apart. But when PRC1 has recruited kinesin 4, PRC1 likely gets compacted to the very tip of the overlapping plus ends and kinesin 4 at this location inhibits microtubule plus end growth, so that midzone length reaches a stable limit creating the stable anaphase midzone after chromosome segregation. More recently, antiparallel non-kinetochore microtubules crosslinked by PRC1 have also been shown to bridge sister kinetochore fibers in metaphase, and were suggested to regulate the tension between the opposing kinetochore fibers (*209*).

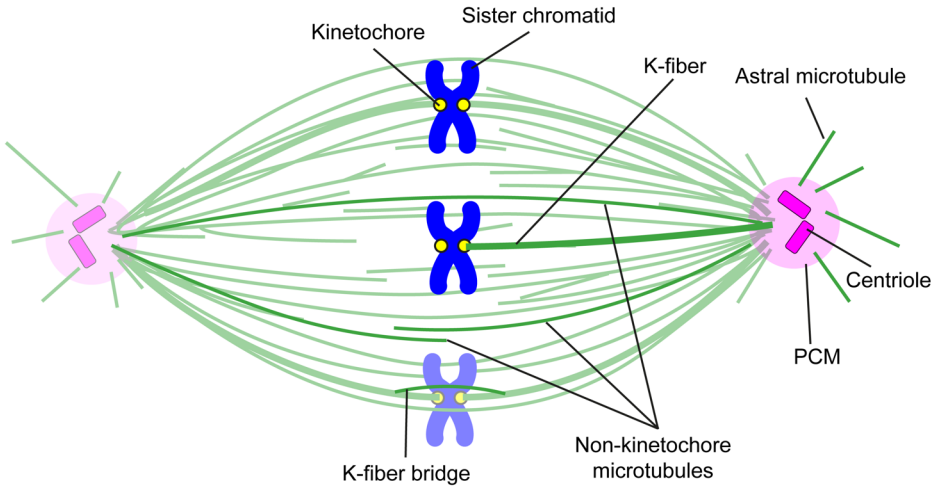

Figure 2: The mitotic spindle. The major purpose of the mitotic spindle is the segregation of the sister chromatids of a chromosome. The major structural components are microtubules. Different spindle microtubule types carry out specific functions. Astral microtubules connect the centrosome consisting of the PCM and the centrioles to the cell cortex and mediate spindle positioning within the cell. K-fibers connect the sister chromatids to the centrosomes, via binding to their kinetochores. Non-kinetochore microtubules are for example interpolar microtubules, which connect the two spindle poles. They also include microtubules from the opposite poles, which overlap at the spindle center in an anti-parallel fashion to create the spindle midzone. K-fiber bridges connect K-fibers that are attached to the two kinetochores of one chromosome.

1.3.6.2 Microtubule dynamics and organization within the spindle

To study the organization and dynamic behavior of microtubules within the spindle has been very challenging [reviewed in (*210*)]. For long it was difficult to collect dynamic information about individual microtubules and how they organize within the context of the bipolar spindle as spindles are huge structures, which consistent of hundreds of thousands of microtubules. Light microscopy could not resolve individual microtubules within these dense structures and electron microscopy gave only static information of spindle subsections. But it was early on described that compared to interphase microtubules, mitotic microtubules are more dynamic with increased catastrophe frequency and reduced rescue frequency (*211*, *212*).

When the first spindle assembly dynamics and mechanisms were described, the centrosomes were thought to be the sole source and minus end organizers of dynamic spindle microtubules, whose plus ends were suggested to be stabilized upon binding to kinetochores finally establishing the bipolar and fusiform spindle with the two centrosomes predefining the poles (*147*, *213*). Albeit the centrosomes being the major MTOC in most animal cells in interphase and also in mitosis, we have become aware of additional factors influencing spindle microtubule organization and dynamics that promote microtubule-kinetochore interactions, especially of microtubules that are not organized by centrosomes [reviewed in (*214*)].

Fluorescence confocal imaging of microtubule end binding protein 1 (EB1) localizing to growing spindle microtubule ends in *X. leavis* egg extracts has shown that the polymerization velocity of microtubules is similar throughout the entire length of the spindle, but that EB1 is more abundant at the spindle center (*215*). This suggested that chromosomes do play an important role in regulating spindle microtubule dynamics and/or nucleation. This was well in line with the earlier finding that microtubules organize into spindles around chromosome beads in the absence of centrosomes in *X. laevis* egg extracts (*216*). Also, with the imaging of EB1 to track growing ends, a study in Drosophila S2 cells showed that multiple microtubules grew from acentrosomal poles within the spindle towards the chromosomal metaphase plate. The authors suggested that bipolar spindles self-organize by stimulating microtubule growth from within the spindle (*217*). That acentrosomal MTOCs could localize within the spindle was further supported by the finding that microtubule minus ends are distributed throughout the meiotic spindle in *X. laevis* eggs and that these ends are sorted by flux towards the poles (*218*). It was also shown that the high density of microtubules within the spindles is likely a

result of enhanced local nucleation as the dynamics of microtubules inside and outside spindle microtubule assemblies were the same (*219*). For example in human cells, the γ-TURC can also be found at the minus ends of non-centrosomal spindle microtubules (*143*). Subsequently, motor activities of dynein, HSET and Eg5 sort minus ends towards the poles. Minus end directed motors like HSET and dynein actively pull minus ends of microtubules towards the poles (*216*, *220*, *221*). In contrast, Eg5 supports this poleward microtubule movement by sliding the anti-parallel microtubules in the central spindle outwards (*124*, *222*, *223*), until this is counteracted by minus end directed activity of dynein, which can also move along antiparallel microtubules towards their respective minus ends (*123*, *206*). The overall poleward movement is slowed down near the poles and the minus ends are then clustered at the poles, probably by dynein-regulated crosslinkers like NuMA (*224*, *225*). Only few microtubules seem to directly connect the pole to the metaphase plate. If centrosomes are present, they nucleate microtubules and bind and organize their minus ends, and it is assumed that NuMA and dynein also establish centrosomal poles (*224–226*).

These observations are in line with modellings of bipolar spindle assembly that suggest that microtubules nucleate within the spindle and are then rearranged and organized through microtubule motors, which drive outward sliding of the minus ends, clustering, and eventually depolymerization [Slide and cluster models (*227*)].

The above-mentioned studies gave insights into the structural organization and dynamics of microtubules within spindles, but they also provided first insights into how and where microtubules start to grow. In the following section I am going to discuss in more detail the various sites of microtubule nucleation relevant for spindle assembly that take place at the centrosomes, chromosomes and kinetochores.

1.3.6.3 Microtubule nucleation pathways in spindle formation

Centrosomal nucleation

Originally the centrosomes were thought to nucleate the spindle microtubules by mechanisms described in 1.3.4.4 and 1.3.5 and illustrated in Figure 3. It was suggested that the dynamic microtubule plus ends, which emanate from the centrosomes—while they grow, shrink and regrow—randomly search the cellular space to attach to the kinetochores of the sister chromatids, where the microtubules would be capped and stabilized (*213*). This model for initial spindle assembly driven by centrosomal microtubules is called the ‘search and

capture model'. It was suggested that over time, more and more individual microtubules would become stabilized at the kinetochores by repetitive capture and thus, the number of kinetochore microtubules would increase, while astral microtubules would decrease proportionally. This was supposed to eventually lead to the well-known fusiform spindle. And indeed, it has been shown that kinetochores can capture astral microtubules (*228*, *229*). However, it was later shown that centrosomal microtubules cannot be faithfully captured by all sister kinetochores through random search during the usually short pro-metaphase of vertebrate somatic cells (*230*) or during meiosis of large germ cells (*231*). Even though, it has been reported that the chromosomes are positioned like a belt at the early spindle surface to favor that microtubules from the opposite poles attach to sister kinetochores (amphitelic attachments) (*232*), additional cues were suggested to be important to assemble a bipolar spindle. Especially since bipolar mitotic spindles do form in the absence of one or both centrosomes (*216*, *233*).

Nucleation around chromosomes

Many studies have indicated that the chromosomes are more than passive components of the spindle waiting to capture centrosomal microtubules. The above mentioned studies in Xenopus egg extracts have shown that chromosomes prime and promote bipolar spindle assembly in the absence of centrosomes and kinetochores (*216*). Even in cells that possess centrosomes, it could be shown that microtubules nucleate around condensed chromosomes if the centrosomes are localized far away from the chromosomes (*234*, *235*). Nucleation around chromosomes thus complements the centrosomal nucleation pathway and facilitates microtubule capture by the kinetochores since the distance by which microtubules have to grow is decreased and their capture by the small kinetochore is more likely [discussed in (*214*)].

A specific local proteome around the chromosomes drives microtubule nucleation in close proximity. At the core of this environment is the small GTPase Ras-related nuclear protein (Ran). Ran can bind guanosine di- or triphosphate, GDP or GTP (*236*). In interphase, the GTP bound form is mainly found in the nucleus, while the smaller amount of the GDP bound form is mainly cytoplasmic. This sharp gradient across the nuclear envelope is used for nucleocytoplasmic transport [reviewed in (*237*)]. The spatial distribution of Ran-GDP and Ran-GTP is driven by different factors. First, Ran is actively transported into the nucleus by

transport factor NTF2 and is thus more abundant in the nucleoplasm (*238*, *239*). Second, regulator of chromatin condensation 1 (RCC1), which is the guanine nucleotide exchange factor for Ran, is nucleoplasmic. Precisely, RCC1 binds to chromatin, especially to histones 2A and B, where it is most active (*240*) and triggers a guanine nucleotide exchange in Ran (*241*). As GTP is ~10-fold higher concentrated than GDP in cells, the RCC1 based nucleotide exchange thermodynamically favors the formation of Ran-GTP in the nucleus (*242*). In the cytoplasm, RCC1 is kept inactive (*243*). Here, instead the Ran GTPase activating protein (RanGAP1) is highly active and stimulates the GTPase activity of Ran (*244*, *245*). Thus, cytoplasmic Ran is mostly bound to GDP. At NEBD, when the membrane compartmentalization of the nucleus is dissolved, a local gradient of Ran-GTP is established around chromatin (*246*, *247*). And Ran-GTP, generated through chromatin bound RCC1, was shown to drive spindle microtubule nucleation and stabilization, and to be essential for the fast assembly of a bipolar spindle (*248–250*). The activity of RCC1 alone on beads can induce spindle formation around them in cell extracts further showing the importance of the Ran-GTP signaling for spindle assembly (*251*).

Ran-GTP influences microtubule nucleation and dynamics through multiple interactions (a selection of Ran-GTP dependent mechanisms is shown in Figure 3). Since it binds to the carrier proteins involved in nucleoplasmic transport, like Importins or Transportin, their cargo proteins play an important role for microtubule nucleation and initiation of spindle assembly. Upon NEBD, Ran-GTP has access to the cytoplasm, where it can activate spindle assembly factors (SAFs) by displacing inhibitory importins from them. The SAFs then act to stabilize microtubules and promote spindle formation (*252–254*). So far this mechanism has been described for multiple SAFs but it is likely true for many more [reviewed in (*210*, *237*)]. One of the most important and well-characterized SAFs is **t**argeting **p**rotein for **X**enopus kinesin like protein **2** (TPX2). Prior to NEBD, TPX2 is inhibited by binding to Importin α and β, which are released upon Ran-GTP binding during M-phase, which leads to spontaneous microtubule assembly around chromosomes (*252*). TPX2 was first reported to promote chromosomal nucleation indirectly by recruiting and binding the Aurora kinase A (*255*, *256*). Activated Aurora A was shown to phosphorylate NEDD1, a γ-TURC anchor protein, at one specific residue, which is essential to promote chromosomal nucleation (*257*). Together with TPX2, NEDD1 was suggested to recruit γ-TURC to the chromosomal environment, but at the same

time TPX2 also seemed to provide a platform for γ-TURC activation (*258*). On the other hand, *in vitro* TPX2 directly promoted microtubule nucleation (*259*), and recently it has been suggested that TPX2 achieves this by stabilizing early nucleation intermediates independently of the γ-TURC (*96*).

Besides these importin mediated mechanisms, Ran-GTP is also involved in stabilizing minus ends of chromosomal microtubules. First, MCRS1 has been identified as a MAP that stabilizes minus ends of short microtubules around the chromosomes after being released from Importin β by Ran-GTP binding (*133*). Shortly afterwards, it was shown that in the presence of Ran-GTP, the KANSL1 and KANSL3 of the chromatin modifying mammalian nonspecific lethal complex, also localize to these minus ends and stabilize them, supposedly in a complex with MCRS1 (*134*).

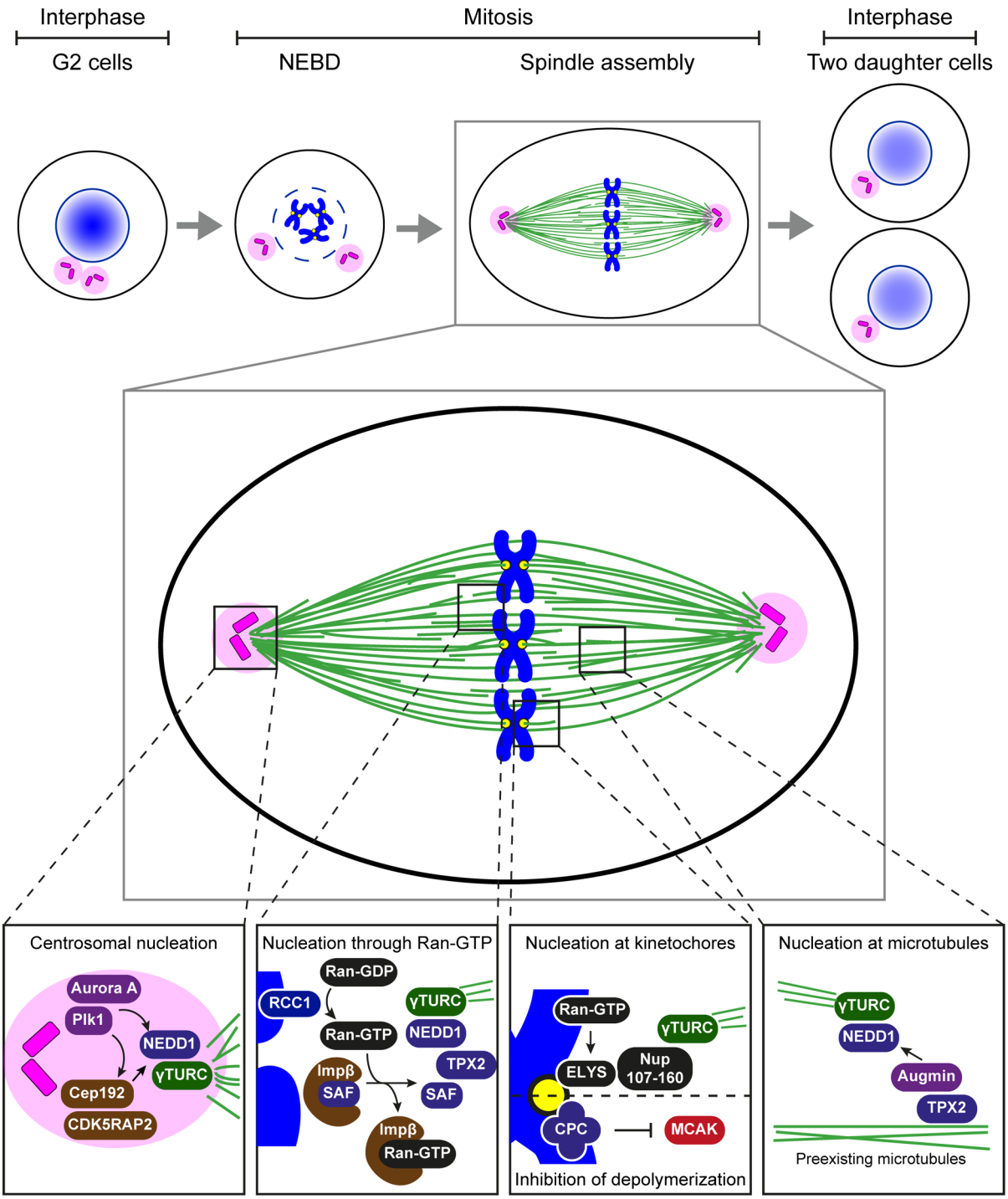

Figure 3: Microtubule nucleation pathways involved in the formation of the mitotic spindle. The upper panel shows a schematic illustration of cell division. After the G_2 interphase stage, in which centrosomes and DNA are already duplicated, the cell enters mitosis. After NEBD, the bipolar spindle assembles around the chromosomes. Chromosomes are then segregated and distributed into the two new daughter cells, which form upon cytokinesis. The magnification in the middle shows a stereotypic metaphase spindle with chromosomes aligned on the metaphase plate and the centrosomes localized at the spindle poles. The four magnifications on the bottom show the different microtubule nucleation mechanisms, which can generate the spindle microtubules (*210*). At the centrosomes, γ-TURC is recruited by direct binding partners like NEDD1. It is also recruited by centrosomal proteins like Cep192 and CDK5AP2, which together with the kinases Aurora A and Plk1 promote microtubule nucleation and polymerization. Based on chromosomes, several mechanisms directly promote microtubule nucleation. One major pathway is based on Ran-GTP (*258*). The Ran guanin nucleotide exchange factor RCC1 is directly bound to chromatin and as RCC1 promotes the conversion of Ran-GDP to Ran-GTP, it

effectively creates a Ran-GTP gradient around chromosomes. A major function of Ran-GTP is to release the cargo from nuclear transport receptors like transportin and importinβ (Impβ). Before NEBD important spindle assembly factors (SAFs), like TPX2 are bound to Impβ, which are released and activated in proximity of chromosomes and then promote spindle assembly around chromosomes together with factors like NEDD1, which recruits the γ-TURC. At kinetochores spindle assembly is regulated by two different means. On the one hand, ELYS localizes to kinetochores and binds to the Nup107-160 complex after release from transportin and γ-TURC gets recruited to promote microtubule nucleation; on the other hand, the chromosomal passenger complex (CPC) inhibits microtubule depolymerases like MCAK in proximity of kinetochores. In addition, microtubules can also be nucleated from TPX2 positive sites on preexisting microtubules by the action of the Augmin complex, which recruits the γ-TURC, e.g., through NEDD1.

Microtubule nucleation at kinetochores

Kinetochores play an important role in the chromosome/Ran-GTP mediated nucleation pathway (*260*), as illustrated in Figure 3. It has been shown that growing microtubules, which formed around chromosomes seem to be preferentially captured and stabilized by kinetochores to form k-fibers without being linked to a spindle pole (*220*, *261*). Initially, these k-fibers were not oriented towards the spindle poles, but while the fibers grew, they were transported poleward with the general poleward flux described in 1.3.6.2. It was suggested that this transport occurs along centrosomal microtubules in a dynein-dependent fashion (*261*). Such mechanism also exists in some meiotic spindles as was shown in crane-fly spermatocytes, where kinetochore fibers can form from outward-growing microtubules, which originated near kinetochores (*235*). How important and generic this 'inside-out' kinetochore mediated nucleation and assembly pathway of k-fibers from the surface of the chromosomes is in comparison to 'outside-in' generation of microtubules from the centrosomes, has been shown recently. During early prometaphase in human cells, most kinetochores develop k-fibers by local capture of microtubules, which were previously nucleated in immediate proximity (*262*). Microtubule plus ends seemed to first interact laterally with the kinetochores, but within three minutes, they were captured end-on by the kinetochores through a mechansims dependent on the plus end directed kinetochore-associated kinesin CenpE.

Several factors, which coordinate microtubule nucleation around kinetochores have been identified: At early prometaphase, the NUP107-160 subcomplex of the nuclear pore complex was shown to recruit the γ-TURC and to promote microtubule nucleation and k-fiber formation around kinetochores in a Ran-GTP dependent manner (*263*). It was later reported that the complex was strongly associating with MEL-28/ELYS to drive kinetochore proximal

nucleation (*264*). This explains local nucleation around kinetochores, since ELYS localizes there in mitosis and has been suggested to fulfil important functions during cell division, especially for cytoskeletal arrangements (*265*). The TPX2 mediated nucleation mentioned above is also particularly strong around kinetochores since TPX2 preferentially localizes to kinetochores in early mitosis. Overall, it could therefore be that k-fibers are assembled from the kinetochore to the spindle pole rather than the other way around. Rather than centrosomes searching the large cytoplasm with long astral microtubules to capture kinetochores, it may be the kinetochore that captures short microtubules nucleated locally on the surface of the chromosome, which then grow longer and get incorporated into the poleward flux of the bipolar spindle to make a mechanical connection to the pole.

Microtubule nucleation through the chromosomal passenger complex

Plk1 accumulation at the kinetochores in early mitosis is essential for faithful division. An additional mechanism for microtubule nucleation near kinetochores independent of Ran-GTP has been identified, which seems to rely on Plk1's localization and function at the centromeric region. Plk1, after being phosphorylated by Cdk1 in early M-phase, can promote the localization of the so-called chromosomal passenger complex (CPC) to centromeric chromatin (*266*), as schematically depicted in Figure 3. Plk1 can directly bind and activate the kinase Haspin, which drives Histone 3 modification at the centromeric region (*267*). And together with Histone 2A phosphyration by the kinase Bub1, the Histone 3 phosphorylation is required for CPC binding (*268–270*).

The CPC consists of Borealin/Dasra-B, survivin, INCENP and the Aurora B kinase. The CPC is generally important to resolve erroneous microtubule-kinetochore attachments, attachments of microtubules from both poles at the same kinetochore or of microtubules from only one pole at both sister kinetochores (*271*, *272*).

But it has also been shown in *X. laevis* egg extracts that a signal from the CPC can mediate spindle assembly in the absence of Ran-GTP (*273*).

The Aurora B kinase activity at kinetochores seems to determine the local Ran-GTP independent microtubule assembly. Localizing the Aurora B activity elsewhere, by induced clustering of the active Aurora B-INCENP complex, was shown to promote microtubule nucleation at centrosomes, but also lead to multiple spindle-like structures without chromosomes and centrosomes (*274*). Thus, Aurora B localization to kinetochores seems to

be important for the spatial organization of early spindle assembly. One very important downstream target in this pathway is the microtubule depolymerase and kinesin MCAK (*275*). MCAK was reported to re-localize from the outer to the inner centromeric region after phosphorylation by Aurora B, and thus could not destabilize microtubules close to the kinetochores anymore (*276*). Another Aurora B target in this pathway is most likely the depolymerase Stathmin (*274*), which is also inhibited upon hyperphosphorylation by the kinases in early mitosis (*277*, *278*). Overall, the picture emerges that Aurora B activity at the kinetochore inactivates microtubule depolymerases, thereby favoring microtubule growth in addition to the Ran-GTP promoted nucleation around chromosomes and kinetochores. The exact molecular mechanism of CPC regulated nucleation is however still unclear.

Microtubule nucleation at microtubules

In addition to the chromosomal, the kinetochore-based and the centrosomal nucleation pathways, the last two decades have shown that the initially generated spindle microtubules themselves promote the nucleation of further spindle microtubules (see Figure 3). Fluorescently tagged microtubule plus ends have been shown to originate from the acentrosomal regions of existing k-fibers (*217*). These 'branched' microtubules were growing at a very shallow angle from an existing microtubule and were oriented preferentially towards the chromosomes. This study was well in line with multiple previous observations of γ-tubulin localizing throughout the spindle and not just near the chromosomes or at the centrosomes. An RNAi screen in Drosophila S2 cells identified new dim γ-tubulin (Dgt) genes encoding proteins involved in recruiting the γ-TURC to the spindle body (*115*). These genes were confirmed in an additional screen in human and drosophila cells, which identified three additional genes, whose knock-down lead to decreased spindle microtubule density (*116*). The encoded proteins were found to form an 8 subunit Augmin/HAUS complex in humans (*279*, *280*). These studies also showed that depleting Augmin/HAUS in HeLa cells strongly impaired the morphology, organization and function of mitotic spindles. Subsequently, a more detailed description of the microtubule dependent microtubule nucleation pathway was published (*194*). By visualizing branching microtubules in *X. laevis* egg extracts, the authors could show that new microtubules could branch from template microtubules at a shallow angle as described before and with same polarity as the template independent of chromosomes. The authors suggested that this would be an optimal system to generate

parallel microtubules as found in the spindle halves. They also showed that branching was dependent on Ran-GTP and its effector TPX2, as well as on Augmin, which had previously been shown to recruit γ-tubulin (*281*). Since this mechanism was shown to also depend on Ran-GTP, it was surprising that no gradual decay of γ-tubulin had been reported in spindles. A more recent study shed some light on this, showing that first, TPX2 localized near minus ends of older microtubules in a Xenopus egg extract system (*195*). The authors suggested that TPX2 was essential to first deposit nucleation sites and showed that subsequently, Augmin and the γ-TURC were required for microtubule branching, while no branching was observed in the initial absence of TPX2. More recently, it has also been shown that TPX2 can undergo phase separation together with tubulin *in vitro*, which appears to be an important property for microtubule branching (*282*).

Although these studies were conducted using an *in vitro* system to investigate branching events at individual microtubules, it is likely that the same sequence of events occurs in mitotic spindles, where TPX2 might localize first at kinetochores, but is then transported poleward (*283*). It could deposit nucleation sites throughout the spindle halves which could explain the homogenous distribution of γ-tubulin throughout the spindle.

In summary, several different nucleation pathways have been found to contribute to spindle assembly in different systems, but we only start to understand how they integrate.

1.4 Preimplantation development

Mammalian life starts when a spermatocyte fertilizes an egg and the formed embryo subsequently goes through preimplantation development while it travels down the fallopian tubes from the ovary to the endometrium, where it finally implants after reaching the blastocyst stage. Preimplantation development is a phase during which the embryo experiences major changes within few days (*284*). From two highly differentiated cells, the sperm and the oocyte, totipotency is established in the zygote. In mouse embryos, first cues for subsequent cell differentiation are established at the 4-cell stage and extended basolateral cell-cell contacts with concomitant cell polarization at the 8-cell stage further influence cell fate specification (*285*). At the 16-cell stage—the first lineage specification into the outer layer of trophectoderm cells and the inner cell mass cells could be traced in live developing embryos (*286*). The patterning of these first two cell lineages within the early

embryo was recently shown to be driven by polarity cues and cell shape (*287*). The trophectoderm will later give rise to the embryonic part of the placenta, while the pluripotent cells of the inner cell mass (ICM) will further differentiate at the late blastocyst stage. Part of the ICM cells differentiate into the primitive endoderm, which will form the extra embryonic yolk sac while the other part of ICM cells gives rise to the epiblast, which will form the fetal tissues (*288*, *289*).

1.4.1 The oocyte to embryo transition

Cell division in gametes is called meiosis and occurs in two steps. The first division—meiosis I—is reductive and whole homologous chromosomes are distributed among the forming cells. Only during the second division—meiosis II—sister chromatid segregation occurs. The two meiotic divisions of the oocyte are highly asymmetric (*27*). On the one hand, small polar bodies form with a minimal cytoplasmic fraction surrounding the homologous chromosomes or sister chromatids, respectively, while on the other hand the oocyte forms with a large cytoplasmic fraction, which contains accumulated proteins and initially dormant messenger RNAs (mRNAs) and proteins. Thus, despite being transcriptionally silent, the large oocyte provides almost all cellular material for the early embryo. Within the matured and fertilized oocyte, protein expression or function are controlled almost exclusively at the level of mRNA translation and stabilization or through posttranslational modifications of stored proteins [discussed in (*290*)]. mRNAs are stored and kept dormant, especially within cytoplasmic granules, and timely controlled disassembly of these granules and translational activation of the stored mRNAs was shown to be essential for proper cell cycle progression after fertilization (*291*).

After maturation, the oocyte remains arrested in metaphase of meiosis II until a sperm fertilizes and activates the oocyte to trigger resumption of the second meiosis. In rodents, the sole essential contribution from the sperm is the second half of the genome. In most other mammalian species, it also delivers the centrosome. Interestingly, in rodents the sperm does not provide a centrosome (*292*) and thus this has to be formed *de novo* in later stages, leading to a switch from acentrosomal to centrosomal mitosis during preimplantation development (*293–296*).

As mentioned above, almost all cytoplasm of the zygote is provided by the oocyte and until the blastocyst stage, the embryo does not grow, as the embryonic cells—the blastomeres—

proceed through the cell cycle without any additional nutrients and without interphase growth, while they still duplicate their genomic DNA. Consequently, during the earliest symmetric mitotic divisions, the cellular volume—and thus the mRNA and protein material—is approximately reduced by half in each round while the amount of DNA is kept constant (*297*, *298*). Due to this size reduction, the spindle apparatus to segregate the same amount of chromosomes has to be made from fewer components and adapt to very different cellular scales in each of the cleavages (*295*, *299*).

After fertilization, paternal chromatin needs to be restructured and both parental genomes are initially inactive. Relying on the stored mRNA and proteins provided by the oocyte, the fertilized egg is thus effectively under maternal control until the embryonic genome becomes activated. In most mammalian embryos analyzed to date, the embryonic genome activation occurs in waves, but among different species the timing of the waves can differ (*300*). In the mouse, the major embryonic genome activation peaks already at the late 2-cell stage and a minor activation follows at the 8-cell stage (*300*, *301*). In bovine and human embryos on the other hand, only a minor activation occurs soon after fertilization, especially between the 2- and 4-cell stages, but the major embryonic genome activation occurs later, between the 4- to 8-cell transition (*300*, *302*–*305*).
As the embryo progresses through the first cell cycles of preimplantation development, the maternal proteins and transcripts are consumed and degraded, whereas the amount of embryonic gene products increases gradually (*303*). This control shift from the maternal to embryonic genome is called the oocyte to embryo transition (see Figure 4 for a schematic overview).

As mentioned in section 1.1, especially postzygotic aneuploidy is very common in preimplantation embryos (*4*). The field assumes that in addition to potential genetic predispositions (*306*), the inherent variability in the amounts of maternal and embryonic gene products might play a major role in driving aneuploidy, especially when affecting the mitotic apparatus and its control mechanisms [discussed in detail in (*3*)].

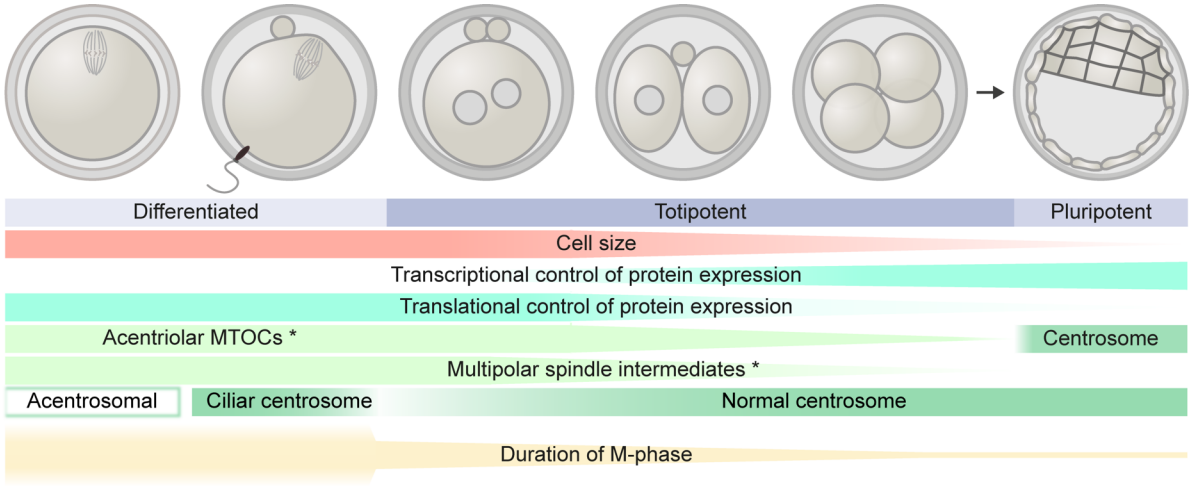

Figure 4: Transitioning from oocyte to embryo in the mammalian zygote. After meiosis I, the fully differentiated oocyte is fertilized by the sperm and resumes meiosis II. The two divisions are very asymmetric to maintain a large cytoplasmic volume for storage. During both meiotic divisions, transcription is inactive and protein expression is translationally and post-translationally regulated. Since centrosomes are degraded during early oogenesis in mammals (*180*, *181*), and in the mouse also in the spermatocytes (*292*, *307*), multiple acentriolar MTOCs functionally replace the centrosomes in early spindle assembly (*295*, *308*), which already self-organize microtubule during meiotic spindle assembly (*185*, *309*) (mouse/rodent-specific aspects are marked by an asterix). The many MTOCs coincide with multipolar spindle intermediates preferentially forming during prometaphase (*295*). In other mammalian embryos, the centrosome is provided by the sperm at fertilization, but its structure is adapted to form the flagellar core (*310*). In general, the duration M-phase is very long at the beginning of mammalian development. In the mouse, meiosis I can take up to 11 hours and meiosis II can be especially delayed due to a metaphase arrest until fertilization (*311–313*). Thus, the totipotent zygote undergoes the first mitosis under unusual conditions and the described and depicted parameters (among others) only gradually change during the early divisions. In every cleavage, the cell size is halved, while the genomic content should remain constant (*297*, *298*). Through stored and activated mRNA, the zygote is still entirely under maternal translational control (*290*, *314*). Only from the 2-cell stage onwards in the mouse and around the 4-8-cell stage in humans – when transcription of the embryonic genome becomes activated – maternal control gets gradually replaced by embryonic control (*300–305*). In the mouse, fewer and fewer MTOCs organize the mitotic spindle until centrosomes form *de novo* at the blastocyst stage; however their function at this later stage is still questioned (*293–296*). Until then, spindle assembly also passes through less marked multipolar organization (*294*, *295*, *315*). The inherited sperm centrosome in other mammalian species has to restructure and its function for mitosis might be impaired (*310*). Also, M-phase duration changes: After very lengthy and even halted meiosis, the zygotic mitosis is still prolonged (~ 90-120 minutes) compared to somatic mitosis (*316*, *317*). Thereafter, the duration decreases until it reaches the timing of a normal somatic cell mitosis. These gradual changes during preimplantation development might contribute to decreased chromosome segregation fidelity during cleavage divisions. Figure and legend were modified from (*3*), but were originally drawn and written by myself.

1.4.1.1 Mitotic errors during the oocyte to embryo transition

Preimplantation development thus confronts the cell division machinery with particular challenges that could render these early mitotic divisions less faithful compared to normal somatic divisions.

For example, the cell cycle of the blastomeres seems less tightly controlled during early preimplantation development (*318*), potentially allowing for progression without intermediate DNA repair or ultimate induction of apoptosis [discussed in (*319*)]. Therefore,

errors that occur at these stages might not be properly corrected and can propagate. It is noteworthy that while the control stages in interphase might be shortened or even entirely skipped, the M-phase in embryos is prolonged, especially in the zygote (*317*, *320–322*).

Chromosome lagging during anaphase appears to be the most frequent cause of embryonic aneuploidy (*323*). Particularly, in mouse preimplantation embryos it was observed that lagging chromosomes occur frequently and that these can get enclosed in separate micronuclei (*324*). Research in our own group has further corroborated that these errors predominantly occur at the 4- and 8-cell division (Reichmann and Ellenberg, unpublished observations). Chromosomes in micronuclei become severely damaged and are not subjected to bilateral segregation in subsequent divisions (*324*). Also in human embryos micronuclei can be observed frequently (*325*) and they seem to have a similar fate as micronuclei in murine embryos (*326*), which could explain why chromosome deletions outnumber gains in blastomeres of mosaic embryos (*4*).

Apart from losing individual chromosomes in micronuclei, many human embryos exhibit multinucleated blastomeres, particularly at the 2-cell stage (*327–331*), which indicates that the zygotic mitosis might be especially vulnerable and distinct from the subsequent divisions. In bovine embryos the loss of a whole haploid parental genome has been observed in embryonic blastomeres after the zygotic division (*332*).

During the early embryonic divisions, common mechanisms of somatic mitosis, which usually ensure faithful genome distribution must behave differently. For example, the machinery, which corrects kinetochore attachment errors (the above mentioned chromosomal passenger complex), exhibits a distinct composition and less efficient centromeric localization, which might lead to higher error rates (*333–336*). In addition, the SAC—which usually halts mitotic progression into anaphase in the presence of an unattached kinetochore (*337*)—despite being present and responsive to many unattached kinetochores in mouse and human embryos (*338*, *339*) —might not function canonically in early embryos (*340*). Research in our group has shown that the SAC activity initially decreases during the earliest cleavages but ramps up again in later stages (Eguren and Ellenberg, unpublished observations). Thus, the oocyte to embryo transition might strongly affect mitotic control and each cleavage stage might be differently equipped to safeguard proper chromosome segregation.

1.4.2 Challenges for the spindle apparatus during mammalian embryonic mitosis

Due to the above discussed frequent occurrence of erroneous mitotic divisions in early embryonic cells it is highly important to understand the underlying mechanisms. The key machine segregating chromosome in every mitotic division is the bipolar spindle. As normal somatic mitotic divisions are highly accurate, it is important to investigate the mitotic apparatus in the early embryo considering the specific challenges that the spindle has to face at the beginning of mammalian life in order to get a mechanistic understanding why errors occur so frequently.

Above I already mentioned some major challenges that the early mouse embryo has to face. Initially, the embryo's genome is silent and thus only maternally provided gene products regulate its division. Also, at the beginning, the zygote is huge but rapidly the size of individual blastomeres decreases with each division and thus the spindle has to adapt to substantially different dimensions. In addition, all oocytes lack centrosomes, and the zygote can at best inherit a specialized centrosome from the sperm and as in normal somatic cells the centrosome is a major organizer of the mitotic spindle, this might pose a significant alteration to its normal function.

The degradation of centrosomes during vertebrate oogenesis seems to be important to avoid parthenogenic multipolar divisions in species, where the sperm introduces a pair of centrioles at fertilization (*341*). In most animal cells, centrosomes are an important source of spindle microtubules, and in *C. elegans* zygotes they are indeed essential for embryonic bipolar spindle assembly and development (*342*). However, in *X. laevis*, they are primarily important to cleave the cells at the end of M-phase (*341*, *343*). These studies have also shown that multipolar spindles form if more than the two centrosomes are present. The centrosome function in early mammalian embryos is not yet precisely understood. However, when bovine parthenogenotes—activated oocytes that have not been fertilized by a sperm cell and thus completely lack a parental centrosome—are provided with a paternal genome via nuclear fusion, they form a bipolar spindle and divide normally, indicating that the centrosome in the cow embryo provided by the sperm is dispensable for spindle assembly (*344*).

As mentioned above, many mammalian zygotes inherit the centrosome from the sperm. However, the centrioles in the sperm centrosome are highly specialized for flagellar functions and thus need to be heavily restructured into a pro-nucleus associated centrosome ready for cell division (*158*, *310*, *345*).

In contrast, early mouse embryos lack centrosomes entirely and here many acentrosomal MTOCs support microtubule nucleation and spindle pole organization (*295*, *346*), similarly to the MTOCs in murine meiosis (*185*). And in fact, zygotic spindle assembly was suggested to still partially rely on Ran-GTP mediated microtubule nucleation around chromosomes, which is essential in mouse oocyte meiosis II (*185*, *295*, *347*). However, it is still unclear how the interplay of acentrosomal MTOCs and Ran-GTP mediated microtubule nucleation affects spindle formation at the oocyte to embryo transition.

While the overall number of acentrosomal MTOCs decreases throughout the cleavages (*295*), it is important for bipolar spindle formation that multiple MTOCs can be clustered at the poles. Clustering appears to depend on microtubule nucleation inside the spindle, which was examined in blastocysts of embryos from Augmin knock-out mice (*315*). Acentrosomal MTOCs contain PCM proteins like Pericentrin (*187*, *188*, *295*) and it was also shown that Plk4, a key factor of centriole duplication and function, is important for spindle assembly and function in acentrosomal early embryos (*348*).

Although centrosomes are formed *de novo* at the blastocyst stage in mouse embryos, their activity and function has been questioned during murine preimplantation development in general, as even after their *de novo* formation at the blastocyst stage, centrosomes do still not seem to organize microtubules in interphase (*296*).

In addition to changes in MTOCs, spindle size and M-phase duration [discussed in (*3*)], also other spindle factors change throughout the preimplantation development (in mice), for example different kinesins are used to bipolarize spindle microtubules at the different stages (*295*, *349*).

A challenge unique to the zygote is that the initially separate parental genomes that can be found in two distinct pronuclei need to be integrated in one mitotic division to yield two diploid and genetically identical daughter cells and we recently showed that this is facilitated by a dual spindle in mouse zygotes (*308*). Intriguingly, although the parental genomes are combined in one nucleus in the 2-cell embryo the genomes still occupy distinct compartments and thus stay spatially separated (Figure 5).

Due to the continuously changing circumstances at each embryonic cleavage, is highly important to further study how the mitotic spindle is formed in early mammalian embryos in general and especially in the zygote, where in addition to accomplish drastic cellular

restructuring, the cytoskeleton needs to form a mitotic apparatus around the two parental genomes.

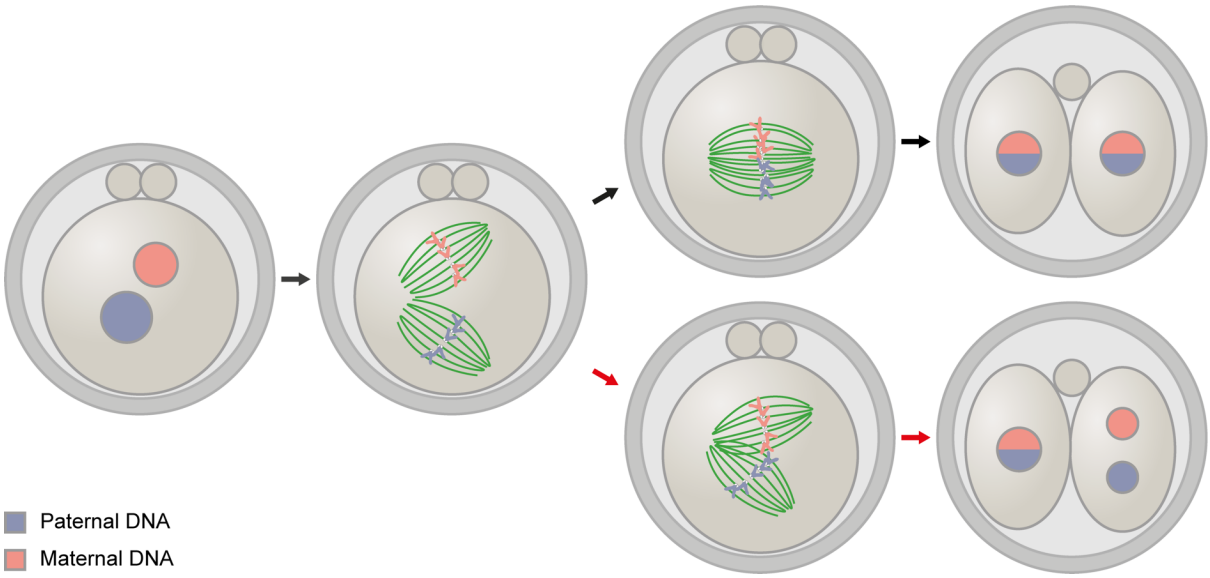

Figure 5: Dual spindle formation in mouse zygotes and its pitfalls for the first mitotic division. We recently showed in mouse zygotes that two separate spindles assemble around the parental genomes, which are presented within separate pronuclei at the beginning of the first mitotic division (*308*). During prometaphase the two spindles usually align in parallel positioning the chromosomes of the two genomes next to each other (upper pathway). The two parallel spindles then jointly segregate the chromosomes, which are enclosed in the nuclei of the 2-cell blastomeres, where the genomes consequently still occupy separate compartments. If the two spindles fail to position themselves in parallel and adjacent to each other before anaphase onset (after artificially enhancing the pronuclear distance in mouse zygotes), chromosomes are segregated along the different axes of the two spindles and potentially enclosed in more than one nucleus within each forming daughter cell, giving rise to binucleated 2-cell blastomeres, which are often observed in fertility clinics for humans and animal husbandry. Zygotic dual spindle formation and erroneous spindle alignment thus provide a rationale for this frequent phenotype. This figure was modified form (*3*), and was originally drawn and assembled by myself.

1.5 Light sheet microscopy to image early mammalian embryos

Fluorescence microscopy offers exquisite molecular selectivity, a high signal to noise ratio, a high acquisition speed and typically does not require to disrupt the specimen. In combination with genetically encoded fluorescent proteins (*350*) or self-labeling tags (*351–353*), it is thus the most widely used method to obtain dynamic information about living systems.

However, light can be harmful to living cells, and in particular to developing mammalian embryos. These are naturally never exposed to light and thus completely lack any protective measures, thus extensive light exposure can retard their division rates (*354*). Particularly, light with short wavelengths was shown to have negative effects. Already standard ambient light conditions in laboratory rooms could affect mammalian embryos (*355*, *356*), with far lower intensities compared to those used for microscopy applications. The negative effect of light

can mostly be attributed to the production of reactive oxygen species (ROS), which leads to oxidative stress in the embryo and can thereby negatively influence its development (*356*). Therefore, in order to allow imaging of embryonic development without major perturbations the effect of light induced ROS production needs to be minimized and carefully controlled.

Confocal fluorescence microscopy is often used to obtain sufficient spatial resolution in three dimensional biological systems, as it effectively blocks out of focus fluorescence from detection. Unfortunately, nevertheless the entire focal depth of the illumination lens is illuminated in the specimen for each focal plane and thus if the entire embryo is to be imaged in three dimensions, light exposure accumulates rapidly. Nevertheless, this method has previously been used to image live preimplantation embryos (*357*, *358*), but it was not possible to perform "in toto" imaging of the entire development from the zygote to the blastocyst or mild time-lapse imaging at second to minute resolution for shorter terms.

An alternative method to reduce out-of-focus fluorescence is light sheet microscopy (*359*), which is also called single-plane illumination microscopy (SPIM). As the name implies, here only one single optical plane of interested is illuminated and directly recorded. Contrasting to confocal microscopy this method ensures that much less of the specimen is irradiated with light unnecessarily, which can reduce the required light dose by up to two orders of magnitude, especially in thick and isotropic specimen such as mammalian embryos (*286*, *360*). Early versions of light sheet microscopy required sample embedding to prevent it from moving out of focus (*359*, *361*), however since then approaches have been developed that eliminate this requirement, which was essential to use this method for imaging of mammalian embryonic development (*362–364*). Still, these methods did not allow to image the entire development of the preimplantation embryo. More recently, our group developed an inverted single plane illumination microscope (iSPIM) that allows to image embryonic development *in toto* from the zygote up to the blastocyst (*286*). This microscope setup allows to image embryos with a thin light sheet of just 1.5 µm thus offering a good spatial resolution (*365*). Besides minimizing phototoxicity by reduced light exposure, in this system embryos can be incubated at 37 ˚C in a low oxygen-controlled environment further minimizing the production of ROS.

The iSPIM system now reduces phototoxicity far enough, that mouse embryos can be imaged without a major impact on their development. It is even possible to implant them back into pseudopregnant mice after in toto imaging and the implanted embryos will fully develop into

living mice at a similar efficiency as non-imaged embryos (*286*). Thus, the iSPIM technology opens up new possibilities to study developmental processes, but also dynamic cellular mechanisms within the pre-implantation embryo.

1.6 Objectives

The high frequency of chromosome segregation errors in early embryonic divisions is a major cause of aneuploidy and early pregnancy loss. It is thus very important to further study how mitosis under the special molecular and physiological conditions at the beginning of mammalian life proceeds in order to understand the molecular mechanisms that cause this calamity. Such findings will advance our basic understanding of the beginning of life but also provide the basis to develop better diagnostic and therapeutic approaches to treat infertility. Mitosis is highly dynamic and transient process in space in time, and fast fluorescence microscopy is needed to analyze the assembly and function of the mitotic apparatus *in vivo*. Our advanced iSPIM technology is a powerful tool to achieve this under mild, near physiological conditions allowing me for the first time to study spindle assembly in detail throughout mitosis in real time with minimal interference with early embryonic development.

Mitosis of the zygote is distinct from all other cell divisions. It has to segregate the sister chromatids from the replicated haploid parental genomes, which are present in two spatially separate pronuclei. Thus, a key open question is how zygotes organize the mitotic apparatus to ensure the formation of two identical daughter cells where both parental genomes are combined in one nucleus. Errors in this division are particularly detrimental as they will propagate throughout the embryo. Yet, this division not only has to deal with two nuclei at once, but also needs to switch from a meiosis-like to a canonical mitosis state at the beginning of the oocyte to embryo transition. Zygotic division can therefore be expected to be particularly fragile and this is indeed evident in the frequent occurrence of multinucleated 2-cell blastomeres in mammalian embryos.

My thesis has therefore focused on studying the mechanism of mitotic spindle assembly in mammalian zygotes. I have pursued this question in a two-pronged approach. My first objective has been to study how spindle assembly proceeds in the mouse zygote. The mouse

model is the most powerful mammalian system for molecular mechanistic experiments as many transgenic mouse lines for fluorescent molecular markers are available and experimental methods and molecular perturbation tools are in general well established. The focus of my work has therefore been to establish specific imaging assays and acute molecular perturbation methods that allow to dissect the contributions of the different microtubule nucleation pathways for zygotic spindle assembly. My second objective has been to establish a non-rodent mammalian model for live imaging of zygotic spindle assembly. The reason for this is that rodent zygotes are acentrosomal and not all aspects of my findings in mouse may therefore be generalizable to other mammals, including humans, that inherit a centrosome from the sperm. To address this, I decided to extend my research on spindle assembly to bovine zygotes, a model organism with inherited centrosomes, which is thus very close to human embryos.

2 RESULTS

2.1 Investigating dual spindle assembly in the mouse zygote around the two parental genomes and in the presence of many acentriolar MTOCs

The Ellenberg group recently reported that a dual spindle forms around the two parental genomes in mouse zygotes. This dual spindle keeps the parental genomes apart throughout mitosis so that even in the 2-cell embryo the parental genomes still occupy distinct compartments in the forming nuclei in the two blastomeres. How this spindle forms is an intriguing question and a major focus of this thesis. In mouse zygotes this is particularly interesting, as they lack centrosomes and instead have many acentriolar MTOCs.

2.1.1 Validating tdEos-hCep192 as marker for the acentriolar MTOCs in mouse zygotes

To obtain detailed insights into the dynamic process of dual spindle assembly, I aimed to image growing microtubules relative to chromosomes and MTOCs in live zygotes using the above mentioned inverted light sheet microscope (section 1.5). While the Ellenberg group had already established fluorescent reporters for microtubules and chromosomes in mouse embryos (*308*), there was no live reporter for MTOCs available in the group when I started my project. I therefore set out to validate fluorescently-tagged human centrosomal protein 192 (tdEos-hCep192) in mouse embryos, which had been reported as MTOC marker in mouse oocytes previously (*309*). To investigate, whether this was a feasible reporter to follow MTOCs in mouse zygotes, I assessed, whether it visibly affected the size or number of native MTOCs. To this end, I injected pronuclear stage zygotes with mRNA encoding tdEos-hCep192 to transiently express the fluorescent protein (*366*). To subsequently compare MTOCs in these reporter expressing and in control zygotes using immunofluorescence (IF), I fixed the zygotes at comparable cell cycle stages as MTOCs will likely change in number and size by fragmentation and clustering at different mitotic stages as described in the oocytes (*309*). Both, the control and injected zygotes were maternally expressing the chromatin reporter mCherry-tagged Histone 2B (H2B-mCherry) from a transgenic mouse strain. Upon live imaging with the inverted light sheet microscope, I first used the H2B-mCherry fluorescence to stage cell cycle progression by monitoring chromosome condensation to finally collect the zygotes for fixation when rod-shaped chromosomes formed in prophase, just prior to NEBD. IF for Pericentrin showed that the MTOCs were similar in size and number and similarly distributed

throughout the cytoplasm in the control (Figure 6, left panel) and injected zygotes (Figure 6, three right panels). The tdEos was still fluorescent after fixation and the signal colocalized with signal from the Pericentrin immunostaining (Figure 6, merged image). This indicated that expression levels of tdEos-hCep192 sufficient for live imaging led to correct subcellular targeting of the reporter to MTOCs containing Pericentrin, whose number and position appeared very similar to control zygotes. I therefore concluded that the reporter was suitable for live imaging of MTOCs in mouse zygotes.

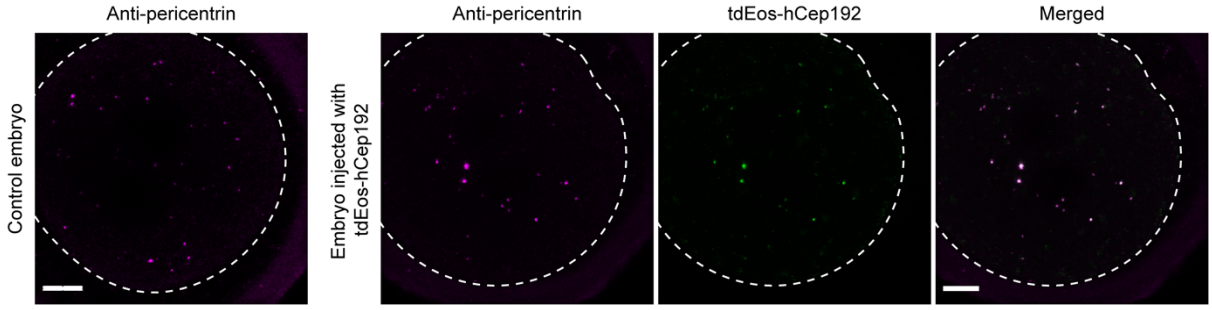

Figure 6: Expression of tdEos tagged hCep192 in mouse zygotes does not visibly impact acentriolar MTOCs. IF images of MTOCs in mouse zygotes fixed in prophase. The embryos were collected from transgenic females (R26/R26-H2B-mCherry) after natural mating with WT males. Pronuclear stage zygotes were injected with mRNA encoding tdEos-hCep192 to validate the impact of the protein expression on acentriolar MTOCs. Mitotic timing was assessed by monitoring chromosome condensation upon live imaging of H2B-mCherry using the above described inverted light sheet microscope (Introduction section 1.5). When rod-shaped chromosomes had formed within the pronuclei, the embryos were collected, fixed and stained with an anti-pericentrin antibody to label native MTOCs. The left image shows a control embryo without mRNA injection. On the right, an embryo injected with tdEos-hCep192 mRNA is shown. The anti-pericentrin staining is shown in magenta, tdEos-hCep192 is shown in green. The merged panel shows clear colocalization of native pericentrin and exogenous hCep192. All images show a maximum intensity projection of selected confocal planes. Scale bars, 10 µm.

2.1.2 Live imaging of acentriolar MTOCs and growing microtubules shows their dynamics in murine zygotic dual spindle assembly

As tdEos-hCep192 seemed a feasible fluorescent MTOC reporter in mouse zygotes, I set out to image MTOCs and growing microtubules in live zygotes using light sheet microscopy to understand how the spindle apparatus formed in the presence of two compartmentalized parental genomes. In addition to injecting mRNA encoding tdEos-hCep192, I also delivered mRNA for EB3-mCherry2 as a reporter for the tips of growing microtubules. Using the inverted light sheet microscope, I maintained standard micro drop culture conditions for preimplantation mouse embryos at reduced oxygen concentration (5 % CO_2 and 5 % O_2), which allowed me to image the MTOC and microtubule dynamics in 3D every 45 or 60 seconds throughout the zygotic mitosis. This data confirmed that dual spindles form around the two

parental genomes in the presence of many cytoplasmic MTOCs in mouse zygotes (Figure 7). In total, 13 embryos were imaged as described and the pronuclear envelopes either broke down simultaneously or with up to 5:15 min delay of the lagging pronucleus (PN2) with respect to the leading pronucleus (PN1).

The approximate pronuclear volumes (Figure 7, blue spheres) could be derived from the exclusion of cytoplasmic EB3-mCherry2 fluorescence prior to or at NEBD. As the protein was not imported into the pronuclear compartments, their spherical volumes devoid of EB3-mCherry signal could be distinguished and segmented manually. Initially, at the time of NEBD, microtubules grew moderately from MTOCs, and increased around them until 7:30 min post NEBD. Interestingly, shortly after NEBD, the EB3-mCherry2 fluorescence increased transiently within the original pronuclear volumes suggesting microtubule nucleation dependent on Ran-GTP around chromosomes (Figure 7A, 4.30 min post NEBD). Subsequently, two bipolar microtubule arrays formed, which progressively aligned in parallel during prometaphase (Figure 7, 9:45-23:15 min post NEBD; aligning spindles are highlighted with surrounding dashed lines). Interestingly, only those MTOCs initially associated with the pronuclei before NEBD or localizing in their immediate surrounding later became part of the assembling spindles and progressively localized at the spindle poles, while MTOCs further away in the cytoplasm did not participate in spindle assembly. This indicated that MTOC self-organization could contribute to clustering of MTOCs at the spindle poles, which is in line with the mechanism described for meiotic spindle assembly in mouse oocytes (*185*).

Intriguingly, the MTOC clusters forming at the adjacent poles of the dual spindles did not merge, highlighting that in fact, the dual spindles are two separate microtubule systems (Figure 7A, white and red arrows mark the MTOC clusters at the separate, but adjacent poles of the dual spindles). This separation of two MTOC clusters at the dual spindle poles was mostly maintained until anaphase as it could be observed on at least one side of the aligning spindles in 70 % of the imaged embryos (n = 13).

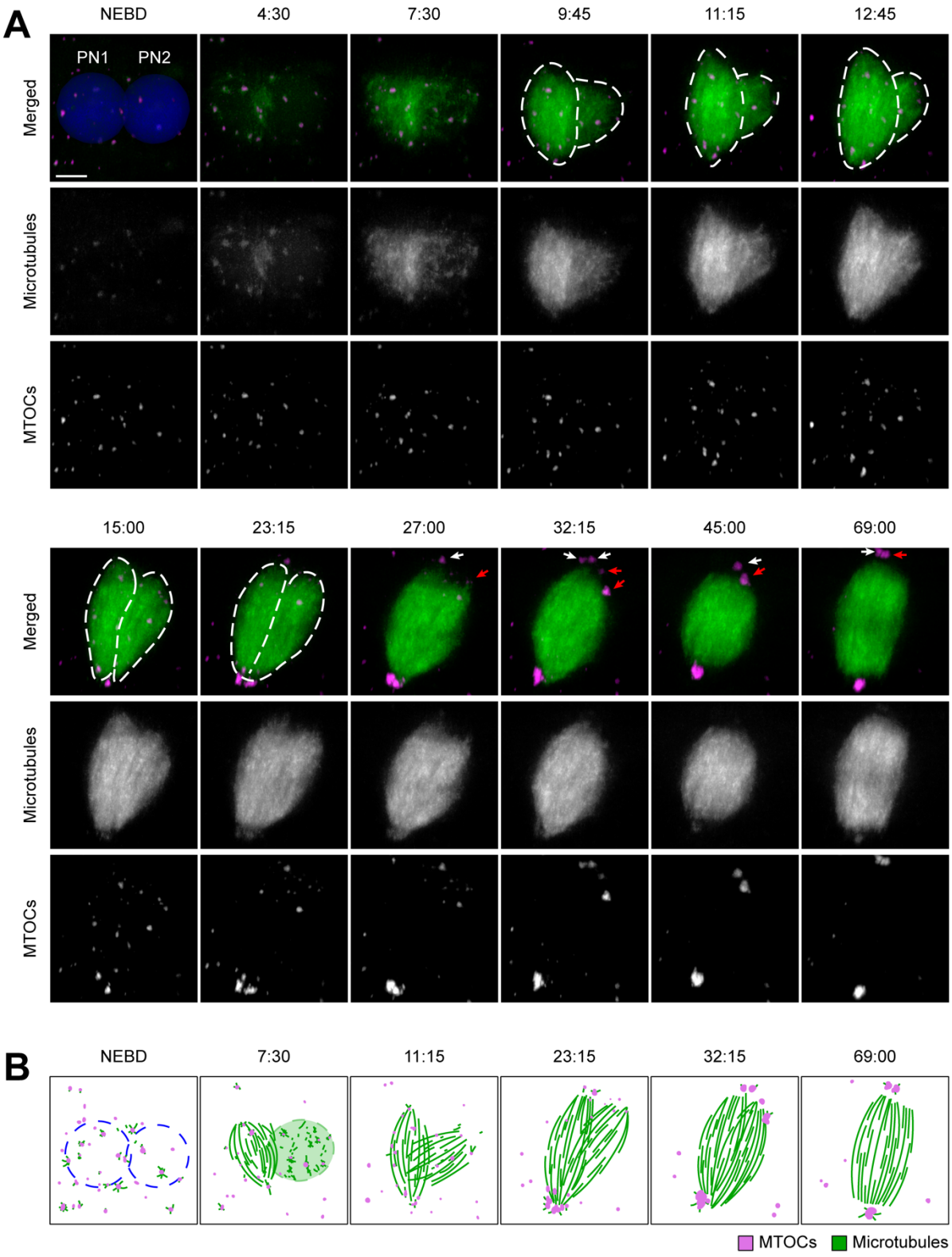

Figure 7: Dual spindle assembly in live mouse zygotes in the presence of many acentriolar MTOCs. (A) Upper panels show merged time lapse images of mouse zygotes (WT) expressing microtubule marker (green) EB3-mCherry2 and MTOC tdEos-Cep192 (magenta) after microinjection at pronuclear stage. Images were acquired by light sheet microscopy every 45 sec throughout the first mitosis and for up to 3 h in total. 3D rendered images of the spindle volumes around the pronuclei are shown. Timings are respective to pronuclear envelope breakdown in min:sec of the leading pronucleus (PN1). PN2: Lagging pronucleus. Lower panels show respective single channel grey scale images of the microtubule marker. Blue spheres are the segmented pronuclear volumes at initial NEBD. White dashed lines mark the rims of the two spindles. White and red arrows indicate

the different MTOC clusters, which seem to mark the separate poles of the pararellizing spindles. Automatically projected scale bar, 10 µm. (B) Illustrations accentuate the dynamics of dual spindle assembly around the two parental genomes observed upon live imaging as shown in (A). A similar figure was originally shown in our publication (*308*). The original figure was assembled by my colleague Dr. Judith Reichmann, but the data was acquired and processed by myself. The depicted figure was drawn and assembled by myself and panel A shows time lapse images of a different zygote from the same data set.

2.1.3 Microtubules predominantly grow in the former pronuclear volumes

The sequence of events in dual spindle assembly is enigmatic in mouse zygotes, especially how much and when the many MTOCs or a Ran-GTP based chromosome nucleation mechanism contribute. Thus, I first aimed to quantitatively assess to what extent the microtubules grew inside the former pronuclear volumes compared to the former cytoplasm just after NEBD. To analyze this, the mean microtubule intensity in the two respective pronuclear volumes, but also in the surrounding cytoplasm was measured over time from synchronous NEBD, or NEBD of the leading pronucleus (PN1) until 10:30 min thereafter (Figure 8). For this analysis only zygotes that passed quality control (as further described in Materials and Methods section 4.1.7) were taken into account (n = 8/13). In all analyzed embryos a substantial increase in microtubule intensity could only be observed within the former pronuclear volumes, while the microtubule intensity in the remainder of the cytoplasm stayed constant. Interestingly, a steep initial increase of microtubule intensity inside the pronuclear volumes within the first 2 minutes of the respective nuclear envelope breakdown indicated that chromosome signaling-based microtubule nucleation might play an important role for assembling the two spindles around the spatially separated parental genomes.

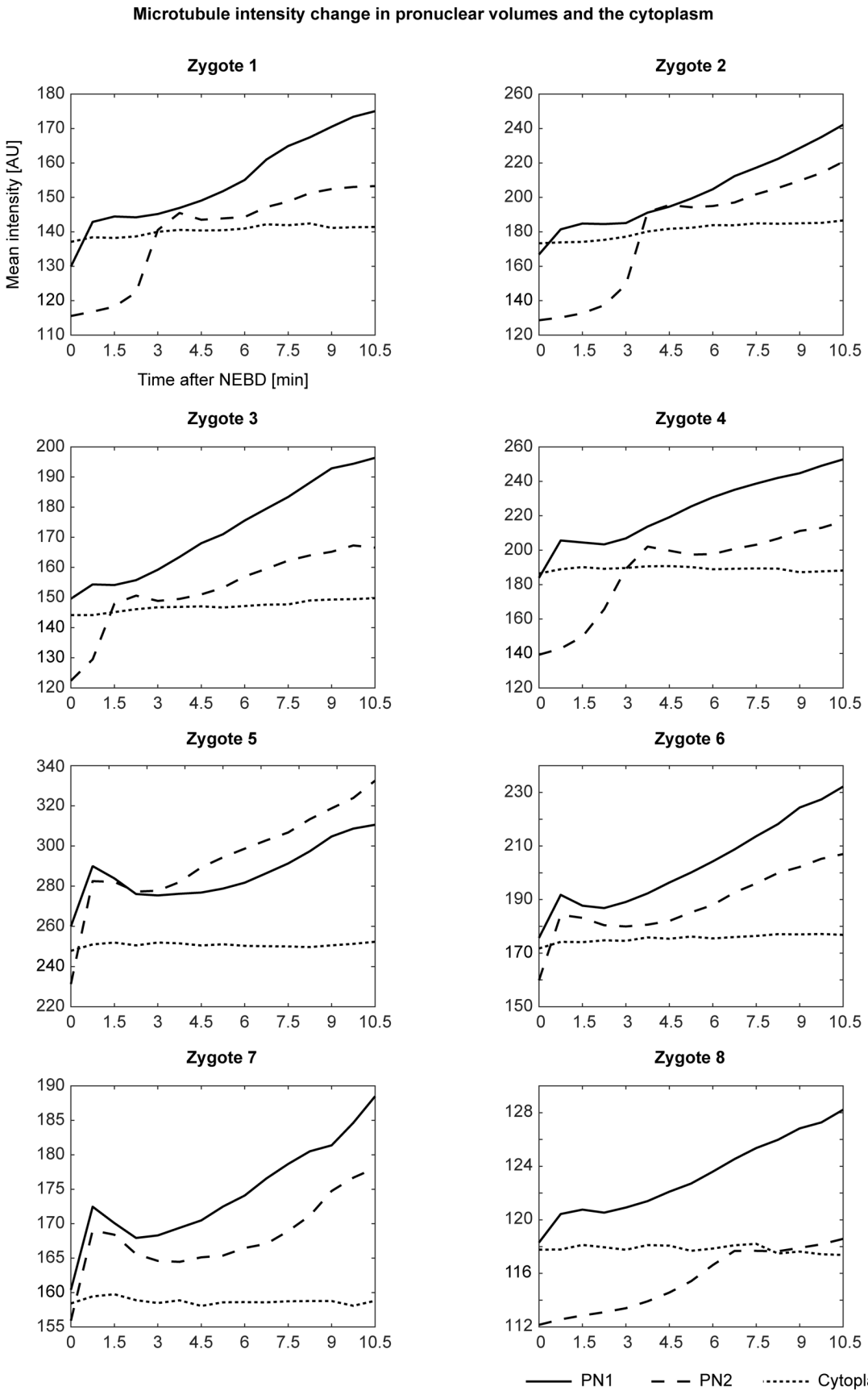

Figure 8: Microtubule intensity change within the original pronuclear volumes compared to the remaining cytoplasm in live mouse zygotes. Microtubule signal (EB3-mCherry2) from live imaging of eight mouse zygotes by light sheet microscopy every 45 sec as shown in Figure 7A was analyzed for 15 time points starting at NEBD

of the leading pronucleus (PN1) or both synchronous pronuclei (for detailed description, see Materials and Methods section 4.1.7). The analysis was performed in collaboration with my colleague Dr. Julius Hossain. Plots show the mean signal intensity [AU] within the two original pronuclear vlumes (determined by manual segmentation illustrated by the blue spheres in Figure 7A) and within the cytplasm over time [min] respective to NEBD. Solid line shows the mean intensity profile for the leading pronucleus, dashed line for the lagging pronucleus (PN2) and dotted line for the cytoplasm. The analyzed data was part of the data used to describe MTOC behavior in zygotic dual spindle assembly in our publication (*308*).

2.1.4 Microtubule nucleation in the nucleus upon NEBD

Considering that only a relatively small fraction of cytoplasmic MTOCs is incorporated into the spindles and their poles and observing the rapid increase in microtubule growth in the pronuclear volumes immediately after NEBD, I set out to further analyze the microtubule growth patterns in the former pronuclear volumes. To this end, I performed IF and high-resolution confocal microscopy of MTOCs, microtubules and kinetochores in transgenic zygotes, which I correlatively fixed when the nuclear envelopes had just become fenestrated (Figure 9). As the zygotes were maternally expressing H2B-mCherry and EGFP-alpha-tubulin, using live imaging I could stage mitotic progression by monitoring how chromosomes condensed into rod-shaped structures during prophase (as already described in section 2.1.1), and I could even precisely capture the moment when the nuclear envelopes became fenestrated by monitoring the entry of fluorescent soluble tubulin into the pronuclear compartments. I hypothesized that if chromosomal nucleation took place, I should be able to detect individual microtubules or bundles in the nucleus at this early time of nuclear permeabilization before the nuclear envelopes are fully broken down and while they still exclude MTOCs and denser cytoplasmic asters. Thus, I collected and fixed the zygotes at this very early stage of NEBD and indeed, IF analysis revealed the presence of individual microtubule bundles growing in the pronuclear volumes (Figure 9). I could detect two categories of nascent microtubules in the nucleus. On the one hand, I observed microtubules that were clearly connected to and thus potentially also nucleated at MTOCs, although IF of the microtubule lattice did not allow me to score the growth directionality directly. Such MTOC connected microtubules penetrated into the pronuclear volume in apparently random directions without visibly making contact to kinetochores or chromosomes (Figure 9, Embryo 1, white arrow). In other cases, such microtubule bundles connected to MTOCs at the pronuclear rim ware also connected to kinetochores (Figure 9, Embryo 2, white arrow). Surprisingly, the same kinetochore was in fact in contact with microtubule fibers, which were

connected to two different MTOCs at opposite sides of one pronucleus. At this very early time point (within the first minute/s) after nuclear permeabilization, it seems however unlikely that a classical search and capture mechanism would already achieve such a dual attachment of one kinetochore in the pronuclear volume. I therefore hypothesized that certain kinetochore dependent signals might promote their capture.

On the other hand, I observed microtubule fibers in the nucleus that were not anchored to MTOCs at all, but in contact with kinetochores (Figure 9, Embryo 3 and 4, white arrows). This suggested that chromosome and maybe in fact kinetochore dependent microtubule nucleation mechanisms contribute to dual spindle assembly upon NEBD. Finally, multiple microtubule bundles of variable length and curvature could be observed in the pronuclear volume that were not clearly connected to either MTOCs or kinetochores, which indicates that in addition to MTOC and kinetochore-promoted nucleation pathways also chromosome signaling through Ran-GTP in general could promote spontaneous microtubule nucleation in the nucleus and thus contribute to the formation of the mitotic dual spindle in mouse zygotes (Figure 9, Embryo 4).

Overall, the assay I developed to analyze spindle microtubule nucleation just after NEBD by correlative live imaging and high resolution IF after single embryo fixation turned out to be very powerful to capture 'pioneer' microtubule fibers in the nucleus. The different connections made by these early nuclear microtubules implicated multiple microtubule nucleation pathways as potentially relevant for spindle assembly in the mouse zygote, namely MTOC, kinetochore as well as nucleoplasmic Ran-dependent nucleation. Despite its high resolution, the static nature of this data from fixed cells made it difficult to assign each nuclear microtubule growth event unambiguously to one or the other pathway. For example, when a microtubule fiber connects to both, a kinetochore and an MTOC, it cannot be determined from which structure it originated and it is thus not clear which pathway is initially most important for zygotic dual spindle assembly. In addition, the correlative fixation assay had rather low throughput, as in embryos fixed slightly too late, microtubules were already too abundant and dense in the cytoplasm and the pronuclear volumes to resolve single bundles and their connections to nucleation centers with certainty even in high resolution IF.

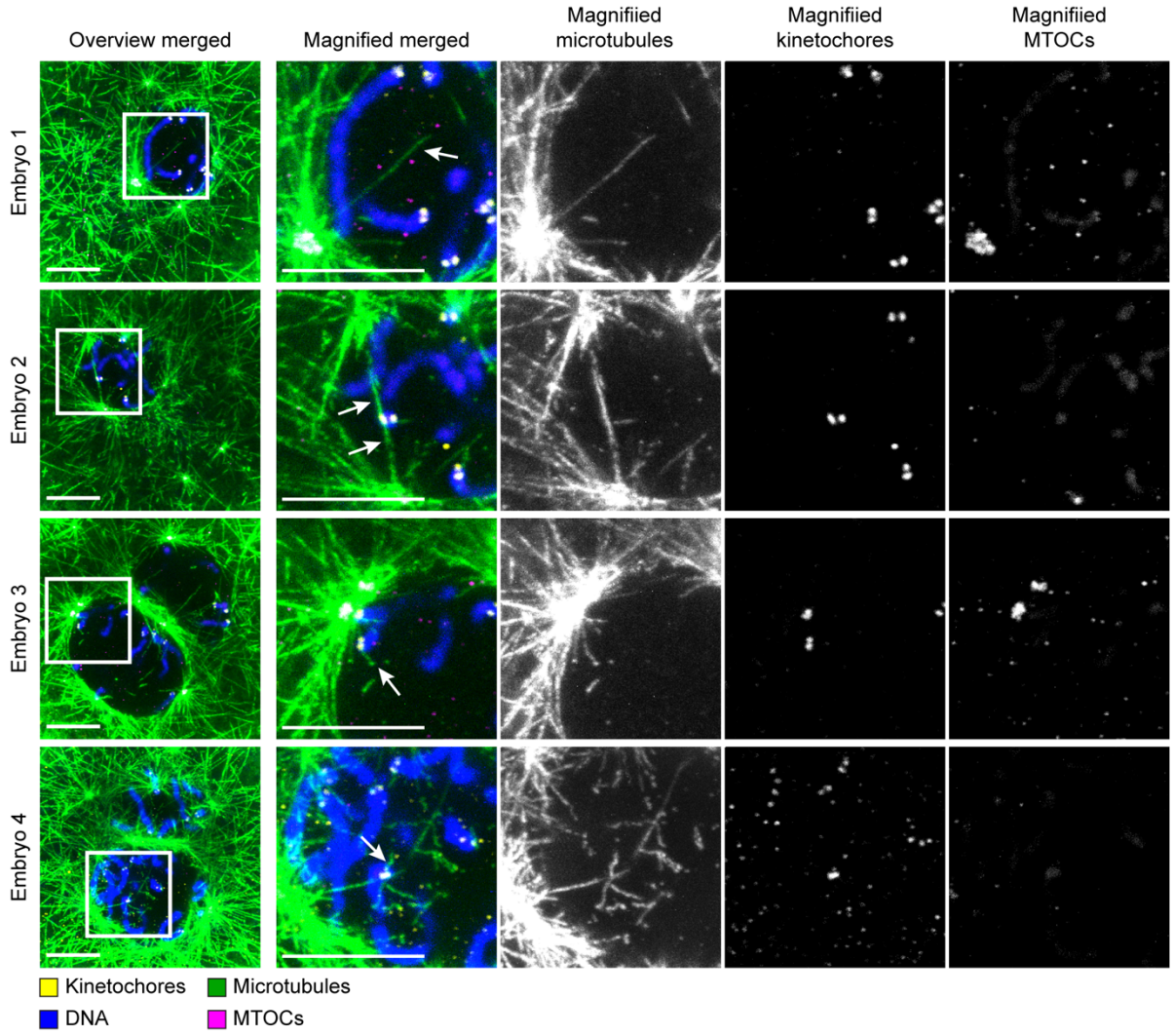

Figure 9: Patterns of microtubule nucleation and growth in mouse zygotes at NEBD. IF images of mouse zygotes fixed at the time of NEBD. The embryos were collected from transgenic females (R26-H2B-mCherry/R26-EGFP-Tuba) after natural mating with WT males. Mitotic timing was monitored by live imaging of H2B-mCherry (Chromatin) and EGFP-alpha-tubulin (Microtubules) using inverted light sheet microscopy. Prophase progression was assessed by the state of chromosome condensation and fenestration of the nuclear envelopes could be observed by imaging EGFP-alpha-tubulin dissociating into the previously compartmentalized pronuclear volumes. The embryos were collected at this early stage of NEBD and immediately fixed for subsequent IF. Individual rows show images different zygotes and all images are maximum intensity projections of selected confocal planes. From left to right: First column shows a merged overview image of the central zygotic region encompassing parts of one or both pronuclear volumes. DNA (Hoechst, blue); microtubules (alpha-tubulin, green; note that this signal can be attributed to both the IF staining and the EGFP-Tuba signal); kinetochores (CREST serum proteins, yellow) and MTOCs (Pericentrin, magenta). White squares indicate the respective magnified region shown in the second column. 3rd to 5th column show respective single channel data for microtubules, kinetochores and MTOCs. Note that some signal from the transgenic H2B-mCherry is sometimes still detectable after fixation (see single channel images of MTOCs). Microtubules seem to nucleate from MTOCs into the pronuclear space (Embryo 1, lower white arrow; Embryo 2, white arrow), but were also observed at kinetochores whithout a connection to MTOCs (Embryo 3 and 4, white arrows). Scale bars, 10 µm.

2.1.5 Chromosome- and/or kinetochore-based microtubule nucleation dominates microtubule regrowth after depolymerization

Thus, I next aimed to set up an assay at which I could eliminate the rapid microtubule crowding caused by fast microtubule nucleation and growth at NEBD, but also by the microtubule network from randomly distributed cytoplasmic MTOCs, which are already active in early prophase. To achieve this, I performed a microtubule regrowth series after initially depolymerizing microtubules at NEBD in mouse zygotes. Initially, I determined the required Nocodazole concentration and incubation time to completely depolymerize microtubules at the time of NEBD as rapidly as possible (see Materials and Methods section 4.1.8 and Figure 27). The aim was to reduce the incubation time compared to previous assays (*308*), where the embryos were incubated in Nocodazole for approximately 5 hours, which might have affected the observed microtubule nucleation patterns due to potential side effects of long exposure of the drug. After careful titration, I established that culturing the embryos in the presence of 10 μM Nocodazole for 30 min is in fact sufficient to depolymerize all microtubules at the onset of spindle assembly just after NEBD in mouse zygotes. I thus set out to determine at which sites microtubules would start to regrow after washing out the drug again after this treatment. To determine the time of NEBD, I again used live imaging of zygotes maternally expressing EGFP-alpha-tubulin and H2B-mCherry and when the chromosomes were highly condensed and soluble fluorescent tubulin dimers started to diffuse into the pronuclear space, I started to culture the embryos in the presence of Nocodazole. Subsequently, I washed out the drug and fixed them in 1-min intervals before processing them for IF (Figure 10).

Compared to control zygotes, which were directly fixed at NEBD without depolymerizing the microtubules (Figure 10, first column, w/o Nocodazole), microtubules were indeed completely depolymerized after the 30 min drug incubation (Figure 10, second column, 0 min washout). As early as 2 min after washing out Nocodazole, I observed that microtubules re-grew more strongly in direct proximity of kinetochores compared to MTOCs in close proximity to the chromosomes. At 3 and 6 min of microtubule regrowth, it became even more evident that strong microtubule fibers grew around the chromosomes, and especially the kinetochores, while the filaments at the MTOCs were fewer, shorter and weaker. Already 8 min after washing out Nocodazole, microtubules were strongly growing all around the genomes again, indicating the rapid reversibility of the short-term drug treatment, but making single fiber connectivity analysis very difficult due to high microtubule density. At this

stage, MTOCs in close proximity to the pronuclei also radiated longer microtubule fibers that were mostly directed towards the chromosomes.

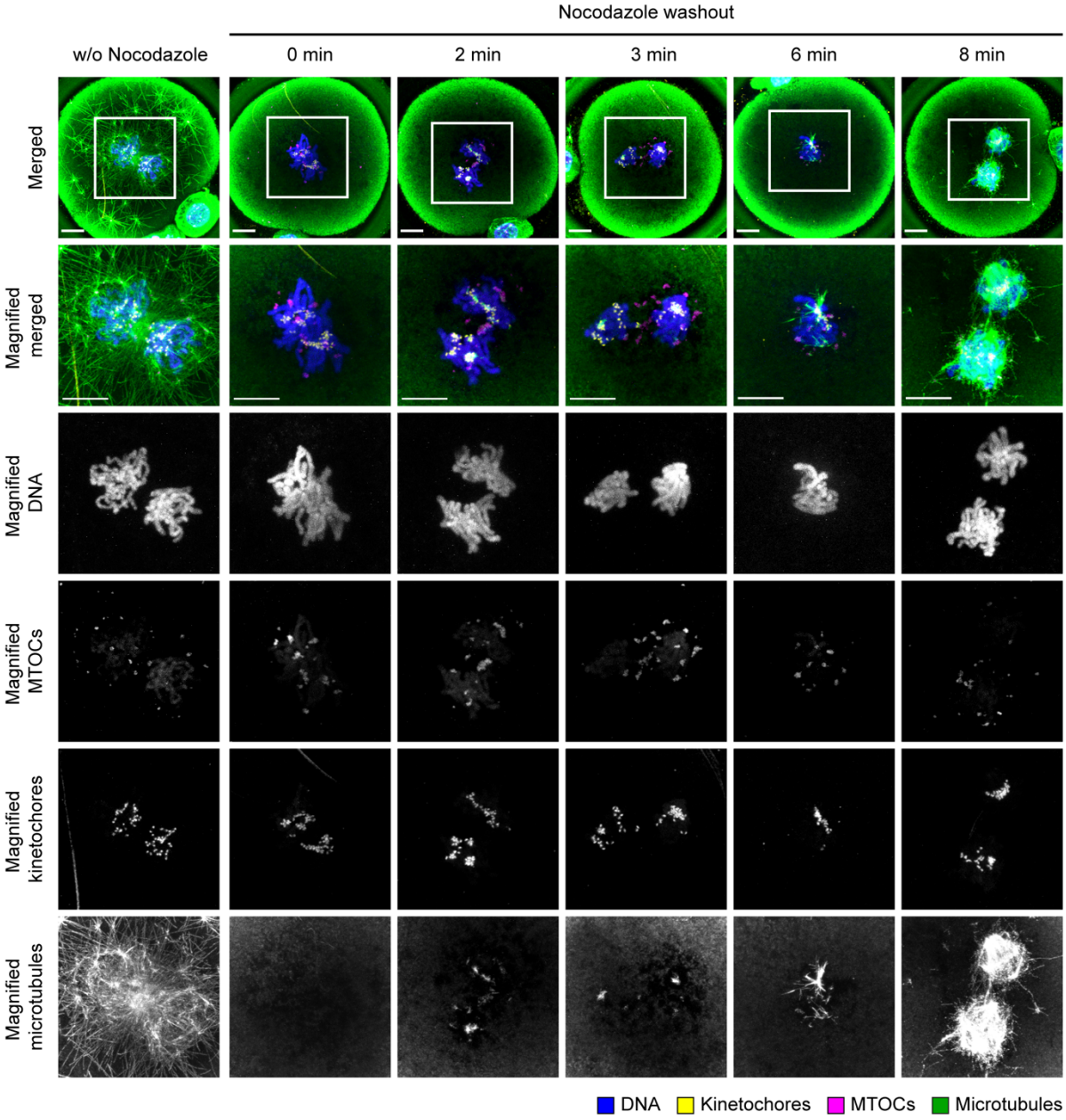

Figure 10: Microtubule regrowth after Nocodazole induced depolymerization at NEBD in mouse zygotes. IF images of mouse zygotes fixed after depolymerizing microtubules at the time of NEBD and subsequently regrowing the microtubules for the indicated time periods. The embryos were collected from transgenic females (R26-H2B-mCherry/R26-EGFP-Tuba) after natural mating with WT males. Mitotic timing was monitored by live imaging of H2B-mCherry (Chromatin) and EGFP-alpha-tubulin (Microtubules) using inverted light sheet microscopy. Prophase progression was assessed by the state of chromosome condensation and NEBD could be observed by imaging EGFP-alpha-tubulin dissociating into the previously compartmentalized pronuclear volumes. The embryos were collected at NEBD and immediately transferred into culture medium containing 10 μM Nocodalzole to incubate for 30-35 min at normal culture conditions. Microtubule regrowth was initiated upon transfer into drug-free culture medium, where zygotes were incubated to be fixed in 1-min time intervals up to 10 min. The first column shows a zygote fixed at NEBD without Nocodazole induced depolymerization of the microtubules. The subsequent columns show IF images of selected zygotes regrowing microtubules for

different time periods ater Nocodazole washout. All images show a maximum intensity projection of selected confocal planes. Top row shows the merged full sized overview images of the zygotes with DNA (Hoechst, blue); MTOCs (Pericentrin, magenta); kinetochores (CREST-serum proteins, yellow) and microtubules (alpha-tubulin, green; note that this signal can be attributed to both the IF staining and the EGFP-Tuba signal). White squares indicate the respective magnified region shown in the second row. The following rows show the respective single channel data of the magnified region. Note that fluorescence from the transgenic H2B-mCherry is sometimes still detectable after fixation (seen in some of the single channel images of MTOCs). Starting 2 min after washing out Nocodazlole, microtubule fibers grew more strongly in proximity of kinetochores compared to MTOCs. Scale bars, 10 µm. In this multi-step experiment I was supported by my colleague Sandra Correia.

Overall, the data of the regrowth assay indicated that chromosome- and kinetochore-mediated microtubule nucleation were the dominant pathways at the onset of spindle assembly (just after NEBD) in mouse zygotes. The extensive nucleation and fast microtubule growth around the spatially separated parental genomes together with the frequently asynchronous pronuclear NEBD between the two pronuclei would be expected to lead to the formation of two separate microtubule systems. Microtubule nucleation around the spatially separated parental chromosome clusters and subsequent microtubule self-organization could indeed explain these two systems can even bipolarize and start to congress their chromosomes independently. To test this hypothesis and dissect the requirements of chromosomal versus MTOC nucleation pathways for dual spindle assembly, perturbation experiments that can inhibit the different pathways selectively and actually prior to the onset of spindle assembly are therefore needed.

2.1.6 Investigating the role of MTOC based microtubule nucleation for zygotic spindle assembly

In cells that contain centrosomes, the MTOC based microtubule nucleation pathway in cells that contain centrosomes, is typically considered to be very important for the assembly of mitotic spindles. Mouse zygotes lack centrosomes but have many acentrosomal MTOCs, which have been suggested to collectively replace centrosome function (*185*, *295*). To assess if MTOCs are essential for zygotic spindle assembly, especially for the formation of a dual spindle—which keeps the parental genomes apart—I thus aimed to acutely remove the MTOCs at the onset of mitosis.

2.1.6.1 Acute depletion of MTOCs in mouse zygotes—implementing the 'Trim-away' method

Recently, the 'Trim-away' method has been reported as a powerful tool to acutely deplete targeted proteins within tens of minutes in a variety of systems including mammalian cells and mouse oocytes and embryos (*367*, *368*). In brief, the Ubiquitin-E3-ligase Trim21 is expressed in the organism of interest. Trim21 canonically recognizes the Fc region of antibodies in the cytoplasm with broad specificity as part of the native immune system and catalyzes its ubiquitination and degradation by the proteasome, which effectively causes degradation of the antibody and its bound protein (*369*, *370*). In the 'Trim-away' method this is exploited, as introducing an antibody specific for the protein of interest in presence of Trim21 leads to its rapid degradation. Degradation only happens if both components of the system are present and as the antibody can for example be introduced via microinjection, this technology provides unprecedented temporal control (*367*, *368*).

To destruct acentriolar MTOCs in mouse zygotes I chose Pericentrin as a target for the antibody. It has been shown that Pericentrin is a component of acentriolar MTOCs in early mouse embryos, and it is even essential for MTOC function in oocytes (*187*, *188*, *295*, *308*).

To perform the experiment, I thus first injected mouse zygotes with Trim21 and H2B-mCherry encoding mRNAs. I then used the H2B-mCherry signal to select successfully injected embryos that reached NEBD and then injected them with a Pericentrin-specific antibody. After incubating the zygotes for 20 minutes, I fixed them and subjected them to IF (Figure 11). When zygotes were injected with the Pericentin-specific antibody, no signal from IF against Pericentrin was visible (in the IF I used an antibody against Pericentrin derived from a different species than the injected one). This demonstrates that using the 'Trim-away' method, complete protein degradation below the detection limit of IF is possible within 20 minutes.

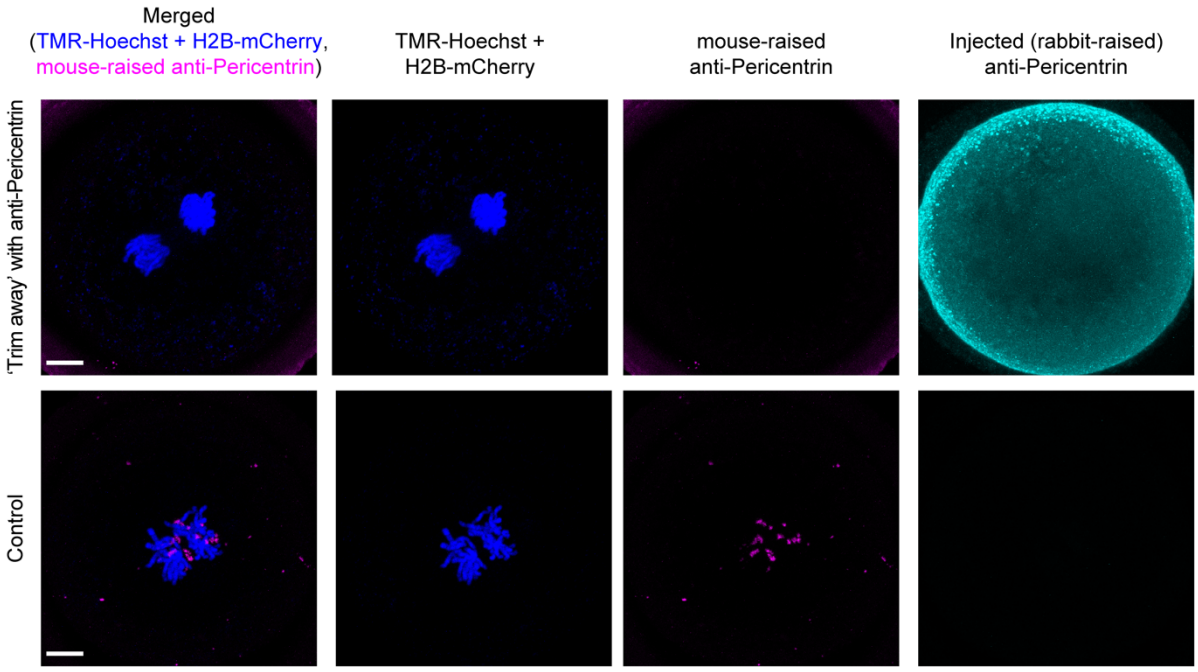

Figure 11: Degrading Pericentrin in mouse zygotes using the 'Trim-away' method. IF to validate acute Pericentrin degradation during Prophase of mouse zygotes using the 'Trim-away' method. The embryos were collected from WT females after natural mating with WT males. Pronuclear stage zygotes were injected with mRNAs encoding the Ubiquitin-E3-ligase Trim21 and H2B-mCherry. mCherry fluorescence of the expressed H2B-mCherry after co-injection was a readout for successful Trim21 injection and was used to monitor chromosome condensation in Prophase upon live imaging. At NEBD, the embryos were collected and injected with a rabbit-raised anti-Pericentrin antibody (top row) and cultured for 20 min prior to fixation. Control embryos were fixed directly (bottom row). For subsequent IF, native Pericentrin-containing MTOCs were labelled using a mouse-raised anti-Pericentrin antibody. To enhance fluorescence at chromatin (decreased H2B-mCherry signal after fixation), TMR-Hoechst was applied during the IF treatment. Successful injection of the rabbit-raised anti-Pericentrin antibody was verified by secondary IF against the rabbit specific antibody region. Using 'Trim-away', Pericentrin can be degraded beyond the detection limit within 20 minutes. All images show a maximum intensity projection of selected confocal planes. Scale bars, 10 µm.

The first experiment established that Pericentrin can be degraded using the 'Trim-away' method in mouse zygotes. However, this does not conclusively show that MTOCs are completely eliminated. In order to prove this, I thus performed the same experiment injecting Trim21 and H2B-mCherry expressing embryos with the Pericentrin-specific antibody but staining for γ-tubulin in subsequent IF (Figure 12), as γ-tubulin is a universal microtubule nucleating factor and thus a core component of active MTOCs. Here, I observed complete absence of MTOC characteristic γ-tubulin foci in injected zygotes compared to control zygotes that were only injected with the buffer solution (lacking the antibody, 'Mock control'). This demonstrates that indeed, the 'Trim-away' method targeting Pericentrin effectively eliminates also γ-tubulin and thus disrupts the functional architecture of the acentriolar MTOC.

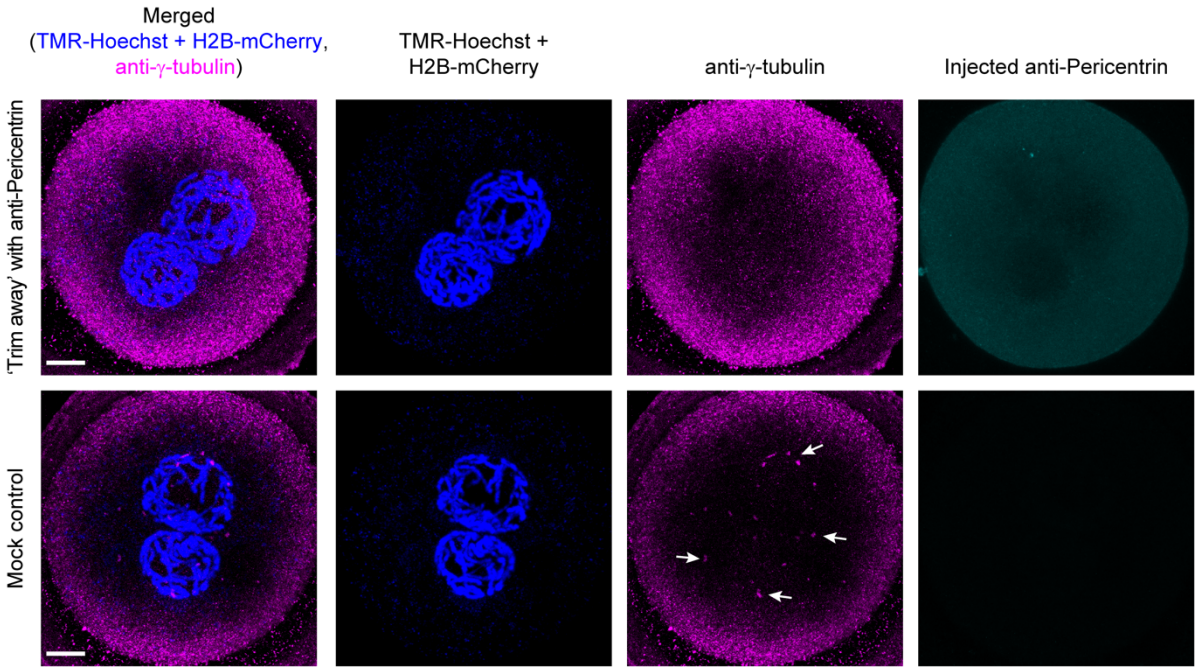

Figure 12: Pericentrin degradation effectively depletes the many acentriolar MTOCs entirely in mouse zygotes. IF to validate if Pericentrin degradation during Prophase of mouse zygotes using the 'Trim-away' method is sufficient to disrupt acentriolar MTOCs. The embryos were collected from R26/R26-EGFP-Tuba females after natural mating with WT males. Pronuclear stage zygotes were injected with mRNAs encoding the Ubiquitin-E3-Ligase Trim21 and H2B-mCherry. mCherry fluorescence of the expressed H2B-mCherry after co-injection was a readout for successful Trim21 injection and was used to monitor chromosome condensation in Prophase upon live imaging. In late prophase (when chromosomes were rod-shaped), the embryos were collected and injected with a rabbit-raised anti-Pericentrin antibody (top row) and cultured for 20 min prior to fixation. Control embryos were injected with the respective buffer solution without the respective antibody (Mock control, bottom row). For subsequent IF, MTOCs were labelled using a mouse-raised anti-γ-tubulin antibody. To enhance fluorescence at chromatin (decreased H2B-mCherry signal after fixation), TMR-Hoechst was applied during the IF treatment. Successful injection of the rabbit-raised anti-Pericentrin antibody was verified by secondary IF against the rabbit specific antibody region. Using 'Trim-away' against Pericentrin, MTOCs seem entirely disrupted, as judged by the absence of characteristic γ-tubulin foci (see white arrows in Mock control). All images show a maximum intensity projection of selected confocal planes. Scale bars, 10 µm. In this multi-step experiment I was supported by my colleague Sandra Correia to monitor incubation after antibody injection and assure timely fixation.

2.1.6.2 MTOC destruction in zygotes leads to two seemingly distinct spindle assembly phenotypes

Having established that Pericentrin degradation disrupts acentriolar MTOCs I then set out to investigate the effect of this perturbation on spindle assembly in zygotes using live imaging. I again used H2B-mCherry to visualize chromosomes and EGFP-α-tubulin to mark the spindle. In mock injected control embryos, I observed normal dual spindle formation, a robust metaphase plate and faithful chromosome segregation (Figure 13A).

Intriguingly, when MTOCs were degraded I observed two distinct phenotypes (Figure 13B, Figure 14). In the seemingly less severe phenotype, a bipolar spindle still formed and

segregated the sister chromatids (Figure 13B). Compared to the control, here the microtubule density within the spindle was substantially reduced and the spindle was smaller. Moreover, the metaphase plate appeared less stable and during anaphase I could clearly observe severely lagging chromosomes (Figure 13), even leading to loss or fragmentation of individual chromosomes. Despite this I was still able to observe that the parental genomes stayed separated throughout mitosis.

In the more severe cases (Figure 14) the spindle completely failed to separate the sister chromatids, leading to enclosure of the sister chromatids in one nucleus and failure of cytokinesis. Initially, also for this phenotype the formation of a spindle can be observed. But, compared to the control and the less severe phenotype spindle assembly was substantially retarded, the microtubule density was even further reduced, and the spindle even smaller. On top of this, bipolarity was only maintained for a short period of time. This small spindle was not able to promote chromosome congression and up to mitotic slippage in these embryos no formation of a proper metaphase plate could be observed. Despite this severe perturbation, still it was apparent that the parental genomes stayed clearly separated until mitotic slippage. Interestingly, small microtubule arrays were seemingly still directed to the separate parental genomes, which is in line with the formation of a dual spindle (Figure 14, 01:04 hours post NEBD).

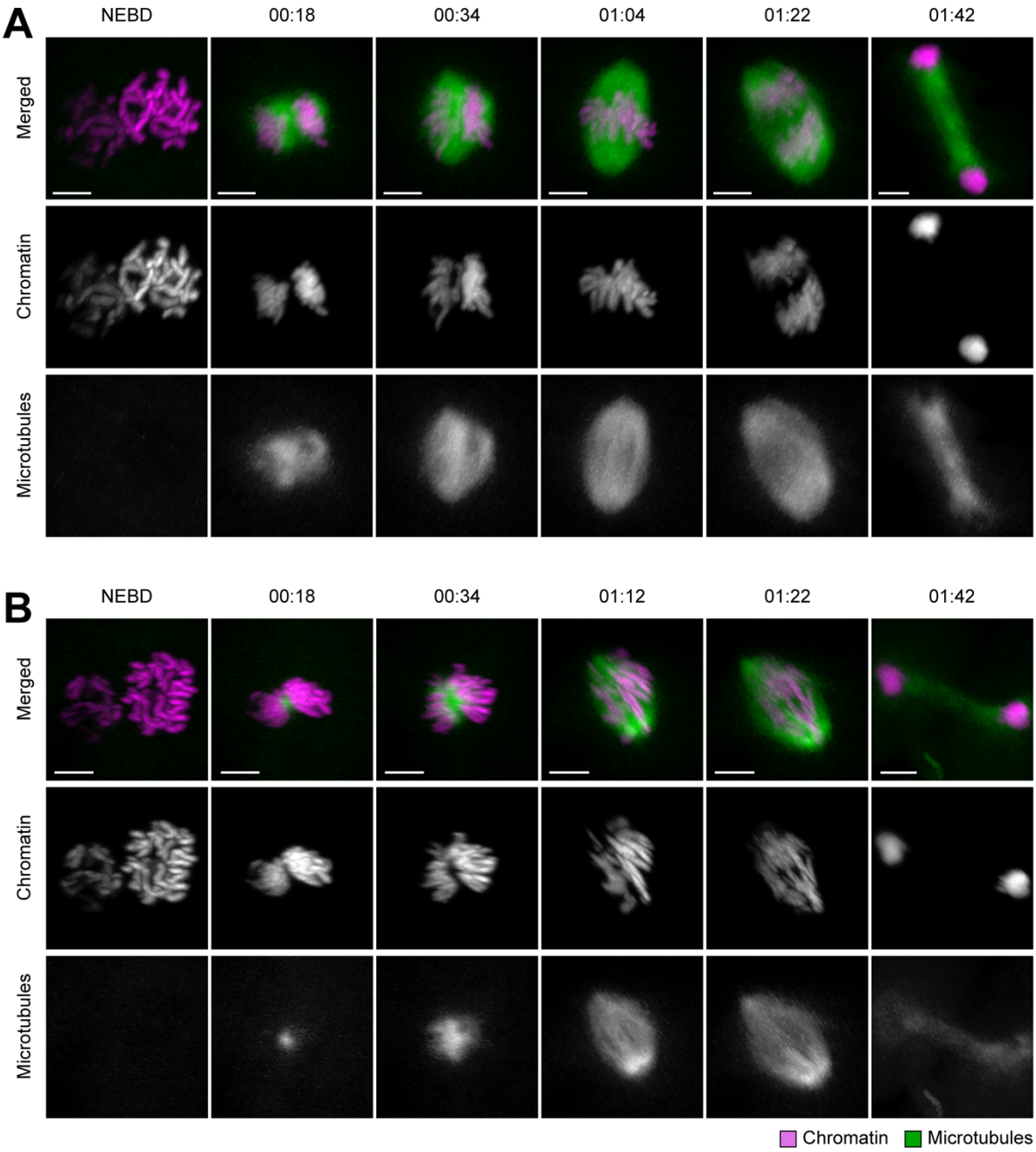

Figure 13: Investigating spindle assembly in mouse zygotes after depleting MTOCs—minor phenotype. (A-B) Time-lapse imaging of mouse zygotes to assess spindle assembly in the presence of MTOCs (**A**, 'Mock control'), or after acute depletion of MTOCs in Prophase prior to NEBD using 'Trim away' against Pericentrin (**B**). Zygotes from both groups were isolated from transgenic females and microinjected with mRNAs encoding Ubiquitin-E3-ligase Trim21 and H2B-mCherry at pronuclear stage. Fluorescence of the expressed H2B-mCherry (magenta) after co-injection was a readout for successful Trim21 injection and was used to monitor chromosome condensation upon live imaging. When chromosome condensation indicated that zygotes were progressing through Prophase, they were collected in small groups of embyros of similar mitotic progression (n = 2 to 4) and microinjected with a solution of anti-Pericentrin antibody in PBS and a minimal amount of detergent to facilitate injection (representative example with minor phenotype shown in B). The 'Mock control' group was injected with the same buffer solution lacking the antibody (representative example shown in A). After injection, the embryos were mounted back for subsequent live imaging starting earliest within 15-20 min post injection. Upper panels show merged time lapse images of mouse zygotes expressing H2B-mCherry (magenta) after mRNA injection and EGFP-α-tubulin (green) through maternal transgenic expression. Images were acquired by light sheet microscopy every 2 min throughout the first mitosis and for up to ~4 h in total. Spindle sections of 3D rendered images of the zygotes are shown. Timings are respective to synchronous pronuclear envelope

breakdown or NEBD of the leading pronucleus in hours:min. Lower panels show respective single channel grey scale images. Despite depleting MTOCs, in mouse zygotes with a 'minor phenotype' bipolar spindles could still form, and the parental genomes stayed apart. However, microtubule density in the spindle was reduced and chromosome congression impaired. Automatically projected scale bar, 10 µm.

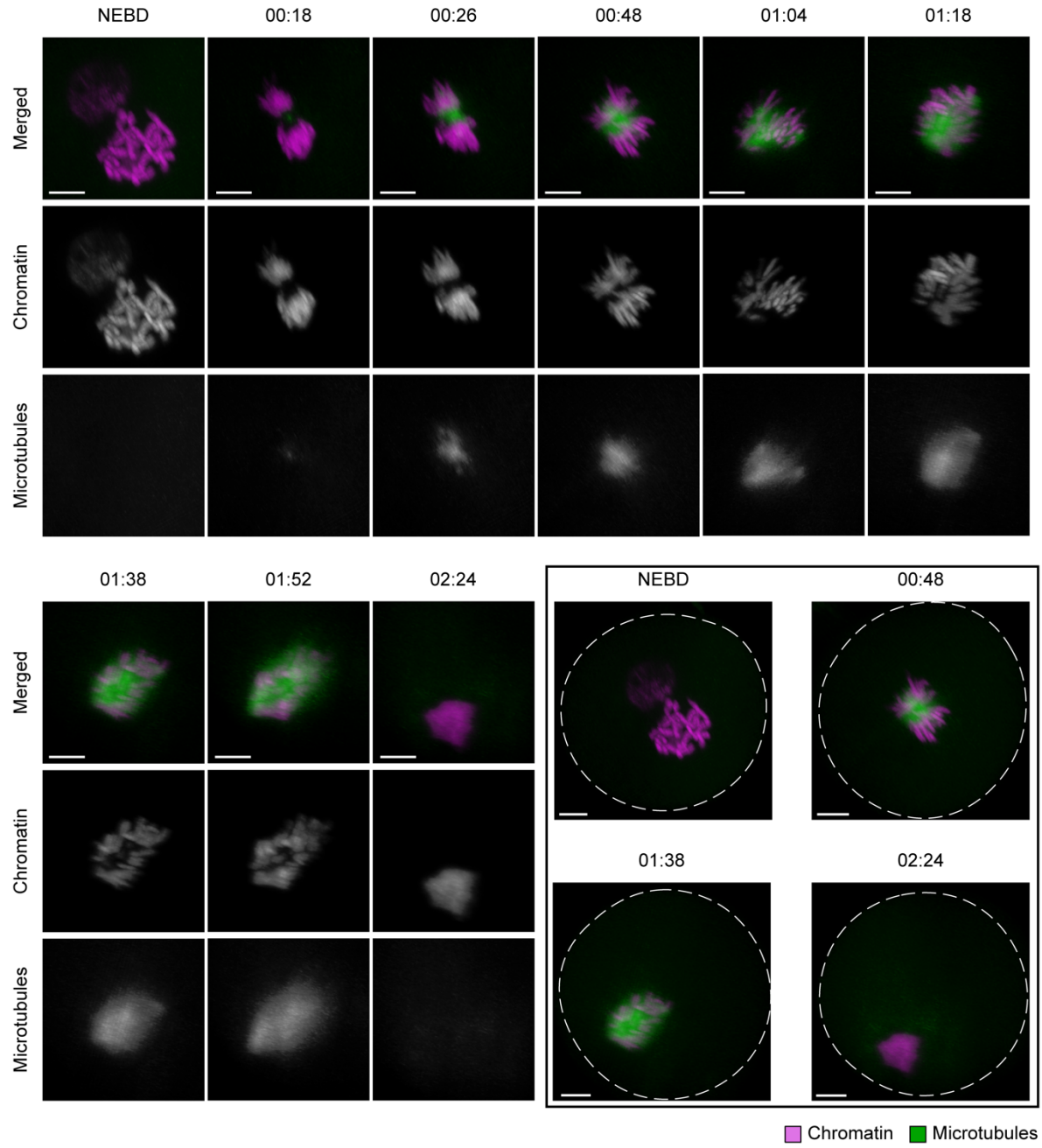

Figure 14: Spindle assembly in mouse zygotes after depleting MTOCs—major phenotype. Experiments performed identical to the treatment described for Figure 13B. Upper panels show merged time lapse images of mouse zygotes expressing H2B-mCherry (magenta) after mRNA injection and EGFP-α-tubulin (green) through maternal transgenic expression. Images were acquired by light sheet microscopy every 2 min throughout the first mitosis and for up to ~4 h in total. Spindle sections of 3D rendered images of the zygotes are shown. Timings are respective to NEBD in hours:min. Lower panels show respective single channel grey scale images. Images in the black box show 3D rendered images of the entire embryonic volume of selected time points to highlight dimensions and the failure of cytokinesis. Even if MTOC degradation leads to a failed chromosome segregation the spindles formed around the different parental genomes are still capable of keeping them separated.

In both perturbation phenotypes (Figure 13B and Figure 14) microtubule nucleation seemed to predominantly take place at the interphase between the two parental genomes and the genomes stayed separated throughout mitosis. These two observations could indicate that (in the absence of acentrosomal MTOCs) chromosome-/kinetochore-associated microtubule nucleation pathways dominate and as this happens around the individual parental genomes this could provide the organizational cues for dual spindle assembly.

Nevertheless, the phenotypes observed are still quite severe and thus MTOCs are clearly important. They contribute to the overall microtubule mass in the spindle, and they could contribute to spindle stability, bipolarization and elongation for proper force generation. Having established the method to acutely disrupt MTOCs will now allow to pursue these interesting phenotypes with further experiments to understand the major mechanism by which MTOCs contribute to zygotic spindle assembly.

2.2 Bovine zygotes as model for the first mitotic spindle assembly in the presence of centrosomes

Rodent zygotes enter the first mitosis with two pronuclei, similar to other mammalian species. However, rodents do not inherit the centrosome from the sperm, and thus, the question still remained, whether dual spindle assembly does also occur in zygotes with two centrosomes that might enforce a single bipolar microtubule array from the start. To investigate this, I aimed to use the bovine zygote as a model for multiple reasons. First, it has been shown that the zygote actually inherits the centrioles from the sperm (*310*, *344*). In addition, developmental timings are more similar between cattle and human (*371–374*), especially the timing of embryonic genome activation, as already mentioned in the introduction (*300*, *302–305*). And importantly, also whole and segmental chromosome abnormalities seem to occur as frequently in cow embryos after IVF as in human preimplantation embryos in fertility clinics (*25*, *332*). In addition, *in vitro* culturing systems were well established and bovine oocytes can be obtained for research from abattoir material (*25*, *375*). To set up the *in vitro* generation and culture of bovine zygotes, I teamed up with Dr. Marta de Ruijter-Villani from the University of Utrecht. We collaboratively set up the experimental approaches and analyses, which lead to the results described in this chapter. I was also greatly supported by my colleague Dr. Julius Hossain, who implemented several automated analysis pipelines to support my quantitative analysis of the data.

The results described in this chapter have already been reported in the preprint Schneider et al. (*376*), where they were originally already written by myself.

2.2.1 Immunofluorescence imaging of dual spindles in bovine zygotes

To get a first impression how spindles assembled in bovine zygotes and how centrosomes distributed and oriented with respect to the two parental genomes, IF imaging of fixed zygotes seemed to be the most feasible and effective approach. NEDD1 or Cep192 were chosen as markers of the pericentriolar material around the centrosomes and alpha-tubulin was used as reporter for the spindle microtubules while acetyl-alpha-tubulin was used to specifically label the sperm flagellum. In addition, Hoechst 33342 labelled the two parental genomes.

2.2.1.1 Two spindles assemble around the two parental genomes despite the presence of only two centrosomes

Confocal microscopy after IF against the different spindle proteins showed two major spindle configurations in the bovine zygote. In most prophase-stage zygotes, the two parental pronuclei were in close contact with both centrosomes localizing directly at or close to the pronuclear contact site (Figure 15A, Prophase). From pro-metaphase stage zygotes, it was evident that two microtubule clouds assembled around the adjacent parental genomes after NEBD, which we termed proximate dual spindles (Figure 15A, Pro-Metaphase, dashed lines around two clouds). Metaphase-stage zygotes with proximate spindles then showed that the two microtubule arrays eventually aligned or even fused along their pole-to-pole axes (Figure 15A, Metaphase, see dashed rim marking the two separate arrays). It was thus not always possible to distinguish fused double spindles from a single spindle. The aligned spindles were able to segregate sister chromatids in anaphase (Figure 15A, Anaphase). Interestingly however, the intensity of the pericentriolar staining decreased in anaphase indicating that the PCM around centrioles dispersed earlier than in usual somatic mitoses.

In contrast to this series of events, another phenotype of dual spindle assembly was also observed (Figure 15B, distant spindles). In ~1/5 of the prophase-stage zygotes the parental genomes were >30 μm apart (Figure 15B-C). It became evident that the distant genomes persisted throughout mitosis and individual spindles were observed around these separate genomes in overall 33 of 178 mitotic zygotes (Figure 15B-C). To make sure that this phenotype was not due to of polyspermic *in vitro* fertilization, the zygotes were either additionally stained with an antibody against acetylated alpha-tubulin to visualize the incorporated sperm flagellum (Figure 15D, white arrows), or the chromosome signal was segmented and quantified to exclude any polyploid zygotes. Among the metaphase-stage zygotes, 17 % showed two distant, bipolar microtubule systems (Figure 15C, grey bar, n = 12/72), and persisting distant spindles throughout anaphase and telophase showed that the individual spindles around each parental genome were still functional to initialize chromosome segregation (Figure 15B-C).

Interestingly, in some zygotes with either proximate or distant dual spindle assembly, mitotic progression was asynchronous between the two parental genomes (Figure 15E). It was evident that nuclear envelope breakdown could be sequential for the two pronuclei, leading to an initial lagging of the second spindle in prophase/pro-metaphase. But, in some zygotes,

the asynchrony was more severe, for example with one spindle being in pro-metaphase while the second one was already progressing through telophase. This clear asynchrony indicated that the two chromosome clusters and surrounding spindles could advance their mitotic progression independently albeit sharing the same cytoplasm.

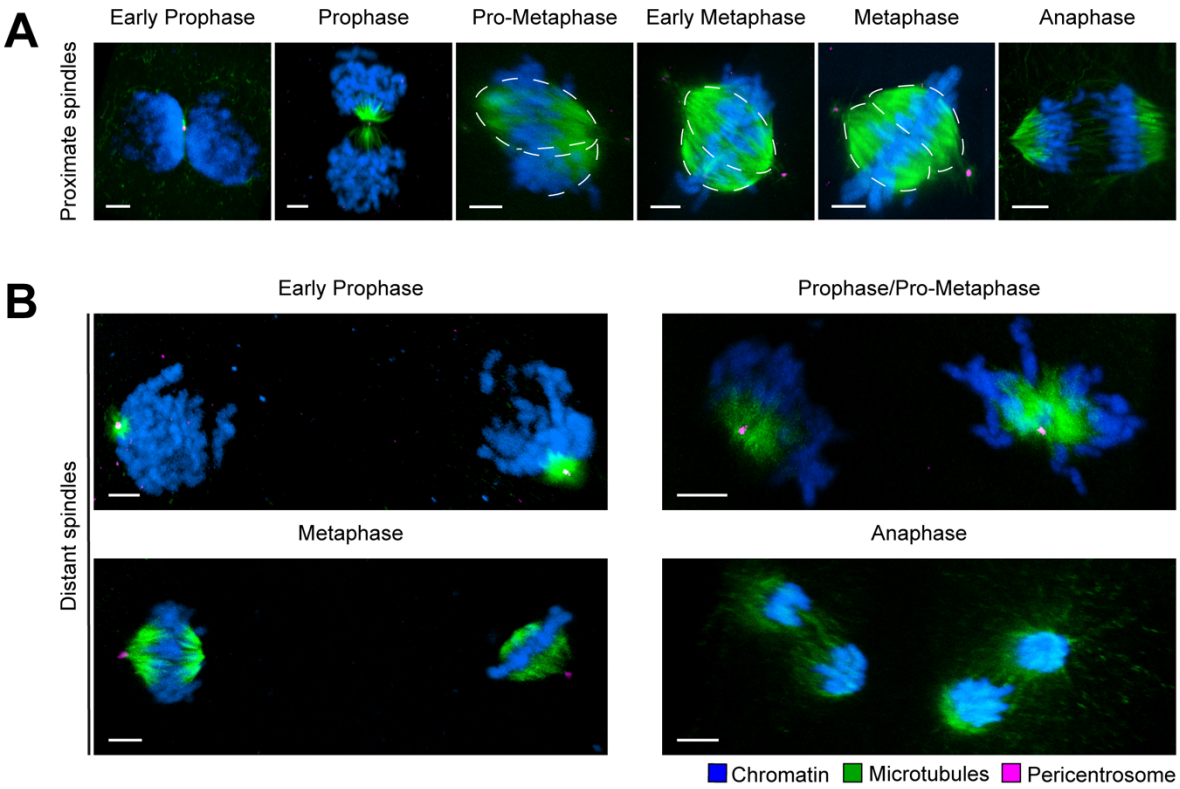
A
Early Prophase
Prophase
Pro-Metaphase
Early Metaphase
Metaphase
Anaphase
Proximate spindles
B
Early Prophase
Prophase/Pro-Metaphase
Distant spindles
Metaphase
Anaphase
Chromatin
Microtubules
Pericentrosome

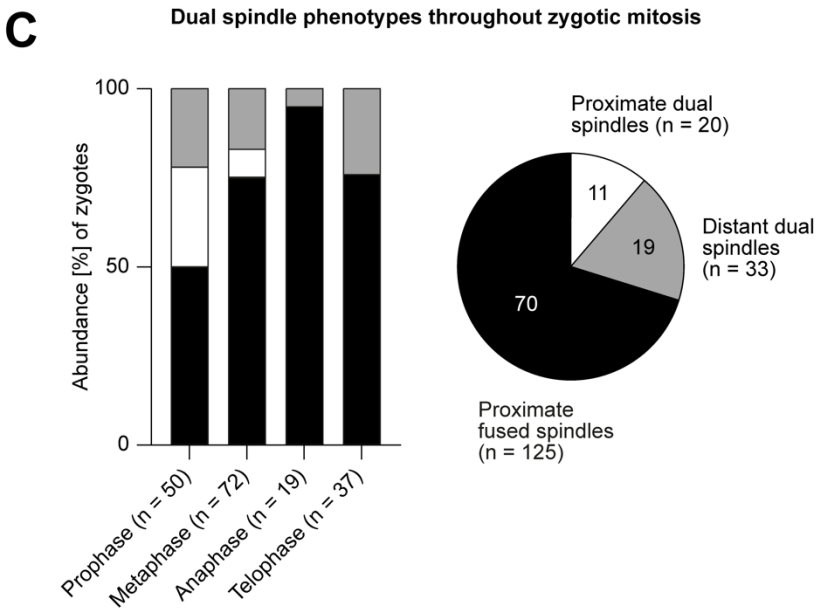
C
Dual spindle phenotypes throughout zygotic mitosis
Abundance [%] of zygotes
100
50
0
Prophase (n = 50)
Metaphase (n = 72)
Anaphase (n = 19)
Telophase (n = 37)
Proximate dual spindles (n = 20)
11
19
Distant dual spindles (n = 33)
70
Proximate fused spindles (n = 125)

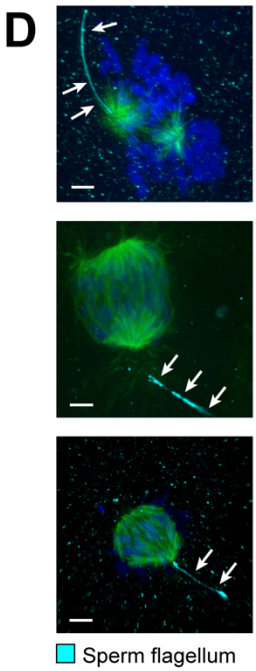
D
Sperm flagellum
Chromatin
Microtubules

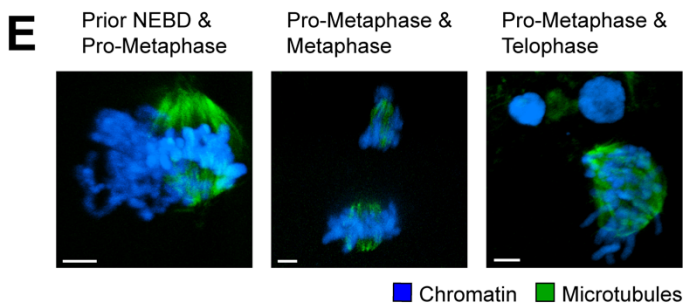
E
Prior NEBD & Pro-Metaphase
Pro-Metaphase & Metaphase
Pro-Metaphase & Telophase
Chromatin
Microtubules

Figure 15: Dual spindle types in bovine zygotes identified through IF imaging. (A-B, D-E) IF of bovine zygotes fixed at 27.5 h post in vitro fertilization at consecutive stages of mitosis. Maximum intensity projections of confocal sections orthogonal to the estimated spindle axis are shown. Microtubules (alpha-tubulin, green); pericentrosomes (Cep192 or NEDD1, magenta); chromatin (Hoechst, blue); Sperm flagellum (acetylated α-tubulin, cyan). Scale bars, 5 μm. Proximate (A) or distant (B) dual spindles were found to assemble around adjacent or disconnected pronuclei. Dashed lines mark the proximate, but distinct microtubule arrays. (C) Bar graph shows abundance [%] of different (dual) spindle types at consecutive mitotic stages. Pie chart visualizes the abundance [%] of the different (dual) spindle types among all mitotic zygotes (n_{total} = 178). (D) IF of bovine zygotes (as in A), but staining the sperm flagellum (cyan) to distinguish monospermic from polyspermic zygotes after the pronuclear stage. I IF of bovine zygotes (as in A) showing asynchronous distant dual spindles with very distinct mitotic timings inside same cytoplasm. All panels of this figure were adapted and modified from our preprint (*376*) and the data was originally acquired in collaboration with Dr. Marta de Ruijter-Villani; the figure was assembled by myself.

Overall, these initial IF experiments showed that dual spindle assembly also occurs in bovine zygotes in the presence of only two centrosomes, indicating that this assembly mechanism is conserved among mammalian zygotes, where the the two parental genomes are compartmentalized in two separate pronuclei at the time of NEBD. The data also showed that, if the parental pronuclei failed to migrate towards each other before NEBD, individual spindles form around the distant pronuclei and most likely persist throughout mitosis.

2.2.1.2 Comparing centrosome localization in proximate and distant dual spindles

Regarding centrosome positioning respective to the spindles, pericentrosomal staining indicated that in a majority of 77 % of the distant metaphase spindles, only one pole per spindle was connected to a centrosome (Figure 16A-B, monocentrosomal spindles, n = 17/22, white arrows indicate centrosome positions). 14 % of distant dual spindles were acentrosomal (n = 3/22) and ~10 % could not be scored due to poor pericentrosomal staining (n = 2/22). In contrast, ~70 % of the proximate, often fused/proximate metaphase spindles showed a centrosome at both poles (Figure 16A-B, bicentrosomal contralateral spindles, n = 30/43), although monocentrosomal spindles were also found in 16 % of these proximate spindles (n = 7/43), and one zygote with a fused metaphase spindle (2 %) had both centrosomes at the same pole (bicentrosomal ipsilateral spindle, n = 1/43).

Overall, this data indicated that polar centrosomes might not be essential to assemble and maintain a spindle or to establish bipolarity.

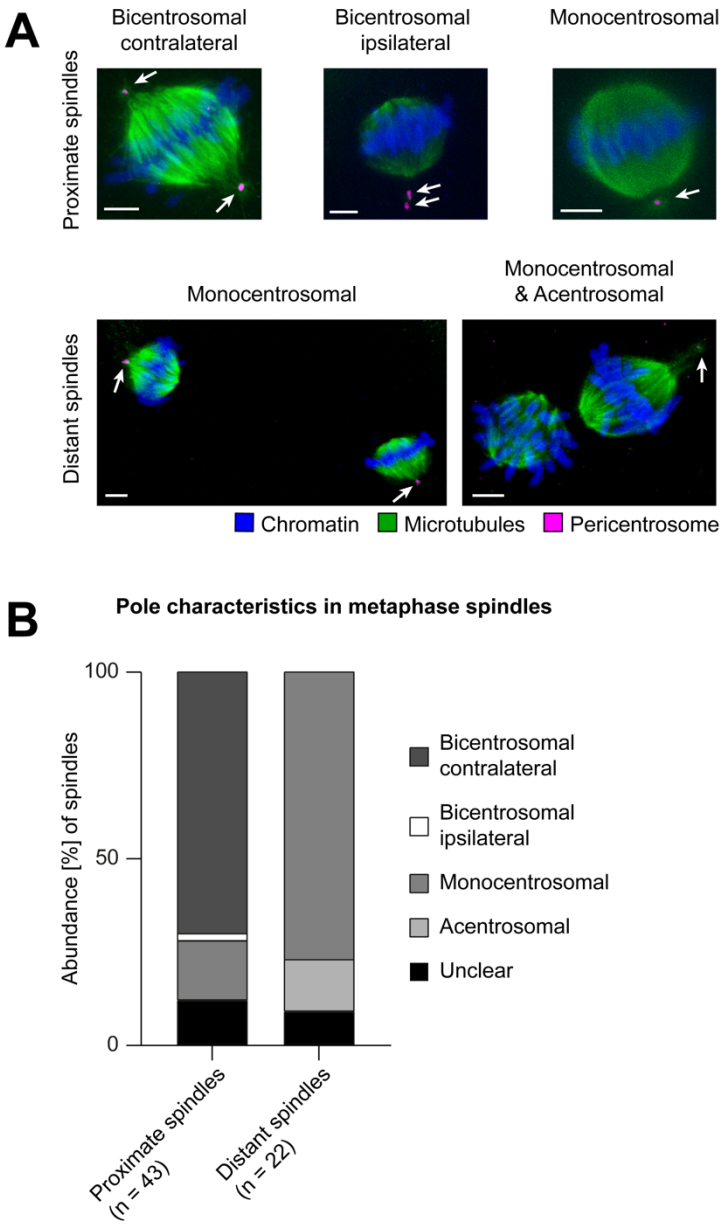

Figure 16: Diverse centrosome positioning in zygotic dual spindles. (A) IF of bovine zygotes fixed at 27.5 h post *in vitro* fertilization showing diverse centrosome positioning in proximate (fused) and distant dual spindles. Maximum intensity projections of confocal sections orthogonal to the estimated spindle axis are shown. White arrows indicate the number and position of centrosomes. Microtubules (α-tubulin, green); chromatin (Hoechst, blue), pericentrosome (NEDD1, Cep192, magenta). Scale bars, 5 µm. (B) Abundance [%] of centrosome positions in proximate (fused) or distant spindles as illustrated in (A). Images and data for graphs of this figure were adapted and modified from our preprint (*376*) and the data was originally acquired in collaboration with Dr. Marta de Ruijter-Villani; the figure was assembled by myself.

2.2.1.3 Centrosome-spindle connections are weak

In contrast to the textbook morphology of a mitotic spindle with the centrosomes closely attached to or even tightly incorporated into the spindle poles as in human HeLa cells (*174*, *377*), the pericentriolar material and the edge of the spindle body/pole did usually not

colocalize in bovine zygotic spindles. Instead, I identified clear micrometer wide intensity gaps of the microtubule signal between the actual spindle poles and the position of the pericentrosome in 63 % of those bicentrosomal contralateral spindles in metaphase, which passed quality control for further quantitative analysis (n = 10/16, i.e. Figure 17A) and in 45 % of the quality controlled distant monocentrosomal spindles (n = 5/11). This intensity gap prompted me to ask, if the centrosomes were actually stably connected to the spindle microtubules, and test if any stable kinetochore fibers were directly linking the centrosome to the chromosomes in the bovine zygotic spindles.

Zygotes were thus fixed at different mitotic stages following a short incubation on ice to depolymerize unstable microtubules. IF of these zygotes confirmed that the microtubules around centrosomes were unstable throughout mitosis since the microtubule signal at these sites decreased below the detection limit (Figure 17B). The astral microtubules linking the centrosomes to the spindle poles in metaphase were thus unstable and kinetochore fiber ends were not detectable at the centrosomes. In contrast, stable spindle microtubules around the chromosomes were conserved, but the signal intensity from microtubule staining now showed also a clear gap between the two microtubule arrays around each of the parental genomes in pro-metaphase (Figure 17B, Late Pro-Metaphase). This indicated that the microtubules, which are initially involved in dual spindle alignment or fusion are probably highly dynamic and thus, also unstable.

With support from my colleague, Dr. Julius Hossain, I analyzed quantitatively how the cold treatment affected the centrosome position with respect to the spindle (Figure 17C-F, $n_{unperturbed} = 16$, $n_{cold\text{-}shock} = 9$). Compared to unperturbed bicentrosomal spindles, the distance between the spindle body and the centrosome (Figure 17C, d_1) increased significantly from 3.9 to 6.5 µm on average in metaphase after the cold treatment (Figure 17D, $p = 0.01$). This centrosome-to-spindle gap was then actually similar to the length of an entire spindle half after cold treatment (Figure 17C, d_2). I annotated this more clearly by annotating the ratio between the centrosome distance and the spindle half-length, which increased from ~49 % in unperturbed zygotes to 87 % after cold treatment (Figure 17C, d_1/d_2; Figure 17E, $p = 0.006$). I also noticed a small increase in the distance between the metaphase plate and the centrosomes in the treated compared to the unperturbed bicentrosomal spindles (Figure 17C, d_3; Figure 17F, $p = 0.15$), indicating that the centrosomes might have moved away from the spindle upon cold treatment. However, this distance increase was not statistically significant.

Overall, this data clearly demonstrated that the sparse microtubules between the centrosomes and the spindle body as well as the microtubules between the dual spindles are unstable.

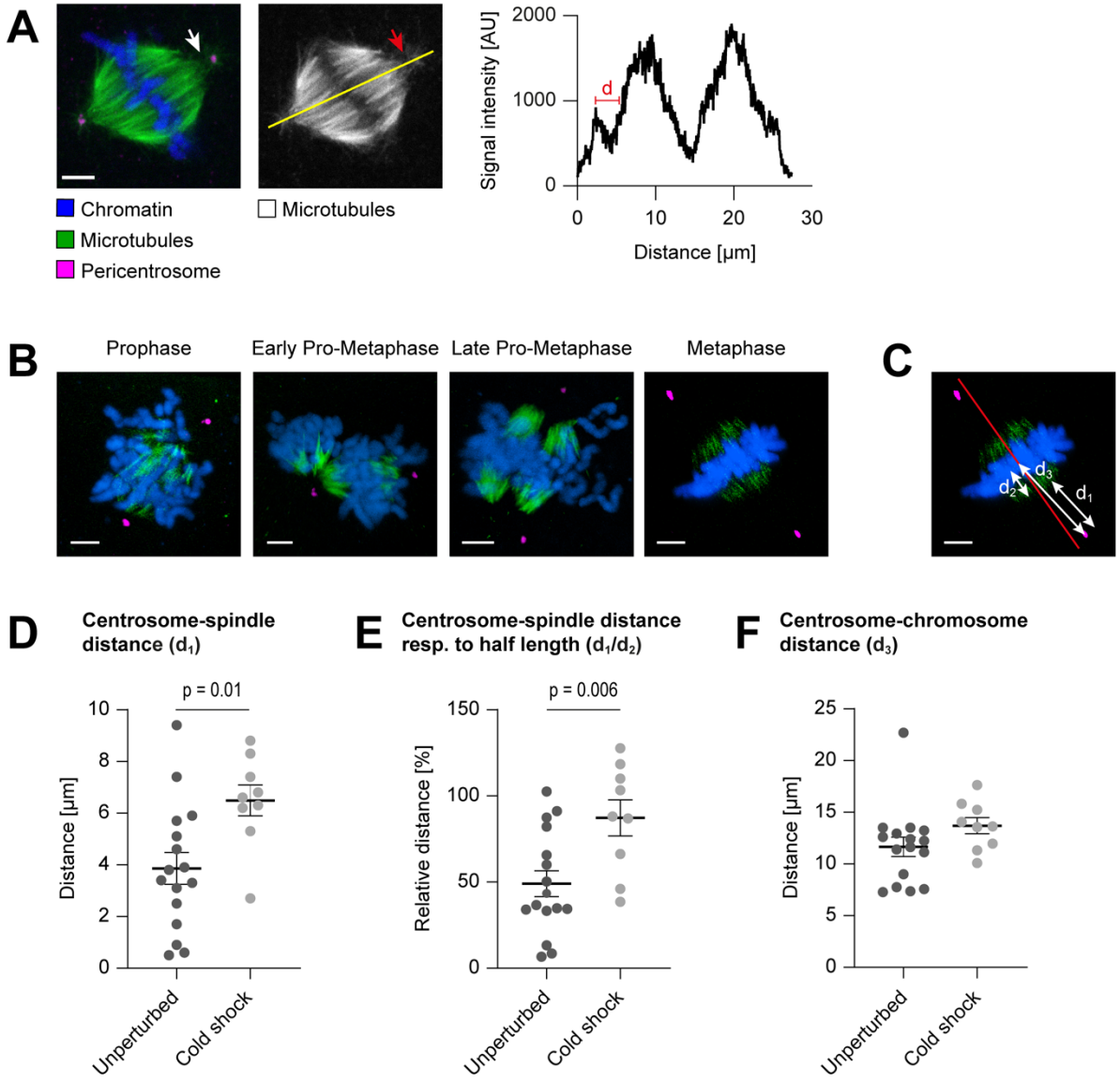

Figure 17: Centrosomes are weakly connected to spindle poles in bovine zygotes. (A) Images from IF of bovine zygotes fixed at 27.5 h post *in vitro* fertilization at consecutive stages of mitosis. Single confocal section through one bicentrosomal (contralateral) zygotic spindle is shown. Scale bar, 5 µm. Left panel: Merged image with microtubules (α-tubulin, green); chromatin (Hoechst, blue), pericentrosome (NEDD1, Cep192, magenta). Middle panel: Single channel image showing microtubules (α-tubulin, grey scale). Right panel: Line profile corresponding to yellow line in central single channel image. White and red arrows indicate signal gap(s) of microtubule staining, corresponding to distance [d] in line profile. (B) Images from IF as described in (A), but the zygotes were incubated on ice for 3 min prior to fixation to depolymerize unstable microtubules. Maximum intensity projections of confocal sections orthogonal to the estimated spindle axis show that astral and 'inter-spindle' microtubules depolymerized beyond the detection limit upon cold treatment. Scale bars, 5 µm. (C) IF image as in (B, Metaphase) with white bidirectional arrows illustrating distance measurements used to compare centrosome positions in bicentrosomal contralateral spindles from unperturbed and cold-treated zygotes. Red line illustrates projected spindle axis orthogonal to chromosomes. D_1: Distance between centrosome and edge of spindle body; d_2: Spindle half length; d_3: Distance between centrosome and metaphase plate (centroid of chromosomal mass). (D-F) Dot plots comparing centrosome positioning with respect to the spindle using IF data

of unperturbed (n = 16) or cold-treated zygotes (n = 9). Average measurements for both centrosomes from same zygote are depicted. Statistical test: Unpaired t-test. (D) Comparing distance [µm] between centrosomes and edge of the spindle body (d_1, see respective arrow in C). For assessment of spindle body, see Material and Methods. Bars indicate standard error of the mean distance of unperturbed (3.9 µm) vs. cold shock treated (6.5 µm) zygotes (p = 0.01, significant). I Comparing relative distance [%] between centrosome and spindle egde respective to spindle half length (d_1/d_2, see respective arrows in C). Bars indicate standard error of the mean distance in unperturbed (49.1 %) vs. cold shock treated (87.3 %) zygotes (p = 0.006, significant). (F) Comparing distance [µm] between centrosomes and the chromosome centroid (d_3, see arrow in C). Bars indicate standard error of the mean distance in unperturbed (11.7 µm) vs. cold shock treated (13.7 µm) zygotes (p = 0.15). Images of panels B-C and graphs D-F of this figure were originally shown in our preprint (*376*). The data was originally acquired in collaboration with Dr. Marta de Ruijter-Villani, and the data analysis was performed by Dr. Julius Hossain and by myself. Graph plots and figure assembly was done by myself.

2.2.1.4 Comparing centrosomal and acentrosomal spindle halves to investigate the role of the centrosome

The weakly connected centrosomes in bovine zygotic spindles prompted me to investigate further to what extent they influence shape and structure of the microtubule array at this early stage of development. The frequently observed distant and monocentrosomal spindles in metaphase allowed me to analyze how centrosomal and acentrosomal spindle halves actually differ within the same spindle. To distinguish clear structural asymmetries between these spindle halves in monocentrosomal spindles (Figure 18A, monocentrosomal, n = 11) from general variability, I also aimed to compare the two centrosomal halves in the proximate bicentrosomal spindles (Figure 18A, bicentrosomal, n = 16). Although the distant spindles were smaller than proximate spindles, because they contained only one parental genome, I could still compare the relative differences of the two halves between both spindle types. In collaboration with my colleague Dr. Julius Hossain, the tubulin signal in both spindle types was segmented and the signal intensity distribution along the spindle axis orthogonal to the metaphase chromosomes was quantified (Figure 18B-D).

First, I wanted to compare the microtubule mass of both spindle halves. To this end, the total intensity of tubulin was calculated as the area under the curve (AUC) of the intensity distribution of each half and subsequently plotted ratiometrically (Figure 18B, E). In the case of monocentrosomal spindles, the centrosomal half had on average an approximately 1.2-fold higher microtubule mass than the acentrosomal one (Figure 18E). However, also in bicentrosomal spindles a similar asymmetry could be observed. Here, the brighter half also has a 1.2-fold higher total microtubule intensity than the dimmer one. No significant difference between the two spindle types could be observed (p-value = 0.99). Thus, it seems

that the polar centrosome does not substantially increase the microtubule mass in its proximal spindle half.

An alternative potential influence of the centrosome might be a broadening of the spatial distribution of the tubulin mass along the spindle axis, away from the metaphase plate towards the pole. To interrogate this, the full width half maximum (FWHM) of the intensity distribution of each spindle half was calculated and compared ratiometrically (Figure 18B, F). In monocentrosomal spindles, a slightly wider distribution was observed for the centrosomal half (ratio of 1.1 compared to the acentrosomal half). However, also for bicentrosomal spindle halves, again a similar distribution was observed, with the brighter half being on average 1.1-fold broader. Thus, also for this parameter no significant difference between the mono- and bicentrosomal spindles could be detected (p-value = 0.12), indicating that polar centrosomes neither broaden the microtubule distribution away from the metaphase plate.

Another relevant parameter of mitotic spindles is their length and I wanted to probe whether centrosomes might elongate their associated spindle half. Therefore, the length of each half in mono- and bicentrosomal spindles was calculated (Figure 18B, G). In monocentrosomal spindles, the centrosomal half was about 1.2-fold longer than the acentrosomal half, in bicentrosomal spindles, one half was ~1.1-fold longer than the other. Again, between both spindle types no significant difference in the spindle length could be observed (p-value = 0.07)

Overall, the quantitative analysis of the different structural spindle parameters of mono- or bicentrosomal spindles in zygotes illustrates that a centrosome at one pole has no significant impact on total microtubule mass, microtubule distribution or spindle length. It is thus likely that centrosomes do not significantly contribute to the structure and function of the metaphase spindle in bovine zygotes.

This strikingly contrasts mammalian somatic cells; for example, in centrinone-treated RPE1 cells (note that these are human cells), centriolar halves were shown to be 1.5- to 1.7-fold longer than acentrosomal halves (*378*). The unexpected symmetry of acentrosomal and centrosomal spindle halves in bovine zygotes strongly suggests that the centrosome-independent microtubule nucleation pathways—like chromosome-dependent microtubule nucleation or intra-spindle microtubule nucleation—are the major drivers of spindle assembly and maintenance. It should be noted that centrosomes may still have other functions in the zygote such as pronuclear migration and chromosome clustering at the pronuclear interface (*379*).

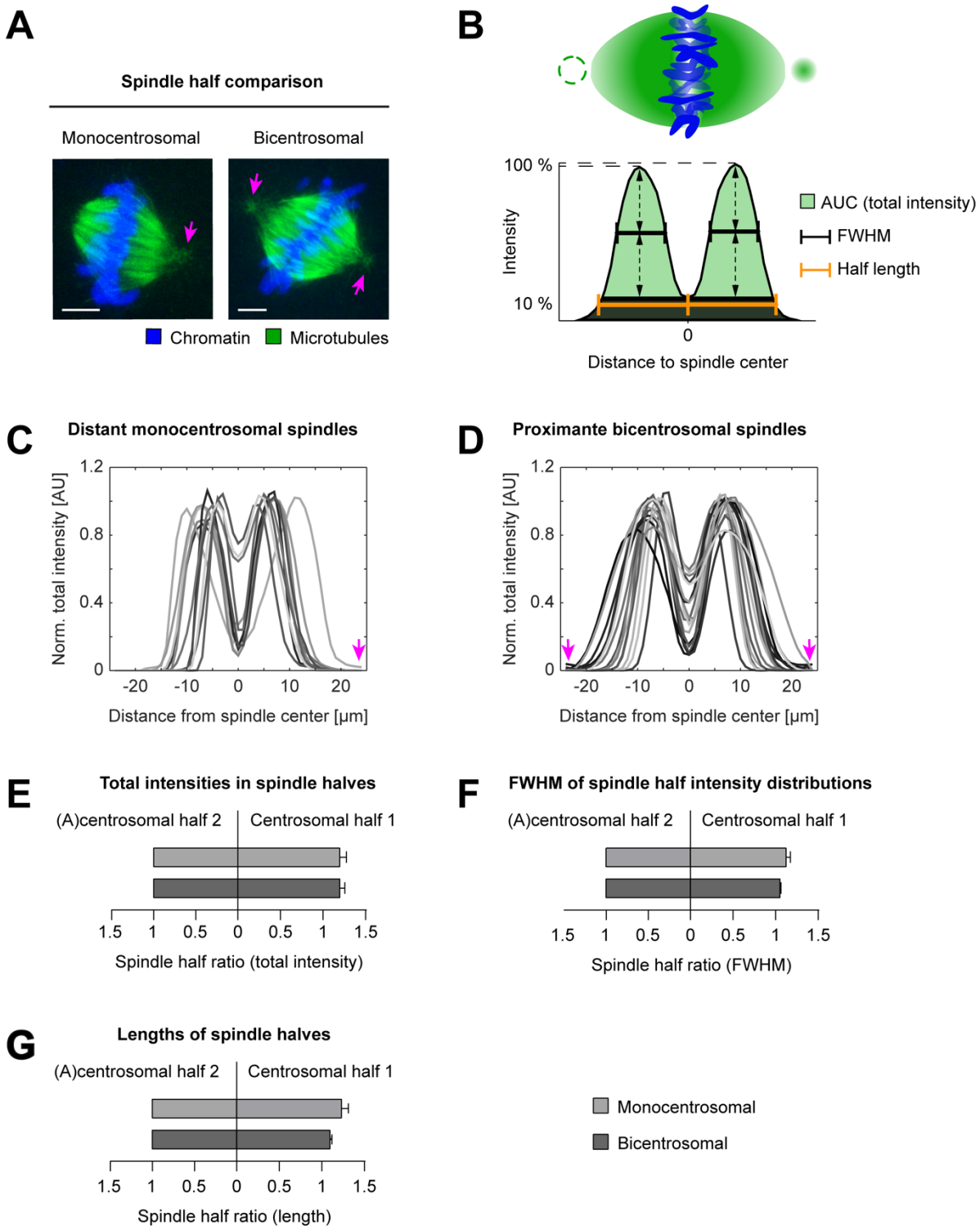

Figure 18: Quantitative comparison of centrosomal and acentrosomal spindle halves. (A) Examples of IF data subjected for quantitative comparison of the two halves in proximate bi-, and distant monocentrosomal spindles in metaphase, see also Fig 1A-B. Zygotes were fixed at 27.5 h post in vitro fertilization. Maximum intensity projections over the imaging plane orthogonal to the estimated spindle axis are shown. Merged images with microtubules (α-tubulin, green) and chromatin (Hoechst, blue). Scale bars: 5 µm. (B) Schematic representation of zygotic metaphase spindle and total intensity distribution along determined spindle axis orthogonal to the chromosomal metaphase plate in bicentrosomal contralateral and monocentrosomal spindles. Note dashed green circle to illustrate second centrosome in bicentrosomal spindles and missing centrosome in monocentrosomal spindles. Full width half maxium (FWHM) and area under the curve (AUC) were calculated to compare intensity distribution and sum of total intensities between the two spindle halves. The spindle half-

lengths were calculated as distances between the intensity distribution's valley (0 position) and the most distant positions along the axis, where the total intensity was 10 % of the respective maximum. (C-D) Intensity distributions of alpha-tubulin immunofluorescence in 2D sections along the calculated spindle axis orthogonal to the metaphase chromosomes in both, distant monocentrosomal (C), and proximate bicentrosomal contralateral (D) spindles, as illustrated in (B). Magenta arrows indicate positions of centrosomes. (E-G) Ratiometric comparison of intensity sum I, FWHM (F), and of the length (G) between the halves of the spindle types. For distant monocentrosomal spindles (n = 11 from 6 embryos), absolute measurements were normalized to acentrosomal half. For proximate bicentrosomal contralateral spindles (n = 16), absolute measurements were normalized to the spindle half with lower sum intensity, or shorter FWHM and length. Error bars indicate standard error of the mean. Statistical test: unpaired t-test. I Equal mean intensity ratio for the halves of mono- (1.21) and bicentrosomal (1.21) spindles (p = 0.99). (F) Comparable mean ratio of FWHM for the halves of mono- (1.14), and bicentrosomal (1.06) spindles (p = 0.12). (G) Overall similar mean ratio of spindle half lengths in mono- (1.24) and bicentrosomal (1.11) spindles (p = 0.07). All panels of this figure were originally shown in our preprint (*376*). The data was originally acquired in collaboration with Dr. Marta de Ruijter-Villani, and the data analysis was performed by Dr. Julius Hossain and by myself. Graph plots and figure assembly was done by myself.

2.2.2 Real time imaging of dual spindle assembly in the bovine zygote

Using IF, 1421 zygotes were imaged, however of these only 178 (13 %) were in mitosis at the time of fixation. In addition, the high variability of pronuclear position further complicated the interpretation of the observed configurations in terms of the dynamic process of spindle assembly. To clearly understand the sequence of events of dual spindle assembly in the presence of paternal centrosomes, live microscopy was therefore indispensable. Hence, I decided to visualize spindle assembly in real time in live bovine zygotes using light sheet microscopy, which was developed in the Ellenberg Group for *in toto* imaging of mouse pre-implantation embryos (*286*, *308*). I adapted the iSPIM imaging pipeline for the larger and substantially stronger scattering bovine embryos (see Material and Methods section 4.2.5).

2.2.2.1 Diverse modes of dual spindle assembly

To visualize spindle assembly in live bovine zygotes, I injected the pronuclear stage zygotes with mRNA to transiently express fluorescent spindle reporter proteins (*366*). I chose human Histone 2B (H2B) and microtubule-associated protein 4 (MAP4) or end-binding protein 3 (EB3) as reporter proteins for chromatin and spindle microtubules, respectively, since these proteins are highly conserved among mammals.

Similar as for mouse embryos, I could maintain the standard IVF culture conditions for bovine embryos using the inverted light sheet microscope setup. In addition, the low light-dose allowed me to visualize the spindle dynamics in 3D every 2.5 minutes throughout the first mitosis.

This unprecedented real time data of bovine zygotic mitosis clearly showed that pronuclei did not fuse, and that the presence of two spatially separated parental genomes at the beginning of mitosis determined the formation of two microtubule arrays around them despite the presence of only two centrosomes. Imaging in total 21 mitoses in live zygotes with two centrosomes, I noticed that spindle assembly dynamics and modes varied in many aspects, especially in how the two initial spindles incorporated the two centrosomes. This allowed me to reconstruct the pathways leading to the diverse centrosome localization phenotypes observed in fixed zygotes.

Overall, in 19 of the 21 zygotes, NEBD was asynchronous, which confirmed the mitotic asynchrony observed in fixed zygotes with proximate or distant dual spindle. In the live zygotes, the second NEBD (lagging PN or PN2) usually followed the initial NEBD (leading PN or PN1) after ~2.5-7.5 min.

In all but one of the imaged zygotes, the pronuclei had migrated to appose each other prior to NEBD (n = 20/21) and both centrosomes usually localized to the pronuclear surfaces (n = 17/21, for examples, see Figure 19A-B and Figure 20A-C). The respective centrosome position relative to the pronuclei then seemed to determine how the two forming spindles incorporated them.

In approximately 60 % of the zygotes, both centrosomes localized at the opposite edges of the pronuclear contact area in prophase (Figure 20A, -2.5 min to NEBD). After NEBD, the centrosomes usually first associated with each spindle pole of the spindle, which initially formed around the parental genome whose nuclear envelope had broken down first (leading pronucleus – PN1, Figure 19A, 7.5 min post NEBD). With nuclear envelope breakdown of the second, lagging pronucleus (PN2, Figure 19A, 15 min post NEBD), microtubules started to grow around and towards the second genome assembling a second, initially often half-spindle between one of the centrosomes and the second genome. A few zygotes with this spindle assembly mode were ideally oriented respective to the light sheet with minimal cytoplasmic scattering. This allowed me to acquire highly resolved images, which showed that the second spindle around the lagging pronucleus eventually pulled the associated centrosome away from the first spindle (Figure 19A, 15 and 20 min post NEBD). Soon afterwards, the two spindles bipolarized while aligning their axes in parallel. In contrast, I also observed that both spindles could initially be monopolar (n = 3/21), eventually merging into a bipolar array.

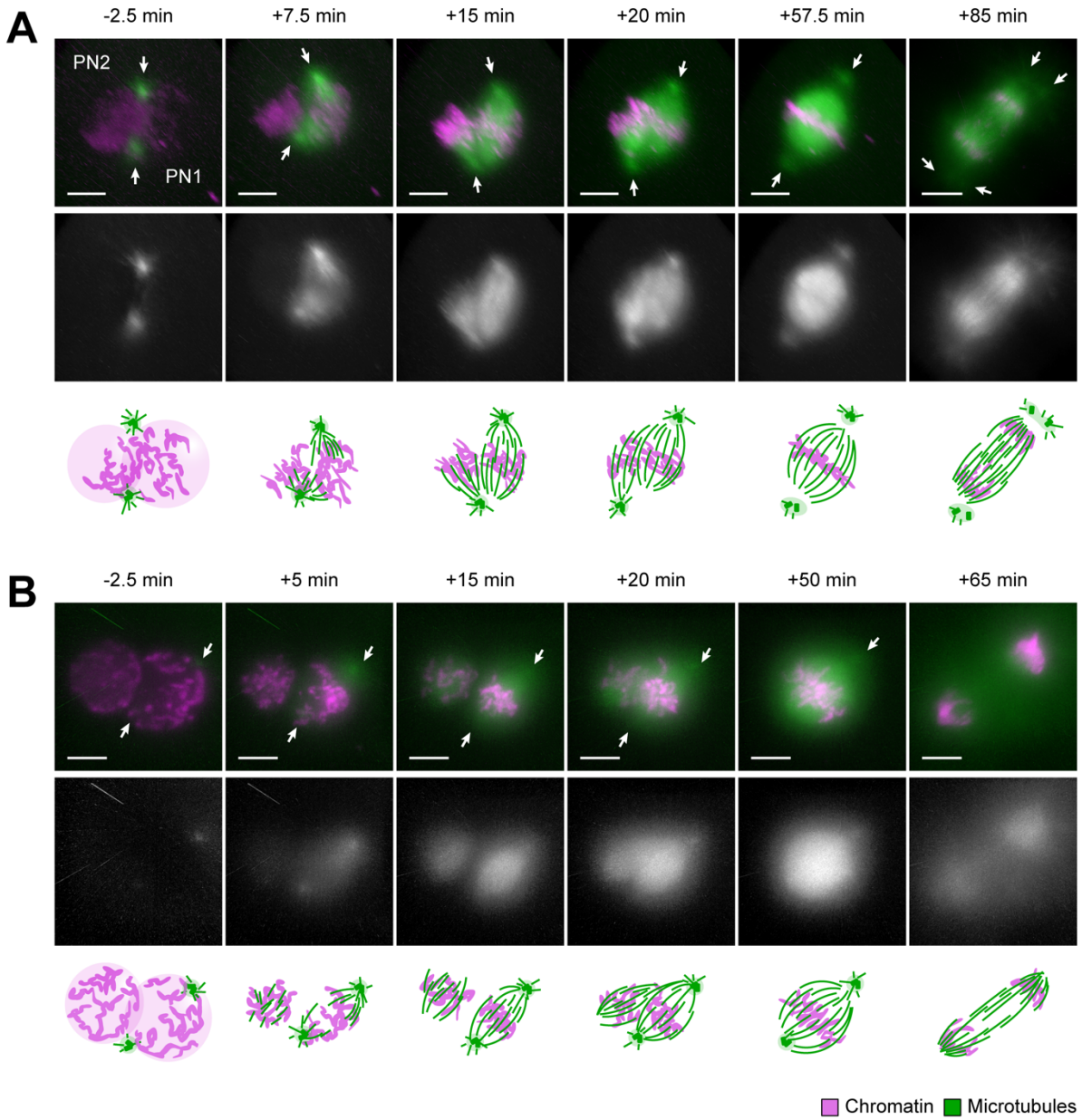

Figure 19: Assembly and dynamics of proximate dual spindles in live bovine zygotes. (A and B) Upper panels show merged time lapse images of bovine zygotes expressing microtubule markers (green) EGFP-MAP4 (A) or EB3-mEGFP2 (B) and chromatin marker H2B-mCherry (magenta). Images were acquired by light sheet microscopy every 2.5 min throughout mitosis and for up to 6 h in total. 3D rendered images of pronuclear volumes are shown. Timings are respective to synchronous pronuclear envelope breakdown (B) or to NEBD of leading pronucleus (PN1) in case of asynchrony (A). PN2: Lagging pronucleus. White arrows indicate positions of centrosomes. Projected scale bars, 10 µm. Lower panels show respective single channel grey scale images of the microtubule marker. Figure shows most frequent (A), and most pronounced (B) example of proximate dual spindle assembly. Subjacent illustrations accentuate the different assembly dynamics observed upon imaging. Panels of this figure were originally shown in our preprint (*376*). The samples were prepared in collaboration with Dr. Marta de Ruijter-Villani and the data acquired and processed by myself. The figure was assembled by myself.

But overall, the eventually fused spindles had the same round shape with very broad poles as most metaphase spindles in the fixed zygotes (Figure 19A, 57.5 min compared to Figure 15A, metaphase). And also confirming the findings from the IF experiments, the centrosomes were usually not closely attached to the spindle body in live zygotes at the metaphase stage (Figure 19A, 20 and 57.5 min post NEBD; white arrows indicate centrosome positions). Interestingly, I also observed that the centrosomes already split and separate comparatively early, starting in late metaphase or early anaphase (Figure 19A, 85 min post NEBD; white arrows indicate split centrosomes).

In one of these 21 zygotes with proximate pronuclei and pronuclear associated centrosomes, I could observe the initially separated spindles around the two genomes clearly until ~20 min post NEBD (Figure 19B). Both centrosomes were initially associated with opposite sides of the same pronucleus in this zygote (Figure 19B, -2.5 min to NEBD), but interestingly, NEBD occurred simultaneously. The two centrosomes then associated with the spindle poles of the spindle, which formed around the pronucleus the centrosomes were originally associated with (Figure 19B, 15 min post NEBD). However, approximately 5 min post NEBD, the second genome already started to promote microtubule nucleation independently of centrosomes assembling a small spherical microtubule array. It increased its microtubule mass within few minutes and bipolarized before it merged pole by pole with the initial centrosomal spindle around the other parental genome (Figure 19B, 15-50 min post NEBD).

Dual spindle assembly was also evident for the remaining (n = 4/21) zygotes with proximate and centrosome-associated pronuclei. However, since the centrosome positions with respect to each other and to the pronuclei differed for these embryos in prophase—instead of immediately assembling an initial dominant bipolar array with polar centrosomes around one parental genome—the configurations for spindle assembly and alignment varied (Figure 20A-C). I observed that initially either two monopolar spindles formed with the same or different polar centrosomes (Figure 20A, C), or two spherical arrays assembled around the two genomes initially rather independent of the centrosomes (Figure 20B). Thus, centrosome positions in these early spindles ranged from ipsilateral (Figure 20A, >10 min post NEBD) to entirely apolar (Figure 20B, 10-22.5 min post NEBD). At later timepoints, centrosomes could be pulled into the spindle at seemingly random positions (e.g., Figure 20B and 6C, 27.5 min and 20 post NEBD, respectively). Proper bipolar positioning could eventually be established after the centrosomes were initially pulled into the spindle close to the poles. However, even

severe aberrant centrosome positioning, like ipsilateral at the same pole (Figure 20A, 37.5 min post NEBD) or at the spindle midzone (Figure 20B, 55 min post NEBD) persisted throughout mitosis. Overall, in the embryos showing dual spindle assembly around adjacent pronuclei with closely associated centrosomes, the first mitosis usually resulted in a symmetrical two cell embryo (>85 %).

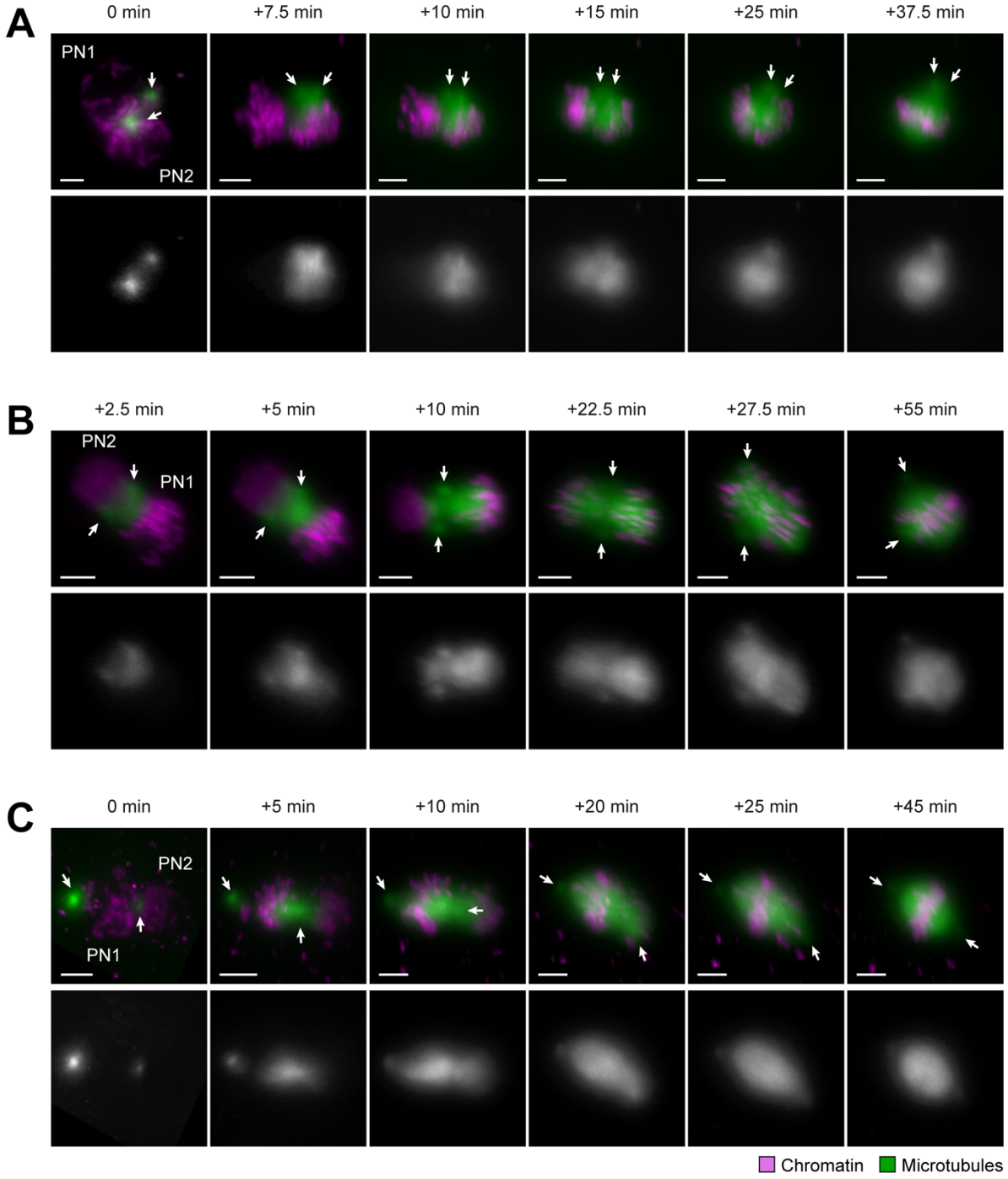

Figure 20: Miscellaneous spindle assembly modes around proximate parental genomes with associated centrosomes in live bovine zygotes. (A-C) Upper panels show merged 3D rendered time lapse images of bovine zygotes expressing microtubule marker EGFP-MAP4 (green) and chromatin marker H2B-mCherry (magenta). Pronuclear volumes after background correction (median based denoising) are shown. 3D images were acquired

by light sheet microscopy every 2.5 min throughout mitosis and for up to 6 h in total. Indicated timings respective to nuclear envelope breakdown of leading pronucleus (PN1). PN2: Lagging pronucleus. White arrows indicate positions of centrosomes. Projected scale bars, 10 µm. Lower panels show respective single channel grey scale images of the microtubule marker alone. Figure shows spindle assembly modes around adjacent pronuclei, where centrosomes localized at pronuclear surfaces, but not (only) at the pronuclear junctions (n = 4). Centrosomes localized either in proximity to each other (A and B), or at opposite sides of same PN, with only one centrosome at pronuclear interphase (C). Panels of this figure were originally shown in our preprint (*376*). The samples were prepared in collaboration with Dr. Marta de Ruijter-Villani and the data acquired and processed by myself. The figure was assembled by myself.

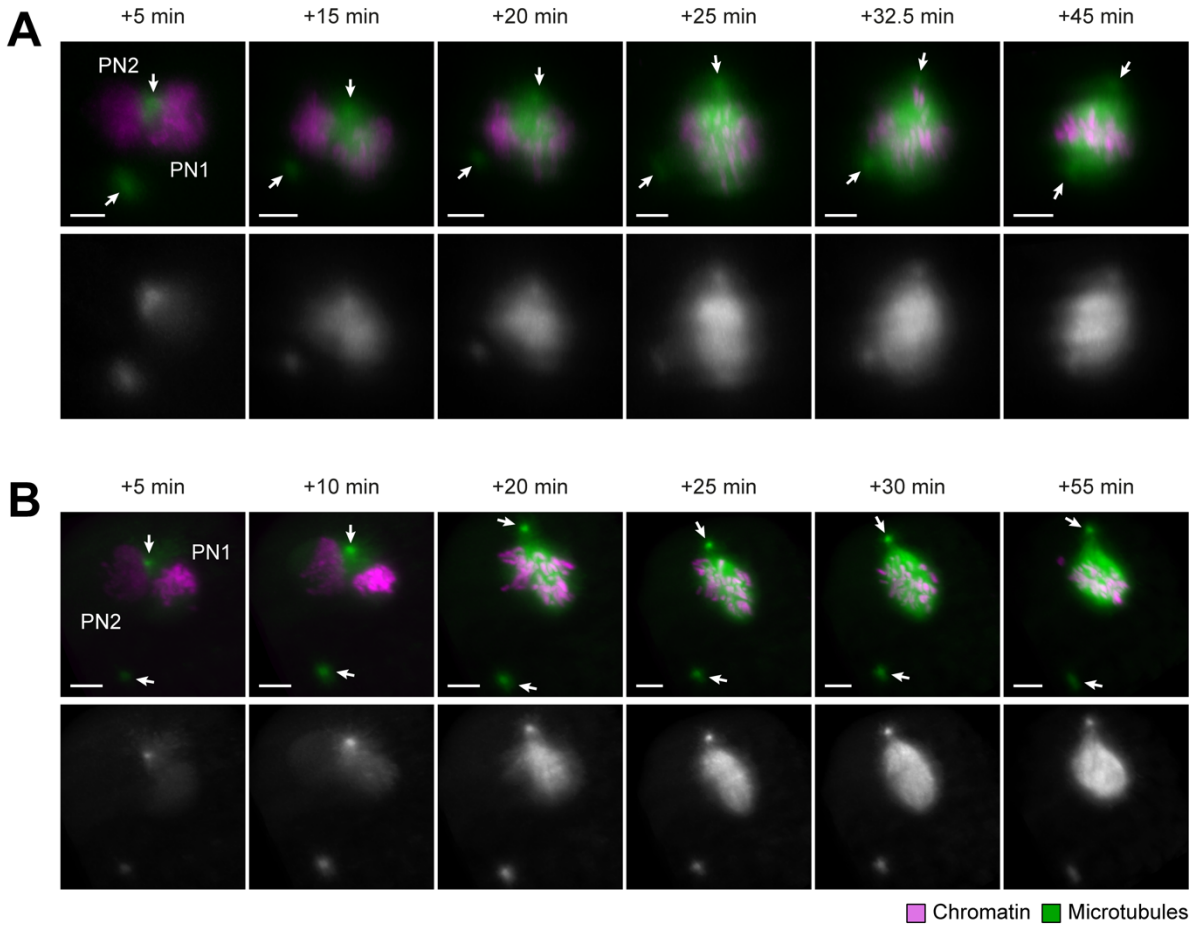

Figure 21: Spindle assembly around adjacent pronuclei with a dissociated centrosome in live bovine zygotes. (A and B) Upper panels show merged 3D rendered time lapse images of bovine zygotes expressing microtubule markers (green) EGFP-MAP4 (A) or EB3-mEGFP2 (B) and chromatin marker H2B-mCherry (magenta). Pronuclear volumes after background correction (median based denoising) are shown. 3D images were acquired by light sheet microscopy every 2.5 min throughout mitosis and for up to 6 h in total. Indicated timings respective to nuclear envelope breakdown of first pronucleus (PN1). PN2: Lagging pronucleus. White arrows indicate positions of centrosomes. Projected scale bars, 10 µm. Lower panels show respective single channel grey scale images of the microtubule marker alone. Figure shows spindle assembly modes around adjacent pronuclei, where one centrosome localized at PN surfaces, while the second was initially randomly positioned in the cytoplasm (n = 3). Polar centrosome position could be established later in mitosis (A), but the centrosome could also be lost within the cytoplasm (B). Panels of this figure were originally shown in our preprint (*376*). The samples were prepared in collaboration with Dr. Marta de Ruijter-Villani and the data acquired and processed by myself. The figure was assembled by myself.

I also imaged zygotes, in which one centrosome seemed detached from the pronuclei and was instead randomly positioned in the cytoplasm (Figure 21A-B, n = 3/21). In these cases, the dissociated centrosome was clearly not contributing any microtubules to the initially forming spindles, but when positioned close enough to the originally acentrosomal spindle pole, it was eventually pulled towards that spindle half and even properly localized at the second pole (Figure 21A, >25 min post NEBD). However, in zygotes, where the centrosome localized too far from the assembled spindle, it remained isolated in the cytoplasm (Figure 21B). Overall, the dynamic live data shows the flexibility of dual spindle assembly and centrosome positioning in the bovine zygote indicating lax regulation. The data also suggests that the centrosome might be dispensable for the zygotic spindle assembly. Consistent with the observation of distant dual spindles in the zygotes after IF, I imaged one zygote (n = 1/21), which entered mitosis when its two pronuclei were approximately 60 µm apart (Figure 22A). The forming distant spindles persisted throughout mitosis, eventually attempting to segregate the single parental genomes. In this case, I observed several mitotic errors including chromosome mis-segregation, ingression of multiple cleavage furrows and cytokinesis failure (Figure 22B, red arrows). In agreement with the IF data, each pronucleus within this zygote was initially associated with one centrosome (Figure 22C-D, -2.5 min prior to initial NEBD, white arrows indicate centrosome positions), which marked one pole within each of the forming spindles around the distant genomes (Figure 22C-D, 17.5 min post initial NEBD). These spindles were first monopolar, but eventually bipolarized without a second polar centrosome.

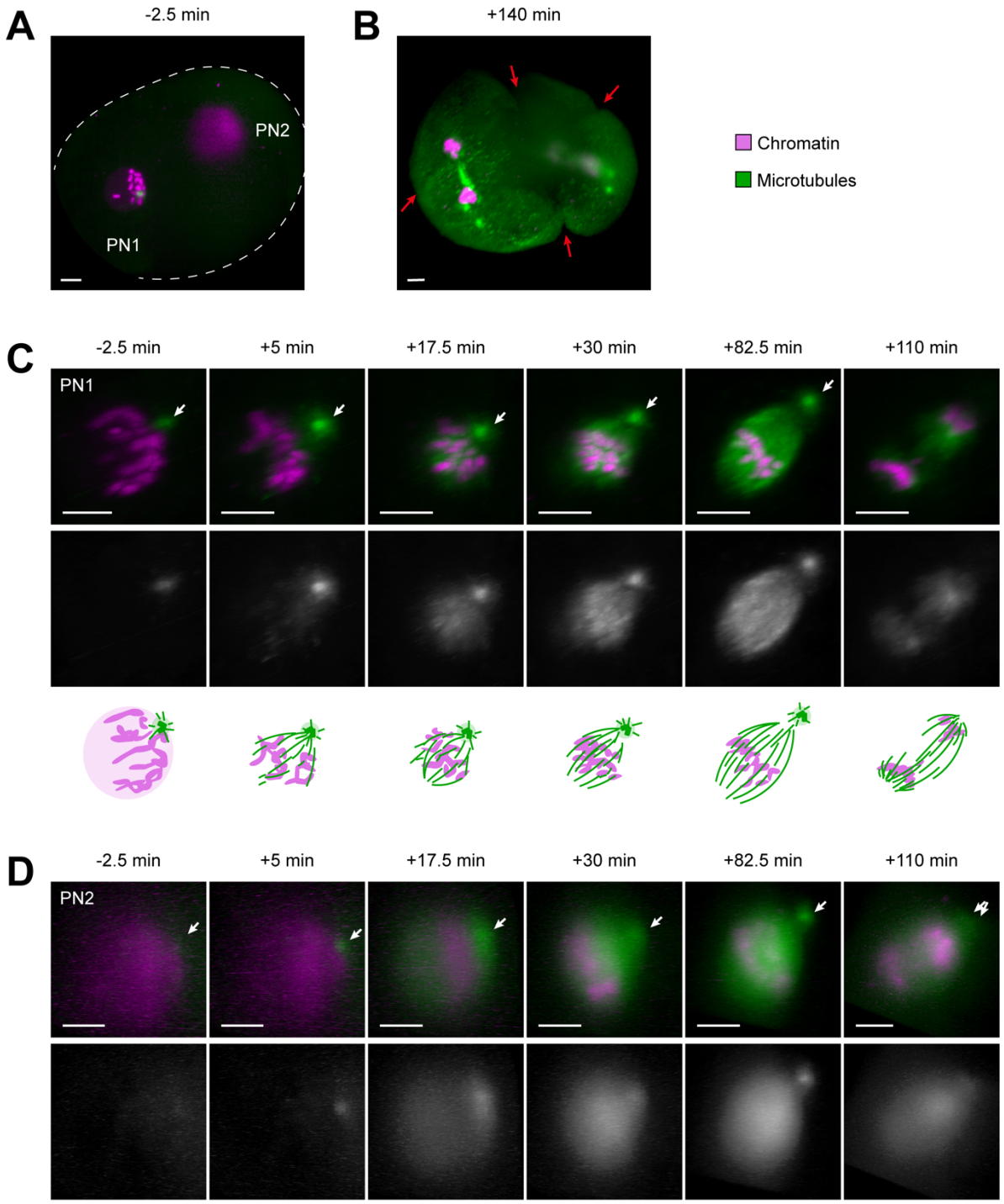

Figure 22: Assembly and dynamics of distant dual spindles in live bovine zygotes. (A, B; and C and D, upper panels) Merged time lapse images of same bovine zygote expressing microtubule marker EB3-mEGFP2 (green) and chromatin marker H2B-mCherry (magenta). Images were acquired by light sheet microscopy every 2.5 min throughout mitosis and for up to 6 h in total. Timings are respective to synchronous pronuclear envelope breakdown of leading pronucleus (PN1). PN2: Lagging pronucleus. Projected scale bars, 10 µm. (A) Overview image to illustrate pronuclear distance. Background corrected (median based denoising) overlay of maximum intensity projections over z of both pronuclear volumes within the zygote. Zygotic rim indicated by dashed lines. Minimal part of the zygote outside the field of view (130 µm x 130 µm). (B) 3D rendered image of entire zygotic volume within field of view after background correction (median based denoising). Red arrows indicate multiple ingression furrows at 140 min post NEBD as consequence of distant dual spindles. (C and D) 3D rendered images of pronuclear volumes, of PN1 (C) and PN2 (D), respectively. White arrows in upper panels indicate positions of centrosomes. Lower panels show respective single channel grey scale images of the microtubule marker alone.

Subjacent illustrations in (B) accentuate the assembly dynamics of distant monocentrosomal spindles. Panels of this figure were originally shown in our preprint (*376*). The samples were prepared in collaboration with Dr. Marta de Ruijter-Villani and the data acquired and processed by myself. The figure was assembled by myself.

Overall, real time imaging of zygotes confirmed the observations from fixed mitotic zygotes. In addition, the data provided a temporal sequence, allowing to order the individual snapshots of mitotic intermediates obtained from the IF experiments in time. This further helped to interpret causes and consequences of the different configurations observed in fixed embryos, which were too poorly synchronized to establish a clear time-course. The live data for example allowed me to understand how the different metaphase spindle types with very diverse centrosome positions (compare Figure 16A) could emerge.

In addition, the live data also confirmed that two—sometimes completely independent—microtubule arrays formed around the two parental genomes despite the presence of only two clear astral microtubule organizing centers, the centrosomes. Moreover, the data showed that polar centrosomes are not essential for initial spindle assembly and bipolarization in bovine zygotes, as centrosomes could initially only be associated with one of the two spindles or a centrosome could be completely dissociated. The data also showed that such a dissociated centrosome was completely lost into the cytoplasm if the distance to the pronuclei or the spindle exceeded ~5 µm. Further confirming our observations from the IF data, the centrosome-to-spindle connection was flexible and not limited to the pole as centrosomes could also be pulled into the spindle midzone. One clear indicator of the weak connection between centrosomes and the spindle was that the centrosome could be pulled from one pole of the first assembling spindle to the adjacent pole of the spindle that formed later in time.

2.2.2.2 Insights into spindle assembly pathways – most spindle microtubules originate in the vicinity of chromosomes

Exploring the live imaging data of the 21 embryos, I noticed a pattern in the microtubule distribution over time: In all live imaged zygotes (n = 21/21), the centrosomes nucleated microtubules shortly before and/or at NEBD. But from the time of NEBD onwards, microtubules grew primarily towards the two genomes. And within approximately 10 min post NEBD, microtubules were nucleated around the chromosomes; this was particularly

clear in the zygote with one pronucleus without any initially associated centrosome (Figure 19B, left PN). Interestingly, the strong microtubule signal around centrosomes before and at NEBD started to decrease few minutes after NEBD, when it strongly increased at the spindle center (Figure 23A).

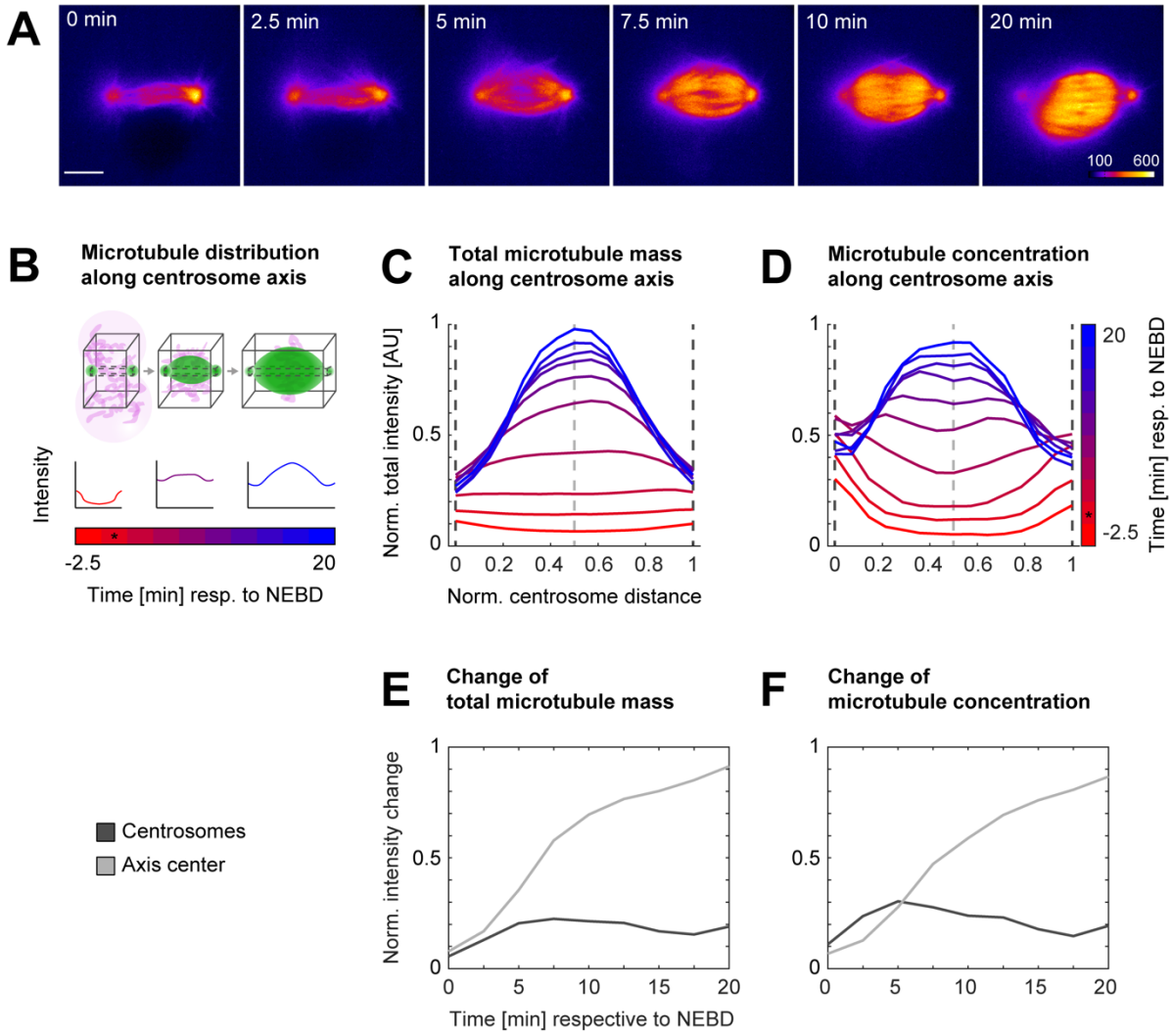

Figure 23: Analysis of dynamic distribution of spindle microtubules in live bovine zygotes. Microtubule signal (EGFP-MAP4 or EB3-mEGFP2) from live imaging of bovine zygotes by light sheet microscopy every 2.5 min with a spindle assembly type as described in Figure 19A was analyzed for 10 time points starting 2.5 min prior to NEBD of the leading pronucleus (PN1) or both PNs. (A) Pseudocolor representation of EGFP-MAP4 signal within single planes through the centers of intensities at centrosomes. Corresponding lookup table is depicted in last frame of the time series. 6 of 10 analyzed time frames were selected to visualize critical time points for microtubule redistribution in early spindle assembly. Indicated time respective to NEBD. Scale bar, 10 µm. (B-D) Measuring intensity distribution of microtubule signal along the centrosomal axis over time. (B) Scheme illustrating the measurements: After background subtraction, total microtubule intensities were calculated for 15 equidistantly distributed 2D slices within the black cuboids along the centrosomal axis for the different time points. Black cuboid with solid line encompasses 351x351 pixel sized slices to measure entire microtubule intensity or mass along the spindle axis. Small black cuboid with dashed line encompasses 15x15 pixel sized slices to indicate relative microtubule concentrations. Maximum normalized total intensities along the normalized centrosome distance were annotated. (C-D) Average distribution of maximum normalized microtubule intensities along centrosomal axis indicating (C) relative microtubule mass within spindles over time (black

cuboid with solid line, as described in B), and (D) relative microtubule concentrations (black cuboid with dashed line, as described in B); n = 6 zygotes. Dashed lines mark the position of the 2D slice through the centrosomes (dashed lines in dark grey) and the centrosome axis mid-point (dashed line in light grey). Color gradient from red to blue indicates time [min] respective to NEBD. Time of NEBD indicated by asterix. (E-F) Average change of normalized total microtubule intensity over time from NEBD until 20 min post NEBD, at centrosomes and the centrosome axis center, indicated by dark and light dashed lines in C and D, respectively. For intensity change at centrosome, mean intensity of both centrosomes was calculated. Figure and legend were originally shown in our preprint (*376*). The samples were originally prepared in collaboration with Dr. Marta de Ruijter-Villani and the data was originally acquired and processed by myself. Data analysis was performed by Dr. Julius Hossain and by myself and the figure assembled by myself.

I aimed to analyze the microtubule signal distribution quantitatively and over time to get an initial idea, where microtubules originated from, and thus understand, which pathways could be more or less relevant in zygotes with centrosomes. To this end, changes in spatial distribution of total microtubule intensity over time along the centrosome-centrosome axis were analyzed during early mitosis from 2.5 min prior to NEBD until 20 min post NEBD (Schematic, see Figure 23B; Figure 23C-D for averaged data (n = 6); Figure 24A and Figure 25A for individual zygotes). The idea was to determine the total spindle microtubule mass along the axis at each timepoint (Figure 23B, large cuboid with solid line) to understand the overall growth dynamics. At the same time, choosing a very small cuboid volume along the centrosomal axis, I also aimed to compare the microtubule concentration at different sites of the axis (Figure 23B, small cuboid with dashed line). With the latter approach I intended to draw first conclusions about microtubule nucleation at different sites along the spindle axis regardless of the volume of the potential nucleation sites—like chromosomes/kinetochores, centrosomes, or existing spindle microtubule bundles. The analysis showed that on average, the total microtubule mass at the center of the centrosomal axis increased almost 3-fold within 5 min between ~2.5-7.5 min post NEBD (Figure 23C, axis center marked by light dashed line; NEBD marked by asterix in timeline). The total microtubule signal continued to increase further until 20 min post NEBD to more than 5-fold of its intensity at NEBD. In contrast, the microtubule mass around the centrosomes only increased 2-fold between NEBD and 5-7.5 min after NEBD (Figure 23C for averaged data, n = 6; centrosome positions marked by dark dashed lines), reaching its peak intensity. Afterwards the microtubule mass at centrosomes stagnated or even declined. And, even upon comparison of the microtubule signal in smaller volumes—in essence, of the microtubule concentration—the overall picture was the same (Figure 23D for averaged data, n = 6; compare signal changes at dark and light dashed lines). To visualize especially the change of microtubule abundance at the two sites of interest—the

centrosomes and the spindle center close to the chromosomes—the change in total mass (Figure 23E for averaged data, n = 6; Figure 24B for individual zygotes) and in concentration (Figure 23F for averaged data, n = 6; Figure 25B for individual zygotes) was plotted over time. In summary, analyzing the dynamics of microtubule abundance along the centrosomal axis, indicated that centrosomes nucleate microtubules shortly before and immediately after NEBD, but that centrosomal nucleation does not account for the striking increase in spindle microtubule mass starting ~5 min post NEBD. More likely, chromosome signaling (Ran-GTP dependent nucleation) and subsequent microtubule nucleation from microtubule within the initial spindle seem to be more relevant for the assembly of the bovine zygotic spindle/s. In combination with the observation that centrosomes localize distant from metaphase spindles, and that the centrosome-to-spindle link is very weak, this indicates that centrosomes contribute comparatively few microtubules to the mitotic spindle in bovine zygotes.

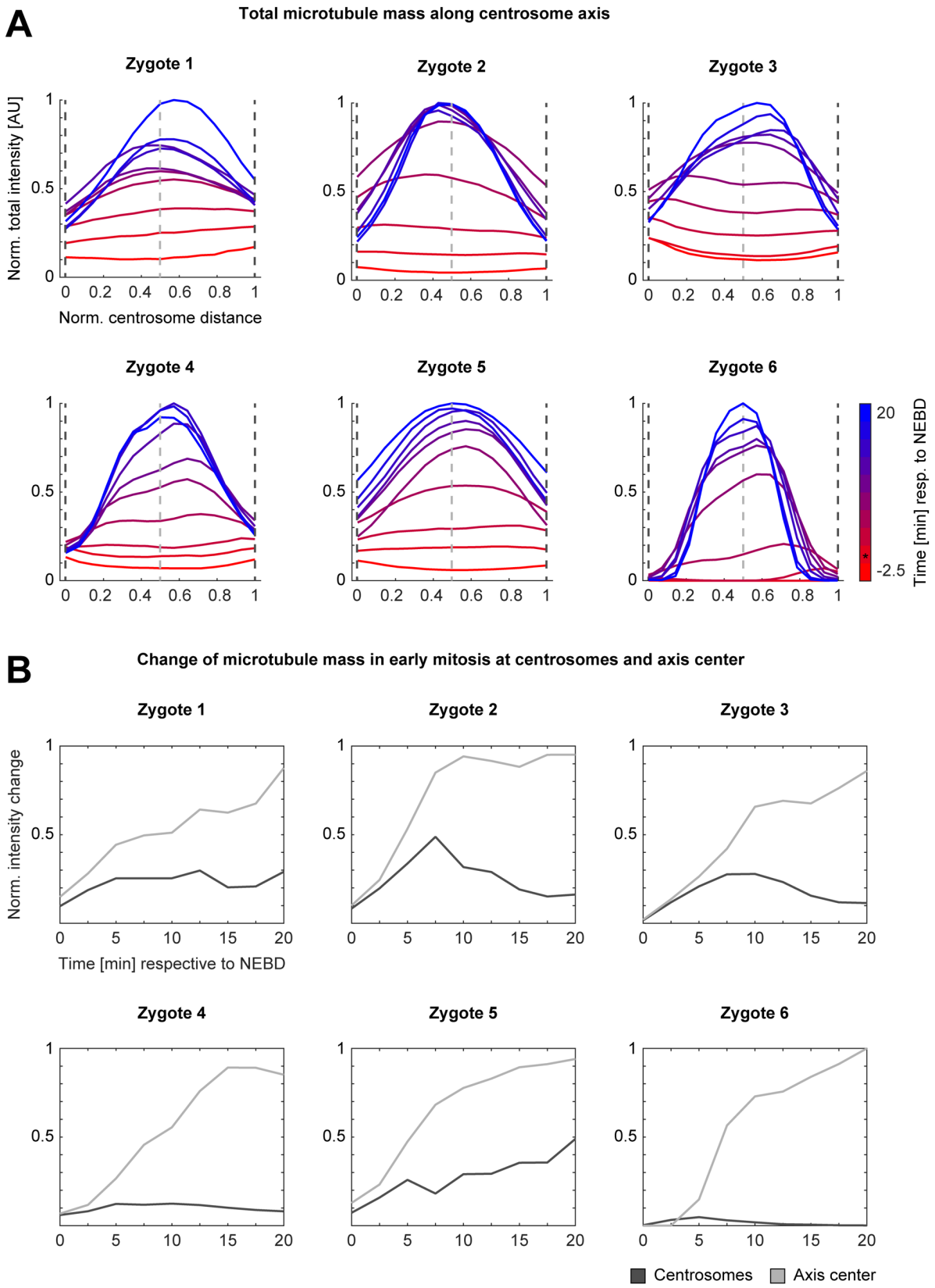

Figure 24: Total microtubule mass along the centrosomal axis within proximate dual spindles troughout early mitosis in live bovine zygotes. Microtubule signal (EGFP-MAP4 or EB3-mEGFP2) from live imaging of six bovine zygotes by light sheet microscopy every 2.5 min with a spindle assembly type as described in Figure 19A was analyzed for 10 time points starting 2.5 min prior to NEBD of the leading pronucleus (PN1) or both synchronous PNs. The microtubule signal in 351x351 pixel sized slices along the centrosomal axis were analyzed to measure

entire microtubule intensity or mass along the spindle axis (see Schematic, Figure 23B). Figure shows plots of individual zygotes underlying the averaged data depicted in Figure 23C and E. (A) Distribution of maximum normalized microtubule intensities along the normalized centrosomal axis over time with respect to initial NEBD. Color gradient from red to blue indicates time [min] respective to NEBD. Time of NEBD indicated by asterix. Dashed lines mark the position of the 2D slice through the centrosomes (dark grey) and the axis center (light grey). (B) Change of normalized total microtubule intensity over time until 20 min post initial NEBD at centrosomes (dark grey) and the centrosome axis center (light grey), indicated by dashed lines in (A) for the different live zygotes in same order as in (A). For the calculation of the intensity change at the centrosome, the intensity means of both centrosomes were used.

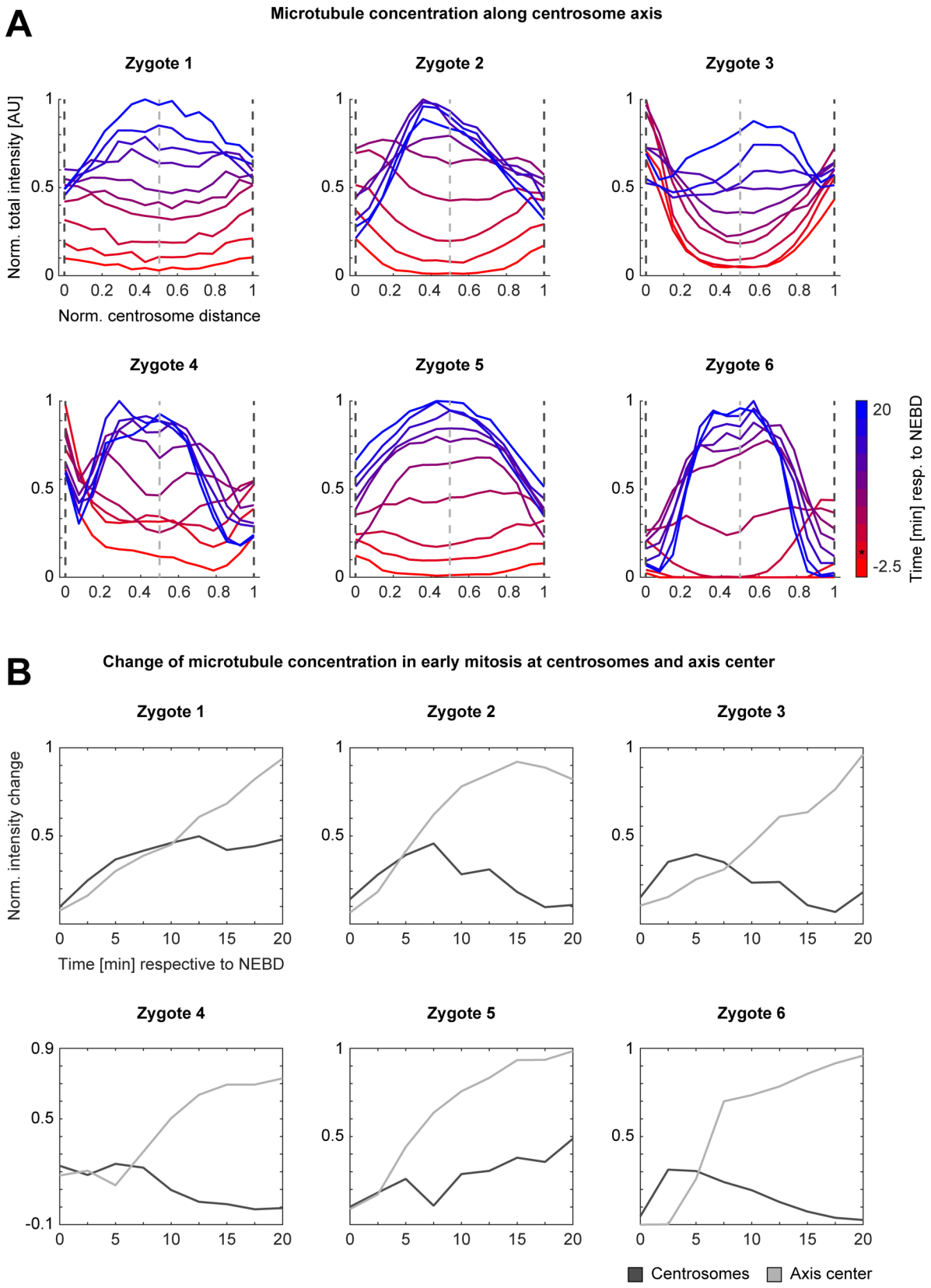

Figure 25: Microtubule concentration along the centrosomal axis within proximate dual spindles troughout early mitosis in live bovine zygotes. Microtubule signal (EGFP-MAP4 or EB3-mEGFP2) from live imaging of six bovine zygotes by light sheet microscopy every 2.5 min with a spindle assembly type as described in Figure 19A was analyzed for 10 time points starting 2.5 min prior to NEBD of the leading pronucleus (PN1) or both synchronous PNs. The microtubule signal in 15x15 pixel sized slices along the centrosomal axis were analyzed to

measure microtubule intensity within a minimum volume along the spindle axis (see Schematic, Figure 23B). Figure shows plots of individual zygotes underlying the averaged data depicted in Figure 23D and F. (A) Distribution of maximum normalized microtubule intensities along the normalized centrosomal axis over time with respect to initial NEBD. Color gradient from red to blue indicates time [min] respective to NEBD. Time of NEBD indicated by asterix. Dashed lines mark the position of the 2D slice through the centrosomes (dark grey) and the axis center (light grey). (B) Change of normalized microtubule intensity over time until 20 min post initial NEBD at centrosomes (dark grey) and the centrosome axis center (light grey), indicated by dashed lines in (A) for the different live zygotes in same order as in (A). For the calculation of the intensity change at the centrosome, the intensity means of both centrosomes were used.

3 DISCUSSION

In this thesis I could show that dual spindle assembly does not only take place in mammalian zygotes devoid of centrosomes but instead with many acentriolar MTOCs, but also in mammalian zygotes, where two centrioles are provided by the sperm upon fertilization, such as cow. Dual spindle assembly is thus most likely conserved across mammals including human, which has important biomedical implications. In addition, I could establish several new perturbation and quantitative imaging assays to investigate the mechanistic details of spindle assembly in the mouse embryo. Using these new approaches, I could provide novel mechanistic insights into how the zygotic dual spindle assembly is potentially initiated.

3.1 Dual spindle assembly in mouse zygotes

When I started my project, we demonstrated that a dual spindle forms in mouse zygotes, which aligns the two parental genomes next to each other in metaphase, but keeps the genomes essentially separated during the first division of the embryo (*308*). This explained, why within the nuclei of the 2-cell mouse embryo the parental genomes still occupy distinct hemispheres. This is not only interesting from a biological and mechanistical point of view, but has also broad ethical implications, as in the German embryonic protection act the beginning of a human life is defined by the mixing of the parental genomes (*380*), which at the time the law was written, was assumed to happen immediately after fertilization.

In our initial work we however did not demonstrate if dual spindle assembly was a conserved mechanism across mammals, nor did we provide mechanistic details on how the assembly of two spindles is initiated in the zygote.

To address this, I first established temporally tightly controlled imaging experiments to study microtubule nucleation at NEBD in both a qualitative and quantitative manner. Second, I conducted microtubule regrowth assays in early zygotic mitosis to investigate, where microtubules originate at the beginning of zygotic spindle assembly. Third, I established a 'Trim away'-based molecular perturbation experiment to acutely remove acentriolar MTOCs. Collectively, these three technological advances will be highly relevant for future mechanistic studies of spindle assembly throughout the preimplantation development of mammalian embryos, and I already applied them to study the zygotic division.

3.1.1 MTOC subclusters at spindle poles of dual spindles

The dual spindle in mouse zygotes most commonly initially assumes a 'V-shape', in which two of the poles (one of each spindle) come already close together, while the other two poles remain further apart (Figure 7). Strikingly, the many acentriolar MTOCs—that were assumed to functionally replace centrosomes in the early mouse embryo (*295*), based on their function in the oocyte (*185*)—form distinct subclusters at each of the four individual spindle poles. Intriguingly, unlike in the oocyte, in the zygote not all cytoplasmic MTOCs are incorporated into the spindle. Only those MTOCs positioned closely to the pronuclear surface at NEBD associate with the forming spindles and become localized to their poles (Figure 7). The MTOCs further away in the cytoplasm do not get in contact with the spindle at all.

The MTOC clusters at the two spindle poles that are closely associated early on, sometimes appear to merge or align so closely next two each other that they cannot be resolved by light sheet imaging anymore. However, at the more distant spindle poles the MTOC clusters typically stay separated (Figure 7).

These independently organized poles indicate that the two spindles remain independent while they bipolarize into stable metaphase spindles and align their axes. The clustering of MTOCs could directly increase nucleation capacity at each spindle pole, which itself could support spindle assembly. Alternatively, it could help stabilize and focus the respective spindle poles without influencing spindle microtubule mass *per se*, which might be relevant for force generation in order to segregate chromosomes.

As mentioned above, the MTOCs that eventually constitute the polar clusters, are initially localized just outside the pronuclei, often directly associated with the pronuclear membrane, likely due to a dynein-based mechanism as has been described for centrosomes (*381*–*383*).

Cytoplasmic MTOCs can in principal promote nucleation into all directions, which is apparent in the common formation of microtubule asters (*384*, *385*). This radial growth from MTOCs is for example highly relevant in the spindle formation in *C. elegans* zygotes, which is almost entirely dominated by large centrosome-based microtubule asters (*342*, *386*). In mouse zygotes I also observed characteristic aster formation around many cytoplasmic MTOCs until NEBD (see Figure 10 and Figure 27, negative control) consistent with previous reports (*295*). Initially, I therefore assumed that the many acentriolar MTOCs must play a major role in nucleating the microtubules for the initial dual spindle assembly. If radial nucleation from all MTOCs was the dominant source of microtubules, one would expect that initially the

microtubule mass grew in both, the former pronuclear volume as well as in the former cytoplasm of the zygote. However, I observed that the microtubule mass predominantly grew inside the pronuclear volumes (Figure 8). This indicates that after NEBD radial MTOC-based nucleation is not dominant. This could be explained by three mechanism: i) after NEBD, MTOC-based nucleation hardly takes place, ii) upon NEBD, growth of MTOC-nucleated microtubules become directed towards the chromosome mass, iii) chromosome-/kinetochore-based microtubule nucleation pathways take over after NEBD, effectively outcompeting MTOC based nucleation.

3.1.2 Several microtubule nucleation pathways are active in the zygote

The key question arising from the just described observation is, which microtubule nucleation pathways are active upon NEBD and how they could facilitate dual spindle assembly.

I addressed this by imaging zygotes (with very high spatial resolution) when NEBD started, to map, where microtubule growth starts. Using live imaging to monitor chromosome condensation during early prophase, I achieved unprecedented temporal targeting of zygote fixation, which allowed me to visualize the very first spindle microtubules in IF experiments (Figure 9). For this experiment it was essential to perform the correlative fixation of single embryos staged by light sheet imaging to capture the brief period, when the nuclear envelope starts to become permeabilized, but is not yet completely broken down and thus still excluded MTOCs. In embryos fixed too late, nuclear envelope fragments and associated MTOCs in fact collapse onto the chromosomes making it impossible to distinguish chromosomal and MTOC-based nucleation upon imaging. During nuclear envelope permeabilization however, soluble cytoplasmic components, such as soluble tubulin dimers and additional spindle assembly factors like TPX2 gain access to the nucleus and are released from their importin-based inhibition upon exposure to nuclear Ran-GTP, and thus boost the initiation of mitotic microtubule nucleation (*210*, *377*).

Strikingly, my targeted imaging-based dissection in late prophase shows that several microtubule nucleation pathways are active at this early stage of spindle assemlby. As expected, I observed microtubules radiating from the acentriolar MTOCs into the pronuclear volume. Interestingly, these occasionally already connected to kinetochores. It is very unlikely that a pure search and capture mechanism was the basis of this, considering that the envelope had just become fenestrated with 1-2 minutes prior to fixation. It therefore seems

more likely that the growth from MTOCs is either directed towards kinetochores, or that fibers growing from kinetochores would meet MTOC fibers, supporting a spindle assembly model with staggered microtubule bundles as described in section 1.3.6.2. It has been shown that a pure search and capture mechanism is insufficient even in centrosome dominated systems that have an inherent bipolarization of the spindle from the start. In the mouse zygote with many MTOCs, it is therefore quite likely that additional, chromosome-based mechanisms complement the nucleation activity of the MTOCs. In somatic cells with centrosomes and acentrosomal mouse ooctyes, it was shown that the chromosomes are arranged in a belt-like fashion early on in mitosis to make kinetochore attachment to microtubules more efficient (*232*, *387*). However, in the mouse zygote, I did not observe clear prometaphase belt-like arrangements of the chromosomes, making it likely that chromosome-/kinetochore-based microtubule nucleation might substantially contribute to spindle assembly.

Well in line with this model are my observations of several microtubules within the pronuclear volumes after fenestration that did not connect to MTOCs at all, but often emanated in the close proximity of kinetochores or appeared isolated in the nucleoplasm. Both could be explained by either kinetochore-based or Ran-GTP dependent spontaneous microtubule nucleation in the nucleoplasm (also referred to as chromosome signaling).

To further clarify, where exactly nuclear microtubules come from, I performed a temporally targeted microtubule regrowth assay. After rapid microtubule depolymerization in late prophase using Nocodazole, I allowed microtubules to regrow for different time periods after washing out the drug. Microtubules actually started to grow at both MTOCs and kinetochores (Figure 10), but nucleation and growth was much stronger and faster at the kinetochores. This observation is in stark contrast to human somatic cells, where regrowth was reported to start at the centrosomes and to occur later in the vicinity of chromosomes (*133*).

Furthermore, microtubules around chromosomes were less sensitive to Nocodazole treatment and persisted longer than MTOC fibers. In Nocodazole titration experiments I observed that they only fully depolymerized after incubation with 10 µM Nocodazole for more than 20 minutes (Figure 27, see also Figure 10 for 0-minute control), while MTOC fibers were disassembled already after 5-10 minutes (Figure 27).

Overall, these observations show that chromosome- and kinetochore-mediated nucleation is present at the beginning of dual spindle assembly in the mouse zygote.

3.1.3 Acentriolar MTOCs are required for spindle function

With the above-described experiments, I was able to identify that kinetochore-/chromosome-mediated nucleation occurs in early dual spindle assembly and given that MTOCs seemed the weaker nucleators and only some of them were incorporated into the spindle, I initially hypothesized that they might be dispensable to make stable bipolar microtubule arrays. To probe this, I adapted the 'Trim-away' method (*367*, *368*) to acutely deplete MTOCs during mitosis in mouse zygotes.

When MTOCs were removed in prophase, initial spindle microtubule nucleation was predominantly observed between the two parental genomes (Figure 13). In absence of MTOCs this can only be caused by the chromosome-/kinetochore-based pathways (described in detail in 1.3.6.3). The observation that this specifically happens in between the two genomes makes Ran-GTP-dependent mechanisms particularly likely. Assuming that Ran-GTP diffuses in all directions away from the chromosomes, the local concentration would be highest in between the genomes, which should thus lead to the strongest nucleation. It would however still be interesting to probe if this is due to general chromosomal nucleation, or potentially CPC-based microtubule nucleation from kinetochores. In order to test this, it will be interesting in the future to deploy the temporally targeted 'Trim-away' approach I established here for MTOCs together with imaging a kinetochore label, or to deplete components of the Ran or CPC pathways using 'Trim-away'.

After MTOC depletion, indeed initial dual spindle assembly still seemed possible, but the resulting spindles showed both structural as well as functional defects. In milder cases, the spindle shape was generally altered, and microtubule density was severely reduced, concomitant with increased chromosome lagging during segregation. In more severe cases, mitosis failed completely, and mitotic slippage was observed (Figure 13 and Figure 14).

What causes these two distinct phenotypes after MTOC depletion? One potential explanation would be technical differences in depletion efficiency, for example due to slight variations in antibody injection volumes, which could lead to residual MTOC activity. I tried to address this concern by IF stainings against the injected antibody and the target protein after the live-imaging experiment. However, since fixation was only possible after completing live imaging of the first mitosis in all embryos from the same experiment, the embryos were fixed at the 2-cell stage, when MTOCs are already highly dispersed, making it difficult to exclude the

presence of residual MTOCs. Additionally, Trim21 also leads to degradation of the injected antibody (*367*, *368*), which makes quantification of the amount of delivered antibody unreliable. To overcome this in the future one could envision to spike the antibody solution with a labeled dextran to infer the injected volumes.

Overall, my results showed that even though MTOCs do not seem to be required for the initiation of dual spindle assembly they are indispensable for the formation of a structurally stable and fully functional bipolar spindle.

3.1.4 Multimodal assembly of the zygotic spindle apparatus in the mouse

Meiotic divisions are comparatively long (*312*, *313*) and in mouse oocytes, particularly in meiosis I, the MTOCs dominate spindle assembly (*185*). An MTOC centric spindle assembly pathway likely predominantly follows a search and capture model (*213*). However, already in meiosis II a Ran-GTP gradient dependent pathway appears to guide the search of microtubules emanating from MTOCs (*347*). This augmentation of search and capture by Ran-guidance is likely required due to the short phase of spindle assembly compared to meiosis I [discussed in (*230*, *347*)].

Similar to meiosis II, zygotic spindle assembly also proceeds faster than in meiosis I. For example, microtubules connecting MTOCs and kinetochores can already be detected a few minutes after NEBD (Figure 9). Therefore, it is unlikely that a pure search and capture model operates here. This is in line with previous findings that showed that Ran-GTP dependent pathways are necessary for normal zygotic spindle assembly and that mitotic timing is delayed upon Ran inhibition (*295*). When I depleted MTOCs, the overall mitotic timing did not seem to be substantially altered and dual spindle assembly could still be initiated, but the assembled spindle was much smaller, contained less microtubules and could not faithfully segregate chromosomes (Figure 13 and Figure 14).

Collectively, the previous findings in the literature and my new data support a model of dual spindle assembly in the zygote driven by multiple synergistic mechanisms. While initially chromosome-/kinetochore-mediated microtubule nucleation dominates, MTOCs are important later on. Thus, the initial assembly and kinetochore attachment is clearly not purely based on search and capture of MTOC-based microtubules. Instead, chromosome signaling likely initiates microtubule nucleation around each genome and especially their kinetochores, from where microtubules subsequently self-organize into antiparallel arrays. Guided search

and capture of MTOC-based microtubules might complement these initial arrays to provide additional microtubule mass, focus their poles and stabilize the two bipolar structures.

3.2 Spindle assembly in zygotes with centrosomes

The experiments discussed so far were performed in mouse preimplantation embryos. This model is in particular powerful as it is well established in basic research and many transgenic mice with fluorescent markers for live imaging are available, which help to look at processes in living embryos without heavily disturbing them. However, transferring observations from this organism to humans has some inherent species-specific limitations; for example, in human embryos the genome activation has a different timing (*300–305*) and human embryos contain centrosomes inherited from the sperm (*388*), while early mouse embryos do not (*180*, *294–296*). When studying the mitotic spindle in early embryos, this might be of particular relevance, as the centrosomes could provide two strong cytoplasmic nucleation centers that could potentially override the chromosome-/kinetochore-mediated nucleation that initiates dual spindle formation in mouse zygotes as discussed above (see section 3.1).

In order to address this limitation of the mouse model, I aimed to investigate zygotic spindle assembly also in a model system that is overall more similar to humans, and in particular also contains centrosomes. Thus, I teamed up with Marta de Ruijter-Villani from the University of Utrecht to investigate how the first spindle assembles in bovine zygotes.

In this thesis I thus present the first real-time imaging of bovine embryos with high spatial and unprecedented temporal resolution and thereby established the bovine embryo as a system to study cellular mechanisms during early embryonic development, in a model system much closer to humans than the commonly used mouse model system.

3.2.1 Dual spindle assembly in bovine zygotes

Despite the presence of centrosomes, I found that also in bovine zygotes a dual spindle assembles and carries out the sister chromatid separation of the two parental genomes next to each other (see Figure 15). Pronuclear envelope breakdown was often asynchronous (with a more pronounced asynchrony than in mice), which might further favor dual spindle assembly.

The dual spindles around the parental genomes were particularly evident when dynamic microtubules were depleted by brief cold treatment (Figure 17). As in mouse embryos, the two spindles eventually aligned (Figure 15 and Figure 19). However, after the cold treatment no connecting microtubules between the two spindle systems were detectable (Figure 17), indicating that only dynamic microtubules were involved in spindle alignment but that there was no intercrossing of kinetochore fibers.

Imaging data from a recent publication show that also in bovine 2-cell embryos the parental genomes occupy distinct sub-compartments (*379*), which is in good agreement with a dual spindle mechanism (*308*).

Where do the microtubules for dual spindle assembly come from in the bovine system? Microtubule mass and concentration around the centrosomes peaked 5-7.5 min after NEBD and subsequently stagnated or even declined (Figure 23, Figure 24 and Figure 25). At this point often one entire parental genome was not interacting with any spindle microtubules, yet. Thus, a pure search and capture mechanism by centrosomal microtubules cannot explain spindle assembly.

In fact, the major source of spindle microtubules appeared to be chromosomal (Figure 23, Figure 24 and Figure 25), which could indicate that chromosome- or kinetochore-mediated microtubule nucleation is key to facilitate dual spindle assembly, even if centrosomes are present. As in the mouse, I also observed strongest microtubule growth between the two parental genomes after NEBD, which could point towards a Ran-GTP dependent mechanism as discussed above.

In addition, microtubule lattice nucleation likely also contributes, and this microtubule self-amplification could for example be relevant for maintaining the metaphase spindle. In the future, it will be important to dissect the contributions of the individual pathways. Adapting the acute perturbation experiments I have established for mouse embryos to the bovine system would thus be of particular interest.

3.2.2 Centrosomes in early mammalian embryos

3.2.2.1 Centrosome functionality

The functional relevance of the centrosomes for spindle assembly is in general questionable in bovine zygotes, as they are only loosely connected to the zygotic spindles and are not connected to chromosomes by stable kinetochore fibers (see Figure 17). Typically,

dynein/dynactin motor activity as well as NuMA-mediated cross-linking of microtubule minus ends are important to tether centrosomes to spindle poles, which was shown in Drosophila S2 cells and Xenopus egg extract (*225*, *226*, *389*, *390*). It is thus possible, that in bovine zygotes, these dynein-dynactin and/or NuMA interactions are weak, which could be tested by injecting mRNA encoding functional dynein-dynactin or NuMA to probe, if this tightens the connections between centrosomes and spindle poles.

Furthermore, in the case of monocentrosomal spindles no structural bias towards the centrosomal half was detected, which supports the notion that centrosomes hardly influence the zygotic metaphase spindle (Figure 18).

Furthermore, the two centrosomes often do not perfectly align with the spindle axis and hence do not determine the axis of chromosome segregation, further supporting a weak centrosome functionality (Figure 20 and Figure 21).

It has been shown that centrosomes are essential for embryogenesis in several species, but in some, they seem to be less relevant for the spindle assembly, but rather important for cell cleavage [Xenopus oocytes (*341*, *343*)] or for cell cycle regulation [Drosophila embryos (*391*)]. Maybe the situation is similar in bovine zygotes and early embryos, where they most likely have spindle-independent functions and are potentially just partitioned into the daughter cells by loosely interacting with the spindle poles. That centrosomes just use the spindle poles to be faithfully distributed to the daughter cells to fulfill essential interphase functions, has already been suggested earlier (*392*).

A study mentioned earlier, also indicates that the centrosomes in bovine zygotes are important for pronuclear positioning and for clustering the chromosomes within the pronuclear volumes during prophase (*379*). This clustering might facilitate chromosome biorientation of the otherwise rather spread out chromosomes from the two pronuclei (*379*). However, this might not be essential, and in this thesis, I showed that chromosomes can also be properly segregated even if the centrosomes do not perfectly localize at the pronuclear interphase and thus do not cluster the genomes next to each other (Figure 19B). Two proximal spindles can still form and eventually come together. However, the sample size of bovine zygotes I followed through live imaging at sufficient resolution is small, and thus it needs to be further investigated if centrosomes and genome clustering are strictly required for faithful chromosome segregation.

3.2.2.2 Centriole splitting in bovine zygotes

In other vertebrate systems, mother and daughter centrioles seem to spatially separate during or shortly after telophase (*393*). In the bovine zygote, the mother and daughter centrioles of each centrosome seem to already dissociate in meta- or anaphase (Figure 19A). Interestingly, centrioles appear to move apart by several micrometers indicating that the linker must either be extremely long and flexible or might actually break. Normally, the two centrioles of each polar centrosome are tightly associated at least in the context of the surrounding PCM during mitosis [discussed in (*159*)]. Centriole disengagement was suggested to be linked to the activation of Separase (*266*). And Separase was shown to cleave the PCM protein pericentrin/kendrin (*394*, *395*), which seems to be relevant for maintaining centriole association (*396*). Separase is only activate after Securin degradation has been initiated through the APC/C and the APC/C should not be active until all chromosomes are properly bioriented and the SAC is satisfied. The APC/C should thus just become active at anaphase onset and the PCM should remain intact until the end of mitosis. As in bovine zygotes centrioles seem to disengage prematurely, it is possible that these mechanisms are not as tightly controlled as for example in somatic cells.

In addition it was recently shown that depleting specific PCM components can promote precocious centriole disengagement in somatic cells (*397*). Since centrosomes are degraded in the oocyte (*180*, *181*) and the sperm provides centrioles with originally very specialized architecture and composition (*310*), pericentriolar components might not be as abundant and concentrated in the zygote as in somatic cells.

3.2.3 Distant dual spindles as a mechanism for haploid blastomere occurrence

For bovine embryos it was also shown that haploid blastomeres—with a single parental genome—can occur after the zygotic division (*332*, *398*). We already suggested that a failure in dual spindle alignment would be a mechanistic explanation for such a phenotype after observing the dual spindle in the mouse zygote (*308*). Interestingly, in the larger bovine zygotes we also observed that two very distant spindles assembled if pronuclear migration failed and the pronuclei were thus far apart at the onset of mitosis (Figure 15, Figure 22). As these distant spindles segregated the chromosomes independently, they could very well induce haploidy after cytokinesis into more than two blastomeres. Thus, our observations in bovine zygotes suggest that haploid blastomeres could not only emerge if proximate dual

spindles failed to align, but also if pronuclei failed to migrate in the first place and chromosomes were then segregated into more than two cells by persisting distant spindles.

In bovine zygotes, the pronuclei were usually associated with one centrosome (approximately 75 %, Figure 16). This indicates that the centrosomal linker easily splits early on, likely already in late interphase instead of in prophase. If pronuclear migration proceeds similarly as in *C. elegans* or zebrafish embryos (*381–383*, *399*), which was recently suggested and partially probed (*379*), a premature split of the centrosomal linker could explain how distant pronuclei can each associate with one centrosome: Both initially tethered centrosomes would first associate with the male pronuclear envelope and nucleate two microtubule asters. Dynein at the female pronuclear envelope would eventually bind to microtubule plus ends from one of the asters and exert a pulling force via these microtubules on the associated centrosome on the male pronucleus. If the centrosomal linker is weak, this pulling could cause it to split. So instead of pulling the pronuclei together resulting in pronuclear migration, the centrosomes would be pulled apart. Similarly premature centrosome separation has been shown to have detrimental effects on spindle positioning in human cells (*177*), where the authors perturbed kinesin 14, which supports microtubule-based centrosome linkage. Such centrosome splitting caused strong nuclear motions influencing cortex cues that usually precisely orient the spindle.

Such uncoordinated movement of the two pronuclei over long distances could also explain why after centrosome splitting, they would not be able to connect and move towards each other despite the presence of dynein on both pronuclear surfaces, which could pull on the respective other aster, if positioned sufficiently close to come within reach.

To test the hypothesis of premature centrosome splitting as a mechanism behind the frequently observed distant dual spindle phenotype in the bovine system (19 % of fixed zygotes in mitosis, Figure 15), it would be very interesting to follow pronuclear migration in a sufficient number of live zygotes. Alternatively, one could also perform IF for the centrosomes at early times during the pronuclear stage to get an overview of how and when the two centrosomes associate with the two pronuclear envelopes. In addition, it would definitely be interesting to get more detailed insights into centrosome structure and composition in the context of bovine zygotes, especially on the linker. A previous study has studied the specialized centrosome in the sperm (*310*), but if and how it is modified in the zygote needs further research.

My new observations of bovine zygotic spindles also revealed that the centrosomes can localize very differently with respect to the two distant pronuclei and forming spindles, such that in some instances both centrosomes are associated with one spindle, while the other spindle is acentrosomal (less than 15 %, Figure 16). This indicates that the entire machinery for pronuclear migration can be impaired, not only can the centrosomes split, but also the dynein-dynactin complex at one of the pronuclei may fail to pull on the centrosomal microtubules emanating from the surface of the other parental pronucleus, which was shown to be absolutely required for zygotic divisions in Drosophila and *C. elegans* (*342*, *399*, *400*).

3.3 Two model systems—one conserved mechanism

This study provides important advances in our understanding of the mechanism driving zygotic dual spindle assembly.

In the powerful and experimentally more accessible system of the early mouse embryo, I could show that a major source of initial microtubules is chromosome signaling, interestingly including kinetochore-mediated microtubule nucleation. The many acentriolar MTOCs seem to be more important to stabilize the spindle than for the initial microtubule nucleation. This is in line with the previous proposal that chromosome dependent nucleation and stabilization of microtubules might be especially important in large embryonic cells, and in general in somatic cells without centrosomes (*233*, *237*), where a pure search and capture mechanism is predicted to be inefficient.

However, how these chromosomal and MTOC nucleation pathways are actually linked, if they are active simultaneously or sequentially and how strong their individual contributions are at the different stages of spindle assembly needs further investigation. It should be possible to answer these questions in the future the assays I developed.

In the less experimentally accessible bovine system, which is however physiologically more similar to humans, I could show that dual spindle assembly is conserved in mammals that inherit two centrosomes paternally. Surprisingly, I found that these centrosomes interact only weakly with the spindles throughout mitosis. It is therefore very likely that the mechanisms of chromosomal nucleation and microtubule self-organization that I found in mouse zygote are conserved in bovine and human.

The dual approach of molecular dissection in mouse and physiological validation in bovine is a powerful combination for future studies on fundamental processes in early mammalian embryology. Conceptually, the assays I developed for mouse embryos can be transferred to the bovine embryo to study the molecular mechanisms of spindle assembly in this model system further. In the long term, research that allows validation of biomedically relevant discoveries—made in the mouse and bovine systems—in human embryos would be highly desirable.

Overall, my work shows that dual spindle assembly driven at least in part by chromosomal nucleation and self-organization of microtubules is a mechanism found in both acentrosomal and centrosomal mammalian zygotes. It is thus very likely that this mechanism is conserved across mammalian species, where the parental genomes are initially present in separate pronuclei as is also the case in humans.

4 MATERIALS AND METHODS

4.1 Materials and methods used for mouse zygotes

4.1.1 Laboratory mouse handling

The animal work was performed in the Laboratory Animal Resources (LAR) Facility at the European Molecular Biology Laboratory (EMBL). The LAR facility is operating according to international animal welfare guidelines (Federation for Laboratory Animal Science Associations guidelines and recommendations) and internally controlled by the Institutional Animal Care and Use Committee (IACUC). The mice were maintained in specific pathogen free conditions on a 12-12-hour light-dark cycle and used between the age of 8-24 weeks.

4.1.2 Mouse strains

In this study, the F1 generation from a cross of C57BL/6J and C3H/HeJ mice was used as WT and all females were generally mated with WT males, as reporter proteins could be expressed in the zygotes entirely by maternal contribution. The following strains were all derived from R26/R26-EGFP-Tuba and R26/R26-H2B-mCherry C57BL/6J mice (*401*): To validate the expression of tdEos-hCep192 after mRNA injection with IF, embryos were isolated from heterozygous R26/R26-H2B-mCherry females (F1 generation from crossing homozygous R26-H2B-mCherry C3H/HeJ and wildtype C57BL/6J animals). To validate the Pericentrin 'Trim away' with IF against Pericentrin, embryos were collected from WT females. To monitor the effect of Pericentrin 'Trim away' by live imaging, embryos were initially collected from homozygous R26-EGFP-Tuba females (F1 generation from crossing homozygous R26-EGFP-Tuba C57BL/6J and homozygous R26-EGFP-Tuba C3H/HeJ animals) and later from heterozygous R26/R26-EGFP-Tuba females (F1 generation from crossing homozygous R26-EGFP-Tuba C57BL/6J and wildtype C3H/HeJ animals), when I noticed that signal intensities were similar, independent of transgene copy number. Embryos collected from females of the latter strain were also used to validate the effect of Pericentrin 'Trim away' on MTOCs in general by IF against γ-tubulin. To assess microtubule regrowth after Nocodazole treatment, embryos were taken from R26-H2B-mCherry/R26-EGFP-Tuba females (F1 generation from crossing homozygous R26-H2B-mCherry C57BL/6J with homozygous R26-EGFP-Tuba C3H/HeJ animals).

4.1.3 Mouse embryo recovery and culture

Female mice between 8-20 weeks old were superovulated by intraperitoneal injection of 7.5 international units (Ius) of pregnant mare's serum gonadotropin (PMSG, Intergonan®, Intervet) and subsequent injection of 7.5 IUs of human chorionic gonadotropin (hCG, Ovogest 1500, Intervet) 46-49 hours later. The females were mated with wildtype males immediately after hCG injection. 18-22 hours post hCG injection, females were sacrificed and the oviducts dissected as described previously (*402*) and placed in 37 °C warm MOPS buffer (10130, G-MOPS™Plus, Vitrolife). The ampulla was opened in drops of 25-50 µl of 1 x Hyaluronidase (10017, HYASE-10X™, Vitrolife) in warm MOPS buffer on a petri dish lid under the stereoscope. After complete dissociation of the cumulus cells within 60-90 seconds, the embryos were first transferred (by mouth-pipetting) into drops of warm MOPS buffer (30-50 µl) to dilute the hyaluronidase, subsequently washed 2-3 times, and finally cultured in drops (25 µl) of pre-equilibrated (37 °C and 6 % CO_2) culture medium (10128, G-1™Plus, Vitrolife) covered with light paraffin oil (10029, Ovoil™- culture oil, Vitrolife) in a 35 mm petri dish incubated >30 min at 37 °C and 6 % CO_2.

4.1.4 Expression constructs and mRNA synthesis

pGEMHE-H2B-mCherry (*387*), pGEMHE-tdEos-hCep192 (*309*) and pGEMHE-Trim21 (*367*, *368*) were described previously (the latter two were kind gifts from Melina Schuh).

To generate pGEMHE-EB3-mCherry2, full length homo sapiens EB3 cDNA (NM_001303050.1, a generous gift from Niels Galjart) was tagged C-terminally with tandem mCherry and cloned into a pGEMHE vector under the control of a T7 promotor by Nathalie Daigle. mRNA was synthesized from linearized template DNA (1 µg), capped and poly-adenylated mRNA *in vitro* using the mMESSAGE mMACHINE™ T7 ULTRA Transcription kit according to manufacturer's instructions (AM1345, ThermoFisher Scientific). mRNA was purified (74104, RNeasy Mini Kit, QUIAGEN) and dissolved in 14 µl nuclease free water.

4.1.5 Micromanipulation of mouse zygotes

The mouse zygotes were injected with mRNA or protein in solution as described previously (*185*, *366*), with minor modifications. In brief, the 'injection slit' between two glass cover slips (~100 µm) was assembled using double-sided adhesive tape (05338, tesa) as a spacer (see Figure 26 for a schematic overview). The coverslip with the injection slit was attached to the

plastic support slide with silicone grease and the whole chamber filled with 37 °C warm MOPS buffer before mouth-pipetting the embryos into the slit. A glass microinjection needle with very thin tip was filled with ~1 µl of mercury and was connected to the paraffin-oil filled injection system. The mercury drop was pushed to the very tip of the capillary using the hydraulic pump. mRNA solution was then aspirated into the very tip, but framed by silicone oil, to minimize the risk of mercury injection and to seal the tip from leakage of the mRNA solution into the MOPS buffer surrounding the embryos. For proteinaceous solutions, an injection needle with slightly wider opening was used and the solution was directly loaded in front of the mercury, without additional silicone oil as a spacer as the detergent within the protein solutions made the spacing less efficient. The injection volumes were adjusted dependent on the application. For live imaging of reporter proteins, 1-2 pl of mRNA solution were injected (~0.4-0.8 % of embryonic volume). The mRNA concentrations were 0.3 µg/µl for EB3-mCherry2 and tdEos-hCep192. For 'Trim away', the injection volumes were adjusted according to Clift et al. (*368*): A volume of ~3.5 pl (~ 1.5 % of embryonic volume) was injected with mRNA for Trim21 and H2B-mCherry at concentrations of 0.4 µg/µl and 0.1 µg/µl, respectively. For the rabbit anti-Pericentrin antibody (ab237034, abcam), ~3.5-4 pl were injected at a concentration of ~0.9 mg/ml antibody in PBS and 0.05 % NP-40 (492015, Calbiochem).

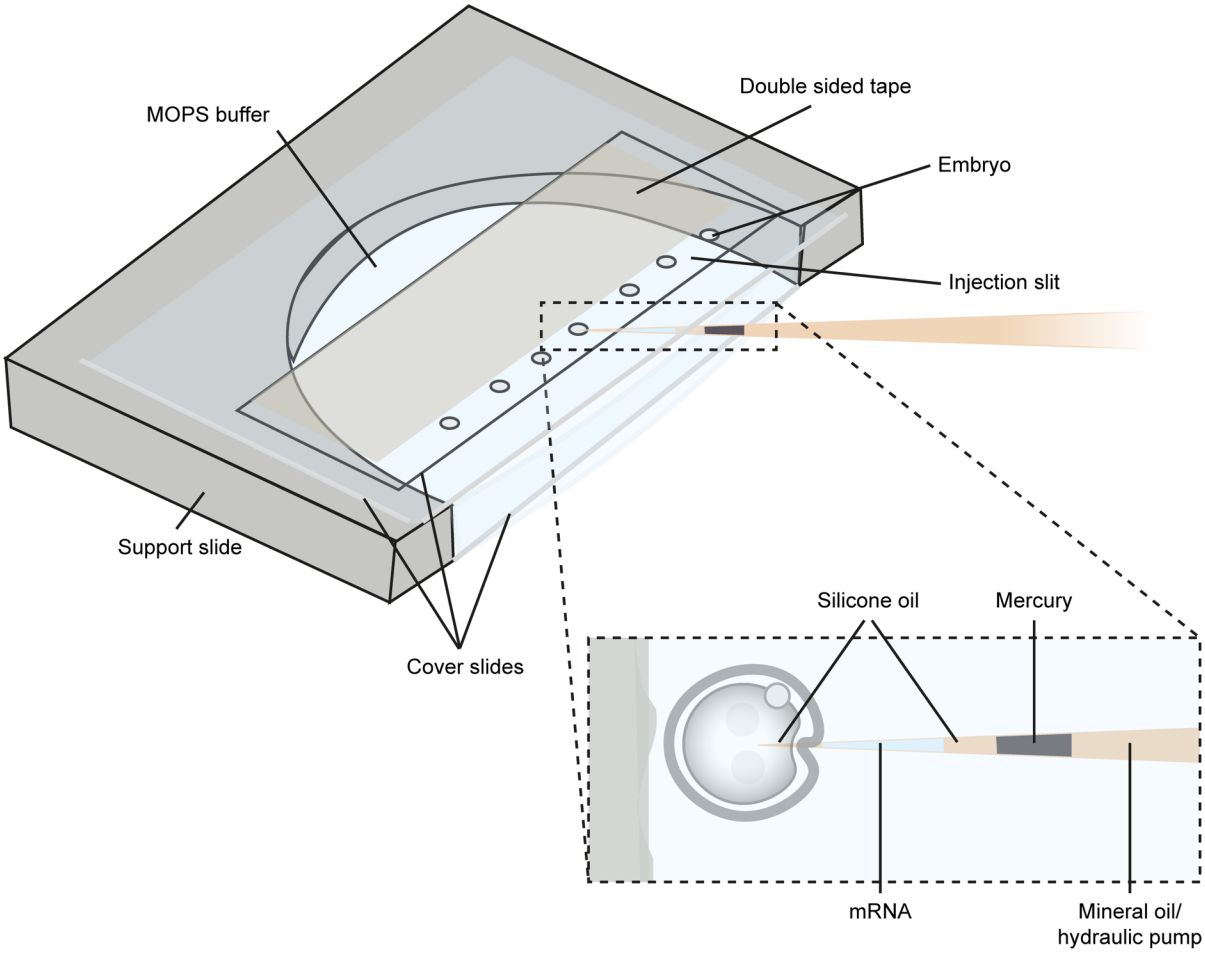

Figure 26. Microinjection of mammalian embryos. An injection chamber was assembled to mount the embryos as previously described by Jaffe et al. (*366*) with minor modifications. Using silicone grease, an intact 22 x 22 mm cover slide was attached to the bottom part of the support slide to cover the half-circled area. One or two (for mouse or bovine embryo injection, respectively) layers of double-sided tape was glued onto a second 22 x 22 mm cover slide approximately 3 mm from one edge. A third 22 x 22 mm cover slide was cut into a piece of ~8 x 18 mm and this glass piece was glued onto the intact cover slide with the provided tape leaving a small ~250 µm wide slit, wherein the embryos were later mounted to be trapped during injection. Again, using silicone grease, the assembled glassware was attached onto the top of the support slide; the injection slit was facing towards the second unmodified cover slide at the bottom and towards the opening of the entire assembled chamber. The chamber was then filled with warm MOPS buffer (37 °C, ~650 µl) and the embryos mounted into the injection slit by mouth-pipetting and using a stereoscope. Using a micromanipulator (Narishige), the zygotes were then injected with mRNA in ultrapure water (or antibody with added detergent and stabilizing salts). The injection solution was always first aspirated into the tip of the injection needle, framed by silicone oil at the back and at the tip (for antibody solutions, additional oil was only aspirated into the tip). This approach made sure that no mixing with the MOPS buffer at the very tip would occur and it helped to avoid accidental injection of mercury, which was used as a plunger between the mRNA solution for injection and the mineral oil at the back used as hydraulic pump. For an experienced user, the silicone oil in front of the mercury plunger is not necessary and it was left out to facilitate injection of the antibody solution for the 'Trim-away' method to avoid mixing due to the detergent.

4.1.6 Live imaging

For live, time-lapse imaging of mouse zygotes, the previously described custom built inverted light sheet microscope was used (*286*) with previously described modifications (*365*), and

using a 25 µm thick FEP foil with reduced rigidity (Lohmann, RD-FEP100A-610) as a transparent base for sample mounting. In this microscope setup, the xy-pixel size is set to 130 nm. The thickness of the light sheet can be adjusted to ~1.5 or ~3 µM.

To monitor cell cycle progression in zygotes expressing H2B-mCherry (and EGFP-alpha-tubulin), chromosome condensation was assessed every 10-15 min in early Prophase and every 2-5 min closer to NEBD. A small central volume (stacks of ~20-40 µm height and ~1 µm z-sampling) around the pronuclei was imaged for that purpose using the 3 µm thick light sheet with an exposure time of 50-100 msec per plane. To image the MTOCs and microtubule tips, fluorescence from H2B-mCherry and tdEos-Cep192 was acquired simultaneously every 45 or 60 seconds with an exposure time of 100 msec per plane. Here, the light sheet of ~1.5 µm thickness was used. Stacks of 52 µm were acquired with a z-step size of 520 nm.

To image chromosomes and microtubules after degrading Pericentrin with the 'Trim away' method (*367*, *368*), fluorescence from EGFP-alpha-tubulin and H2B-mCherry was acquired simultaneously every 2 minutes with an exposure time of 100 msec per plane. Here, either stacks of 100 µm or 50 µm were imaged with a z-step of 1 µm or 0.5 µm, respectively. Single color data from the raw camera data was extracted from the time-lapse images as described previously (*286*). Alternatively, we used Fiji (*403*) with a new in-house built plugin for processing large imaging data (*404*). For 3D visualization and data representation arivis Vision4D Release 3.3 was used, where projected scale bars were automatically annotated.

4.1.7 Quantification of microtubule increase within pronuclear volumes and the cytoplasm using EB3-mCherry2 signal from live imaging

Segmentation of individual pronuclei was performed manually using an interactive tool, developed in MATLAB, that allows the user to draw the boundary of the object(s) of interest and subsequently saves the binary mask of the object(s) automatically. Segmentation was performed only on the single timepoint 45 s prior to detectable synchronous NEBD or NEBD of the leading pronucleus. The segmented volume was applied on subsequent time frames and quantified for 15 frames from NEBD to 10.5 min post NEBD. Only embryos with no movement over this imaging period were analyzed. In addition, embryos were excluded, in which the silicone oil delivered with the mRNA injection caused too many aberrations or in which the pronuclear volume was not entirely included in the acquired stacks. Segmented masks were used to calculate the mean EB3-mCherry2 intensity within the original pronuclear

volumes in the 15 frames. The cytoplasmic EB3-mCherry2 intensity in each frame was calculated with respect to each pronuclear volume in the respective z-slice having the largest pronuclear area. For this, a rim of 6 pixels wide, 24 pixels apart from the segmented pronuclear region was generated first. Part of the rim spanned in the other pronuclear region, if any, was excluded from the analysis. Intensities inside the rim were used to construct a histogram and 20 % of the total pixels were truncated from both the top and bottom parts of the histogram in order to exclude noise. Mean cytoplasmic intensity of a pronucleus was calculated from the remaining 60 % of the pixels in the histogram. This process was performed for both pronuclei to obtain two cytoplasmic intensity values and the annotated mean cytoplasmic intensity is the average of these two values.

4.1.8 Microtubule regrowth assay

For the microtubule regrowth assay, the necessary concentration of Nocodazole and the necessary incubation time to depolymerize all microtubules were first determined. Zygotes from R26-H2B-mCherry/R26-EGFP-Tuba females (F1 from C57BL/6J and C3H/HeJ) mated with WT males were monitored for chromosome condensation and NEBD using the inverted light sheet microscope (as described in 4.1.6). Rod-shaped chromosomes in prophase close to NEBD could be observed by imaging H2B-mCherry and the time of NEBD could additionally be derived by imaging EGFP-alpha-tubulin dissociating into the previously compartmentalized pronuclear volumes. Upon NEBD, the zygotes were collected and cultured in 3 or 10 µM Nocodazole (487928, Sigma, dissolved at 10 mM in DMSO) in the above-mentioned culture medium (37 °C, 6 % CO_2) for 5, 10, 20 and 60 min and were then fixed for IF, as described below in section 4.1.9.. Figure 27 shows that incubation at 10 µM Nocodazole for 20-60 min was necessary to depolymerize filamentous microtubules around chromosomes and MTOCs in mouse zygotes. However, the groups were heterogenous. For the final microtubule regrowth assay, the zygotes were incubated in 10 µM Nocodazole in culture medium (see 4.1.3) at 37 °C and 6 % CO_2 for 30-35 min directly following NEBD. Nocodazole was then washed out and the embryos transferred into drug free culture medium, and they were finally fixed in 1-min intervals for subsequent IF (see section 4.1.9).

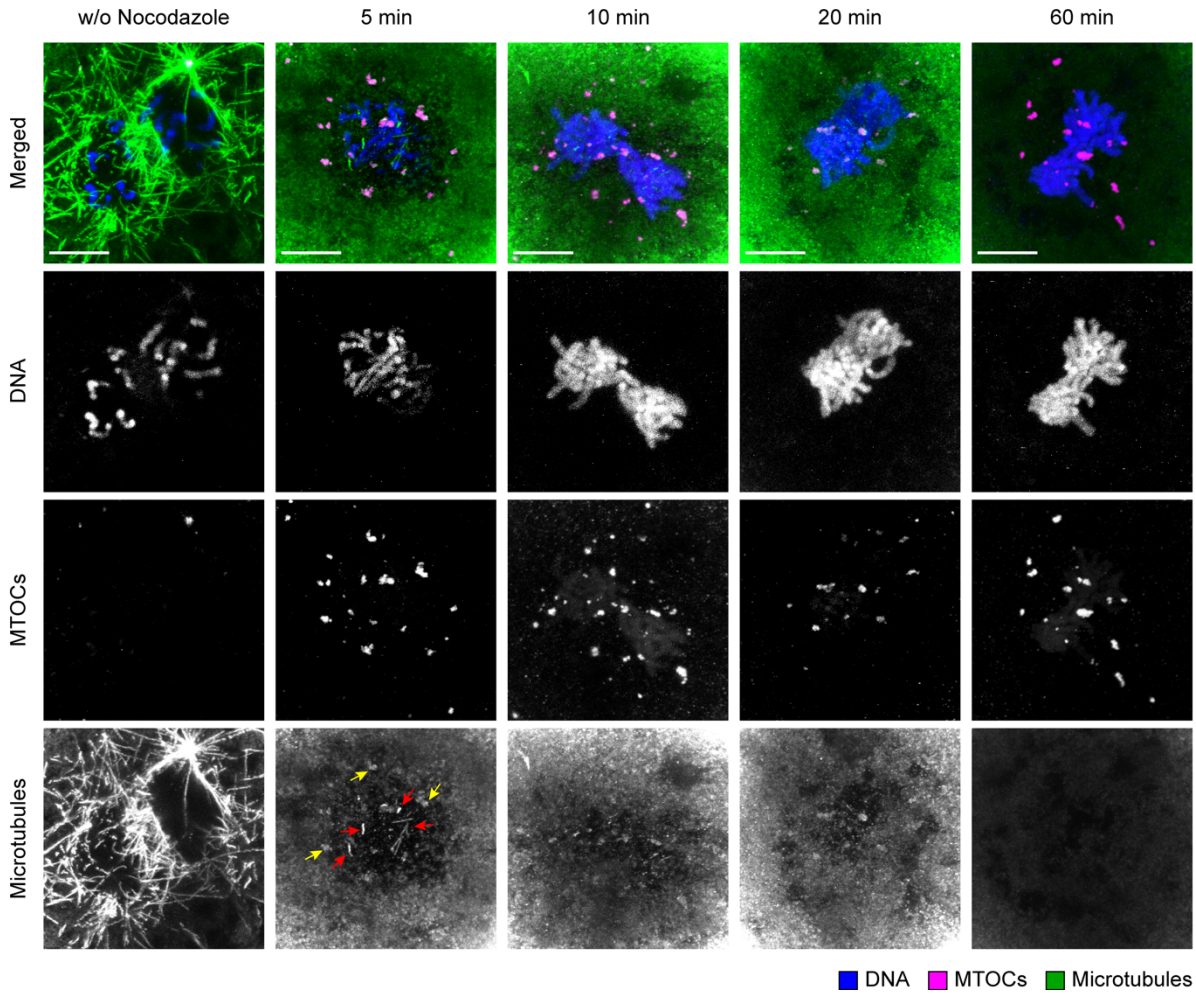

Figure 27: Determining the required incubation time of mouse zygotes within culture medium containing 10 µM Nocodazole to depolymerize microtubules at NEBD. IF images of mouse zygotes fixed after depolymerizing microtubules at the time of NEBD by culturing the zygotes at 10 µM Nocodazole for different time periods from 5-60 min. The embryos were collected from transgenic females (R26-H2B-mCherry/R26-EGFP-Tuba) after natural mating with WT males. Mitotic timing was monitored by live imaging of H2B-mCherry (Chromatin) and EGFP-alpha-tubulin (Microtubules) using inverted light sheet microscopy. Prophase progression was assessed by the state of chromosome condensation and NEBD could be observed by imaging EGFP-alpha-tubulin dissociating into the previously compartmentalized pronuclear volumes. The embryos were collected at NEBD and immediately transferred into culture medium containing 10 µM Nocodalzole to incubate for the indicated time periods prior to fixation (2nd to 5th column). The negative control (first column) was fixed at NEBD without any incubation in Nocodazole. All images show a maximum intensity projection of selected confocal planes. Top row shows the merged images with DNA (Hoechst, blue); MTOCs (Pericentrin, magenta) and microtubules (alpha-tubulin, green; note that this signal can be attributed to both the IF staining and the EGFP-Tuba signal). 2nd to 4th row show the respective single channel data. Note that some signal from the transgenic H2B-mCherry is sometimes still detectable after fixation (seen in some of the single channel images of MTOCs). Stable microtubules are clearly still present after 5 min of Nocodazole treatment; the red and yellow arrows indicate fibrous micorutubules in the proximity of chromosomes and nucleating microtubules at more distant MTOCs. Filamentous microtubules were not visible after 20 min of Nocodazole treatment and micrtobules seemed fully depolymerized after 60 min in the presence of Nocodazole. N(timing condition) = 3. Scale bars, 10 µm. In this experiment I was supported by my colleague Sandra Correia helping me adhere to the indicated timings for the consecutive steps.

4.1.9 Immunofluorescence (IF) and confocal microscopy

Zygotes were fixed by two different approaches. To validate the effect of tdEos-hCep192 on MTOCs after injection of the encoding mRNA, zygotes were fixed using a HEPES based fixation buffer as previously described (*185*), but with minor modifications. To assess microtubule regrowth after Nocodazole treatment and to validate 'Trim away' of Pericentrin, embryos were fixed using a PIPES based fixation buffer similarly as previously described to optimally conserve microtubules (*308*, *387*). For both approaches, the zygotes were transferred from the culture medium into 37 °C warm MOPS buffer for a brief wash. All the following treatments were done within wells of ibidi µ-Slides (81501, µ-Slide Angiogenesis, ibidi) filled with 40 µl of solution per well. The embryos were pipetted into the respective fixation-buffer. HEPES based: 100 mM HEPES, 50 mM EGTP, 10 mM $MgSO_4$, 0.2 % Triton X-100 and 2 % PFA. PIPES based: 94 mM PIPES pH 7.0, 0.94 mM $MgCl_2$, 94 µM $CaCl_2$, 0.1 % Triton X-100 and 1 % PFA. They were briefly washed through one well and then incubated in a second for 30 min at room temperature. The embryos were then washed 4 x 5 min in PBS with 0.1 % Triton (PBS-T) at room temperature and extracted in a well with fresh PBS-T overnight at 4 °C. Embryos were blocked in 5 % normal goat serum, 3 % BSA in PBS-T and then incubated with the primary antibodies in fresh blocking solution overnight at 4 °C. Embryos were then washed 3 x 5 min with 3 % BSA in PBS-T. They were incubated with the secondary antibodies in fresh blocking solution for 1 hour at room temperature. The embryos were then washed 3 x 5-10 minutes with 3 % BSA in PBS-T and finally transferred into wells with 3 % BSA in PBS (for multi-day imaging, embryos were stored at this step at 4 °C in a dark and humidified environment). For imaging, the embryos were also mounted using the same solution. Whenever TMR-Hoechst was used to label chromatin, TMR-Hoechst in DMSO (*405*) was diluted in in the final wash and imaging buffers (1:40000). When Hoechst 33342 (B2261, Sigma) was used to label chromatin, 10 mg/ml Hoechst dissolved in DMSO was diluted 1:2000 in the blocking solution together with the secondary antibodies.

To validate tdEos-hCep192 expression for live imaging in mouse zygotes by IF, the subsequent primary antibody was used: mouse anti-Pericentrin (611815, BD Bioscience, 1:500, 0.5 µg/ml). As secondary antibody, goat anti-mouse IgG with AF 647 (A-21236, Invitrogen, 2 µg/ml) was used.

For the microtubule regrowth assay, the following primary antibodies were used at the indicated dilutions. To visualize centromeres/kinetochores: anti-CREST (CS1058, Europe

Bioproducts, 1:100) or anti-centromeric proteins (15-235, Antibodies Incorporated, 1:50, ~40 µg/ml); for staining of microtubules: mouse anti-alpha-tubulin (T6199, Sigma, 2 µg/ml); to visualize MTOCs: rabbit anti-Pericentrin (ab4448, abcam, 2 µg/ml). The following secondary antibodies were used subsequently: goat anti-mouse IgG with Alexa Fluor (AF) 488 (A-11029, Molecular Probes, 2 µg/ml), goat anti-rabbit IgG with AF 561 (A-11035, ThermoFisher, 2 µg/ml) and goat anti-human IgG with AF 647 (A-21445, Invitrogen, 2 µg/ml). To label chromosomes in addition to the H2B-mCherry, Hoechst 33342 (B2261, Sigma, 5 µg/ml) was added to the secondary antibodies in blocking solution.

To assess 'Trim away' of Pericentrin, the embryos were incubated with the following primary antibodies. For microtubules: chicken anti-alpha-tubulin (ab89984, abcam, 1:150, 2 µg/ml); for MTOCs: either mouse anti-Pericentrin (611815, BD Bioscience, 1:500, 0.5 µg/ml) or mouse anti-gamma tubulin (Sigma,T5326, 1:500, 2 µg/ml). The following secondary antibodies were used subsequently: goat anti-mouse IgG with AF 405 (A-31553, ThermoFisher, 2 µg/ml) and to label (successfully) injected rabbit polyclonal anti-hPericentrin (ab237034, abcam); goat anti-rabbit IgG with AF 647 (A-21245, Invitrogen, 2 µg/ml). To label chromosomes in addition to the H2B-mCherry, TMR-Hoechst [(*405*), 1:40000] was used.

3D volumes of fixed zygotes were imaged on a Leica SP8 using a 63x C-Apochromat 1.2 NA water immersion objective.

4.1.10 'Trim away' of Perticentrin

Pericentrin was targeted for degradation in mouse zygotes as previously described for protein degradation in mouse oocytes (*367*, *368*), with some modifications: mRNA and antibody solutions were injected sequentially. mRNA encoding Trim21 (and H2B-mCherry) was injected 3-5 h before mitotic entry. For acute protein degradation at a specific time during the cell cycle, either the H2B-mCherry signal was monitored to assess the progression of chromosome compaction in prophase or rarely (if this was not possible for technical reasons), the time of HCG administration to the mother was used as a reference and the antibody solution injected >26h post HCG injection, when the zygotes should be close to or already in mitotic prophase. The zygote was then injected with the antibody solution containing rabbit polyclonal anti-hPericentrin in PBS (ab237034, abcam; original concentration 0.974 mg/ml) diluted to 0.88 mg/ml with 0.5 % NP-40 in PBS to achieve a final detergent concentration of 0.05 %, which was used to avoid clogging of the injection capillary. Injection was done without loading oil in

front of the mercury to avoid mixing of the oil and detergent-containing protein solution. Control zygotes ('mock-injected') were injected with 0.05 % NP-40 in PBS without any antibody. For subsequent live imaging, the zygotes were mounted onto the microscope within 10-20 min. For IF, the embryos were first incubated in culture medium for 20 min and then chemically fixed as described above in section 4.1.9.

4.2 Materials and methods used for bovine zygotes

4.2.1 Collection of bovine oocytes, *in vitro* maturation, fertilization and zygote culture

Bovine ovaries were collected from slaughterhouses and cumulus-oocyte complexes (COCs) were subsequently collected as described by Ferraz and colleagues (*375*). COCs with at least three cumulus cell layers were selected and washed in HEPES-buffered M199 (22340-020, Gibco BRL, Paisley, U.K.). These were either directly matured for 23 hours *in vitro* in cohorts of 35-70 COCs in 500 µl of maturation medium (31100-027, NaHCO3-buffered M199 [11150059, Gibco BRL] supplemented with 1 % (v/v) penicillin-streptomycin [15140122, Gibco BRL], 0.02 IU/ml FSH [Sioux Biochemical Inc., Sioux Centre, IA, USA], 0.02 LH IU/ml [Sioux Biochemical Inc.], 7.7 µg/ml cysteamine [30070, Sigma-Aldrich, St. Louis, Missouri, USA] and 10 ng/ml epidermal growth factor [E4127, Sigma-Aldrich]) at 38 °C in a humidified atmosphere at 5 % CO_2. Alternatively, they were kept at ambient temperature (~23 °C) for 19 hours in synthetic oviduct fluid (H-SOF, Avantea, Italy) prior to *in vitro* maturation. Following oocyte maturation, they were fertilized using sperm cells from a bull of a proven fertility (frozen and thawed). Thawed spermatozoa were purified via discontinuous Percoll gradient centrifugation (90/45 %; P1644, Sigma-Aldrich) and the spermatocyte fraction spiked with concentrated fertilization medium (*406*). COCs were washed and finally prepped in the same groups of 35-70 in fertilization medium supplemented with 1.8 IU/ml heparin (H3393, Sigma-Aldrich), 20 µM d-penicillamine (P4875, Sigma-Aldrich), 10 µM hypotaurine (H1384, Sigma-Aldrich), and 1 µM epinephrine (E4250, Sigma-Aldrich). The purified sperm cells were added at a final concentration of 1×10^6 cells/ml to the prepped COCs. *In vitro* fertilization was done at 38 °C for 6-9 hours under humidified atmosphere at 5 % CO_2. Then, to remove cumulus cells from presumptive zygotes, they were vortexed for 3 min and transferred to synthetic oviductal fluid (SOF) (*407*), in which they were cultured at 38 °C under humidified

atmosphere, at 5 % CO_2 and 5 % O_2. Zygotes used for live imaging were cultured under the same conditions but without Phenol Red in the SOF medium.

4.2.2 Immunofluorescence (IF) and confocal microscopy

27.5 hours after addition of the spermatocytes to the COCs, the presumptive bovine zygotes were rinsed in PBS at 38 °C and fixed in 500 µl of the above-described fixation buffer (94 mM PIPES pH 7.0, 0.94 mM $MgCl_2$, 94 µM $CaCl_2$, 0.1 % Triton X-100, 1 % PFA). Alternatively, they were incubated in ice cold PBS for 3 minutes (cold shock treatment) as previously described for mouse oocytes and embryos (*308*, *387*) and fixed subsequently. Similar as for IF of the mouse zygotes, the cow embryos were then washed 4 x 5 min in 3 % BSA in PBS with 0.1 % Triton (PBS-T) at room temperature and extracted in PBS-T overnight at 4 °C. All subsequent steps were performed in wells of ibidi µ-Slides (81501, µ-Slide Angiogenesis, ibidi) filled with 40 µl of each solution per well. First, embryos were blocked in 5 % normal goat serum and 3 % BSA in PBS-T and then incubated with the primary antibodies diluted in blocking solution overnight at 4 °C. Primary antibodies used to stain spindle components: chicken anti-alpha-tubulin (10 µg/ml; abcam, ab89984); rabbit anti-CEP192 (3.5 µg/ml; Ab frontier AR07-PA001); mouse anti-acetylated alpha-tubulin (5 µg/ml; T7451 Sigma-Aldrich) or mouse anti-NEDD1 (2.5 µg/ml; H00121441-M05, clone 7D10, Abnova). Afterwards, embryos were washed 3 x 5 min with 3 % BSA in PBS-T and incubated with Hoechst 33342 to stain DNA (0.2 mM, Sigma-Aldrich) and secondary antibodies diluted in blocking solution for 3 hours at room temperature. Used secondary antibodies: goat anti-chicken Alexa Fluor® 647 (4 µg/ml, A-21449, Molecular Probes), goat anti-mouse Alexa Fluor® 488 antibody (8 µg/ml, A-11029 Invitrogen), goat anti-rabbit Alexa Fluor® 568 antibody (8 µg/ml, A-11036 Invitrogen). Subsequently, embryos were washed 3 x 10 minutes with 3 % BSA in PBS-T and 2 x 10 minutes with PBS alone and mounted on glass slides (Superfrost Plus, Menzel, Braunschweig, Germany) with anti-fade mounting medium (Vectashield, Vector Laboratories, Burlingame, California, USA).

Fixed and stained bovine zygotes were imaged on a Leica SPE-II with a 63x oil immersion objective. Z-stacks of approximately 80 µm were acquired with 42.7 nm pixel size in xy and a z-step size of 420 nm. Cep192 staining lead to a comparatively high background. The specificity of the staining was thus validated by co-localization with the alpha-tubulin signal or (especially in case of cold shock treatment), it was replaced with NEDD1 staining, with

substantially lower background signal. To exclude polyspermy in the zygotes (which might also cause dual spindle formation), they were additionally stained for acetylated alpha-tubulin. Acetylated tubulin is a core component of cilia and can thus be observed in the residual sperm flagellum (Figure 15D). Thus, if an oocyte was fertilized multiple times, the zygote would exhibit multiple flagella signals and these zygotes were thus excluded. Alternatively, cells were scored for diploidy based on the apparent DNA volumes. IF data was processed using Fiji (*403*) or Imaris Cell Imaging Software. DNA volume determination was also done by manual segmentation using Imaris and centrosome coordinates were manually determined using Fiji.

4.2.3 Expression constructs and mRNA synthesis

pGEMHE-H2B-mCherry (*387*), pGEMHE-EGFP-MAP4 (*185*) were reported previously.

To generate pGEMHE-EB3-EGFP2, full length *homo sapiens* EB3 cDNA (NM_001303050.1, a generous gift from Niels Galjart) was tagged C-terminally with tandem mEGFP and cloned into a pGEMHE vector under the control of a T7 promotor by Nathalie Daigle. mRNA was synthesized from linearized template DNA (1 µg), capped and poly-adenylated mRNA *in vitro* using the mMESSAGE mMACHINE™ T7 ULTRA Transcription kit according to manufacturer's instructions (AM1345, ThermoFisher Scientific). mRNA was purified (74104, RNeasy Mini Kit, QUIAGEN) and dissolved in 14 µl nuclease free water.

4.2.4 Micromanipulation

The mRNA microinjection protocol for cow zygotes was adapted from previous protocols (*185*, *366*), as already described in section 4.1.5 for mouse zygotes (for schematic overview, see Figure 26). But to accommodate the larger cow zygotes (diameter ~120 µm) the 'injection slit', created between two glass cover slips, was widened by using a spacer of two layers of double-sided adhesive tape (05338, tesa) tightly pressed together (~170-190 µm). Silicone grease was used to attach the coverslip (with the injection slit) to the plastic support slide and the whole chamber was filled with 37-38 °C warm MOPS buffer before mouth-pipetting the embryos into the slit. The injection volume was adjusted to ~0.5 % of the bovine zygotic volume (approximately 4-5 pl used) and microinjection needles with wider opening were used for injection (usually used to inject proteinaceous solutions into mouse embyros). The mRNA

concentrations ranged between 0.1-0.2 µg/µl for H2B-mCherry, 0.5 or 0.9 µg/µl for EB3-mEGFP2 and 0.3-0.4 µg/µl for MAP4-EGFP.

4.2.5 Live imaging

For live, time-lapse imaging of bovine zygotes, the same inverted light sheet microscope previously reported for mouse embryo imaging was used (*286*), with the above described modifications (section 4.1.6). To image chromatin and either the microtubule tips or the microtubule lattice, H2B-mCherry and either EB3-mEGFP2 or EGFP-MAP4 fluorescence was acquired simultaneously using a 488 nm laser (~25-30 µW) and a 561 nm laser (~5-10 µW) with an exposure time of 100 ms (time resolution 2.5 minutes). Stacks of 100 or 104 µm were acquired with a z-step size of 1 and 1.04 µm, respectively.

As for processing of imaging data from live mouse zygotes, also for the bovine zygotes, single color data from the raw camera data was extracted from the time-lapse images as described previously (*286*). Alternatively, we also used Fiji (*403*) with a new in-house built plugin for processing large imaging data (*404*). For 3D visualization and data representation arivis Vision4D Releases 3.1 to 3.2 were used and scale bars were calculated and manually inserted.

4.2.6 Comparing spindle halves within mono- and bicentrosomal spindles from IF data

To quantify IF intensity of the alpha-tubulin staining and to robustly compare the intensity distributions of one spindle half with respect to the other, a customized MATLAB (The MathWorks, Inc.) script was used. In summary, first the metaphase chromosome signal from the separate Hoechst channel was segmented and used to predict the orthogonal spindle axis (in relation to the shape of metaphase chromosomes). Then a set of parallel, equidistant cross sections of the tubulin channel orthogonal to the predicted axis was created for further analysis.

In more detail, to segment chromosomes, the signal from the Hoechst channel was first interpolated along the z-axis to generate an isotropic 3D stack from the anisotropic raw data. For noise reduction a 3D Gaussian filter was applied on the interpolated stack (sigma = 2, kernel = 3). The Hoechst channel was converted to a binary signal by combining parameters from adaptive thresholding (*408*) applied on individual xy-planes of a z-stack, as well as on all xy-planes of the entire stack (*409*). Connected component analysis of the detected binary

objects followed by smoothing operations was used to identify the chromosome mass. The spindle region was detected analogously. Centrosome coordinates however, were picked manually. A Hessian matrix was constructed based on the 3D coordinates of all the voxels belonging to the identified chromosome mass. In this matrix, the Eigenvector with the lowest Eigenvalue is approximately orthogonal to the metaphase plate and was therefore taken as the predicted spindle axis.

The predicted spindle axis served as a reference to slice the microtubule channel with a spacing of 500 nm, to generate a set of parallel cross sections orthogonal to the spindle axis. The slicing procedure was already described in detail previously (*59*). The spindle axis was sliced for 12 µm in both directions from the centroid of the chromosome mass resulting in a total length of 24 µm. Each slice had a size 621x621 pixels, and the cross-section of the predicted spindle axis was used as a center of the slice. The average background intensity of the tubulin signal was determined and subtracted from the data before slicing to quantify the microtubule intensity. To determine the average background, the average intensity in a rim of 2 pixels-width, 8 pixels away from the boundary of the segmented spindle region was calculated. The total background subtracted tubulin intensity inside each slice was then plotted against the respective distance from the centroid of the chromosome mass (see Figure 18B-D). This intensity profile was further analyzed to extract parameters to describe the shape and total signal intensity and respective distribution of the two spindle halves.

First, the minimum (valley) between the two intensity maxima from the profile was calculated to define which parts of the profile belong to each individual spindle half. The total intensity of each spindle half was calculated by summing up the area under the intensity profile curve (AUC, Figure 18B). To estimate the width of intensity distribution of each spindle half, the intensity at the minimum was first subtracted from the full profile (indicated by the opaque area under distribution valley, Figure 18B). The full-width at half maximum (FWHM, Figure 18B) of the valley subtracted intensity distribution from each spindle half was subsequently calculated. Both parameters (total intensities and FWHMs of spindle halves) were normalized to the acentrosomal half for monocentrosomal spindles or to the half with the smaller value for bicentrosomal spindles (Figure 18E-F).

The length of each spindle half was determined from the respective part of the original intensity profile without subtracting the valley intensity (half length, Figure 18B). To this end, the distance between the valley and the other edge of the intensity distribution, represented

by the slice at the periphery of a spindle half, was calculated. The spindle edge/pole of each spindle half was detected by taking the peripheral position closest to the peak of the profile, where intensity value was below 10 % of the peak intensity. If all values were higher than 10 % of the maximum (n = 1), the furthest slice from the peak was taken as the periphery of the half. The spindle half lengths were also normalized either to the acentrosomal half (for monocentrosomal spindles) or to the shorter half (for bicentrosomal spindles) (Figure 18G).

4.2.7 Calculating distances from centrosomes to the spindle body and to chromosomes from IF data

To calculate the distance between centrosome and spindle body (d_1; Figure 17C), the axis between the centrosome and chromosome centroid was used as a reference for slicing the microtubule channel as described in section 4.2.6. In this case slicing along this axis was performed with a spacing of 200 nm, starting from the centrosome towards the chromosome centroid. An intensity profile along the axis was genereated by calculating the total intensity of each slice. First, the maximum and minimum intensity values were determined and then the minimum intensity was subtracted from the entire profile. The minimum subtracted profile of each spindle half was then analyzed starting from the centrosomal end. The periphery of the spindle half was defined as the last location in the profile, where the total intensity was less than 10 % of the maximum intensity. In addition to the distance between the manually annotated centrosome coordinates and the determined spindle body (d_1; Figure 17C-D), the distances between the centrosome and the chromosome centroid (d_3; Figure 17C, F) and between the chromosome centroid and the spindle body (d_2; Figure 17C) were calculated. The centrosome-spindle distance (d_1) was additionally normalized to the length of the respective spindle half (d_2) to quantify distance relations (d_1/d_2; Figure 17C, E).

4.2.8 Data transformation into 2D sections parallel to the centrosomal axis using EGFP-MAP4 and EB3-mEGFP2 fluorescence from live imaging

To display the kinetics of microtubule intensity (Figure 23A), 3D data was transformed and re-sliced orthogonally to the centrosomal axis so that both centrosomes were visible in the same 2D slice. Original anisotropic stacks were first interpolated along the z-direction to create isotropic 3D stacks. The interpolated data was then translated in xy so that the central point between two centrosomes moved to the center of the image. The angle between the

centrosomal axis (defined by the two centrosomes), and xy-plane was calculated and the translated stack was rotated such that the centrosomal axis aligned to the xy-plane. The angle between the centrosomal axis and the x-axis was calculated, and the data was further rotated to align the centrosomal axis to the original x-axis. During the rotation bicubic interpolation was used. All the data was transformed in the same way so that the kinetics of microtubule intensity at centrosomes as well as the center of the centrosome axis could be observed in the same 2D slice in consecutively acquired stacks.

4.2.9 Quantification of dynamic microtubule distribution of EGFP-MAP4 and EB3-mEGFP2 signal from live imaging

Microtubule signal intensity (EGFP-MAP4 or EB3-mEGFP2) was quantified along the centrosomal axis as defined by the two centrosomes. The central coordinates of the centrosomes were determined from manually segmented microtubule signal at centrosomes using arivis Vision4D by calculating the center of the signal intensities. Original anisotropic stacks were first interpolated along the z-direction to create isotropic 3D stacks and the microtubule intensity profile between the two centrosomes was generated. For each time point 15 equidistant parallel slices were generated between the two centrosomes. The slices were orthogonal to the centrosomal axis and the intersection point between the axis and the slice determined the center of each slice. Two different slice sizes were chosen for different purposes: Either slices of 351x351 pixels were used (black cuboid with solid line, Figure 23B) to determine the total microtubule mass along the centrosomal axis and within the entire spindle at a given time (Figure 23C and Figure 24A). Alternatively, the slice size was set to 15x15 pixels (black cuboid with dashed line, Figure 23B) to estimate the microtubule concentration along the centrosomal axis over time (Figure 23D and Figure 25A).

The distance between two centrosomes within one zygote as well as between different zygotes was not constant. To account for this, a fixed number of slices between two centrosomes was generated, thus normalizing the distances between two consecutive slices in different stacks relative to the intercentrosome distance. The total intensity of each slice was calculated and normalized to the maximum intensity considering all slices and all time points within a zygote. Due to the normalization of intensity and inter-slice distance the extracted intensity profiles can be compared within a zygote as well as between different zygotes. Hence, an average intensity profile (Figure 23C-D) over time and intensity change

over time at different landmarks, such as centrosomes and the center of the spindle (see Figure 23E-F and for individual plots Figure 24B and Figure 25B) could be computed using the data from all analyzed zygotes (n = 6).

5 REFERENCES

1. K. A. Knouse, J. Wu, C. A. Whittaker, A. Amon, Single cell sequencing reveals low levels of aneuploidy across mammalian tissues. *Proc. Natl. Acad. Sci.* **111**, 13409–13414 (2014).
2. A. Webster, M. Schuh, Mechanisms of Aneuploidy in Human Eggs. *Trends Cell Biol.* **27**, 55–68 (2017).
3. I. Schneider, J. Ellenberg, Mysteries in embryonic development: How can errors arise so frequently at the beginning of mammalian life? *PLOS Biol.* **17**, e3000173 (2019).
4. R. C. McCoy, Z. P. Demko, A. Ryan, M. Banjevic, M. Hill, S. Sigurjonsson, M. Rabinowitz, D. A. Petrov, Evidence of Selection against Complex Mitotic-Origin Aneuploidy during Preimplantation Development. *PLOS Genet.* **11**, e1005601 (2015).
5. D. Wells, J. D. A. Delhanty, Comprehensive chromosomal analysis of human preimplantation embryos using whole genome amplification and single cell comparative genomic hybridization. *Mol. Hum. Reprod.* **6**, 1055–1062 (2000).
6. E. Vanneste, T. Voet, C. Le Caignec, M. Ampe, P. Konings, C. Melotte, S. Debrock, M. Amyere, M. Vikkula, F. Schuit, J.-P. Fryns, G. Verbeke, T. D'Hooghe, Y. Moreau, J. R. Vermeesch, Chromosome instability is common in human cleavage-stage embryos. *Nat. Med.* **15**, 577–583 (2009).
7. A. Mertzanidou, L. Wilton, J. Cheng, C. Spits, E. Vanneste, Y. Moreau, J. R. Vermeesch, K. Sermon, Microarray analysis reveals abnormal chromosomal complements in over 70% of 14 normally developing human embryos. *Hum. Reprod.* **28**, 256–264 (2013).
8. T. H. Taylor, S. A. Gitlin, J. L. Patrick, J. L. Crain, J. M. Wilson, D. K. Griffin, The origin, mechanisms, incidence and clinical consequences of chromosomal mosaicism in humans. *Hum. Reprod. Update*. **20**, 571–581 (2014).
9. M. Vera-Rodriguez, S. L. Chavez, C. Rubio, R. A. Reijo Pera, C. Simon, Prediction model for aneuploidy in early human embryo development revealed by single-cell analysis. *Nat. Commun.* **6**, 1–14 (2015).
10. D. D. Daphnis, E. Fragouli, K. Economou, S. Jerkovic, I. L. Craft, J. D. A. Delhanty, J. C. Harper, Analysis of the evolution of chromosome abnormalities in human embryos from Day 3 to 5 using CGH and FISH. *Mol. Hum. Reprod.* **14**, 117–125 (2007).
11. J. van Echten-Arends, S. Mastenbroek, B. Sikkema-Raddatz, J. C. Korevaar, M. J. Heineman, F. van der Veen, S. Repping, Chromosomal mosaicism in human preimplantation embryos: A systematic review. *Hum. Reprod. Update*. **17**, 620–627 (2011).
12. E. Mantikou, K. M. Wong, S. Repping, S. Mastenbroek, Molecular origin of mitotic aneuploidies in preimplantation embryos. *Biochim. Biophys. Acta - Mol. Basis Dis.* **1822** (2012), pp. 1921–1930.
13. E. Fragouli, S. Alfarawati, K. Spath, D. Babariya, N. Tarozzi, A. Borini, D. Wells, Analysis of implantation and ongoing pregnancy rates following the transfer of mosaic diploid–aneuploid blastocysts. *Hum. Genet.* **136**, 805–819 (2017).
14. S. Munné, D. Wells, Detection of mosaicism at blastocyst stage with the use of high-resolution next-generation sequencing. *Fertil. Steril.* **107** (2017), pp. 1085–1091.
15. N. S. Macklon, J. P. M. Geraedts, B. C. J. M. Fauser, Conception to ongoing pregnancy: the "black box" of early pregnancy loss. *Hum. Reprod. Update*. **8**, 333–343 (2002).
16. E. Greco, M. G. Minasi, F. Fiorentino, Healthy Babies after Intrauterine Transfer of Mosaic

Aneuploid Blastocysts. *N. Engl. J. Med.* **373**, 2089–2090 (2015).

17. H. Bolton, S. J. L. Graham, N. Van der Aa, P. Kumar, K. Theunis, E. Fernandez Gallardo, T. Voet, M. Zernicka-Goetz, Mouse model of chromosome mosaicism reveals lineage-specific depletion of aneuploid cells and normal developmental potential. *Nat. Commun.* **7**, 11165 (2016).

18. S. Bowling, A. Di Gregorio, M. Sancho, S. Pozzi, M. Aarts, M. Signore, M. D. Schneider, J. P. M. Barbera, J. Gil, T. A. Rodríguez, P53 and mTOR signalling determine fitness selection through cell competition during early mouse embryonic development. *Nat. Commun.* **9**, 1763 (2018).

19. S. Singla, L. K. Iwamoto-Stohl, M. Zhu, M. Zernicka-Goetz, Autophagy-mediated apoptosis eliminates aneuploid cells in a mouse model of chromosome mosaicism. *Nat. Commun.* **11**, 1–15 (2020).

20. S. Munné, J. Blazek, M. Large, P. A. Martinez-Ortiz, H. Nisson, E. Liu, N. Tarozzi, A. Borini, A. Becker, J. Zhang, S. Maxwell, J. Grifo, D. Babariya, D. Wells, E. Fragouli, Detailed investigation into the cytogenetic constitution and pregnancy outcome of replacing mosaic blastocysts detected with the use of high-resolution next-generation sequencing. *Fertil. Steril.* **108**, 62-71.e8 (2017).

21. M. Vera-Rodriguez, C. Rubio, Assessing the true incidence of mosaicism in preimplantation embryos. *Fertil. Steril.* **107** (2017), pp. 1107–1112.

22. D. Zudova, O. Rezacova, S. Kubickova, J. Rubes, Aneuploidy detection in porcine embryos using fluorescence in situ hybridization. *Cytogenet. Genome Res.* **102**, 179–183 (2003).

23. C. Dupont, J. Segars, A. DeCherney, B. D. Bavister, D. R. Armant, C. A. Brenner, Incidence of chromosomal mosaicism in morphologically normal nonhuman primate preimplantation embryos. *Fertil. Steril.* **93**, 2545–2550 (2010).

24. M. Hornak, D. Kubicek, P. Broz, P. Hulinska, K. Hanzalova, D. Griffin, M. Machatkova, J. Rubes, Aneuploidy Detection and mtDNA Quantification in Bovine Embryos with Different Cleavage Onset Using a Next-Generation Sequencing-Based Protocol. *Cytogenet. Genome Res.* **150**, 60–67 (2016).

25. O. Tšuiko, M. Catteeuw, M. Zamani Esteki, A. Destouni, O. Bogado Pascottini, U. Besenfelder, V. Havlicek, K. Smits, A. Kurg, A. Salumets, T. D'Hooghe, T. Voet, A. Van Soom, J. Robert Vermeesch, Genome stability of bovine in vivo-conceived cleavage-stage embryos is higher compared to in vitro-produced embryos. *Hum. Reprod.* **32**, 2348–2357 (2017).

26. C. A. Shilton, A. Kahler, B. W. Davis, J. R. Crabtree, J. Crowhurst, A. J. McGladdery, D. C. Wathes, T. Raudsepp, A. M. de Mestre, Whole genome analysis reveals aneuploidies in early pregnancy loss in the horse. *Sci. Rep.* **10**, 1–12 (2020).

27. K. R. and P. W. B. Alberts, A. Johnson, J. Lewis, M. Raff, *Molecular Biology of the Cell* (Garland Science, ed. 6th, 2015).

28. A. W. Murray, Recycling the Cell Cycle: Cyclins Revisited. *Cell*. **116** (2004), pp. 221–234.

29. M. J. Solomon, J. W. Harper, J. Shuttleworth, CAK, the p34cdc2 activating kinase, contains a protein identical or closely related to p40MO15. *EMBO J.* **12**, 3133–3142 (1993).

30. C. L. Asbury, Anaphase A: Disassembling Microtubules Move Chromosomes toward Spindle Poles. *Biology (Basel).* **6** (2017), doi:10.3390/biology6010015.

31. J. M. Scholey, G. Civelekoglu-Scholey, I. Brust-Mascher, Anaphase B. *Biology (Basel).* **5** (2016), , doi:10.3390/biology5040051.

32. V. Joukov, A. De Nicolo, Aurora-PLK1 cascades as key signaling modules in the regulation of mitosis. *Sci. Signal.* **11**, eaar4195 (2018).

33. L. L. Parker, H. Piwnica-Worms, Inactivation of the p34cdc2-cyclin B complex by the human WEE1 tyrosine kinase. *Science (80-.).* **257**, 1955–1957 (1992).

34. F. Liu, J. J. Stanton, Z. Wu, H. Piwnica-Worms, The human Myt1 kinase preferentially phosphorylates Cdc2 on threonine 14 and localizes to the endoplasmic reticulum and Golgi complex. *Mol. Cell. Biol.* **17**, 571–583 (1997).

35. A. Kumagai, W. G. Dunphy, Purification and molecular cloning of Plx1, a Cdc25-regulatory kinase from Xenopus egg extracts. *Science (80-.).* **273**, 1377–1380 (1996).

36. O. Timofeev, O. Cizmecioglu, F. Settele, T. Kempf, I. Hoffmann, Cdc25 phosphatases are required for timely assembly of CDK1-cyclin B at the G2/M transition. *J. Biol. Chem.* **285**, 16978–16990 (2010).

37. N. Watanabe, H. Arai, Y. Nishihara, M. Taniguchi, N. Watanabe, T. Hunter, H. Osada, M-phase kinases induce phospho-dependent ubiquitination of somatic Wee1 by SCFβ-TrCP. *Proc. Natl. Acad. Sci. U. S. A.* **101**, 4419–4424 (2004).

38. F. Qi, Q. Chen, H. Chen, H. Yan, B. Chen, X. Xiang, C. Liang, Q. Yi, M. Zhang, H. Cheng, Z. Zhang, J. Huang, F. Wang, WAC Promotes Polo-like Kinase 1 Activation for Timely Mitotic Entry. *Cell Rep.* **24**, 546–556 (2018).

39. A. Seki, J. A. Coppinger, C. Y. Jang, J. R. Yates, G. Fang, Bora and the kinase Aurora A cooperatively activate the kinase Plk1 and control mitotic entry. *Science (80-.).* **320**, 1655–1658 (2008).

40. L. Macůrek, A. Lindqvist, D. Lim, M. A. Lampson, R. Klompmaker, R. Freire, C. Clouin, S. S. Taylor, M. B. Yaffe, R. H. Medema, Polo-like kinase-1 is activated by aurora A to promote checkpoint recovery. *Nature*. **455**, 119–123 (2008).

41. D. Kachaner, D. Garrido, H. Mehsen, K. Normandin, H. Lavoie, V. Archambault, Coupling of Polo kinase activation to nuclear localization by a bifunctional NLS is required during mitotic entry. *Nat. Commun.* **8** (2017), doi:10.1038/s41467-017-01876-8.

42. L. Gheghiani, D. Loew, B. Lombard, J. Mansfeld, O. Gavet, PLK1 Activation in Late G2 Sets Up Commitment to Mitosis. *Cell Rep.* **19**, 2060–2073 (2017).

43. A. Crncec, H. Hochegger, Triggering mitosis. *FEBS Lett.* **593**, 2868–2888 (2019).

44. J. Pines, Cubism and the cell cycle: The many faces of the APC/C. *Nat. Rev. Mol. Cell Biol.* **12**, 427–438 (2011).

45. R. Visintin, S. Prinz, A. Amon, CDC20 and CDH1: A family of substrate-specific activators of APC-dependent proteolysis. *Science (80-.).* **278**, 460–463 (1997).

46. C. M. Pfleger, E. Lee, M. W. Kirschner, Substrate recognition by the Cdc20 and Cdh1 components of the anaphase-promoting complex. *Genes Dev.* **15**, 2396–2407 (2001).

47. E. R. Kramer, N. Scheuringer, A. V Podtelejnikov, M. Mann, J. M. Peters, Mitotic regulation of the APC activator proteins CDC20 and CDH1. *Mol. Biol. Cell*. **11**, 1555–1569 (2000).

48. C. Alfieri, S. Zhang, D. Barford, Visualizing the complex functions and mechanisms of the anaphase promoting complex/cyclosome (APC/C). *Open Biol.* **7** (2017), doi:10.1098/rsob.170204.

49. R. Qiao, F. Weissmann, M. Yamaguchi, N. G. Brown, R. VanderLinden, R. Imre, M. A. Jarvis, M. R. Brunner, I. F. Davidson, G. Litos, D. Haselbach, K. Mechtler, H. Stark, B. A. Schulman, J. M. Peters, Mechanism of APC/CCDC20 activation by mitotic phosphorylation. *Proc. Natl. Acad. Sci. U. S. A.* **113**, E2570–E2578 (2016).

50. I. T. Foe, S. A. Foster, S. K. Cheung, S. Z. Deluca, D. O. Morgan, D. P. Toczyski, Ubiquitination of

Cdc20 by the APC occurs through an intramolecular mechanism. *Curr. Biol.* **21**, 1870–1877 (2011).

51. W. Flemming, *Zellsubstanz, Kern und Zelltheilung* (Verlag von F.C.W. Vogel, 1882).

52. G. Sauer, R. Körner, A. Hanisch, A. Ries, E. A. Nigg, H. H. W. Silljé, Proteome analysis of the human mitotic spindle. *Mol. Cell. Proteomics*. **4**, 35–43 (2005).

53. S. Inoué, E. D. Salmon, in *Collected Works of Shinya Inoue: Microscopes, Living Cells, and Dynamic Molecules* (2008), vol. 6, pp. 749–770.

54. A. S. Belmont, Mitotic chromosome structure and condensation. *Curr. Opin. Cell Biol.* **18** (2006), pp. 632–638.

55. N. Naumova, M. Imakaev, G. Fudenberg, Y. Zhan, B. R. Lajoie, L. A. Mirny, J. Dekker, Organization of the mitotic chromosome. *Science (80-.).* **342**, 948–953 (2013).

56. M. Kschonsak, C. H. Haering, Shaping mitotic chromosomes: From classical concepts to molecular mechanisms. *BioEssays*. **37**, 755–766 (2015).

57. Y. Kagami, M. Ono, K. Yoshida, Plk1 phosphorylation of CAP-H2 triggers chromosome condensation by condensin II at the early phase of mitosis. *Sci. Rep.* **7**, 1–12 (2017).

58. S. Abe, K. Nagasaka, Y. Hirayama, H. Kozuka-Hata, M. Oyama, Y. Aoyagi, C. Obuse, T. Hirota, The initial phase of chromosome condensation requires Cdk1-mediated phosphorylation of the CAP-D3 subunit of condensin II. *Genes Dev.* **25**, 863–874 (2011).

59. N. Walther, M. J. Hossain, A. Z. Politi, B. Koch, M. Kueblbeck, Ø. Ødegård-Fougner, M. Lampe, J. Ellenberg, A quantitative map of human Condensins provides new insights into mitotic chromosome architecture. *J. Cell Biol.* **217**, 2309–2328 (2018).

60. J. H. Gibcus, K. Samejima, A. Goloborodko, I. Samejima, N. Naumova, J. Nuebler, M. T. Kanemaki, L. Xie, J. R. Paulson, W. C. Earnshaw, L. A. Mirny, J. Dekker, A pathway for mitotic chromosome formation. *Science (80-.).* **359** (2018), doi:10.1126/science.aao6135.

61. J. R. Paulson, U. K. Laemmli, The structure of histone-depleted metaphase chromosomes. *Cell*. **12**, 817–828 (1977).

62. D. Gerlich, B. Koch, F. Dupeux, J. M. Peters, J. Ellenberg, Live-Cell Imaging Reveals a Stable Cohesin-Chromatin Interaction after but Not before DNA Replication. *Curr. Biol.* **16**, 1571–1578 (2006).

63. A. L. Lafont, J. Song, S. Rankin, Sororin cooperates with the acetyltransferase Eco2 to ensure DNA replication-dependent sister chromatid cohesion. *Proc. Natl. Acad. Sci. U. S. A.* **107**, 20364–20369 (2010).

64. R. Ladurner, E. Kreidl, M. P. Ivanov, H. Ekker, M. H. Idarraga-Amado, G. A. Busslinger, G. Wutz, D. A. Cisneros, J. Peters, Sororin actively maintains sister chromatid cohesion. *EMBO J.* **35**, 635–653 (2016).

65. T. Nishiyama, R. Ladurner, J. Schmitz, E. Kreidl, A. Schleiffer, V. Bhaskara, M. Bando, K. Shirahige, A. A. Hyman, K. Mechtler, J. M. Peters, Sororin mediates sister chromatid cohesion by antagonizing Wapl. *Cell*. **143**, 737–749 (2010).

66. I. C. Waizenegger, S. Hauf, A. Meinke, J. M. Peters, Two distinct pathways remove mammalian cohesin from chromosome arms in prophase and from centromeres in anaphase. *Cell*. **103**, 399–410 (2000).

67. T. Nishiyama, M. M. Sykora, P. J. Huis, K. Mechtler, J. M. Peters, Aurora B and Cdk1 mediate Wapl activation and release of acetylated cohesin from chromosomes by phosphorylating Sororin. *Proc. Natl. Acad. Sci. U. S. A.* **110**, 13404–13409 (2013).

68. C. Morales, A. Losada, Establishing and dissolving cohesion during the vertebrate cell cycle. *Curr. Opin. Cell Biol.* **52** (2018), pp. 51–57.

69. K. Nagasaka, M. J. Hossain, M. J. Roberti, J. Ellenberg, T. Hirota, Sister chromatid resolution is an intrinsic part of chromosome organization in prophase. *Nat. Cell Biol.* **18**, 692–699 (2016).

70. Z. Liang, D. Zickler, M. Prentiss, F. S. Chang, G. Witz, K. Maeshima, N. Kleckner, Chromosomes progress to metaphase in multiple discrete steps via global compaction/expansion cycles. *Cell*. **161**, 1124–1137 (2015).

71. A. M. Farcas, P. Uluocak, W. Helmhart, K. Nasmyth, Cohesin's Concatenation of Sister DNAs Maintains Their Intertwining. *Mol. Cell*. **44**, 97–107 (2011).

72. H. Liu, S. Rankin, H. Yu, Phosphorylation-enabled binding of SGO1-PP2A to cohesin protects sororin and centromeric cohesion during mitosis. *Nat. Cell Biol.* **15**, 40–49 (2013).

73. T. S. Kitajima, T. Sakuno, K. I. Ishiguro, S. I. Iemura, T. Natsume, S. A. Kawashima, Y. Watanabe, Shugoshin collaborates with protein phosphatase 2A to protect cohesin. *Nature*. **441**, 46–52 (2006).

74. L. Zhou, C. Liang, Q. Chen, Z. Zhang, B. Zhang, H. Yan, F. Qi, M. Zhang, Q. Yi, Y. Guan, X. Xiang, X. Zhang, S. Ye, F. Wang, The N-Terminal Non-Kinase-Domain-Mediated Binding of Haspin to Pds5B Protects Centromeric Cohesion in Mitosis. *Curr. Biol.* **27**, 992–1004 (2017).

75. R. C. C. Hengeveld, M. J. M. Vromans, M. Vleugel, M. A. Hadders, S. M. A. Lens, Inner centromere localization of the CPC maintains centromere cohesion and allows mitotic checkpoint silencing. *Nat. Commun.* **8**, 1–12 (2017).

76. F. Uhlmann, F. Lottspelch, K. Nasmyth, Sister-chromatid separation at anaphase onset is promoted by cleavage of the cohesin subunit Scc1. *Nature*. **400**, 37–42 (1999).

77. O. Stemmann, H. Zou, S. A. Gerber, S. P. Gygi, M. W. Kirschner, Dual Inhibition of Sister Chromatid Separation at Metaphase. *Cell*. **107**, 715–726 (2001).

78. S. Hellmuth, L. Gómez-H, A. M. Pendás, O. Stemmann, Securin-independent regulation of separase by checkpoint-induced shugoshin–MAD2. *Nature*. **580**, 536–541 (2020).

79. S. Cuylen, C. Blaukopf, A. Z. Politi, T. Muller-Reichert, B. Neumann, I. Poser, J. Ellenberg, A. A. Hyman, D. W. Gerlich, Ki-67 acts as a biological surfactant to disperse mitotic chromosomes. *Nature*. **535**, 308–312 (2016).

80. S. Cuylen-Haering, M. Petrovic, A. Hernandez-Armendariz, M. W. G. Schneider, M. Samwer, C. Blaukopf, L. J. Holt, D. W. Gerlich, Chromosome clustering by Ki-67 excludes cytoplasm during nuclear assembly. *Nature*. **587**, 285–290 (2020).

81. A. Musacchio, A. Desai, A molecular view of kinetochore assembly and function. *Biology (Basel).* **6**, 5 (2017).

82. K. L. McKinley, I. M. Cheeseman, The molecular basis for centromere identity and function. *Nat. Rev. Mol. Cell Biol.* **17**, 16–29 (2016).

83. T. Fukagawa, W. C. Earnshaw, The centromere: Chromatin foundation for the kinetochore machinery. *Dev. Cell*. **30**, 496–508 (2014).

84. M. E. Pesenti, J. R. Weir, A. Musacchio, Progress in the structural and functional characterization of kinetochores. *Curr. Opin. Struct. Biol.* **37**, 152–163 (2016).

85. J. K. Monda, I. M. Cheeseman, The kinetochore–microtubule interface at a glance. *J. Cell Sci.* **131**, jcs214577 (2018).

86. M. Hara, T. Fukagawa, Kinetochore assembly and disassembly during mitotic entry and exit.

Curr. Opin. Cell Biol. **52**, 73–81 (2018).

87. I. M. Cheeseman, J. S. Chappie, E. M. Wilson-Kubalek, A. Desai, The Conserved KMN Network Constitutes the Core Microtubule-Binding Site of the Kinetochore. *Cell*. **127**, 983–997 (2006).

88. G. Itoh, M. Ikeda, K. Iemura, M. A. Amin, S. Kuriyama, M. Tanaka, N. Mizuno, H. Osakada, T. Haraguchi, K. Tanaka, Lateral attachment of kinetochores to microtubules is enriched in prometaphase rosette and facilitates chromosome alignment and bi-orientation establishment. *Sci. Rep.* **8**, 3888 (2018).

89. D. K. Cheerambathur, R. Gassmann, B. Cook, K. Oegema, A. Desai, Crosstalk between microtubule attachment complexes ensures accurate chromosome segregation. *Science (80-.).* **342**, 1239–1242 (2013).

90. E. A. Foley, T. M. Kapoor, Microtubule attachment and spindle assembly checkpoint signalling at the kinetochore. *Nat. Rev. Mol. Cell Biol.* **14** (2013), pp. 25–37.

91. V. Sudakin, G. K. T. Chan, T. J. Yen, Checkpoint inhibition of the APC/C in HeLa cells is mediated by a complex of BUBR1, BUB3, CDC20, and MAD2. *J. Cell Biol.* **154**, 925–936 (2001).

92. A. C. Faesen, M. Thanasoula, S. Maffini, C. Breit, F. Müller, S. Van Gerwen, T. Bange, A. Musacchio, Basis of catalytic assembly of the mitotic checkpoint complex. *Nature*. **542**, 498–502 (2017).

93. C. Alfieri, L. Chang, Z. Zhang, J. Yang, S. Maslen, M. Skehel, D. Barford, Molecular basis of APC/C regulation by the spindle assembly checkpoint. *Nature*. **536**, 431–436 (2016).

94. D. Izawa, J. Pines, The mitotic checkpoint complex binds a second CDC20 to inhibit active APC/C. *Nature*. **517**, 631–634 (2015).

95. R. C. Weisenberg, G. G. Borisy, E. W. Taylor, The Colchicine-Binding Protein of Mammalian Brain and Its Relation to Microtubules. *Biochemistry*. **7**, 4466–4479 (1968).

96. J. Roostalu, T. Surrey, Microtubule nucleation: beyond the template. *Nat. Rev. Mol. Cell Biol.* **18**, 702–710 (2017).

97. L. Amos, A. Klug, Arrangement of subunits in flagellar microtubules. *J. Cell Sci.* **14**, 523–49 (1974).

98. T. J. Mitchison, Localization of an exchangeable GTP binding site at the plus end of microtubules. *Science (80-.).* (1993), doi:10.1126/science.8102497.

99. G. J. Brouhard, L. M. Rice, Microtubule dynamics: An interplay of biochemistry and mechanics. *Nat. Rev. Mol. Cell Biol.* **19** (2018), pp. 451–463.

100. L. Schaedel, K. John, J. Gaillard, M. V. Nachury, L. Blanchoin, M. Thery, Microtubules self-repair in response to mechanical stress. *Nat. Mater.* (2015), doi:10.1038/nmat4396.

101. L. Schaedel, S. Triclin, D. Chrétien, A. Abrieu, C. Aumeier, J. Gaillard, L. Blanchoin, M. Théry, K. John, Lattice defects induce microtubule self-renewal. *Nat. Phys.* **15**, 830–838 (2019).

102. T. Mitchison, M. Kirschner, Dynamic instability of microtubule growth. *Nature*. **312**, 237–242 (1984).

103. M. F. Carlier, D. Pantaloni, Kinetic Analysis of Guanosine 5’-Triphosphate Hydrolysis Associated with Tubulin Polymerization. *Biochemistry* (1981), doi:10.1021/bi00510a030.

104. T. David-Pfeuty, H. P. Erickson, D. Pantaloni, Guanosinetriphosphatase activity of tubulin associated with microtubule assembly. *Proc. Natl. Acad. Sci. U. S. A.* **74**, 5372–6 (1977).

105. A. A. Hyman, D. Chrétien, I. Arnal, R. H. Wade, Structural changes accompanying GTP hydrolysis in microtubules: information from a slowly hydrolyzable analogue guanylyl-(alpha,beta)-

methylene-diphosphonate. *J. Cell Biol.* **128**, 117–125 (1995).

106. G. M. Alushin, G. C. Lander, E. H. Kellogg, R. Zhang, D. Baker, E. Nogales, High-Resolution Microtubule Structures Reveal the Structural Transitions in αβ-Tubulin upon GTP Hydrolysis. *Cell*. **157**, 1117–1129 (2014).

107. E. M. Mandelkow, E. Mandelkow, R. A. Milligan, Microtubule dynamics and microtubule caps: A time-resolved cryo-electron microscopy study. *J. Cell Biol.* **114**, 977–991 (1991).

108. D. Chrétien, S. D. Fuller, E. Karsenti, Structure of growing microtubule ends: Two-dimensional sheets close into tubes at variable rates. *J. Cell Biol.* **129**, 1311–1328 (1995).

109. T. L. Hill, M. F. Carlier, Steady-state theory of the interference of GTP hydrolysis in the mechanism of microtubule assembly. *Proc. Natl. Acad. Sci. U. S. A.* **80**, 7234–7238 (1983).

110. M. F. Carlier, T. L. Hill, Y. D. Chen, Interference of GTP hydrolysis in the mechanism of microtubule assembly: An experimental study. *Proc. Natl. Acad. Sci. U. S. A.* **81**, 771–775 (1984).

111. R. A. Walker, E. T. O'Brien, N. K. Pryer, M. F. Soboeiro, W. A. Voter, H. P. Erickson, E. D. Salmon, Dynamic instability of individual microtubules analyzed by video light microscopy: rate constants and transition frequencies. *J. Cell Biol.* **107**, 1437–1448 (1988).

112. M. K. Gardner, B. D. Charlebois, I. M. Jánosi, J. Howard, A. J. Hunt, D. J. Odde, Rapid microtubule self-assembly kinetics. *Cell* (2011), doi:10.1016/j.cell.2011.06.053.

113. C. Aumeier, L. Schaedel, J. Gaillard, K. John, L. Blanchoin, M. Théry, Self-repair promotes microtubule rescue. *Nat. Cell Biol.* **18**, 1054–1064 (2016).

114. H. de Forges, A. Pilon, I. Cantaloube, A. Pallandre, A. M. Haghiri-Gosnet, F. Perez, C. Poüs, Localized Mechanical Stress Promotes Microtubule Rescue. *Curr. Biol.* **26**, 3399–3406 (2016).

115. G. Goshima, R. Wollman, S. S. Goodwin, N. Zhang, J. M. Scholey, R. D. Vale, N. Stuurman, Genes required for mitotic spindle assembly in Drosophila S2 cells. *Science (80-.).* **316**, 417–421 (2007).

116. J. R. Hughes, A. M. Meireles, K. H. Fisher, A. Garcia, P. R. Antrobus, A. Wainman, N. Zitzmann, C. Deane, H. Ohkura, J. G. Wakefield, A Microtubule Interactome: Complexes with Roles in Cell Cycle and Mitosis. *PLoS Biol.* **6**, e98 (2008).

117. J. R. A. Hutchins, Y. Toyoda, B. Hegemann, I. Poser, J. K. Hériché, M. M. Sykora, M. Augsburg, O. Hudecz, B. A. Buschhorn, J. Bulkescher, C. Conrad, D. Comartin, A. Schleiffer, M. Sarov, A. Pozniakovsky, M. M. Slabicki, S. Schloissnig, I. Steinmacher, M. Leuschner, A. Ssykor, S. Lawo, L. Pelletier, H. Stark, K. Nasmyth, J. Ellenberg, R. Durbin, F. Buchholz, K. Mechtler, A. A. Hyman, J. M. Peters, Systematic analysis of human protein complexes identifies chromosome segregation proteins. *Science (80-.).* **328**, 593–599 (2010).

118. S. L. Reck-Peterson, W. B. Redwine, R. D. Vale, A. P. Carter, The cytoplasmic dynein transport machinery and its many cargoes. *Nat. Rev. Mol. Cell Biol.* **19**, 382–398 (2018).

119. R. J. McKenney, W. Huynh, M. E. Tanenbaum, G. Bhabha, R. D. Vale, Activation of cytoplasmic dynein motility by dynactin-cargo adapter complexes. *Science (80-.).* **345**, 337–341 (2014).

120. J. P. I. Welburn, The molecular basis for kinesin functional specificity during mitosis. *Cytoskeleton*. **70**, 476–493 (2013).

121. N. Hirokawa, Y. Noda, Y. Tanaka, S. Niwa, Kinesin superfamily motor proteins and intracellular transport. *Nat. Rev. Mol. Cell Biol.* **10**, 682–696 (2009).

122. D. Vanneste, V. Ferreira, I. Vernos, Chromokinesins: Localization-dependent functions and regulation during cell division. *Biochem. Soc. Trans.* **39**, 1154–1160 (2011).

123. M. E. Tanenbaum, R. D. Vale, R. J. McKenney, Cytoplasmic dynein crosslinks and slides anti-parallel microtubules using its two motor domains. *Elife*. **2** (2013), doi:10.7554/eLife.00943.

124. L. C. Kapitein, E. J. G. Peterman, B. H. Kwok, J. H. Kim, T. M. Kapoor, C. F. Schmidt, The bipolar mitotic kinesin Eg5 moves on both microtubules that it crosslinks. *Nature*. **435**, 114–118 (2005).

125. H. Drechsler, T. McHugh, M. R. Singleton, N. J. Carter, A. D. McAinsh, The Kinesin-12 Kif15 is a processive track-switching tetramer. *Elife*. **2014**, 1–17 (2014).

126. P. Bieling, I. A. Telley, T. Surrey, A minimal midzone protein module controls formation and length of antiparallel microtubule overlaps. *Cell*. **142**, 420–432 (2010).

127. R. Subramanian, T. M. Kapoor, Building Complexity: Insights into Self-Organized Assembly of Microtubule-Based Architectures. *Dev. Cell*. **23** (2012), pp. 874–885.

128. C. Duellberg, M. Trokter, R. Jha, I. Sen, M. O. Steinmetz, T. Surrey, Reconstitution of a hierarchical +TIP interaction network controlling microtubule end tracking of dynein. *Nat. Cell Biol.* **16**, 804–811 (2014).

129. A. Akhmanova, M. O. Steinmetz, Control of microtubule organization and dynamics: two ends in the limelight. *Nat. Rev. Mol. Cell Biol.* **16**, 711–726 (2015).

130. M. C. Hendershott, R. D. Vale, Regulation of microtubule minus-end dynamics by CAMSAPs and Patronin. *Proc. Natl. Acad. Sci. U. S. A.* **111**, 5860–5865 (2014).

131. K. Jiang, S. Hua, R. Mohan, I. Grigoriev, K. W. Yau, Q. Liu, E. A. Katrukha, A. F. M. Altelaar, A. J. R. Heck, C. C. Hoogenraad, A. Akhmanova, Microtubule Minus-End Stabilization by Polymerization-Driven CAMSAP Deposition. *Dev. Cell*. **28**, 295–309 (2014).

132. N. Tanaka, W. Meng, S. Nagae, M. Takeichi, Nezha/CAMSAP3 and CAMSAP2 cooperate in epithelial-specific organization of noncentrosomal microtubules. *Proc. Natl. Acad. Sci. U. S. A.* **109**, 20029–20034 (2012).

133. S. Meunier, I. Vernos, K-fibre minus ends are stabilized by a RanGTP-dependent mechanism essential for functional spindle assembly. *Nat. Cell Biol.* **13**, 1406–1414 (2011).

134. S. Meunier, M. Shvedunova, N. Van Nguyen, L. Avila, I. Vernos, A. Akhtar, An epigenetic regulator emerges as microtubule minus-end binding and stabilizing factor in mitosis. *Nat. Commun.* **6**, 1–10 (2015).

135. G. J. Brouhard, L. M. Rice, The contribution of αβ-tubulin curvature to microtubule dynamics. *J. Cell Biol.* **207**, 323–334 (2014).

136. C. T. Friel, J. Howard, The kinesin-13 MCAK has an unconventional ATPase cycle adapted for microtubule depolymerization. *EMBO J.* **30**, 3928–3939 (2011).

137. P. Ayaz, S. Munyoki, E. A. Geyer, F. A. Piedra, E. S. Vu, R. Bromberg, Z. Otwinowski, N. V. Grishin, C. A. Brautigam, L. M. Rice, A tethered delivery mechanism explains the catalytic action of a microtubule polymerase. *Elife*. **3**, 1–19 (2014).

138. F. J. McNally, A. Roll-Mecak, Microtubule-severing enzymes: From cellular functions to molecular mechanism. *J. Cell Biol.* **217**, 4057–4069 (2018).

139. J. J. Hartman, J. Mahr, K. McNally, K. Okawa, A. Iwamatsu, S. Thomas, S. Cheesman, J. Heuser, R. D. Vale, F. J. McNally, Katanin, a Microtubule-Severing Protein, Is a Novel AAA ATPase that Targets to the Centrosome Using a WD40-Containing Subunit. *Cell*. **93**, 277–287 (1998).

140. F. J. McNally, R. D. Vale, Identification of katanin, an ATPase that severs and disassembles stable microtubules. *Cell*. **75**, 419–429 (1993).

141. Y. Zheng, M. K. Jung, B. R. Oakley, γ-Tubulin is present in Drosophila melanogaster and homo

sapiens and is associated with the centrosome. *Cell*. **65**, 817–823 (1991).

142. T. Stearns, L. Evans, M. Kirschner, γ-Tubulin is a highly conserved component of the centrosome. *Cell*. **65**, 825–836 (1991).

143. N. Lecland, J. Lüders, The dynamics of microtubule minus ends in the human mitotic spindle. *Nat. Cell Biol.* **16**, 770–778 (2014).

144. J. M. Kollman, A. Merdes, L. Mourey, D. A. Agard, Microtubule nucleation by γ-tubulin complexes. *Nat. Rev. Mol. Cell Biol.* **12** (2011), pp. 709–721.

145. J. M. Kollman, J. K. Polka, A. Zelter, T. N. Davis, D. A. Agard, Microtubule nucleating γ 3-TuSC assembles structures with 13-fold microtubule-like symmetry. *Nature*. **466**, 879–882 (2010).

146. P. Liu, E. Zupa, A. Neuner, A. Böhler, J. Loerke, D. Flemming, T. Ruppert, T. Rudack, C. Peter, C. Spahn, O. J. Gruss, S. Pfeffer, E. Schiebel, Insights into the assembly and activation of the microtubule nucleator γ-TuRC. *Nature*. **578**, 467–471 (2020).

147. T. Mitchison, M. Kirschner, Microtubule assembly nucleated by isolated centrosomes. *Nature*. **312**, 232–237 (1984).

148. A. D. Sanchez, J. L. Feldman, Microtubule-organizing centers: from the centrosome to non-centrosomal sites. *Curr. Opin. Cell Biol.* **44** (2017), pp. 93–101.

149. L. Evans, T. Mitchison, M. Kirschner, Influence of the centrosome on the structure of nucleated microtubules. *J. Cell Biol.* **100**, 1185–1191 (1985).

150. P. Guichard, V. Hamel, P. Gönczy, The Rise of the Cartwheel: Seeding the Centriole Organelle. *BioEssays*. **40**, 1700241 (2018).

151. R. Gould, G. Borisy, The pericentriolar material in Chinese hamster ovary cells nucleates microtubule formation. *J. Cell Biol.* **73**, 601–615 (1977).

152. A. Dammermann, T. Müller-Reichert, L. Pelletier, B. Habermann, A. Desai, K. Oegema, Centriole assembly requires both centriolar and pericentriolar material proteins. *Dev. Cell*. **7**, 815–829 (2004).

153. J. Loncarek, P. Hergert, V. Magidson, A. Khodjakov, Control of daughter centriole formation by the pericentriolar material. *Nat. Cell Biol.* **10**, 322–328 (2008).

154. A. Pimenta-Marques, M. Bettencourt-Dias, Pericentriolar material. *Curr. Biol.* **30**, R687–R689 (2020).

155. N. J. Ganem, S. a Godinho, D. Pellman, A mechanism linking extra centrosomes to chromosomal instability. *Nature*. **460**, 278–82 (2009).

156. P. Gönczy, Centrosomes and cancer: Revisiting a long-standing relationship. *Nat. Rev. Cancer*. **15**, 639–652 (2015).

157. E. A. Nigg, T. Stearns, The centrosome cycle: Centriole biogenesis, duplication and inherent asymmetries. *Nat. Cell Biol.* **13** (2011), pp. 1154–1160.

158. M. Bornens, The centrosome in cells and organisms. *Science (80-.).* **335** (2012), pp. 422–426.

159. E. A. Nigg, A. J. Holland, Once and only once: Mechanisms of centriole duplication and their deregulation in diseases. *Nat. Rev. Mol. Cell Biol.* **19** (2018), pp. 297–312.

160. D. Kitagawa, I. Vakonakis, N. Olieric, M. Hilbert, D. Keller, V. Olieric, M. Bortfeld, M. C. Erat, I. Flückiger, P. Gönczy, M. O. Steinmetz, Structural basis of the 9-fold symmetry of centrioles. *Cell*. **144**, 364–375 (2011).

161. M. Van Breugel, M. Hirono, A. Andreeva, H. A. Yanagisawa, S. Yamaguchi, Y. Nakazawa, N. Morgner, M. Petrovich, I. O. Ebong, C. V. Robinson, C. M. Johnson, D. Veprintsev, B. Zuber,

Structures of SAS-6 suggest its organization in centrioles. *Science (80-.).* **331**, 1196–1199 (2011).

162. D. Keller, M. Orpinell, N. Olivier, M. Wachsmuth, R. Mahen, R. Wyss, V. Hachet, J. Ellenberg, S. Manley, P. Gönczy, Mechanisms of HsSAS-6 assembly promoting centriole formation in human cells. *J. Cell Biol.* **204**, 697–712 (2014).

163. P. Guichard, A. Desfosses, A. Maheshwari, V. Hachet, C. Dietrich, A. Brune, T. Ishikawa, C. Sachse, P. Gönczy, Cartwheel architecture of Trichonympha basal body. *Science (80-.).* **337** (2012), p. 553.

164. T. I. Schmidt, J. Kleylein-Sohn, J. Westendorf, M. Le Clech, S. B. Lavoie, Y. D. Stierhof, E. A. Nigg, Control of Centriole Length by CPAP and CP110. *Curr. Biol.* **19**, 1005–1011 (2009).

165. A. Khodjakov, C. L. Rieder, G. Sluder, G. Cassels, O. Sibon, C. L. Wang, De novo formation of centrosomes in vertebrate cells arrested during S phase. *J. Cell Biol.* **158**, 1171–1181 (2002).

166. S. La Terra, C. N. English, P. Hergert, B. F. McEwen, G. Sluder, A. Khodjakov, The de novo centriole assembly pathway in HeLa cells: Cell cycle progression and centriole assembly/maturation. *J. Cell Biol.* **168**, 713–722 (2005).

167. A. M. Fry, J. Sampson, C. Shak, S. Shackleton, Recent advances in pericentriolar material organization: ordered layers and scaffolding gels. *F1000Research*. **6**, 1622 (2017).

168. S. Lawo, M. Hasegan, G. D. Gupta, L. Pelletier, Subdiffraction imaging of centrosomes reveals higher-order organizational features of pericentriolar material. *Nat. Cell Biol.* **14**, 1148–1158 (2012).

169. K. F. Sonnen, L. Schermelleh, H. Leonhardt, E. A. Nigg, 3D-structured illumination microscopy provides novel insight into architecture of human centrosomes. *Biol. Open*. **1**, 965–976 (2012).

170. V. Mennella, B. Keszthelyi, K. L. Mcdonald, B. Chhun, F. Kan, G. C. Rogers, B. Huang, D. A. Agard, Subdiffraction-resolution fluorescence microscopy reveals a domain of the centrosome critical for pericentriolar material organization. *Nat. Cell Biol.* **14**, 1159–1168 (2012).

171. J. Fu, D. M. Glover, Structured illumination of the interface between centriole and peri-centriolar material. *Open Biol.* **2**, 120104 (2012).

172. J. B. Woodruff, B. Ferreira Gomes, P. O. Widlund, J. Mahamid, A. Honigmann, A. A. Hyman, The Centrosome Is a Selective Condensate that Nucleates Microtubules by Concentrating Tubulin. *Cell*. **169**, 1066–1077 (2017).

173. K. Lee, K. Rhee, PLK1 phosphorylation of pericentrin initiates centrosome maturation at the onset of mitosis. *J. Cell Biol.* **195**, 1093–101 (2011).

174. M. A. Gomez-Ferreria, U. Rath, D. W. Buster, S. K. Chanda, J. S. Caldwell, D. R. Rines, D. J. Sharp, Human Cep192 Is Required for Mitotic Centrosome and Spindle Assembly. *Curr. Biol.* **17**, 1960–1966 (2007).

175. L. Haren, T. Stearns, J. Lüders, Plk1-Dependent Recruitment of γ-Tubulin Complexes to Mitotic Centrosomes Involves Multiple PCM Components. *PLoS One*. **4**, e5976 (2009).

176. S. R. Norris, R. Ohi, Cell Division: Centrosomes Have Separation Anxiety. *Curr. Biol.* **27**, R601–R603 (2017).

177. J. Decarreau, M. Wagenbach, E. Lynch, A. R. Halpern, J. C. Vaughan, J. Kollman, L. Wordeman, The tetrameric kinesin Kif25 suppresses pre-mitotic centrosome separation to establish proper spindle orientation. *Nat. Cell Biol.* **19**, 384–390 (2017).

178. J. A. Raaijmakers, R. G. H. P. Van Heesbeen, J. L. Meaders, E. F. Geers, B. Fernandez-Garcia, R. H. Medema, M. E. Tanenbaum, Nuclear envelope-associated dynein drives prophase

centrosome separation and enables Eg5-independent bipolar spindle formation. *EMBO J.* **31**, 4179–4190 (2012).

179. Z. Jahed, M. Soheilypour, M. Peyro, M. R. K. Mofrad, The LINC and NPC relationship - it's complicated! *J. Cell Sci.* **129**, 3219–3229 (2016).

180. D. Szollosi, P. Calarco, R. P. Donahue, Absence of centrioles in the first and second meiotic spindles of mouse oocytes. *J. Cell Sci.* **11**, 521–541 (1972).

181. A. H. Sathananthan, K. Selvaraj, M. Lakshmi Girijashankar, V. Ganesh, P. Selvaraj, A. O. Trounson, From oogonia to mature oocytes: Inactivation of the maternal centrosome in humans. *Microsc. Res. Tech.* **69**, 396–407 (2006).

182. A. Pimenta-Marques, I. Bento, C. A. M. Lopes, P. Duarte, S. C. Jana, M. Bettencourt-Dias, A mechanism for the elimination of the female gamete centrosome in Drosophila melanogaster. *Science (80-.).* **353**, aaf4866 (2016).

183. T. Mikeladze-Dvali, L. von Tobel, P. Strnad, G. Knott, H. Leonhardt, L. Schermelleh, P. Gönczy, Analysis of centriole elimination during C. elegans oogenesis. *Development*. **139**, 1670–1679 (2012).

184. C. Simerly, M. Manil-Ségalen, C. Castro, C. Hartnett, D. Kong, M. H. Verlhac, J. Loncarek, G. Schatten, Separation and Loss of Centrioles From Primordidal Germ Cells To Mature Oocytes In The Mouse. *Sci. Rep.* **8**, 1–17 (2018).

185. M. Schuh, J. Ellenberg, Self-Organization of MTOCs Replaces Centrosome Function during Acentrosomal Spindle Assembly in Live Mouse Oocytes. *Cell*. **130**, 484–498 (2007).

186. I. W. Lee, Y. J. Jo, S. M. Jung, H. Y. Wang, N. H. Kim, S. Namgoong, Distinct roles of Cep192 and Cep152 in acentriolar MTOCs and spindle formation during mouse oocyte maturation. *FASEB J.* (2018), doi:10.1096/fj.201700559RR.

187. W. Ma, M. M. Viveiros, Depletion of pericentrin in mouse oocytes disrupts microtubule organizing center function and meiotic spindle organization. *Mol. Reprod. Dev.* **81**, 1019–1029 (2014).

188. C. Baumann, X. Wang, L. Yang, M. M. Viveiros, Error-prone meiotic division and subfertility in mice with oocyte-conditional knockdown of pericentrin. *J. Cell Sci.* **130**, 1251–1262 (2017).

189. C. Wiese, Y. Zheng, A new function for the γ-tubulin ring complex as a microtubule minus-end cap. *Nat. Cell Biol.* **2**, 358–364 (2000).

190. M. M. Mogensen, A. Malik, M. Piel, V. Boukson-Castaing, M. Bornens, Microtubule minus-end anchorage at Centrosomal and non-centrosomal sites: The role of ninein. *J. Cell Sci.* **113**, 3013–3023 (2000).

191. M. Takahashi, A. Yamagiwa, T. Nishimura, H. Mukai, Y. Ono, Centrosomal proteins CG-NAP and kendrin provide microtubule nucleation sites by anchoring γ-tubulin ring complex. *Mol. Biol. Cell*. **13**, 3235–3245 (2002).

192. W. C. Zimmerman, J. Sillibourne, J. Rosa, S. J. Doxsey, Mitosis-specific anchoring of γ tubulin complexes by pericentrin controls spindle organization and mitotic entry. *Mol. Biol. Cell*. **15**, 3642–3657 (2004).

193. G. Goshima, M. Mayer, N. Zhang, N. Stuurman, R. D. Vale, Augmin: A protein complex required for centrosome-independent microtubule generation within the spindle. *J. Cell Biol.* **181**, 421–429 (2008).

194. S. Petry, A. C. Groen, K. Ishihara, T. J. Mitchison, R. D. Vale, Branching microtubule nucleation in xenopus egg extracts mediated by augmin and TPX2. *Cell*. **152**, 768–777 (2013).

195. A. Thawani, H. A. Stone, J. W. Shaevitz, S. Petry, Spatiotemporal organization of branched microtubule networks. *Elife*. **8** (2019), doi:10.7554/eLife.43890.

196. A. Muroyama, L. Seldin, T. Lechler, Divergent regulation of functionally distinct γ-tubulin complexes during differentiation. *J. Cell Biol.* **213**, 679–692 (2016).

197. M. Toya, S. Kobayashi, M. Kawasaki, G. Shioi, M. Kaneko, T. Ishiuchi, K. Misaki, W. Meng, M. Takeichi, CAMSAP3 orients the apical-to-basal polarity of microtubule arrays in epithelial cells. *Proc. Natl. Acad. Sci. U. S. A.* **113**, 332–337 (2016).

198. S. Dumont, T. J. Mitchison, Force and Length in the Mitotic Spindle. *Curr. Biol.* **19**, R749–R761 (2009).

199. R. B. Nicklas, D. F. Kubai, Microtubules, chromosome movement, and reorientation after chromosomes are detached from the spindle by micromanipulation. *Chromosoma*. **92**, 313–324 (1985).

200. G. C. Rogers, S. L. Rogers, D. J. Sharp, Spindle microtubules in flux Commentary. *J. Cell Sci.* **118**, 1105–1116 (2005).

201. V. Sikirzhytski, V. Magidson, J. B. Steinman, J. He, M. Le Berre, I. Tikhonenko, J. G. Ault, B. F. McEwen, J. K. Chen, H. Sui, M. Piel, T. M. Kapoor, A. Khodjakov, Direct kinetochore-spindle pole connections are not required for chromosome segregation. *J. Cell Biol.* **206**, 231–243 (2014).

202. R. A. Heil-Chapdelaine, N. R. Adames, J. A. Cooper, Formin' the Connection between Microtubules and the Cell Cortex. *J. Cell Biol.* **144**, 809–811 (1999).

203. K.-F. Tseng, M. Foss, D. Zhang, Astral microtubules physically redistribute cortical actin filaments to the incipient contractile ring. *Cytoskeleton*. **69**, 983–991 (2012).

204. S. Bonaccorsi, M. G. Giansanti, M. Gatti, Spindle assembly in Drosophila neuroblasts and ganglion mother cells. *Nat. Cell Biol.* **2**, 54–56 (2000).

205. S. Busson, D. Dujardin, A. Moreau, J. Dompierre, J. R. De Mey, Dynein and dynactin are localized to astral microtubules and at cortical sites in mitotic epithelial cells. *Curr. Biol.* **8**, 541–544 (1998).

206. N. P. Ferenz, R. Paul, C. Fagerstrom, A. Mogilner, P. Wadsworth, Dynein Antagonizes Eg5 by Crosslinking and Sliding Antiparallel Microtubules. *Curr. Biol.* **19**, 1833–1838 (2009).

207. C. K. Hu, M. Coughlin, C. M. Field, T. J. Mitchison, KIF4 regulates midzone length during cytokinesis. *Curr. Biol.* **21**, 815–824 (2011).

208. J. Hannabuss, M. Lera-Ramirez, N. I. Cade, F. J. Fourniol, F. Nédélec, T. Surrey, Self-Organization of Minimal Anaphase Spindle Midzone Bundles. *Curr. Biol.* **29**, 2120-2130.e7 (2019).

209. J. Kajtez, A. Solomatina, M. Novak, B. Polak, K. Vukušić, J. Rüdiger, G. Cojoc, A. Milas, I. Šumanovac Šestak, P. Risteski, F. Tavano, A. H. Klemm, E. Roscioli, J. Welburn, D. Cimini, M. Glunčić, N. Pavin, I. M. Tolić, Overlap microtubules link sister k-fibres and balance the forces on bi-oriented kinetochores. *Nat. Commun.* **7**, 10298 (2016).

210. S. Petry, Mechanisms of Mitotic Spindle Assembly. *Annu. Rev. Biochem.* **85**, 659–683 (2016).

211. L. D. Belmont, A. A. Hyman, K. E. Sawin, T. J. Mitchison, Real-time visualization of cell cycle-dependent changes in microtubule dynamics in cytoplasmic extracts. *Cell*. **62**, 579–589 (1990).

212. F. Verde, M. Dogterom, E. Stelzer, E. Karsenti, S. Leibler, Control of microtubule dynamics and length by cyclin A- and cyclin B-dependent kinases in Xenopus egg extracts. *J. Cell Biol.* **118**, 1097–1108 (1992).

213. M. Kirschner, T. Mitchison, Beyond self-assembly: From microtubules to morphogenesis. *Cell*.

45 (1986), pp. 329–342.

214. R. Heald, A. Khodjakov, Thirty years of search and capture: The complex simplicity of mitotic spindle assembly. *J. Cell Biol.* **211**, 1103–1111 (2015).

215. J. S. Tirnauer, E. D. Salmon, T. J. Mitchison, Microtubule Plus-End Dynamics in Xenopus Egg Extract Spindles. *Mol. Biol. Cell*. **15**, 1776–1784 (2004).

216. R. Heald, R. Tournebize, T. Blank, R. Sandaltzopoulos, P. Becker, A. Hyman, E. Karsenti, Self-organization of microtubules into bipolar spindles around artificial chromosomes in Xenopus egg extracts. *Nature*. **382**, 420–425 (1996).

217. N. M. Mahoney, G. Goshima, A. D. Douglass, R. D. Vale, Making microtubules and mitotic spindles in cells without functional centrosomes. *Curr. Biol.* **16**, 564–569 (2006).

218. K. S. Burbank, A. C. Groen, Z. E. Perlman, D. S. Fisher, T. J. Mitchison, A new method reveals microtubule minus ends throughout the meiotic spindle. *J. Cell Biol.* **175**, 369–375 (2006).

219. D. J. Needleman, A. Groen, R. Ohi, T. Maresca, L. Mirny, T. Mitchison, Fast microtubule dynamics in meiotic spindles measured by single molecule imaging: Evidence that the spindle environment does not stabilize microtubules. *Mol. Biol. Cell*. **21**, 323–333 (2010).

220. A. Khodjakov, L. Copenagle, M. B. Gordon, D. A. Compton, T. M. Kapoor, Minus-end capture of preformed kinetochore fibers contributes to spindle morphogenesis. *J. Cell Biol.* **160**, 671–683 (2003).

221. C. L. Hueschen, S. J. Kenny, K. Xu, S. Dumont, NuMA recruits dynein activity to microtubule minus-ends at mitosis. *Elife*. **6**, 1–26 (2017).

222. N. P. Ferenz, A. Gable, P. Wadsworth, Mitotic functions of kinesin-5. *Semin. Cell Dev. Biol.* **21** (2010), pp. 255–259.

223. G. Yang, B. R. Houghtaling, J. Gaetz, J. Z. Liu, G. Danuser, T. M. Kapoor, Architectural dynamics of the meiotic spindle revealed by single-fluorophore imaging. *Nat. Cell Biol.* **9**, 1233–1242 (2007).

224. A. D. Silk, A. J. Holland, D. W. Cleveland, Requirements for NuMA in maintenance and establishment of mammalian spindle poles. *J. Cell Biol.* **184**, 677–690 (2009).

225. A. Merdes, R. Heald, K. Samejima, W. C. Earnshaw, D. W. Cleveland, Formation of spindle poles by dynein/dynactin-dependent transport of NuMA. *J. Cell Biol.* **149**, 851–861 (2000).

226. R. Heald, R. Tournebize, A. Habermann, E. Karsenti, A. Hyman, Spindle Assembly in Xenopus Egg Extracts: Respective Roles of Centrosomes and Microtubule Self-Organization. *J. Cell Biol.* **138**, 615–628 (1997).

227. K. S. Burbank, T. J. Mitchison, D. S. Fisher, Slide-and-Cluster Models for Spindle Assembly. *Curr. Biol.* **17**, 1373–1383 (2007).

228. J. H. Hayden, S. S. Bowser, C. L. Rieder, Kinetochores capture astral microtubules during chromosome attachment to the mitotic spindle: Direct visualization in live newt lung cells. *J. Cell Biol.* **111**, 1039–1045 (1990).

229. C. L. Rieder, S. P. Alexander, Kinetochores are transported poleward along a single astral microtubule during chromosome attachment to the spindle in newt lung cells. *J. Cell Biol.* **110**, 81–95 (1990).

230. R. Wollman, E. N. Cytrynbaum, J. T. Jones, T. Meyer, J. M. Scholey, A. Mogilner, Efficient chromosome capture requires a bias in the “search-and-capture” process during mitotic-spindle assembly. *Curr. Biol.* **15**, 828–832 (2005).

231. P. Lénárt, C. P. Bacher, N. Daigle, A. R. Hand, R. Eils, M. Terasaki, J. Ellenberg, A contractile nuclear actin network drives chromosome congression in oocytes. *Nature*. **436**, 812–818 (2005).

232. V. Magidson, C. B. O'Connell, J. Lončarek, R. Paul, A. Mogilner, A. Khodjakov, The spatial arrangement of chromosomes during prometaphase facilitates spindle assembly. *Cell*. **146**, 555–567 (2011).

233. A. Khodjakov, R. W. Cole, B. R. Oakley, C. L. Rieder, Centrosome-independent mitotic spindle formation in vertebrates. *Curr. Biol.* **10**, 59–67 (2000).

234. E. Rebollo, S. Llamazares, J. Reina, C. Gonzalez, Contribution of Noncentrosomal Microtubules to Spindle Assembly in Drosophila Spermatocytes. *PLoS Biol.* **2**, e8 (2004).

235. J. R. LaFountain, R. Oldenbourg, Kinetochore-driven outgrowth of microtubules is a central contributor to kinetochore fiber maturation in crane-fly spermatocytes. *Mol. Biol. Cell*. **25**, 1437–1445 (2014).

236. F. R. Bischoff, H. Ponstingl, Mitotic regulator protein RCC1 is complexed with a nuclear ras-related polypeptide. *Proc. Natl. Acad. Sci. U. S. A.* **88**, 10830–10834 (1991).

237. P. R. Clarke, C. Zhang, Spatial and temporal coordination of mitosis by Ran GTPase. *Nat. Rev. Mol. Cell Biol.* **9** (2008), pp. 464–477.

238. A. Smith, A. Brownawell, I. G. Macara, Nuclear import of Ran is mediated by the transport factor NTF2. *Curr. Biol.* **8**, 1403–1406 (1998).

239. K. Ribbeck, G. Lipowsky, H. M. Kent, M. Stewart, D. Görlich, NTF2 mediates nuclear import of Ran. *EMBO J.* **17**, 6587–6598 (1998).

240. M. E. Nemergut, C. A. Mizzen, T. Stukenberg, C. D. Allis, I. G. Macara, Chromatin docking and exchange activity enhancement of RCC1 by histones H2A and H2B. *Science (80-.).* **292**, 1540–1543 (2001).

241. F. R. Bischoff, H. Ponstingl, Catalysis of guanine nucleotide exchange on Ran by the mitotic regulator RCC1. *Nature*. **354**, 80–82 (1991).

242. C. Klebe, F. R. Bischoff, H. Ponstingl, A. Wittinghofer, Interaction of the Nuclear GTP-Binding Protein Ran with Its Regulatory Proteins RCC1 and RanGAP1. *Biochemistry*. **34**, 639–647 (1995).

243. M. S. Zhang, A. Arnaoutov, M. Dasso, RanBP1 governs spindle assembly by defining mitotic Ran-GTP production. *Dev. Cell*. **31**, 393–404 (2014).

244. F. R. Bischoff, C. Klebe, J. Kretschmer, A. Wittinghofer, H. Ponstingl, RanGAP1 induces GTPase activity of nuclear Ras-related Ran. *Proc. Natl. Acad. Sci. U. S. A.* **91**, 2587–2591 (1994).

245. F. R. Bischoff, H. Krebber, E. Smirnova, W. Dong, H. Ponstingl, Co-activation of RanGTPase and inhibition of GTP dissociation by Ran-GTP binding protein RanBP1. *EMBO J.* **14**, 705–715 (1995).

246. P. Kalab, A. Pralle, E. Y. Isacoff, R. Heald, K. Weis, Analysis of a RanGTP-regulated gradient in mitotic somatic cells. *Nature*. **440**, 697–701 (2006).

247. P. Kalab, K. Weis, R. Heald, Visualization of a Ran-GTP gradient in interphase and mitotic Xenopus egg extracts. *Science (80-.).* **295**, 2452–2456 (2002).

248. R. E. Carazo-Salas, G. Guarguaglini, O. J. Gruss, A. Segref, E. Karsenti, L. W. Mattaj, Generation of GTP-bound ran by RCC1 is required for chromatin-induced mitotic spindle formation. *Nature*. **400**, 178–181 (1999).

249. R. E. Carazo-Salas, O. J. Gruss, I. W. Mattaj, E. Karsenti, Ran-GTP coordinates regulation of microtubule nucleation and dynamics during mitotic-spindle assembly. *Nat. Cell Biol.* **3**, 228–

234 (2001).

250. A. Wilde, S. B. Lizarraga, L. Zhang, C. Wiese, N. R. Gliksman, C. E. Walczak, Y. Zheng, Ran stimulates spindle assembly by altering microtubule dynamics and the balance of motor activities. *Nat. Cell Biol.* **3**, 221–227 (2001).

251. D. Halpin, P. Kalab, J. Wang, K. Weis, R. Heald, Mitotic Spindle Assembly around RCC1-Coated Beads in Xenopus Egg Extracts. *PLoS Biol.* **9**, e1001225 (2011).

252. O. J. Gruss, R. E. Carazo-Salas, C. A. Schatz, G. Guarguaglini, J. Kast, M. Wilm, N. Le Bot, I. Vernos, E. Karsenti, I. W. Mattaj, Ran induces spindle assembly by reversing the inhibitory effect of importin α on TPX2 activity. *Cell*. **104**, 83–93 (2001).

253. M. V. Nachury, T. J. Maresca, W. C. Salmon, C. M. Waterman-Storer, R. Heald, K. Weis, Importin β is a mitotic target of the small GTPase ran in spindle assembly. *Cell*. **104**, 95–106 (2001).

254. C. Wiese, A. Wilde, M. S. Moore, S. A. Adam, A. Merdes, Y. Zheng, Role of importin-β in coupling ran to downstream targets in microtubule assembly. *Science (80-.).* **291**, 653–656 (2001).

255. T. A. Kufer, H. H. W. Silljé, R. Körner, O. J. Gruss, P. Meraldi, E. A. Nigg, Human TPX2 is required for targeting Aurora-A kinase to the spindle. *J. Cell Biol.* **158**, 617–623 (2002).

256. M. Y. Tsai, C. Wiese, K. Cao, O. Martin, P. Donovan, J. Ruderman, C. Prigent, Y. Zheng, A Ran signalling pathway mediated by the mitotic kinase Aurora A in spindle assembly. *Nat. Cell Biol.* **5**, 242–248 (2003).

257. R. Pinyol, J. Scrofani, I. Vernos, The role of NEDD1 phosphorylation by aurora a in chromosomal microtubule nucleation and spindle function. *Curr. Biol.* **23**, 143–149 (2013).

258. J. Scrofani, T. Sardon, S. Meunier, I. Vernos, Microtubule Nucleation in Mitosis by a RanGTP-Dependent Protein Complex. *Curr. Biol.* **25**, 131–140 (2015).

259. C. A. Schatz, R. Santarella, A. Hoenger, E. Karsenti, I. W. Mattaj, O. J. Gruss, R. E. Carazo-Salas, Importin α-regulated nucleation of microtubules by TPX2. *EMBO J.* **22**, 2060–2070 (2003).

260. C. B. O'Connell, J. Lončarek, P. Kaláb, A. Khodjakov, Relative contributions of chromatin and kinetochores to mitotic spindle assembly. *J. Cell Biol.* **187**, 43–51 (2009).

261. H. Maiato, C. L. Rieder, A. Khodjakov, Kinetochore-driven formation of kinetochore fibers contributes to spindle assembly during animal mitosis. *J. Cell Biol.* **167**, 831–840 (2004).

262. V. Sikirzhytski, F. Renda, I. Tikhonenko, V. Magidson, B. F. McEwen, A. Khodjakov, Microtubules assemble near most kinetochores during early prometaphase in human cells. *J. Cell Biol.* **217**, 2647–2659 (2018).

263. R. K. Mishra, P. Chakraborty, A. Arnaoutov, B. M. A. Fontoura, M. Dasso, The Nup107-160 complex and γ-TuRC regulate microtubule polymerization at kinetochores. *Nat. Cell Biol.* **12**, 164–169 (2010).

264. H. Yokoyama, B. Koch, R. Walczak, F. Ciray-Duygu, J. C. González-Sánchez, D. P. Devos, I. W. Mattaj, O. J. Gruss, The nucleoporin MEL-28 promotes RanGTP-dependent γ-tubulin recruitment and microtubule nucleation in mitotic spindle formation. *Nat. Commun.* **5**, 3270 (2014).

265. B. A. Rasala, A. V. Orjalo, Z. Shen, S. Briggs, D. J. Forbes, ELYS is a dual nucleoporin/kinetochore protein required for nuclear pore assembly and proper cell division. *Proc. Natl. Acad. Sci. U. S. A.* **103**, 17801–17806 (2006).

266. L. Zhou, X. Tian, C. Zhu, F. Wang, J. M. Higgins, Polo-like kinase-1 triggers histone phosphorylation by Haspin in mitosis. *EMBO Rep.* **15**, 273–281 (2014).

267. C. Zierhut, C. Jenness, H. Kimura, H. Funabiki, Nucleosomal regulation of chromatin composition and nuclear assembly revealed by histone depletion. *Nat. Struct. Mol. Biol.* **21**, 617–625 (2014).

268. A. E. Kelly, C. Ghenoiu, J. Z. Xue, C. Zierhut, H. Kimura, H. Funabiki, Survivin Reads Phosphorylated Histone H3 Threonine 3 to Activate the Mitotic Kinase Aurora B. *Science (80-.).* **330**, 235–239 (2010).

269. F. Wang, J. Dai, J. R. Daum, E. Niedzialkowska, B. Banerjee, P. T. Stukenberg, G. J. Gorbsky, J. M. G. Higgins, Histone H3 Thr-3 phosphorylation by haspin positions Aurora B at centromeres in mitosis. *Science (80-.).* **330**, 231–235 (2010).

270. Y. Yamagishi, T. Honda, Y. Tanno, Y. Watanabe, Two Histone Marks Establish the Inner Centromere and Chromosome Bi-Orientation. *Science (80-.).* **330**, 239–243 (2010).

271. M. A. Lampson, K. Renduchitala, A. Khodjakov, T. M. Kapoor, Correcting improper chromosomes-spindle attachments during cell division. *Nat. Cell Biol.* **6**, 232–237 (2004).

272. G.-Y. Chen, F. Renda, H. Zhang, A. Gokden, D. Z. Wu, D. M. Chenoweth, A. Khodjakov, M. A. Lampson, *bioRxiv*, in press, doi:10.1101/2020.06.01.127795.

273. T. J. Maresca, A. C. Groen, J. C. Gatlin, R. Ohi, T. J. Mitchison, E. D. Salmon, Spindle Assembly in the Absence of a RanGTP Gradient Requires Localized CPC Activity. *Curr. Biol.* **19**, 1210–1215 (2009).

274. A. E. Kelly, S. C. Sampath, T. A. Maniar, E. M. Woo, B. T. Chait, H. Funabiki, Chromosomal Enrichment and Activation of the Aurora B Pathway Are Coupled to Spatially Regulate Spindle Assembly. *Dev. Cell*. **12**, 31–43 (2007).

275. S. C. Sampath, R. Ohi, O. Leismann, A. Salic, A. Pozniakovski, H. Funabiki, The chromosomal passenger complex is required for chromatin-induced microtubule stabilization and spindle assembly. *Cell*. **118**, 187–202 (2004).

276. P. D. Andrews, Y. Ovechkina, N. Morrice, M. Wagenbach, K. Duncan, L. Wordeman, J. R. Swedlow, Aurora B regulates MCAK at the mitotic centromere. *Dev. Cell*. **6**, 253–268 (2004).

277. B. B. Gadea, J. V. Ruderman, Aurora B is required for mitotic chromatin-induced phosphorylation of Op18/Stathmin. *Proc. Natl. Acad. Sci. U. S. A.* **103**, 4493–4498 (2006).

278. P. Niethammer, P. Bastiaens, E. Karsenti, Stathmin-Tubutin Interaction Gradients in Motile and Mitotic Cells. *Science (80-.).* **303**, 1862–1866 (2004).

279. R. Uehara, R. S. Nozawa, A. Tomioka, S. Petry, R. D. Vale, C. Obuse, G. Goshima, The augmin complex plays a critical role in spindle microtubule generation for mitotic progression and cytokinesis in human cells. *Proc. Natl. Acad. Sci. U. S. A.* **106**, 6998–7003 (2009).

280. S. Lawo, M. Bashkurov, M. Mullin, M. G. Ferreria, R. Kittler, B. Habermann, A. Tagliaferro, I. Poser, J. R. A. Hutchins, B. Hegemann, D. Pinchev, F. Buchholz, J. M. Peters, A. A. Hyman, A. C. Gingras, L. Pelletier, HAUS, the 8-Subunit Human Augmin Complex, Regulates Centrosome and Spindle Integrity. *Curr. Biol.* **19**, 816–826 (2009).

281. J.-G. Song, M. R. King, R. Zhang, R. S. Kadzik, A. Thawani, S. Petry, Mechanism of how augmin directly targets the γ-tubulin ring complex to microtubules. *J. Cell Biol*. **217**, 2417 (2018).

282. M. R. King, S. Petry, Phase separation of TPX2 enhances and spatially coordinates microtubule nucleation. *Nat. Commun.* **11**, 1–13 (2020).

283. N. Ma, U. S. Tulu, N. P. Ferenz, C. Fagerstrom, A. Wilde, P. Wadsworth, Poleward transport of TPX2 in the mammalian mitotic spindle requires dynein, Eg5, and microtubule flux. *Mol. Biol. Cell*. **21**, 979–988 (2010).

284. T. P. Fleming, M. H. Johnson, From egg to epithelium. *Annu. Rev. Cell Biol.* **4**, 459–485 (1988).

285. C. Y. Leung, M. Zernicka-Goetz, Mapping the journey from totipotency to lineage specification in the mouse embryo. *Curr. Opin. Genet. Dev.* **34**, 71–76 (2015).

286. P. Strnad, S. Gunther, J. Reichmann, U. Krzic, B. Balazs, G. de Medeiros, N. Norlin, T. Hiiragi, L. Hufnagel, J. Ellenberg, Inverted light-sheet microscope for imaging mouse pre-implantation development. *Nat. Methods*. **13**, 139–42 (2016).

287. R. Niwayama, P. Moghe, Y. J. Liu, D. Fabrèges, F. Buchholz, M. Piel, T. Hiiragi, A Tug-of-War between Cell Shape and Polarity Controls Division Orientation to Ensure Robust Patterning in the Mouse Blastocyst. *Dev. Cell*. **51**, 564-574.e6 (2019).

288. K. K. Niakan, J. Han, R. A. Pedersen, C. Simon, R. A. R. Pera, Human pre-implantation embryo development. *Development*. **139**, 829–841 (2012).

289. R. L. Gardner, J. Rossant, Investigation of the fate of 4.5 day post-coitum mouse inner cell mass cells by blastocyst injection. *J. Embryol. Exp. Morphol.* **Vol 52**, 141–152 (1979).

290. A. Susor, D. Jansova, M. Anger, M. Kubelka, Translation in the mammalian oocyte in space and time. *Cell Tissue Res.* **363**, 69–84 (2016).

291. T. Kotani, K. Yasuda, R. Ota, M. Yamashita, Cyclin B1 mRNA translation is temporally controlled through formation and disassembly of RNA granules. *J. Cell Biol.* **202**, 1041–55 (2013).

292. G. Manandhar, P. Sutovsky, H. C. Joshi, T. Stearns, G. Schatten, Centrosome reduction during mouse spermiogenesis. *Dev. Biol.* **203**, 424–434 (1998).

293. P. D. Calarco-Gillam, M. C. Siebert, R. Hubble, T. Mitchison, M. Kirschner, Centrosome development in early mouse embryos as defined by an autoantibody against pericentriolar material. *Cell*. **35**, 621–629 (1983).

294. C. Gueth-Hallonet, C. Antony, J. Aghion, A. Santa-Maria, I. Lajoie-Mazenc, M. Wright, B. Maro, gamma-Tubulin is present in acentriolar MTOCs during early mouse development. *J. Cell Sci.* **105**, 157–66 (1993).

295. A. Courtois, M. Schuh, J. Ellenberg, T. Hiiragi, The transition from meiotic to mitotic spindle assembly is gradual during early mammalian development. *J. Cell Biol.* **198**, 357–370 (2012).

296. K. Howe, G. FitzHarris, A non-canonical mode of microtubule organization operates throughout pre-implantation development in mouse. *Cell Cycle*. **12**, 1616–1624 (2013).

297. C. E. M. Aiken, P. P. L. Swoboda, J. N. Skepper, M. H. Johnson, The direct measurement of embryogenic volume and nucleo-cytoplasmic ratio during mouse pre-implantation development. *Reproduction*. **128**, 527–535 (2004).

298. E. Tsichlaki, G. FitzHarris, Nucleus downscaling in mouse embryos is regulated by cooperative developmental and geometric programs. *Sci. Rep.* **6**, 28040 (2016).

299. K. Yamagata, G. FitzHarris, 4D imaging reveals a shift in chromosome segregation dynamics during mouse pre-implantation development. *Cell Cycle*. **12**, 157–165 (2013).

300. T. Boroviak, G. G. Stirparo, S. Dietmann, I. Hernando-Herraez, H. Mohammed, W. Reik, A. Smith, E. Sasaki, J. Nichols, P. Bertone, Single cell transcriptome analysis of human, marmoset and mouse embryos reveals common and divergent features of preimplantation development. *Development*. **145** (2018), doi:10.1242/dev.167833.

301. T. Hamatani, M. G. Carter, A. A. Sharov, M. S. Ko, Dynamics of global gene expression changes during mouse preimplantation development. *Dev Cell*. **6**, 117–131 (2004).

302. A. Graf, S. Krebs, V. Zakhartchenko, B. Schwalb, H. Blum, E. Wolf, Fine mapping of genome

activation in bovine embryos by RNA sequencing. *Proc. Natl. Acad. Sci. U. S. A.* **111**, 4139–4144 (2014).

303. R. Vassena, S. Boué, E. González-Roca, B. Aran, H. Auer, A. Veiga, J. C. I. Belmonte, Waves of early transcriptional activation and pluripotency program initiation during human preimplantation development. *Development*. **138**, 3699–3709 (2011).

304. P. Blakeley, N. M. E. Fogarty, I. del Valle, S. E. Wamaitha, T. X. Hu, K. Elder, P. Snell, L. Christie, P. Robson, K. K. Niakan, Defining the three cell lineages of the human blastocyst by single-cell RNA-seq. *Development*. **142**, 3613–3613 (2015).

305. Braude P., Bolton V, Moore S., Human gene expression first occurs between the four- and eight-cell stages of preimplantation development. *Nature*. **332**, 459–461 (1988).

306. R. C. McCoy, Z. Demko, A. Ryan, M. Banjevic, M. Hill, S. Sigurjonsson, M. Rabinowitz, H. B. Fraser, D. A. Petrov, Common variants spanning PLK4 are associated with mitotic-origin aneuploidy in human embryos. *Science (80-.).* **348**, 235–238 (2015).

307. G. Manandhar, H. Schatten, P. Sutovsky, Centrosome reduction during gametogenesis and its significance. *Biol. Reprod.* **72** (2005), pp. 2–13.

308. J. Reichmann, B. Nijmeijer, M. J. Hossain, M. Eguren, I. Schneider, A. Z. Politi, M. J. Roberti, L. Hufnagel, T. Hiiragi, J. Ellenberg, Dual-spindle formation in zygotes keeps parental genomes apart in early mammalian embryos. *Science (80-.).* **361**, 189–193 (2018).

309. D. Clift, M. Schuh, A three-step MTOC fragmentation mechanism facilitates bipolar spindle assembly in mouse oocytes. *Nat. Commun.* **6**, 1–12 (2015).

310. E. L. Fishman, K. Jo, Q. P. H. Nguyen, D. Kong, R. Royfman, A. R. Cekic, S. Khanal, A. L. Miller, C. Simerly, G. Schatten, J. Loncarek, V. Mennella, T. Avidor-Reiss, A novel atypical sperm centriole is functional during human fertilization. *Nat. Commun.* **9**, 2210 (2018).

311. S. Madgwick, K. T. Jones, How eggs arrest at metaphase II: MPF stabilisation plus APC/C inhibition equals Cytostatic Factor. *Cell Div.* **2**, 4 (2007).

312. Z. Polański, Strain difference in the timing of meiosis resumption in mouse oocytes: Involvement of a cytoplasmic factor(s) acting presumably upstream of the dephosphorylation of p34cdc2 kinase. *Zygote*. **5**, 105–109 (1997).

313. Z. Polanski, In-vivo and in-vitro maturation rate of oocytes from two strains of mice. *J. Reprod. Fertil.* **78**, 103–109 (1986).

314. V. L. Horner, M. F. Wolfner, Transitioning from egg to embryo: Triggers and mechanisms of egg activation. *Dev. Dyn.* **237**, 527–544 (2008).

315. S. Watanabe, G. Shioi, Y. Furuta, G. Goshima, Intra-spindle Microtubule Assembly Regulates Clustering of Microtubule-Organizing Centers during Early Mouse Development. *Cell Rep.* **15**, 54–60 (2016).

316. J. Z. Kubiak, F. Bazile, A. Pascal, L. Richard-Parpaillon, Z. Polanski, M. A. Ciemerych, F. Chesnel, Temporal regulation of embryonic M-phases. *Folia Histochem. Cytobiol.* **46**, 5–9 (2008).

317. A. Ajduk, B. Strauss, J. Pines, M. Zernicka-Goetz, Delayed APC/C activation extends the first mitosis of mouse embryos. *Sci. Rep.* **7**, 9682 (2017).

318. A. A. Kiessling, R. Bletsa, B. Desmarais, C. Mara, K. Kallianidis, D. Loutradis, Evidence that human blastomere cleavage is under unique cell cycle control. *J. Assist. Reprod. Genet.* **26**, 187–195 (2009).

319. R. C. McCoy, Mosaicism in Preimplantation Human Embryos: When Chromosomal Abnormalities Are the Norm. *Trends Genet.* **33**, 448–463 (2017).

320. M. A. Ciemerych, B. Maro, J. Z. Kubiak, Control of duration of the first two mitoses in a mouse embryo. *Zygote*. **7**, 293–300 (1999).

321. J. Z. Kubiak, M. A. Ciemerych, A. Hupalowska, M. Sikora-Polaczek, Z. Polanski, On the transition from the meiotic to mitotic cell cycle during early mouse development. *Int. J. Dev. Biol.* **52**, 201–17 (2008).

322. M. Sikora-Polaczek, A. Hupalowska, Z. Polanski, J. Z. Kubiak, M. A. Ciemerych, The First Mitosis of the Mouse Embryo Is Prolonged by Transitional Metaphase Arrest1. *Biol. Reprod.* **74**, 734–743 (2006).

323. E. Coonen, J. G. Derhaag, J. C. M. Dumoulin, L. C. P. van Wissen, M. Bras, M. Janssen, J. L. H. Evers, J. P. M. Geraedts, Anaphase lagging mainly explains chromosomal mosaicism in human preimplantation embryos. *Hum. Reprod.* **19**, 316–324 (2004).

324. C. Vázquez-Diez, K. Yamagata, S. Trivedi, J. Haverfield, G. FitzHarris, Micronucleus formation causes perpetual unilateral chromosome inheritance in mouse embryos. *Proc. Natl. Acad. Sci.* **113**, 626–631 (2016).

325. S. L. Chavez, K. E. Loewke, J. Han, F. Moussavi, P. Colls, S. Munne, B. Behr, R. A. Reijo Pera, Dynamic blastomere behaviour reflects human embryo ploidy by the four-cell stage. *Nat. Commun.* **3**, 1251 (2012).

326. D. H. Kort, G. Chia, N. R. Treff, A. J. Tanaka, T. Xing, L. B. Vensand, S. Micucci, R. Prosser, R. A. Lobo, M. V. Sauer, D. Egli, Human embryos commonly form abnormal nuclei during development: A mechanism of DNA damage, embryonic aneuploidy, and developmental arrest. *Hum. Reprod.* **31**, 312–323 (2016).

327. E. Van Royen, K. Mangelschots, M. Vercruyssen, D. De Neubourg, M. Valkenburg, J. Gerris, G. Ryckaert, Multinucleation in cleavage stage embryos. *Hum. Reprod.* **18**, 1062–1069 (2003).

328. B. Kalatova, R. Jesenska, D. Hlinka, M. Dudas, Tripolar mitosis in human cells and embryos: Occurrence, pathophysiology and medical implications. *Acta Histochem.* **117**, 111–125 (2015).

329. A. Egashira, N. Yamauchi, K. Tanaka, C. Mine, H. Otsubo, M. Murakami, M. R. Islam, M. Ohtsuka, N. Yoshioka, T. Kuramoto, Developmental capacity and implantation potential of the embryos with multinucleated blastomeres. *J. Reprod. Dev.* **61**, 595–600 (2015).

330. J. Meriano, C. Clark, K. Cadesky, C. A. Laskin, Binucleated and micronucleated blastomeres in embryos derived from human assisted reproduction cycles. *Reprod. Biomed. Online*. **9**, 511–520 (2004).

331. I. Kligman, C. Benadiva, M. Alikani, S. Munne, Fertilization and early embryology: The presence of multinucleated blastomeres in human embryos is correlated with chromosomal abnormalities. *Hum. Reprod.* **11**, 1492–1498 (1996).

332. A. Destouni, M. Z. Esteki, M. Catteeuw, O. Tšuiko, E. Dimitriadou, K. Smits, A. Kurg, A. Salumets, A. Van Soom, T. Voet, J. R. Vermeesch, Zygotes segregate entire parental genomes in distinct blastomere lineages causing cleavage-stage chimerism and mixoploidy. *Genome Res.* **26**, 567–578 (2016).

333. G. Fernández-Miranda, M. Trakala, J. Martín, B. Escobar, A. González, N. B. Ghyselinck, S. Ortega, M. Cañamero, I. P. de Castro, M. Malumbres, Genetic disruption of aurora B uncovers an essential role for aurora C during early mammalian development. *Development*. **138**, 2661–2672 (2011).

334. M. Avo Santos, C. Van De Werken, M. De Vries, H. Jahr, M. J. M. Vromans, J. S. E. Laven, B. C. Fauser, G. J. Kops, S. M. Lens, E. B. Baart, A role for Aurora C in the chromosomal passenger complex during human preimplantation embryo development. *Hum. Reprod.* **26**, 1868–1881

(2011).

335. K. Schindler, O. Davydenko, B. Fram, M. A. Lampson, R. M. Schultz, Maternally recruited Aurora C kinase is more stable than Aurora B to support mouse oocyte maturation and early development. *Proc. Natl. Acad. Sci. U. S. A.* **109**, 1–8 (2012).

336. C. van de Werken, M. Avo Santos, J. S. E. Laven, C. Eleveld, B. C. J. M. Fauser, S. M. A. Lens, E. B. Baart, Chromosome segregation regulation in human zygotes: altered mitotic histone phosphorylation dynamics underlying centromeric targeting of the chromosomal passenger complex. *Hum. Reprod.* **30**, 2275–2291 (2015).

337. A. Musacchio, E. D. Salmon, The spindle-assembly checkpoint in space and time. *Nat. Rev. Mol. Cell Biol.* **8**, 379–393 (2007).

338. K. Jacobs, H. Van de Velde, C. De Paepe, K. Sermon, C. Spits, Mitotic spindle disruption in human preimplantation embryos activates the spindle assembly checkpoint but not apoptosis until Day 5 of development. *MHR Basic Sci. Reprod. Med.* **23**, 321–329 (2017).

339. Y. Wei, S. Multi, C.-R. Yang, J. Ma, Q.-H. Zhang, Z.-B. Wang, M. Li, L. Wei, Z.-J. Ge, C.-H. Zhang, Y.-C. Ouyang, Y. Hou, H. Schatten, Q.-Y. Sun, Spindle Assembly Checkpoint Regulates Mitotic Cell Cycle Progression during Preimplantation Embryo Development. *PLoS One*. **6**, e21557 (2011).

340. C. Vázquez-Diez, L. M. G. Paim, G. FitzHarris, Cell-Size-Independent Spindle Checkpoint Failure Underlies Chromosome Segregation Error in Mouse Embryos. *Curr. Biol.* **29**, 865-873.e3 (2019).

341. J. Maller, D. Poccia, D. Nishioka, P. Kidd, J. Gerhart, H. Hartman, Spindle formation and cleavage in Xenopus eggs injected with centriole-containing fractions from sperm. *Exp. Cell Res.* **99**, 285–294 (1976).

342. P. Gönczy, S. Pichler, M. Kirkham, A. A. Hyman, Cytoplasmic dynein is required for distinct aspects of MTOC positioning, including centrosome separation, in the one cell stage Caenorhabditis elegans embryo. *J. Cell Biol.* **147**, 135–50 (1999).

343. C. Klotz, M. C. Dabauvalle, M. Paintrand, T. Weber, M. Bornens, E. Karsenti, Parthenogenesis in Xenopus eggs requires centrosomal integrity. *J. Cell Biol.* **110**, 405–415 (1990).

344. C. S. Navara, N. L. First, G. Schatten, Microtubule Organization in the Cow during Fertilization, Polyspermy, Parthenogenesis, and Nuclear Transfer: The Role of the Sperm Aster. *Dev. Biol.* **162**, 29–40 (1994).

345. G. Palermo, S. Munné, J. Cohen, The human zygote inherits its mitotic potential from the male gamete. *Hum. Reprod.* **9**, 1220–1225 (1994).

346. H. Schatten, G. Schatten, D. Mazia, R. Balczon, C. Simerly, Behavior of centrosomes during fertilization and cell division in mouse oocytes and in sea urchin eggs. *Proc. Natl. Acad. Sci. U. S. A.* **83**, 105–109 (1986).

347. J. Dumont, S. Petri, F. Pellegrin, M. E. Terret, M. T. Bohnsack, P. Rassinier, V. Georget, P. Kalab, O. J. Gruss, M. H. Verlhac, A centriole- and RanGTP-independent spindle assembly pathway in meiosis I of vertebrate oocytes. *J. Cell Biol.* **176**, 295–305 (2007).

348. P. Coelho, L. Bury, B. Sharif, M. Riparbelli, J. Fu, G. Callaini, D. Glover, M. Zernicka-Goetz, Spindle formation in the mouse embryo requires Plk4 in the absence of centrioles. *Dev. Cell*. **27**, 586–597 (2013).

349. G. FitzHarris, A shift from kinesin 5-dependent metaphase spindle function during preimplantation development in mouse. *Development*. **136**, 2111–2119 (2009).

350. R. Y. Tsien, The green fluorescent protein. *Annu. Rev. Biochem.* **67**, 509–544 (1998).

351. A. Keppler, S. Gendreizig, T. Gronemeyer, H. Pick, H. Vogel, K. Johnsson, A general method for the covalent labeling of fusion proteins with small molecules in vivo. *Nat. Biotechnol.* **21**, 86–89 (2003).

352. A. Keppler, H. Pick, C. Arrivoli, H. Vogel, K. Johnsson, Labeling of fusion proteins with synthetic fluorophores in live cells. *Proc. Natl. Acad. Sci. U. S. A.* **101**, 9955–9959 (2004).

353. G. V. Los, L. P. Encell, M. G. McDougall, D. D. Hartzell, N. Karassina, C. Zimprich, M. G. Wood, R. Learish, R. F. Ohana, M. Urh, D. Simpson, J. Mendez, K. Zimmerman, P. Otto, G. Vidugiris, J. Zhu, A. Darzins, D. H. Klaubert, R. F. Bulleit, K. V. Wood, HaloTag: A novel protein labeling technology for cell imaging and protein analysis. *ACS Chem. Biol.* **3**, 373–382 (2008).

354. J. C. Daniel, Cleavage of Mammalian Ova inhibited by Visible Light. *Nature*. **201**, 316–317 (1964).

355. R. M. Schultz, Of light and mouse embryos: Less is more. *Proc. Natl. Acad. Sci. U. S. A.* **104**, 14547–14548 (2007).

356. M. Takenaka, T. Horiuchi, R. Yanagimachi, Effects of light on development of mammalian zygotes. *Proc. Natl. Acad. Sci. U. S. A.* **104**, 14289–14293 (2007).

357. T. Watanabe, J. S. Biggins, N. B. Tannan, S. Srinivas, Limited predictive value of blastomere angle of division in trophectoderm and inner cell mass specification. *Development*. **141**, 2279–2288 (2014).

358. S. A. Morris, R. T. Y. Teo, H. Li, P. Robson, D. M. Glover, M. Zernicka-Goetz, Origin and formation of the first two distinct cell types of the inner cell mass in the mouse embryo. *Proc. Natl. Acad. Sci. U. S. A.* **107**, 6364–6369 (2010).

359. J. Huisken, J. Swoger, F. Del Bene, J. Wittbrodt, E. H. K. Stelzer, Optical sectioning deep inside live embryos by selective plane illumination microscopy. *Science (80-.).* **305**, 1007–1009 (2004).

360. R. McGorty, H. Liu, D. Kamiyama, Z. Dong, S. Guo, B. Huang, Open-top selective plane illumination microscope for conventionally mounted specimens. *Opt. Express*. **23**, 16142 (2015).

361. A. Kaufmann, M. Mickoleit, M. Weber, J. Huisken, Multilayer mounting enables long-term imaging of zebrafish development in a light sheet microscope. *Development*. **139**, 3242–3247 (2012).

362. T. Ichikawa, K. Nakazato, P. J. Keller, H. Kajiura-Kobayashi, E. H. K. Stelzer, A. Mochizuki, S. Nonaka, Live Imaging of Whole Mouse Embryos during Gastrulation: Migration Analyses of Epiblast and Mesodermal Cells. *PLoS One*. **8**, e64506 (2013).

363. J. Capoulade, M. Wachsmuth, L. Hufnagel, M. Knop, Quantitative fluorescence imaging of protein diffusion and interaction in living cells. *Nat. Biotechnol.* **29**, 835–839 (2011).

364. R. S. Udan, V. G. Piazza, C. W. Hsu, A. K. Hadjantonakis, M. E. Dickinson, Quantitative imaging of cell dynamics in mouse embryos using light-sheet microscopy. *Development*. **141**, 4406–4414 (2014).

365. J. Reichmann, M. Eguren, Y. Lin, I. Schneider, J. Ellenberg, in *Methods in Cell Biology* (2018; https://linkinghub.elsevier.com/retrieve/pii/S0091679X1830030X), vol. 145, pp. 279–292.

366. L. A. Jaffe, M. Terasaki, Quantitative Microinjection of Oocytes, Eggs, and Embryos. *Methods Cell Biol.* **74**, 219–242 (2004).

367. D. Clift, W. A. McEwan, L. I. Labzin, V. Konieczny, B. Mogessie, L. C. James, M. Schuh, A Method for the Acute and Rapid Degradation of Endogenous Proteins. *Cell*. **171**, 1692-1706.e18 (2017).

368. D. Clift, C. So, W. A. McEwan, L. C. James, M. Schuh, Acute and rapid degradation of endogenous proteins by Trim-Away. *Nat. Protoc.* **13**, 2149–2175 (2018).

369. D. L. Mallery, W. A. McEwan, S. R. Bidgood, G. J. Towers, C. M. Johnson, L. C. James, Antibodies mediate intracellular immunity through tripartite motif-containing 21 (TRIM21). *Proc. Natl. Acad. Sci. U. S. A.* **107**, 19985–90 (2010).

370. S. Foss, R. Watkinson, I. Sandlie, L. C. James, J. T. Andersen, TRIM21: A cytosolic Fc receptor with broad antibody isotype specificity. *Immunol. Rev.* **268**, 328–339 (2015).

371. L. Carbone, S. L. Chavez, Mammalian pre-implantation chromosomal instability: Species comparison, evolutionary considerations, and pathological correlations. *Syst. Biol. Reprod. Med.* **61**, 321–335 (2015).

372. P. Holm, N. . Shukri, G. Vajta, P. Booth, C. Bendixen, H. Callesen, Developmental kinetics of the first cell cycles of bovine in vitro produced embryos in relation to their in vitro viability and sex. *Theriogenology*. **50**, 1285–1299 (1998).

373. N. Desai, S. Ploskonka, L. R. Goodman, C. Austin, J. Goldberg, T. Falcone, Analysis of embryo morphokinetics, multinucleation and cleavage anomalies using continuous time-lapse monitoring in blastocyst transfer cycles. *Reprod. Biol. Endocrinol.* **12**, 1–10 (2014).

374. S. Sayed, M. M. Reigstad, B. M. Petersen, A. Schwennicke, J. W. Hausken, R. Storeng, Time-lapse imaging derived morphokinetic variables reveal association with implantation and live birth following in vitro fertilization: A retrospective study using data from transferred human embryos. *PLoS One*. **15**, 1–16 (2020).

375. M. A. M. M. Ferraz, H. S. Rho, D. Hemerich, H. H. W. Henning, H. T. A. van Tol, M. Hölker, U. Besenfelder, M. Mokry, P. L. A. M. Vos, T. A. E. Stout, S. Le Gac, B. M. Gadella, An oviduct-on-a-chip provides an enhanced in vitro environment for zygote genome reprogramming. *Nat. Commun.* **9**, 4934 (2018).

376. I. Schneider, M. de Ruijter-Villani, M. J. Hossain, T. A. E. Stout, J. Ellenberg, *bioRxiv*, in press, doi:10.1101/2020.10.16.342154.

377. S. L. Prosser, L. Pelletier, Mitotic spindle assembly in animal cells: A fine balancing act. *Nat. Rev. Mol. Cell Biol.* **18** (2017), pp. 187–201.

378. D. Dudka, C. Castrogiovanni, N. Liaudet, H. Vassal, P. Meraldi, Spindle-Length-Dependent HURP Localization Allows Centrosomes to Control Kinetochore-Fiber Plus-End Dynamics. *Curr. Biol.* **29**, 3563-3578.e6 (2019).

379. T. Cavazza, A. Z. Politi, P. Aldag, C. Baker, K. Elder, M. Blayney, A. Lucas-Hahn, H. Niemann, M. Schuh, *bioRxiv*, in press, doi:10.1101/2020.08.27.269779.

380. German embryo protection act (October 24th, 1990): Gesetz zum Schutz von Embryonen (Embryonenschutzgesetz-ESchG). *Hum. Reprod.* **6** (1991), pp. 605–606.

381. C. J. Malone, L. Misner, N. Le Bot, M. C. Tsai, J. M. Campbell, J. Ahringer, J. G. White, The C. elegans Hook Protein, ZYG-12, Mediates the Essential Attachment between the Centrosome and Nucleus. *Cell*. **115**, 825–836 (2003).

382. R. E. Lindeman, F. Pelegri, Localized Products of futile cycle/ lrmp Promote Centrosome-Nucleus Attachment in the Zebrafish Zygote. *Curr. Biol.* **22**, 843–851 (2012).

383. C. R. Bone, D. A. Starr, Nuclear migration events throughout development. *J. Cell Sci.* **129**, 1951–1961 (2016).

384. K. Ishihara, K. S. Korolev, T. J. Mitchison, Physical basis of large microtubule aster growth. *Elife*. **5** (2016), doi:10.7554/eLife.19145.

385. R. C. Weisenberg, A. C. Rosenfeld, In vitro polymerization of microtubules into asters and spindles in homogenates of surf clam eggs. *J. Cell Biol.* **64**, 146–158 (1975).

386. T. Müller-Reichert, G. Greenan, E. O'Toole, M. Srayko, The elegans of spindle assembly. *Cell. Mol. Life Sci.* **67**, 2195–2213 (2010).

387. T. S. Kitajima, M. Ohsugi, J. Ellenberg, Complete kinetochore tracking reveals error-prone homologous chromosome biorientation in mammalian oocytes. *Cell*. **146**, 568–581 (2011).

388. P. Sutovsky, G. Manandhar, G. Schatten, Biogenesis of the centrosome during mammalian gametogenesis and fertilization. *Protoplasma*. **206**, 249–262 (1999).

389. S. Morales-Mulia, J. M. Scholey, Spindle Pole Organization in Drosophila S2 Cells by Dynein, Abnormal Spindle Protein (Asp), and KLP10A □ D. *Mol. Biol. Cell*. **16**, 3176–3186 (2005).

390. G. Goshima, F. Nédélec, R. D. Vale, Mechanisms for focusing mitotic spindle poles by minus end-directed motor proteins. *J. Cell Biol.* **171**, 229–240 (2005).

391. N. R. Stevens, A. A. S. F. Raposo, R. Basto, D. St Johnston, J. W. W. Raff, From Stem Cell to Embryo without Centrioles. *Curr. Biol.* **17**, 1498–1503 (2007).

392. W. F. Marshall, Centriole evolution. *Curr. Opin. Cell Biol.* **21** (2009), pp. 14–19.

393. M. Piel, P. Meyer, A. Khodjakov, C. L. Rieder, M. Bornens, The respective contributions of the mother and daughter centrioles to centrosome activity and behavior in vertebrate cells. *J. Cell Biol.* **149**, 317–329 (2000).

394. K. Lee, K. Rhee, Separase-dependent cleavage of pericentrin B is necessary and sufficient for centriole disengagement during mitosis. *Cell Cycle*. **11**, 2476–2485 (2012).

395. K. Matsuo, K. Ohsumi, M. Iwabuchi, T. Kawamata, Y. Ono, M. Takahashi, Kendrin is a novel substrate for separase involved in the licensing of centriole duplication. *Curr. Biol.* **22**, 915–921 (2012).

396. F. G. Agircan, E. Schiebel, B. R. Mardin, Separate to operate: Control of centrosome positioning and separation. *Philos. Trans. R. Soc. B Biol. Sci.* **369** (2014), p. 20130461.

397. K. Watanabe, D. Takao, K. K. Ito, M. Takahashi, D. Kitagawa, The Cep57-pericentrin module organizes PCM expansion and centriole engagement. *Nat. Commun.* **10**, 931 (2019).

398. A. Destouni, J. R. Vermeesch, How can zygotes segregate entire parental genomes into distinct blastomeres? The zygote metaphase revisited. *BioEssays*. **39** (2017), pp. 1–7.

399. A. De Simone, A. Spahr, C. Busso, P. Gönczy, Uncovering the balance of forces driving microtubule aster migration in C. elegans zygotes. *Nat. Commun.* **9**, 938 (2018).

400. J. T. Robinson, E. J. Wojcik, M. A. Sanders, M. McGrail, T. S. Hays, Cytoplasmic dynein is required for the nuclear attachment and migration of centrosomes during mitosis in Drosophila. *J. Cell Biol.* **146**, 597–608 (1999).

401. T. Abe, H. Kiyonari, G. Shioi, K. I. Inoue, K. Nakao, S. Aizawa, T. Fujimori, Establishment of conditional reporter mouse lines at ROSA26 locus for live cell imaging. *Genesis*. **49**, 579–590 (2011).

402. Nagy A. ; Vintersten K. ; Behringer R., *Manipulating the Mouse Embryo: A Laboratory Manual, 3rd ed.* (2003).

403. J. Schindelin, I. Arganda-Carreras, E. Frise, V. Kaynig, M. Longair, T. Pietzsch, S. Preibisch, C. Rueden, S. Saalfeld, B. Schmid, J.-Y. Tinevez, D. J. White, V. Hartenstein, K. Eliceiri, P. Tomancak, A. Cardona, Fiji: an open-source platform for biological-image analysis. *Nat. Methods*. **9**, 676–682 (2012).

404. C. Tischer, A. Ravindran, S. Reither, R. Pepperkok, N. Norlin, *bioRxiv*, in press, doi:10.1101/2020.09.23.244095.

405. J. Bucevičius, J. Keller-Findeisen, T. Gilat, S. W. Hell, G. Lukinavičius, Rhodamine-Hoechst positional isomers for highly efficient staining of heterochromatin. *Chem. Sci.* **10**, 1962–1970 (2019).

406. J. J. Parrish, J. Susko-Parrish, M. A. Winer, N. L. First, Capacitation of bovine sperm by heparin. *Biol. Reprod.* **38**, 1171–1180 (1988).

407. Y. Takahashi, N. L. First, In vitro development of bovine one-cell embryos: Influence of glucose, lactate, pyruvate, amino acids and vitamins. *Theriogenology*. **37**, 963–978 (1992).

408. N. Otsu, A threshold selection method from gray-level histograms. *IEEE Trans. Syst. Man. Cybern.* **9**, 62–66 (1979).

409. J. K. Hériché, J. G. Lees, I. Morilla, T. Walter, B. Petrova, M. J. Roberti, M. J. Hossain, P. Adler, J. M. Fernández, M. Krallinger, C. H. Haering, J. Vilo, A. Valencia, J. A. Ranea, C. Orengo, J. Ellenberg, Integration of biological data by kernels on graph nodes allows prediction of new genes involved in mitotic chromosome condensation. *Mol. Biol. Cell*. **25**, 2522–2536 (2014).

ACKNOWLEDGEMENTS

Many kind people have supported me throughout the time of my PhD contributing to the completion of this thesis in different ways and I would like to take the opportunity to thank them here.

First of all, I thank my supervisor Jan Ellenberg for giving me the opportunity to work on this PhD project and for guiding me from writing PhD fellowship applications at the beginning to paper manuscripts at the end. I would also like to thank him for always being excited about the research and still optimistic, when technical difficulties were challenging the progress of the project.
I would also like to thank the members of my thesis advisory committee, Sylvia Erhardt, Peter Lénart and Takashi Hiiragi for their constructive input and kind support throughout the last years; their suggestions were critical to shape the project and this thesis.

When I started to work on this PhD project, especially my former colleagues Judith Reichmann, Bianca Nijmeijer-Winter and Manuel Eguren greatly helped me to get familiar with the handling of the challenging preimplantation mouse embryo model and with the inverted light sheet microscope. I would like to thank them warmly for taking the time to teach me initially and for being supportive throughout my PhD and sharing their expertise, whenever I asked for advice.
I would also like to thank Marta de Ruijter-Villani for being the best collaborator I could have wished for. Her positive attitude and our interaction and exchange of ideas have been a great asset to my PhD experience.
In addition, I warmly thank my colleague Julius M. Hossain, who has greatly supported Marta and I throughout the last two years. I would describe him as the most humorous, but also most committed, supportive and selfless colleague one could imagine. It has been a blast for me to work with him and I truly learned a lot from him – not only about mathematical approaches for automated data analysis, but also about values in life.
I would also like to thank my colleague Sandra Correia for offering a helping hand with all complicated experiments, for taking over the animal genotyping, and for being supportive all

through. I am extremely glad about the friendship we have developed and thank her for not only supporting me at work, but also when I faced any personal problems.
I would also like to thank my former colleague Beatriz Serrano-Solano for helping me with cluster computing and for building bridges between disciplines. We have developed a nice friendship and I also thank her for many fun conversations and her personal support. In addition, I thank my former colleague Vilma Jimenez Sabinina for sharing her experience, and lots of materials while still being a group member, but also for our really nice and motivating conversations thereafter.
For sharing materials, scripts and scientific thoughts, I would also like to thank my former PhD peer Øyvind Ødegård-Fougner. I would also like to thank Jean-Karim Hériché for providing scripts for data processing and for his support with cluster computing.
I also warmly thank Nathalie Daigle for support with every work-related question, from cloning to data archiving, but I also thank her for lots of personal advice.
Also, I would like to thank Stephanie Alexander for her input on the project, as well as on fellowship applications and manuscripts.
In addition, I would like to thank all other former and current members of the Ellenberg group for their scientific suggestions, for participating in lots of common fun activities and for creating a nice working atmosphere. Thank you to Arina and Nike for the nice breaks and cheerful discussions; to Merle and Franzi for strengthening the team spirit of the lab and for their help and advice; to Andi for our really nice and motivating conversations during 'Corona-conform' lunch meetings; to Hannah, Anniken and Eirini for help with animal genotyping; to Andrea and Moritz for their kind support whenever I asked for it; to Natalia for being so friendly and always ready to help out spontaneously; to Dimi for his help with any microscopy related issues; to Kai, who would answer any scientific question; to Wanlu for always being friendly and supportive; to Koki for his excitement about the project; and to Jana and Taisha for their investment in team activities for the group throughout the last year.
I would also like to thank Adele and Marjolein for their great support throughout my PhD, for organizing many fun activities for the group and for always having an open ear.

The inverted light sheet microscope used in this project provided the technological basis to investigate cellular mechanisms within the mammalian embryo with unprecedented temporal and spatial resolution, and I would like to thank Petr Strnad for initially building it. I

would also like to thank co-developer Lars Hufnagel, especially for his support to maintain the system. I also thank Yu Lin for her additional help with the setup. A gigantic 'thank you' goes also to the EMBL electronical workshop, especially to Christian Kieser, who has always reliably helped me with any hick-ups of the system, from adjusting the microscope's atmosphere control system to replacing stages.

Light sheet microscopy generates gigantic data sets, and I thank Christian Tischer for developing a new image processing pipeline. It has been a great pleasure to work with him.

I would also like to thank the laboratory animal resource (LAR) facility at EMBL for lots of support with handling and breeding the mice. Especially Daniel Stoga has made a huge effort by keeping an eye on the details to improve experiments and maintain animal colonies. I would also like to thank George-Eugen Maftei and Alessandro Grassi for their training, and a special thanks goes to the former LAR members Andrea Genthner and Klaus Schmitt, who have been particularly patient and helpful throughout.

I would also like to thank Jacob Scheurich and Kim Remans from the Protein Expression and Purification Core Facility and all members of the Advanced Light Microscopy Core Facility for their support, training and advice, and I also thank the members of the Szilard Library for being so responsive and helpful.

In addition, I would like to say thank you to the current and previous members of the EMBL Graduate Office for their kind support throughout the years making sure to always answer all of my questions.

I also thank Boehringer Ingelheim Fonds (BIF) for a fantastic PhD fellowship and I very warmly thank the BIF team for the personal support throughout the time of the fellowship, but also thereafter.

Finally, I would like to thank my family, my parents and sisters, for supporting me and for being ok with me investing lots of time and energy into this PhD.

I also thank Christopher, my partner in life, for his relentless support throughout the last years, I would not have completed my PhD without him. He is the most energetic, driven and optimistic person I know, and I thank him for sharing his optimism. And I would also like to thank his family for their kindness, and especially for helping me throughout difficult times.